LEGIBILITY NOTICE

A major purpose of the Technical Information Center is to provide the broadest dissemination possible of information contained in DOE's Research and Development Reports to business, industry, the academic community, and federal, state and local governments.

Although a small portion of this report is not reproducible, it is being made available to expedite the availability of information on the research discussed herein.

1

ORNL/M--672

DE89 004298

PROPOSAL FOR

A HEAVY ION STORAGE RING FOR ATOMIC PHYSICS

November 1988

OAK RIDGE NATIONAL LABORATORY
Oak Ridge, Tennessee 37831
operated by
MARTIN MARIETTA ENERGY SYSTEMS, INC.
for the
U.S. DEPARTMENT OF ENERGY
under Contract No. DE-AC05-840R21400

C O N T E N T S

1.0 INTRODUCTION

This document presents a proposal for a Heavy Ion Storage Ring for Atomic Physics, HISTRAP, to be operated as a National User Facility for advanced atomic physics research. With ions injected either from the 25-MV tandem of the ORNL Holifield Facility, or from its own stand-alone injector system, HISTRAP represents a new class of scientific instrument that will provide new opportunities for basic and applied research with multicharged ions. HISTRAP will provide research capabilities not available from any other facility in North America.

The proposed research program on HISTRAP places its emphasis on atomic physics. This program will be directed toward solving problems in fundamental atomic collision and structure physics, and toward producing data of direct application to technologies in which regions of high energy density are produced and utilized, such as nuclear fusion, fission, X-ray lasers, etc. Such systems deal with high temperature plasmas involving collisions and radiation from multiply charged ions. It is particularly in this area of physics that HISTRAP can make major new and unique contributions. Additional areas of research include molecular ion physics, new forms of "solid state systems" consisting of highly ordered structures in cooled ion beams, and certain experiments in nuclear physics which require high energy, high quality ion beams.

This proposal centers on the construction of a small synchrotron storage ring with a circumference of 47 meters and a maximum bending power of 2.7 Tesla-meters. The ring will be capable of accelerating light ions to 83 MeV/nucleon and uranium to 12 MeV/nucleon. An essential component of this ring is an electron beam cooler. The resultant cooling capability

for heavy ions will enable production of beams of extremely high quality for precision spectroscopic and collision studies. In addition, the electron beam cooler will allow deceleration of highly charged heavy ions down to energies of 20 keV/nucleon. The ring will be located adjacent to the 25-MV electrostatic tandem accelerator of the Holifield Facility in order to capitalize on the wide range of ion beams produced by this accelerator. The HISTRAP project also includes a dedicated injector system to allow continuous operation of the facility when the 25-MV tandem is operating for other programs. Storage of low-energy, multicharged heavy ions in the ring will require an extremely good vacuum: The ring is designed to achieve pressures in the 10^{-12} Torr region. The project includes building additions to house the ring and to house the associated power supplies and electrical distribution equipment. The project is expected to take about 51 months to complete, with first beam scheduled 45 months after start of the project. The total project cost is $16 million, assuming an FY 1990 construction start and including engineering, escalation, and contingencies.

Chapter 2 presents an overview of the physics capabilities of HISTRAP together with a brief description of the facility and a sampling of the beams which will be available for experimentation. Chapter 3 surveys some of the lines of investigation in the physics of multicharged ions, molecular ion spectroscopy, condensed beams, and nuclear physics that will become possible with the advent of HISTRAP. Chapter 4 details the accelerator design, including computer studies of beam tracking in the HISTRAP lattice, a discussion of the HHIRF tandem and ECR/RFQ injectors, and a description of the electron beam cooling system.

In the past three years, HISTRAP has received substantial support from Oak Ridge National Laboratory management and staff. The project has used discretionary funds to develop hardware prototypes and carry out design studies. Construction has been completed on (1) a vacuum test stand which models 1/16 of the storage ring and has attained a pressure of 4×10^{-12} Torr; (2) a prototype rf cavity capable of accelerating beams up to 90 MeV/nucleon and decelerating to 20 keV/nucleon; and (3) a prototype dipole magnet, one of the eight required for the HISTRAP lattice. These studies are described in Chapter 5. This chapter also contains a summary of the work on electron cooling carried out by one of our staff members at CERN.

Building structures and services are described in Chapter 6. Details of cost and schedule are discussed in Chapter 8 of this proposal.

From the inception of ORNL interest in this project, in 1984, staff members have published more than 30 papers on HISTRAP and HISTRAP-related physics. These papers are listed in Appendix A. A "Workshop on Atomic Physics witn Stored Cooled Heavy Ion Beams" was held at ORNL in April 1986 and was attended by 60 physicists. A copy of the workshop program is included as Appendix B. A follow-up on the workshop was held in February 1987, when a users advisory group was convened to discuss the experimental program and facilities for HISTRAP. A summary of the salient reasons for the location of a heavy ion storage ring for atomic physics at Oak Ridge is given in Chapter 7.

2.0 HISTRAP - NEW OPPORTUNITIES IN ATOMIC PHYSICS

"The recent history of collision physics has been initially linked to a specific expertise – namely that of electron and ion beams technology. Every significant advance in the production of such beams has resulted in new crops of important scientific advances." Atomic Physics: A Renewed Vitality, Physics Today, November 1981. Prof. B. Bederson, New York University, Editor of Physical Review A.

Although the concept of storage rings with cooling capability has been with us for some time, their application to atomic physics is a new development. These facilities will supply beams of very high brightness for precision experiments into realms which have, heretofore, been impossible to attain either because of lack of intensity or lack of precision, or too high a degree of random motion within the beam or source. There are many advantages that these devices have over the conventional arrangements. In plasma sources, high temperatures (Maxwell-Boltzman distributions) and multiple chain events obscure individual processes. Even the very promising Electron Beam Ion Trap claims only 70 eV resolution in electron ion collisions. Accelerator beam-stationary target arrangements are often limited by too low a current, too short an interaction time, or too thin a target. One of the disadvantages of all existing sources of ions beams is the lack of control over the distribution of states in the extracted beams. In many cases, the beams are found to be mixtures of ground and metastable states. The mix is often statistical, sometimes unreasonably dominated by metastables, but almost never predictable. It has proven difficult, in most cases, to determine the metastable fraction since there is no accepted diagnostic which is

reliable and universal, and control of the metastable fraction by changing source conditions or through controlled collisions along the beam line has not yet been successful for highly charged ions.

Circulating beams provide an elegant solution to the problem of controlling the target ion beam metastable fraction. Since most metastable levels of highly charged ions have lifetimes on the order of 100 microseconds or less, a beam that has been circulating for a few milliseconds will be essentially pure ground state. The use of a pure projectile ion beam greatly increases the usefulness of data for many of the specific examples which will be discussed in Chapter 3.

A subcommittee set up by the Committee on Atomic, Molecular and Optical Sciences (CAMOS) of the National Academy of Science/National Research Council has studied the need for heavy ion storage rings in the United States, and issued a report "Ion Storage Rings for Atomic Physics Research" [Ca88] which contains the following statement:

> **"After judging the scientific opportunities, the value of the research to other areas of science and to our national programs in controlled fusion and defense and the quality of proposals generated by the U.S. scientific community, the Panel recommends that the Department of Energy undertake to support the construction of at least one electron-cooled heavy-ion storage ring facility in the United States."**

The advantages obtainable in HISTRAP are manifold. By circulating the beam in the ring, one is able to purify the beam of metastable states by allowing time for decay; to obtain an effectively high current; and to obtain better emittance by phase space "cooling". This cooling is accomplished by merged electron beams or laser interactions. Properly cooled beams can be used to study electron-ion collisions with

resolution of ~0.1 eV, which is sufficient to separate closely spaced resonances, or, in some cases, it may be possible to study "crystalized" ion beams. Another advantage is the capability to accumulate more rare ionic species through multiturn injection and to utilize the same, and possibly expensive, ions passing through a thin target many times. Sometimes a thin target is unavoidable, as in the case of a free electron target of limited density, and sometimes a thin target is necessary for the experiment, as when one is searching for a small cross section event in the presence of large cross seccion events. An example would be an investigation which requires very high energy resolution. Here, one cannot use a thick target in which the particle energy is degraded and straggled. Another example is the interference of sequential, large cross section, single-electron-transfer events where one is searching for small cross section, multiple-electron-transfer events in a single collision.

HISTRAP will have two injection systems. First, the HHIRF which is the highest voltage, 25 MV, electrostatic accelerator extant together with its highly developed wide variety of ion beams. Since the 25 MV tandem facility is also in demand by other programs, the second and dedicated source is a 14.5 GHz electron cyclotron ion source (ECR) coupled with a 250 keV/nucleon radio frequency quadrupole (RFQ). With these two systems, the facility is capable of 100% time utilization with the entire range of ions available at the choice of the HISTRAP experimenter.

Because of large, ±4%, momentum aperture, HISTRAP will have the capability of simultaneously storing several adjacent charge states that may have been built up from the primary beam by ionization or recombination.

Because of its dual ion injection system, HISTRAP will have the capability of merging beams of equal rigidity but differing charge and energy, or beams which vary in rigidity by as much as 8%, which will allow study of a wide range of collisions between multicharged ions.

Because of its acceleration and deceleration capabilities, cooled beams with energies as low as 20 keV/nucleon can be used in precision spectroscopy, and with the upper bending power of 2.67 Tm, beams of 82 MeV/nucleon ions (for A/Z = 0.5) of higher brightness and overall quality (not available elsewhere in the U.S.) could be used for precision nuclear experimentation.

The idea of the utility of cooled heavy ion storage rings has not escaped notice elsewhere, and several projects are presently underway around the world. These projects, listed in Table 2.0-1, all have different capabilities and goals. The larger rings at GSI and JÜlich are oriented towards nuclear physics. The Heidelberg ring, although it is somewhat smaller in scale than HISTRAP, in both its injector capability and ultimate energy, should have significant atomic physics components. However, its present primary goal is the development of a method to polarize a stored proton beam by polarized electron interactions, the purpose being, ultimately, to produce a polarized antiproton beam in the LEAR ring at CERN. The atomic physics program centers on the production

of ultracold beams. Compared to HISTRAP, the Stockholm ring has significantly lower injection capability and lower magnetic rigidity. The Aarhus ring is to have three functions: (1) to store low-energy, singly charged ions for experiments in laser cooling; (2) to serve as an electron synchrotron light source; and (3) ultimately to accept heavy ion injection from an EN Tandem Van de Graaff with a maximum terminal voltage of 6 MV.

Table 2.0-1. Heavy-ion storage rings with electron beam cooling presently under construction.

Site	Approximate Strength	Heavy Ion Injection
Aarhus, Denmark "ASTRID"	1.8 T•m	200-keV isotope separator or EN tandem
Heidelberg, W. Germany "TSR"	1.5 T•m	MP Tandem + Linac
Stockholm, Sweden "CRYRING"	1.4 T•m	CRYEBIS + RFQ
CERN, Switzerland[a] "LEAR"	7.0 T•m	Linac - RFQ
GSI, Darmstadt, W. Germany "ESR"	10.0 T•m	GSI - UNILAC
Uppsala, Sweden[b] "CELCIUS"	7.0 T•m	Cyclotron
Tokyo, Japan[b] "TARN II"	6.9 T•m	Cyclotron

a) Electron beam cooling and heavy ion capability to be added to this functioning facility.

b) Heavy ion capability is planned for future.

The HISTRAP facility has significant differences in both objective and capability. Compared with the other atomic physics machines at Stockholm, Aarhus, and, to some extent, Heidelberg, HISTRAP's injection system can supply ions with significantly higher charge states at significantly higher energies. Since the space charge limit on loading the ring is determined by the injection energy, this leads to higher ion density in the ring. HISTRAP's higher magnetic rigidity, 2.7 Tm compared to ~1.6 Tm, leads to acceleration and storage at energies up to ~3 times higher. The higher energy results in higher flux, faster cooling and, because of lower capture cross section on background gas, longer storage time. In addition, for recombination experiments, the higher energies give higher signals because of the increased electron beam density at relevant relative velocities, and lower noise because of reduced capture background.

2.1 A Brief Description of the HISTRAP Facility

The synchrotron ring of ~46.8 m in circumference is shown in Fig. 2.1-1 and some overall parameters are given in Table 2.1-1. The ring will consist of 8 dipole bending magnets, 12 quadrupole focussing magnets, and 16 sextapoles, all arranged in a fourfold symmetric lattice. The magnets will be clustered into four 90° bending sections so as to leave four 4-m-long straight sections free for placement of injection and possibly future ejection devices, a radio frequency accelerating/decelerating cavity, an electron beam cooling system, and various pieces of experimental apparatus. The magnet gaps and straight

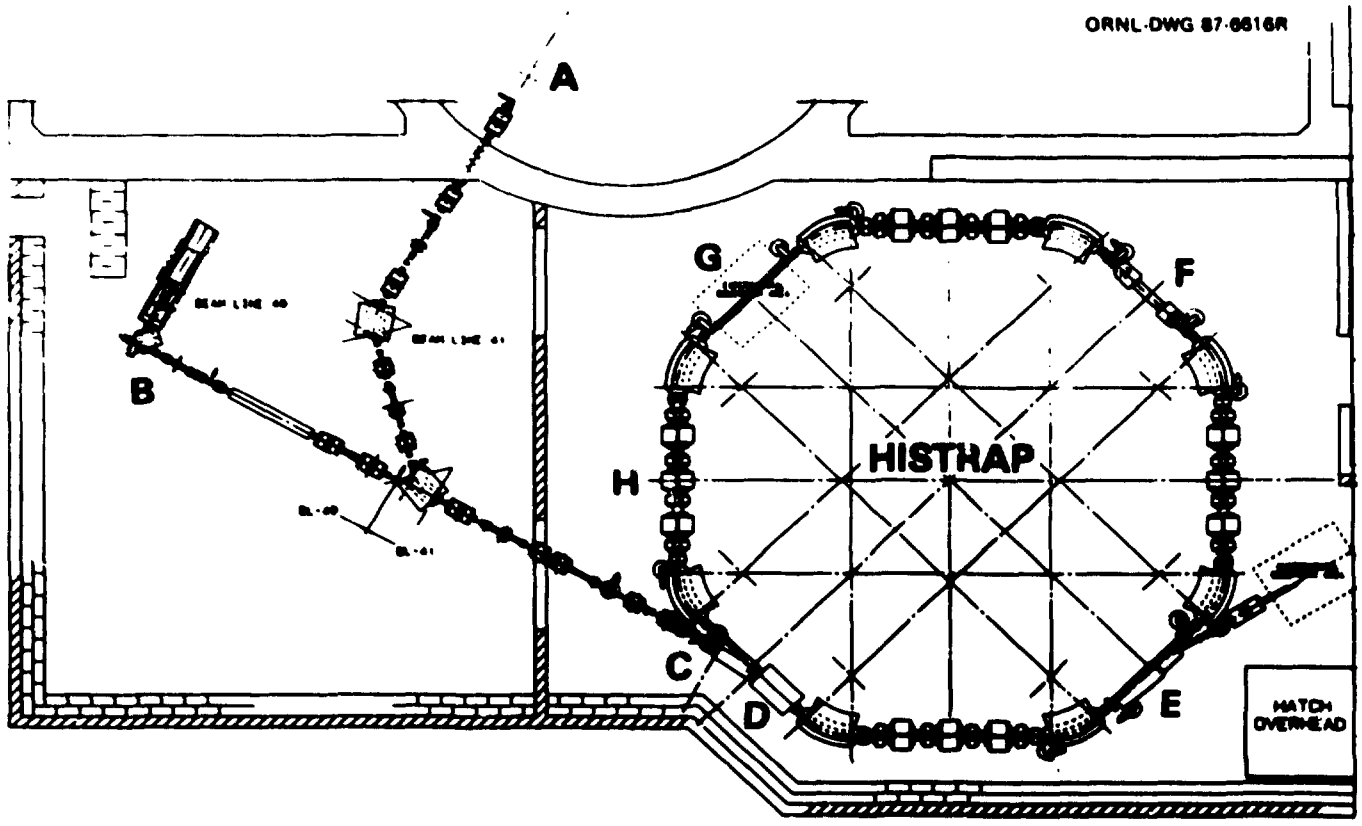

Fig. 2.1-1 Plan view of HISTRAP which will be injected with either the tandem accelerator or a dedicated ECR/RFQ accelerator.

Table 2.1-1. ORNL HISTRAP: Heavy-Ion Storage Rings for Atomic Physics.

PARAMETERS:	
Circumference	46.8 meters
Maximum Rigidity	2.67 Tesla meters
Maximum Energy ($^{12}C^{6+}$ $^{238}U^{43+}$)	82-11 MeV/nucleon
Minimum Energy ($^{238}U^{43+}$)	20 keV/nucleon
Magnet System	
Betatron Acceptance	200π(h) x 60π(v) mm mrad
Momentum Acceptance	±4%
Dipole Field	1.6 T
Number of Dipoles	8
Good Field Aperture	12 cm x 5 cm
Quadrupole Gradients	7.3 T/m
Number of Quadrupoles	12
Good Field Aperture	±8 cm
Total I^2R Loss at Maximum Field	400 kW
Injectors	
(a) Existing 25-MV tandem electrostatic generator	
(b) ECR source on 60-kV platform plus 200 keV/nucleon RFQ	
Radio Frequency System	
Voltage	2.5 kV
Tuning Range	0.2-2.6 MHz
Harmonic	1-6
Vacuum System	
Composition	950°C vacuum baked S.S.
Base Pressure	10^{-12} Torr
In Situ Bakeout Temperature	300°C
Pumping (UHV)	NEG, ion, and TSP
Electron Beam Cooler	
Voltage	60 kV
Current	5 A
Regulation	$\pm 10^{-5}$
Beam Diameter	5 cm
Cooling Region Length	100 cm

sections will be threaded by a continuous, stainless steel beam pipe that can be evacuated to pressures as low as 10^{-12} Torr.

The magnet system will be able to bend and focus beams of magnetic rigidity up to 2.67 Tm. This corresponds to maximum kinetic energies of 82 MeV/nucleon for light ions, such as $^{12}C^{6+}$, which have Q/A = 1/2, and 20 MeV/nucleon for very heavy ions, such as $^{197}Au^{48+}$, which have Q/A ~ 1/4. The resulting energy per nucleon versus mass number performance is shown in Fig. 2.1-2 for the various injection modes.

To inject beams of ions at high charge states into the ring, an injection line capable of a very high degree of charge discrimination will be constructed from the nearby tandem electrostatic accelerator of the Holifield Heavy Ion Research Facility. Operating at 25 MV, this accelerator can provide beams ranging from $^{12}C^{6+}$ to $^{238}U^{51+}$ by poststripping. Any lower charge state is also available.

The HHIRF tandem is the primary accelerator for the fixed target nuclear physics research program at ORNL, and is run by ORNL as a national users' facility. It will be available, therefore, only part of the time for injecting into the HISTRAP ring. Thus, a second, local injector consisting of a 14.5 GHz ECR ion source coupled to an RFQ linac pre-accelerator is included in this proposal. This injector would produce beams of 250 keV/nucleon for injection. Although, for the heaviest ions, it produces lower charge states than those obtained by poststripping after the tandem, it is a relatively simple device to operate, has a small power consumption, and will be always available for use by the atomic physics program.

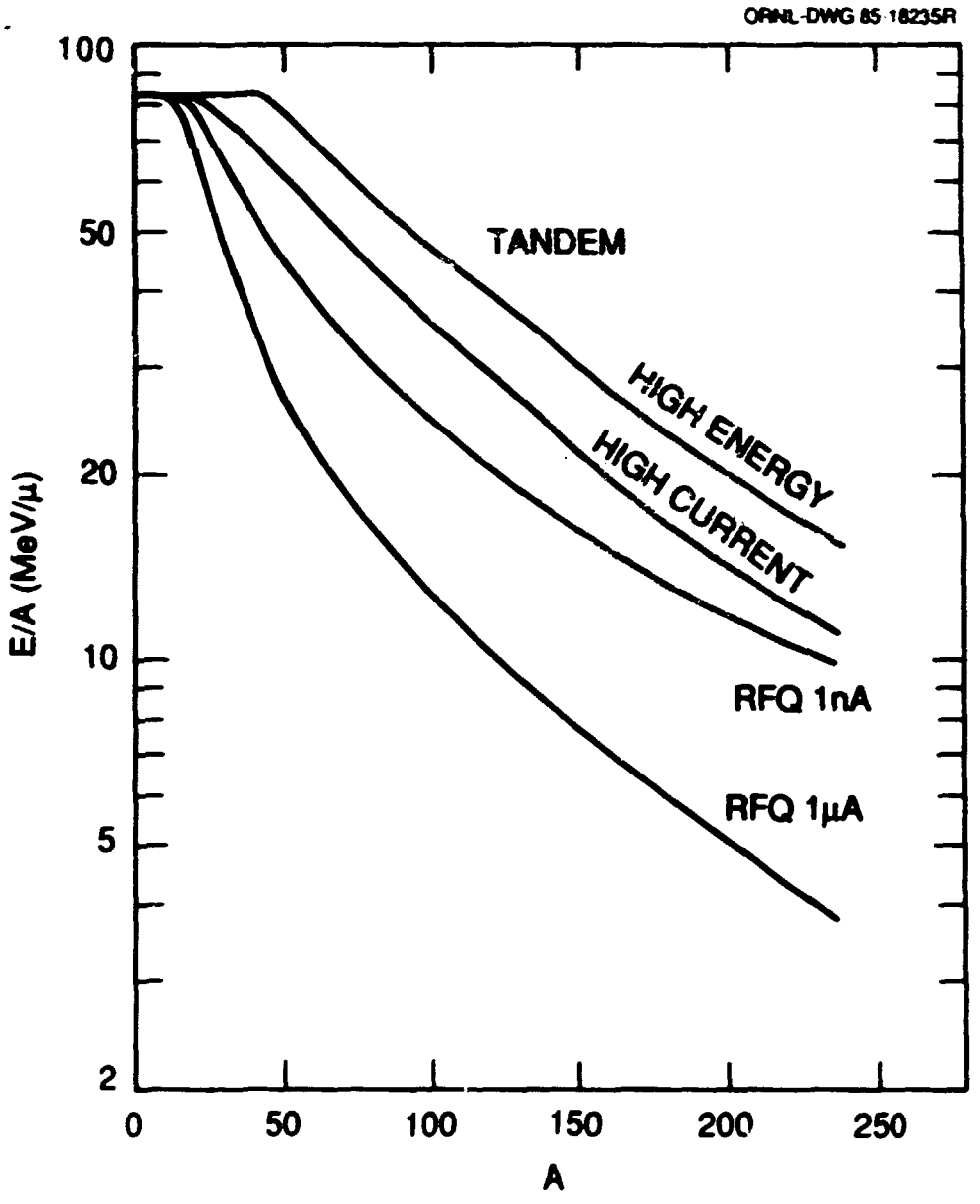

Fig. 2.1-2 Maximum energy in MeV/nucleon versus mass number for both tandem and ECR/RFQ injection of HISTRAP. For each injector, a high-current case and a high-energy case are shown.

One of the HISTRAP straight sections is equipped with an electron beam cooling system. This system can generate an intense beam of cold electrons with a beam diameter of about 5 cm. If this electron beam, using appropriate toroidal and solenoidal magnets, is merged with the ion beam and matched in velocity, it can shrink the phase-space volume of the ion beam. Improvements in emittance and energy spread by factors of 10 or more are possible. The electron beam, whose energy can range from 1 to 60 keV, can be used as a precise electron target for in-ring ion-electron collision experiments.

The ring has been designed to accept a momentum/charge state spread of ±4%. Consequently, more than one charge state can circulate in the ring for beams of $Q > 12^+$. This is a useful feature in experiments resulting in electron capture or ionization. This feature also allows injection using both the tandem and ECR/RFQ sources for in-ring ion-ion collision experiments.

Space has been left in the ring circumference to allow the addition, in the future, of a slow resonant extraction system to extract any beam which might be accelerated by the ring. It would be used, for example, to extract decelerated beams, whose vacuum lifetimes would not allow them to be stored for more than a few seconds in the ring, for experimentation in the more familiar single-pass fixed-target type arrangement. It would also be used for very high energy beams which could be guided through the HHIRF beam lines for experiments with the extensive set of existing instruments and detectors.

The dipole magnets have been designed as C magnets to allow ease of merging a laser beam with the ion beam. The vacuum chamber in a dipole

could be replaced with a special chamber containing, for example, apparatus for measuring multiple charge-state distributions. One entire 4-m-long straight section has been kept free in order to allow experimenters to insert their own apparatus. In addition, space with dispersion will be available between the quadrupole magnets for experimental apparatus. Moreover, the lattice has been designed so that dispersion can be adjusted into the 4-m straight section as required by the experiment. The vacuum system is designed to bake at 350°C. It includes all-metal UHV valves at the ends of each straight so that apparatus in any one octant of the ring can be accessed without affecting the ultra-high vacuum in the remainder of the ring.

The ring will be housed in a new, shielded room to the south of the HHIRF tandem tower and just east of the new Atomic Physics and Applications Annex. The site plan is shown in Fig. 2.1-3. The facility will be self-contained so that it can operate independently of the HHIRF accelerators. Access to the powerful data collection computers of the HHIRF will be provided. It is intended to operate the facility as a national user facility, as is the HHIRF, and effort has been expended to make it easily accessible to outside users.

2.2 Electron Cooling

The principle of the electron cooling process is the removal of random motion within the ion beam by Coulomb scattering from a cold array of electrons and is similiar to electronic stopping. It is accomplished by "bathing" the circulating hot ion beam in a continuously replenished "cold" electron beam moving at the same velocity.

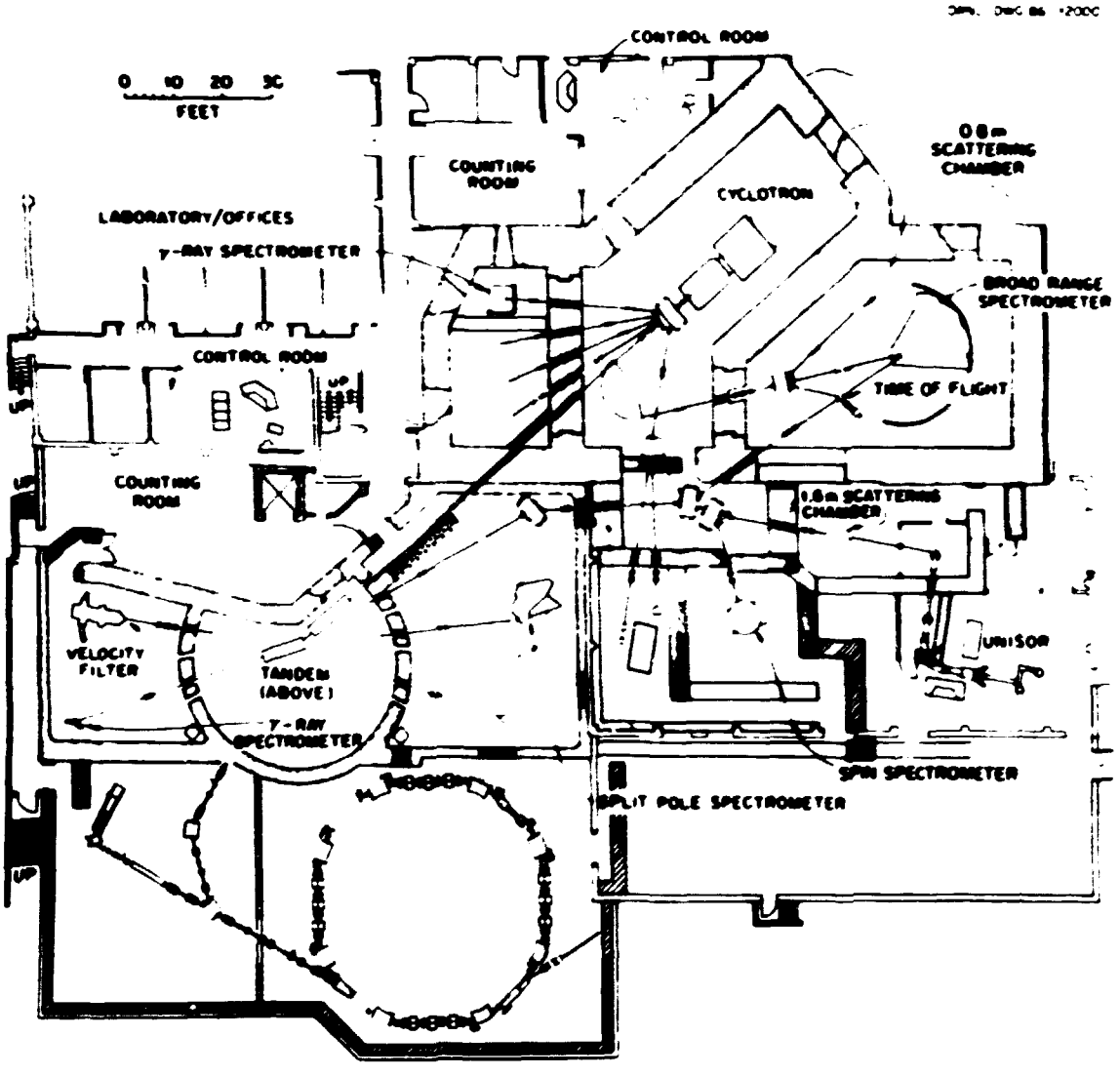

Fig. 2.1-3 Site plan for the HISTRAP facility showing its location in the HHIRF complex.

The velocity spread of the two particle beams can be characterized by two temperatures, the ion temperature T_i and the electron temperature T_e. In the case of HISTRAP, it is planned to have an electron beam 5 cm in diameter, variable energy between 1 keV and 60 keV, a current of up to 5 amperes, and a transverse temperature of 0.2 eV. Under cooling conditions, the average electron longitudinal velocity $\langle u \rangle$ is equal to the average ion longitudinal velocity $\langle v \rangle$. In this frame of reference, the temperatures can be related to the spreads of the two velocities:

$$\Delta v = (2kT_i/m_i)^{1/2}, \qquad \Delta u = (2kT_e/m_e)^{1/2}, \qquad (2.2\text{-}1)$$

where m_i and m_e are ion and electron mass, respectively. Cooling is mediated by collisions between ions and electrons moving with a relative velocity $\vec{v}_r = \vec{v} - \vec{u}$ with respect to each other. This leads to a $1/v_r^2$ dependence of the cooling force up to the equilibrium temperature as shown in Fig. 2.2-1. At thermal equilibrium $T_i = T_e$ and $\Delta v = (m_e/m_i)^{1/2}$ Δu. This would result in a very small ion velocity spread if there were no beam heating processes, such as intrabeam scattering, target scattering, etc. Because beam cooling is in equilibrium with heating, these heating effects determine the ion temperature. Because of heating from intrabeam scattering, the energy spread of a cooled beam in HISTRAP is estimated to be in the order of $\Delta E/E = 10^{-4}$. This energy spread is proportional to the number of stored ions, and values in the order of 10^{-5} can be reached by reducing the stored ion density. After the beam is cooled, it is expected that the electron beam velocity can be varied relative to the ion beam velocity for electron ion collision experiments or for cooling two simultaneously stored beams of different velocity but the same magnetic rigidity.

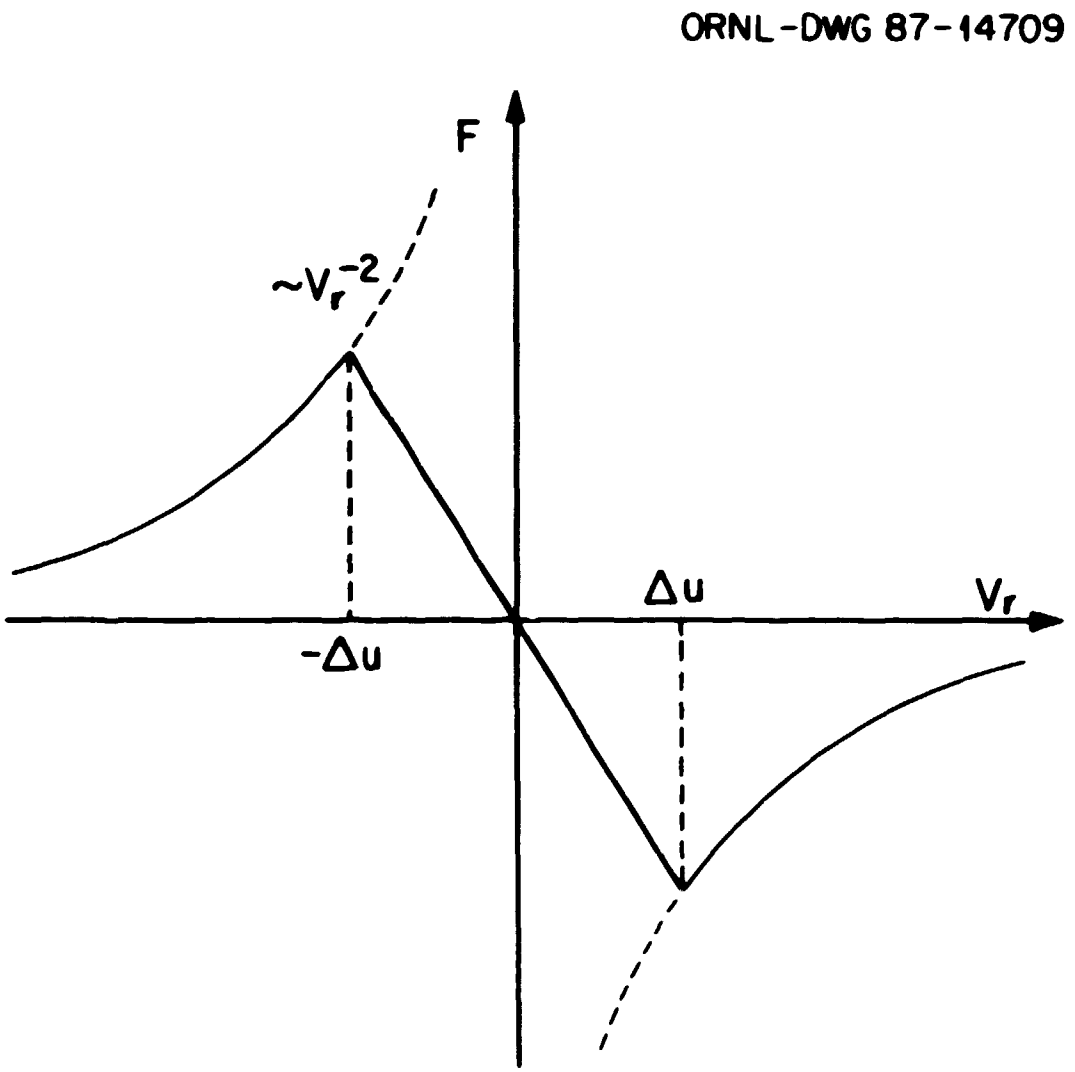

Fig. 2.2-1 Dependence of the electron beam cooling force on the equilibrium temperature.

2.3 Heavy Ion Beams

2.3.1. Circulating Beams

The species, charge state, energy, circulating current, momentum width, and emittance of stored beams are all interrelated and are a strong function of the nature of the injection system, as well as the design parameters of the ring. The number of ions, N_{sc}, which can be stored in the ring is limited by space charge. In the nonrelativistic limit

$$N_{sc} = 2.3 \times 10^{14} \, (E/A) \, (A/Q^2)\varepsilon \qquad (2.3\text{-}1)$$

where E/A is the ion energy in MeV per atomic mass unit, A; Q is the ion charge; and ε is the beam emittance in units of π meters assuming equal horizontal and vertical emittances. Another limit on the number of ions which can be stored, the Kiel-Schnell limit, is given by

$$N_{ks} = 3.5 \times 10^{15} \, (E/A) \, (A/Q^2) \, (\Delta P/P)^2 \qquad (2.3\text{-}2)$$

where $(\Delta P/P)$ is the relative momentum spread in the beam. Above this limit plasma instabilities may set in.

From these relationships, it is clear that the number of ions which can be stored depends on the beam energy at injection and upon the emittance of the stored beam in the ring. The emittance of a HHIRF tandem beam is small and will permit at least 35-turn injection and, when taken together with its higher charge state capability, is a better injector than the ECR/RFQ system with its poorer emittance which will permit only about 9-turn injection.

A plasma sputter cusp field negative-ion source at the HHIRF will be capable of supplying pulsed beams with intensities greater than

about 1 mA. This beam will be accelerated, stripped, and injected into HISTRAP. With the large acceptance aperture of HISTRAP, at least 35 turns of such a beam can be stored. Taken with the circumference of 46.8 m and assuming a 40% tandem transmission and a 20% rf loss, a 1-mA beam will provide a stored ion number N_{st} given by,

$$N_{st} = 2.4 \times 10^{11} (E/A)^{-1/2} f, \qquad (2.3\text{-}3)$$

where (E/A) is the energy at injection in MeV/A and f is the charge state fraction transmitted to the target.

Table 2.3-1 lists the maximum energies and circulating currents for injection from the HHIRF tandem under two sets of conditions. The left-hand portion (A) assumes tandem operation at 22 MV, the present routine operating voltage for injection of the Oak Ridge Isochronous Cyclotron, and the most probable charge state obtained by foil stripping first at the terminal and then just prior to injection into HISTRAP. For this table, it was assumed HISTRAP would be filled at injection to the space charge limit which would require between 1 and 2 mA of negative beam injected into the tandem. The right-hard portion (B) of Table 2.3-1 assumes the same injection current but a 25-MV terminal voltage (the present maximum) and a higher, but a factor of 20 less probable, charge state. This is obtained by choosing at the terminal stripper, a charge state which is one-half as abundant as the most probable, and at the second stripper, a charge state one-tenth of the most probable.

Table 2.3-2 shows the results for two cases of injection from the ECR/RFQ system at 250 keV/nucleon. In the first case, a charge state which can be supplied at a current of 1 pμA from the ECR/RFQ is chosen.

Table 2.3-1. For HHIRF tandem injection, the charge state, maximum energy, and circulating current (at that energy) for beams (A) of most probable charge at 22-MV terminal voltage and (B) 5% of most probable charge state intensity at 25-MV terminal voltage.

Ion	(A) 22-MV Terminal Voltage Most Probable Charge			(B) 25-MV Terminal Voltage 5% Most Probable Charge		
	Q	$(MeV/A)_{max}$	Circulating pmA	Q	$(MeV/A)_{max}$	Circulating pmA
$^{12}C_6$	6	82.2	37.6	6	82.2	1.9
$^{16}O_8$	8	82.2	27.8	8	82.2	1.4
$^{32}S_{16}$	15	72.7	10.8	16	82.2	0.58
$^{40}Ca_{20}$	18	67.1	7.5	20	82.2	0.41
$^{58}Ni_{28}$	24	57.1	4.7	27	71.7	0.26
$^{79}Br_{35}$	27	39.3	3.1	32	54.8	0.18
$^{127}I_{53}$	36	27.2	1.7	42	36.8	0.10
$^{150}Nd_{60}$	38	21.8	1.4	44	29.1	0.08
$^{197}Au_{79}$	40	14.1	1.1	48	20.2	0.07
$^{238}U_{92}$	43	11.1	0.9	51	15.6	0.05

Table 2.3-2. For ECR/RFQ injection, the charge state, maximum energy, and circulating current (at that energy) for beam available at 1 pμA and 1 pμA.

Ion	1 pμA Injection			1 pnA Injection		
	Q	$(MeV/A)_{max}$	Circulating pμA	Q	$(MeV/A)_{max}$	Circulating pμA
$^{12}C_6$	6	82.2	486	6	82.2	0.486
$^{16}O_8$	8	82.2	486	8	82.2	0.486
$^{32}S_{16}$	12	47.1	366	14	53.6	0.427
$^{40}Ca_{20}$	13	35.6	318	16	43.5	0.391
$^{58}Ni_{28}$	15	22.7	252	20	40.0	0.336
$^{79}Br_{35}$	17	15.8	210	23	28.8	0.284
$^{127}I_{53}$	21	9.3	162	30	19.0	0.230
$^{150}Nd_{60}$	22	7.4	143	33	16.5	0.215
$^{197}Au_{79}$	24	5.1	119	39	13.4	0.193
$^{238}U_{92}$	25	3.3	103	41	10.1	0.169

For all species, 1.2×10^9 ions are injected in 10 turns with a $\Delta P/P = 5 \times 10^{-3}$. For all species, the stored number of ions is below the space-charge limit. For the second case, the same conditions are applied and a higher charge state is chosen. In particular, an ECR/RFQ beam with a charge state such that only 1 pnA intensity is injected. Ten turns are injected, giving 1.2×10^6 stored ions.

The above limits pertain to the beam upon injection. When the beam is cooled, both the emittance and $\Delta P/P$ is decreased, thereby lowering both N_{SC} and N_{KS}. Again, the advantages of the higher values of E/A achievable in HISTRAP are obvious, that is, acceleration to high energies before cooling can increase ring capability for a given emittance. Let us consider an extreme case: A beam of U^{51+} is injected and then decelerated to 20 keV/nucleon and cooled so that $\varepsilon = 1.0\ \pi$ mm-mrad and $\Delta E/E = 0.0005$. In this case, the space-charge limit is 1×10^6 ions with circulating current of 0.34 pμA. In this example, the ring could be filled with only a single turn from the tandem, operated in the high charge state mode. On the other hand, this example points up another important advantage of the HISTRAP. Substantially, the same circulating current could be achieved for a higher charge state, which is 35 times less probable than U^{51+}, using the 35-turn injection prior to cooling at the high energy.

2.3.2. Extracted Beams

The extracted beam currents depend upon the cycle rate which, in turn, is limited by the cost of the magnet power supplies. The power supplies specified in the current proposal can cycle the magnets at

about 0.4 Hz repetition rate. The extracted beam currents could be increased by about a factor of four, but this would require considerable additional investment. The extracted beam currents using the ECR/RFQ injector and a 0.4-Hz cycle rate would, in all cases, be limited to about 1.0 ppA. The extracted beam currents for tandem injections are listed in Table 2.3-3 for both 0.4-Hz and 1.6-Hz cycle rates.

Table 2.3-3. Circulating and extracted beam currents at maximum energy for maximum current tandem injection. HISTRAP will operate with about a 0.4-Hz cycle rate; 1.6 Hz could be possible. The currents are calculated assuming HISTRAP will be filled to the space charge limit.

ION	CHARGE	$(MeV/A)_{max}$	CIRCULATING pmA	EXTRACTED pnA 0.4 Hz	1.6 Hz
^{12}C	6	82.2	37.6	6.8	27.4
^{16}O	8	82.2	27.8	4.4	17.7
^{32}S	15	72.7	10.0	1.8	6.9
^{40}Ca	18	67.1	7.5	1.3	5.1
^{58}Ni	24	57.1	4.7	0.87	3.5
^{79}Br	27	39.3	3.1	0.69	2.8
^{127}I	36	27.2	1.7	0.45	1.8
^{150}Nd	38	21.8	1.4	0.40	1.6
^{197}Au	40	14.1	1.1	0.38	1.5
^{238}U	43	11.1	0.9	0.36	1.4

3.0 SCIENTIFIC JUSTIFICATION

HISTRAP is a multipurpose user facility capable of carrying out research in multiply-charged-ion atomic physics, molecular ion spectroscopy, condensed "crystalline" beams, atomic physics related to nuclear physics, and some areas of nuclear physics. A number of workshops on physics in heavy-ion storage rings have been held in the past few years [Ec84, Mp84, Or86, St87, Ic88] and the CAMS study of 1988 [Ca88] contains a valuable summary of research areas of interest. Below, we describe the types of programs presently envisioned and illustrate some of these with related experiments which have been carried out by ORNL personnel.

3.1 The Atomic Physics of Multiply Charged Ions

The objective of research in this area is to achieve a detailed understanding of a broad class of phenomena occurring when multiply charged ions interact with photons, with free and bound electrons, with atoms, and with other ions. Results in these areas affect our understanding of fundamental atomic structure and the electromagnetic fields experienced during the collision process.

At the most fundamental level, these studies may be used as a means of testing concepts in quantum mechanics and quantum electrodynamics. Since the forces are well understood, solutions to the important and pervasive many-body problems so important in solid state and nuclear physics may be tested in simple atomic systems. The study of the atomic physics of multicharged ions is of importance to basic science and to a

number of energy-related technologies. The native habitat of multiply charged ions is in regions of high energy density in high temperature plasmas, in dilute plasmas, such as those found in stellar coronae or magnetic fusion devices, and in more dense plasmas such as stellar interiors, inertial fusion and laser ablation systems. Rapidly moving heavy particles, such as those created in a nuclear fission event, are multiply charged when they interact with matter. The energy levels of multicharged ions are widely spaced, leading to the emission of X rays from relaxation of outer shell states of the ion, and hence the possibility of X-ray lasers from these systems. The need for information, concerning the structure and collision processes of multiply charged ions, in other branches of science and various developing technologies is manifold.

3.1.1 Electron-Ion Interactions

The dominant processes which occur in high temperature plasmas are controlled by electron-ion collisions. These give rise to excitation, ionization, and radiative and dielectronic recombination which, in turn, control the ionic charge-state distribution and the composition and flux of radiation emitted from the plasmas. The HISTRAP facility, with its electron beam cooling section, offers an almost ideal system for the study of these processes. In this region a space-charge-limited electron beam will be merged with the stored ion beam, permitting the study of low-relative-energy electron-ion collisions at high laboratory energies. When the ion beam is cooled, it shrinks in size and will be positioned at

the center of the electron beam. These actions serve to define the electron energy and the positional overlap of the two beams. With the immersed cathode system used in electron beam cooling, the space-charge potential across the electron beam manifests itself in higher longitudinal velocity in the outer portion of the beam rather than as a rotation of the entire beam as in Brillouin flow. Because of the merged-beam kinematics, the longitudinal spread in the velocity of one beam will be grossly reduced, in the center-of-mass system, resulting in much greater energy resolution.

The rate R at which a process with cross section σ occurs in the merged beam is $R = \sigma\,(v_r/v_i)\rho(e)\ell\alpha\phi_i$, where v_r is the relative velocity, v_i is the ion velocity, $\rho(e)$ is the electron density, ϕ_i is the ion current density, α is the beam overlap cross sectional area, and ℓ is the length of the overlapping beam region. Here we can see directly the advantages of high-energy circulating ion beams. The disadvantage of a high v_i present in a single pass experiment is removed by the associated increase in $\phi_i = \rho(i)v_i$. To achieve the desired v_r, a high v_i requires a high electron velocity, v_e, and for space-charge-limited beams $\rho(e) \propto V^{3/2}/v_e \propto v_e^2$. For a given $\Delta P/P$ value, the ion current in the circulating beam at the Keil-Schnell stability limit $\phi_i \propto v_i^3/L$, where L is the ring's circumference. Since in most experiments $v_e \approx v_i$, we have

$$R \propto v_i^4\,(\ell/L)\ . \qquad (3.1\text{-}1)$$

Recombination

When an unbound electron recombines with an ion, the gain in potential energy must be removed in some way. Two processes are known to be important in recombination: radiative recombination (RR) in which a photon is released whose energy is exactly equal to the potential energy gain, and dielectronic recombination (DR) in which a continuum electron excites a previously bound electron and in so doing loses just enough energy to be captured into a bound state ($n\ell$). The latter process results in a doubly excited ion in a lower charge state which may either autoionize or emit a photon, resulting in a stabilized recombination. For both RR and DR, the result is an ion of reduced charge and a photon. The principal background arises from electron capture from residual gas. Since capture cross sections decrease very strongly with v_i ($\propto v_i^{-11}$), the advantage of high v_i is again evident.

Radiative Recombination

Radiative recombination peaks at $v_r = 0$, and is in fact, a process which competes with electron beam cooling. The magnitude and energy dependence of the cross section for RR into a given n state of bare ions are well known theoretically,

$$\sigma_{RR}(n) = 2.11 \times 10^{-22} \frac{E_0^2}{nE_e(E_0 + n^2E_e)} \text{ cm}^2 , \qquad (3.1\text{-}2)$$

where E_0 is the ionization potential and E_ℓ is the electron energy. Although RR for bare ions is well understood, RR cross sections for capture into low n states of ions with already bound electrons are not. This is a problem of some considerable interest in high temperature

plasmas. Here studies of the RR emission spectra will yield valuable information on the n dependence of RR cross sections for these systems.

The result of the recombination is an ion of reduced charge and the emission of a photon. Measurement of the number of reduced charge ions as a function of electron beam energy can be used to diagnose the electron beam cooler region. Because of the high luminosity of the stored beams, it will also be possible to measure light emitted from the merged beam region. Measurement of the photon energy for RR to an initially bare ion can give direct information on the 1s binding energy and the 1s Lamb shift.

Photoionization

Photoionization is the time reverse process to radiative recombination. Thus, photoionization cross sections from ground and excited states can be determined from a measurement of the gross RR rate via charge state reduction coupled with a measurement of the relative intensities of the photons, in general X rays, emitted from the recombination region.

Dielectronic Recombination

Unlike radiative recombination in which the dependence of the cross section on energy is continuous and monotonic, dielectronic recombination is characterized by a set of resonances. The process may be represented as follows: an ion A of charge q^+ in its ground state α is excited to a core state β and captures the electron into a given (n,ℓ) state,

$$A^{q+}(\alpha) + e \rightleftarrows [A^{(q-1)+}(\beta,n\ell)]^{**} \rightarrow A^{(q-1)+}(\alpha,n\ell) + h\nu \ . \qquad (3.1\text{-}3)$$

The doubly-excited intermediate state decays either by autoionization to its original ion-electron pair or radiatively into a recombined ion. The exact levels of doubly excited states are not well determined.

Since DR is a resonant process, it could be used for precision spectroscopy of doubly excited states in which QED and correlation effects can be measured, e.g.,

$$A^{(z-1)+}(1s) + e \rightarrow [A^{(z-2)+}(2p,n\ell)]^{**} \downarrow [A^{(z-2)+}(1s,n\ell)]^{*} + h\nu \,. \qquad (3.1\text{-}4)$$

A precise measure of the collision energy at resonance gives the level of the two-electron excited state.

Until 1983, the only experimental information on DR had come from spectroscopic observations of plasmas from which only thermally averaged rates may be inferred for a mixture of charge states. Moreover, spectroscopic studies are limited to capture into low $n\ell$ states. The effect of high $n\ell$ spectator electrons on the spectral lines is too small to separate. In 1983-84, four groups reported DR cross-section measurements. A group at the Joint Institute for Laboratory Astrophysics measured the DR cross section for Mg^+ atoms and stabilizing photons from the collision region [Be83]. A similar experiment was carried out in Australia for Ca^+ [Wi84]. Two groups used merged electron-ion beam methods which are similar in geometry to electron beam cooling systems. One experiment at the University of Western Ontario [Mi83] used a tenuous emission-limited, highly monoenergetic electron beam merged with a 450-keV C^+ beam to reach the requisite collision energies of a few eV (the signal levels here were very low). At ORNL, multiply charged ion

beams obtained from an EN Tandem Van de Graaff were merged with a compressed space-charge-limited electron beam. The recombination cross sections were obtained from the fraction of reduced-charge ions as a function of relative energy [Di83].

The ORNL technique, which resembles the method which will be used in HISTRAP, is the only one which has thus far given results for multi-charged ions. A schematic of the ORNL merged beam apparatus is shown in Fig. 3.1-1. An ion beam from the ORNL EN Tandem Accelerator enters the interaction region through an axial, 0.64-mm-diameter hole in the cathode of the electron gun. After exiting the interaction region, the ion beam is subjected to charge state analysis. The initial charge state of the ion beam, q+, is deflected into a Faraday cup. The cup is connected to a current integrator and the output pulses are counted by a scaler. Ions that have picked up an electron {charge = $(q-1)^+$} are deflected onto a solid-state position-sensitive detector (PSD). The ions having charge (q-1)+ arise from electron pickup of the q+ ions from the residual gas, slit-edge scattering, and the sought-after effect, DR. Details of the experiment are given in Ref. [Di86].

The source of the electron beam is a double-gridded Pierce-type, high-intensity electron gun which is designed to produce a convergent, laminar electron beam. The gun is operated in the space-charge-limited mode. The electron beam enters a coaxial, solenoidal, magnetic field 0.84-m long which is adjusted to establish Brillouin flow.

The experimental procedure consisted of optimizing the electron beams at a particular cathode voltage and counting the $A^{(q-1)+}$ and A^{q+}

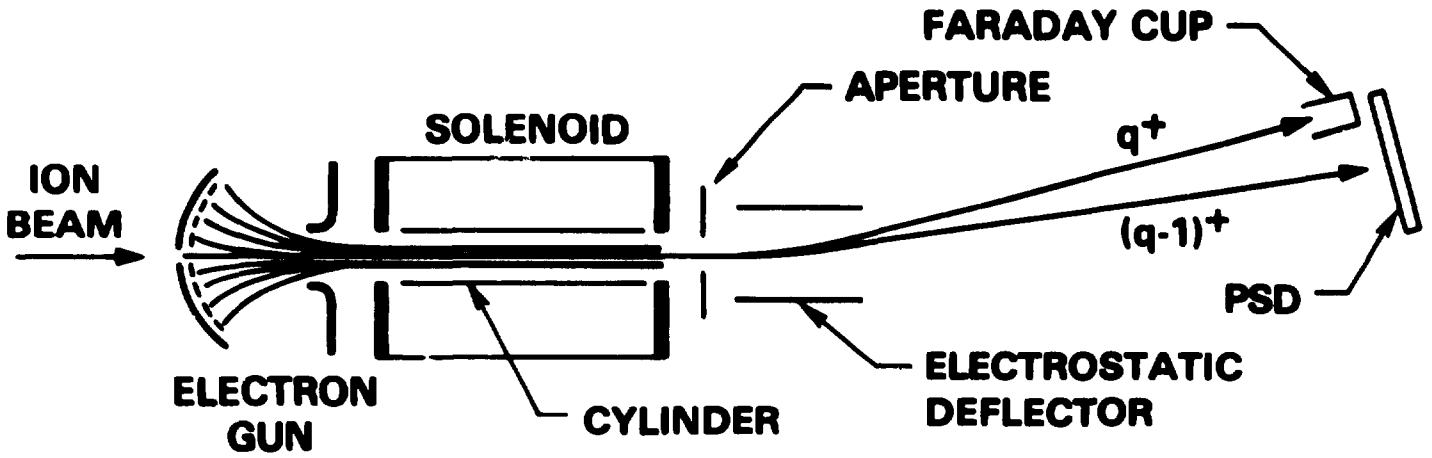

Fig. 3.1-1 Schematic of the ORNL merged electron-ion beam apparatus.

beams while stepping through the relative energies of interest by changing the energy of the ion beam. Results have been obtained from $\Delta n=0$ transitions in Li-like (B^{2+}, C^{3+}, N^{4+}, and O^{5+}) [Di87a], Be-like (C^{2+}, N^{3+}, O^{4+}, and F^{5+}) [Di87b], B-like (N^{2+}, O^{3+}, F^{4+}) [Di88], and Na-like (P^{4+}, S^{5+}, Cl^{6+}) [Di86] ions. An example is shown in Fig. 3.1-2 for F^{4+}. Note that the F ion energies were in the range of 2 MeV/nucleon and the relative energies are in eV. Although the ^2D state is resolvable with our resolution of 5 eV, the $n\ell$ distributions within that state are not. Cross sections for $\Delta n=1$ transitions are an order of magnitude lower than $\Delta n=0$ and have, thus far, not been measurable with this system.

In a recent measurement carried out at Aarhus University with the participation of an ORNL staff member, a "cooler" geometry electron target coupled to an EN Tandem Van de Graaff was used to measure $\Delta n=0$ resonances in C^{3+} [An88]. A resolution of 0.15 - 0.25 eV was obtained. This very encouraging experiment proves the method but, because of the single pass nature and low maximum electron energy, it is limited to very abundant ions with high cross sections ($\Delta n=0$) and relatively low Z.

These experiments are particularly germane here since they resemble in concept a single pass of the ion beam through the "cooler" region and, by contrast, they point up the advantages of the HISTRAP system. With a resolution of ~0.1 – 0.2 eV, experiments in HISTRAP would be able to resolve structure and individual resonances in the DR spectrum. The high luminosity of the HISTRAP beam will allow measurement of cross sections which are orders of magnitude lower than those obtained in the single-pass experiments. Backgrounds in the ORNL single-pass experiments

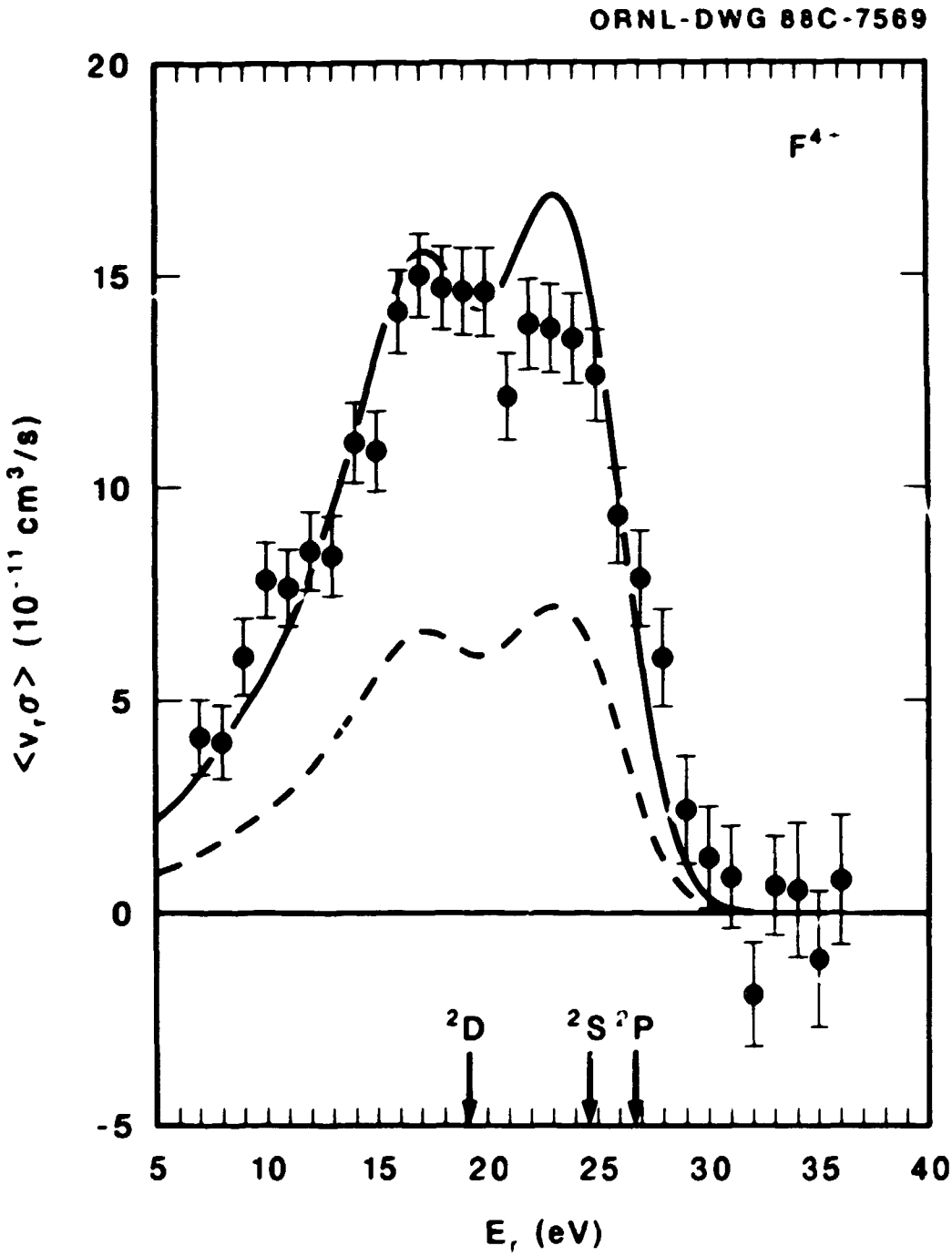

Fig. 3.1-2 Dielectronic recombination rates as a function of relative energy for F^{4+}. The lower and upper curves show theoretical results for zero field and saturation fields, respectively.

arise from charge capture from residual gas and from slit-edge scattering. These effects will be much mitigated in HISTRAP because of the higher ion beam velocity, better background vacuum, and the complete absence of slits in the system.

The recent experiments have shown significant flaws in the previously accepted theory, and the present interaction between theory and experiment has been highly iterative. All of this has pointed up the need for further and more detailed information on systems over a wide range of charge states.

One of the primary and far-reaching effects revealed by the dielectronic recombination measurements to date concerns the effects of external fields on the recombination process. This effect has since been confirmed theoretically, but the trend with increasing target ion charge is untested above charge +6, and fine details of the theoretical predictions are masked by the overwhelming influence of fields in all measurements to date. The effects of fields are also predicted by theory to be much smaller for dielectronic recombination events involving $\Delta n > 0$ transitions. This prediction is untested. Dielectronic recombination measurements, at the HISTRAP facility, on highly charged ions and involving $\Delta n > 0$ transitions would be the first serious test of the detailed DR theories.

Laser-Induced Radiative Recombination

As we have seen, the radiative recombination cross section $\sigma_{RR}(n) \propto q^2/ne$. By merging a laser beam with the merged electron-ion beam, we should be able to populate preferentially a given $n\ell$ state

in a recombined (q-1)+ ion. If the (q-1)+ ion fits into the ring's momentum aperture, we should be able to store and build up population in selected states. The ratio g(n) between the rate for spontaneous recombination to induced recombination is given by

$$g(n) = u(\nu)\ (B/A)\ , \tag{3.1-5}$$

where $u(\nu)$ is the spectral energy density and A and B are the Einstein coefficients for spontaneous and induced recombination, respectively, with $A = 8\pi(h\nu^3/c^3)B$. With available laser powers in the visible and UV regions, enhancements by factors of 100 to 500 should be possible. For very highly stripped ions, photons in the 2- to 5-eV range would enhance Rydberg levels. By choosing high ℓ values, one might be able to store long-lived states of the (q-1)+ ions for separate experimentation.

Laser-Induced Dielectronic Recombination

Dielectronic recombination can be thought of as a two-step process. The first involves the formation of a doubly excited state of the recombined ion $[A^{(q-1)+}(\beta,n\ell)]^{**}$ and the second is a radiative stabilization which drops the total energy of the ion below the autoionizing limit. The cross section for dielectronic recombination is proportional to

$$\sigma_{DR} \propto \frac{A_A\ \Sigma\ A_{R_i}}{\Sigma(A_{R_i} + A_{A_i})}\ , \tag{3.1-6}$$

where A_A is the autoionizing rate of the initial state and A_{R_i} and A_{A_i} are the radiative and autoionizing rates for any of i pathways for relaxing the intermediate state. Recombination to a specific $n\ell$ state could be laser enhanced by increasing the radiative rate for either the $\beta \rightarrow \alpha$ relaxation or a $(n\ell) \rightarrow (n'\ell')$ transition. The $\beta \rightarrow \alpha$ transition

energy will be a function of the nℓ state of the second electron; hence, the enhanced recombination rate will be tuneable to a given (n,ℓ) value. In most cases, presently available laser photons are too low in energy to induce the $\beta \rightarrow \alpha$ transition. However, some cases of $(n\ell) \rightarrow (n'\ell')$ pumping appear feasible.

Equation (3.1-6) has a peculiar property. Because the formation of the doubly excited state is the time reverse of autoionization, a high σ_{DR} requires a high A_A and a high A_A means that $\sigma_{DR} \propto A_R$. On the other hand, a high A_A means a low fluorescence yield which leads to a low σ_{DR}! One way to overcome this dilemma is to pump the intermediate state into a close lying state with low A_A [Ca88].

For example, a threefold enhancement in dielectronic recombination can be obtained by laser pumping the $[2s2p\ ^3P]^{**}$ state of C^{3+}, formed by dielectronic excitation, to the $[2p^2\ ^3P]^{**}$ state. The enhancement is limited by saturation effects. On the other hand, the laser power required is only 10^3 w/m. Measurements of this type should also yield precision spectroscopic information on doubly excited states.

Ionization and Excitation

Experiments on ionization and excitation are presently carried out using crossed beams of electrons with multicharged ions obtained from ECR or EBIS sources. For multicharged ions these experiments have yielded a number of surprises. A simple universal formula due to Lotz predicts that the ionization cross section should have a gradual slope at threshold, rise to a broad peak, and then decline as $\sim \ell n(E/I)/E$, where E is the collision energy. For a number of multicharged ions,

this formula underestimates the ionization cross section by more than an order of magnitude. Moreover, detailed structure is visible in the energy dependence. This enhanced cross section and structure is due to the formation of autoionizing states by excitation of inner shell electrons. The limitations of present techniques are twofold. First, the small cross sections require intense crossed electron beam currents which, in turn, leads to poor energy resolution and hence inability to resolve details of the structure. Second, the lower limit on the size of the cross sections that can be measured using crossed beams precludes measurement of high ionization stages. In addition to these fundamental problems, the ion currents obtainable from even the best modern ion sources and accelerators are inadequate for crossed beam measurements on highly charged ions.

The availability of HISTRAP could do much to remove these limitations and open some new areas of investigation. The experiments would be carried out in the merged electron beam region, and the signal would be in the form of ions of higher charge $(q+1)+$. The advantages here are the increase in signal because of the much higher luminosity, and increased energy resolution because of the merged-beam kinematics and the nature of the "cooling beam." Because of the increased energy resolution, sharp thresholds in the energy dependence due to inner shell excitation should become visible, and the measurement of positions of these discontinuities can be used in atomic structure determination.

Because of the recycling through the electron beam, it may be possible to measure outer shell excitation by multielectron ionization.

If the relative energy E_r in the electron-ion merged-beam region is scanned over the region, $(I/2) < E_r < I$, where I is the ionization potential, direct ionization cannot occur, but excitation to some level in this region could. If this level is either metastable or cascades to a metastable state with lifetimes long compared to $\sim 10^{-6}$ sec (the ring transit time), the ion may be ionized by a second electron collision while passing through the merged-beam region again. This would be evidenced by ionization events occurring for $E_r < I$. Since we would really be measuring excitation, the thresholds in cross section should be sharp rather than gradual.

Electron ion crossed beam measurements at ORNL have focussed in recent years on studying the role of indirect ionization for highly charged ion targets. The systematics of ionization are now understood for intermediate-charge (+5 to +16) ions of intermediate-Z (10 to 25). This understanding was arrived at only through the study of numerous related measurements, however, and it is not at all clear how these systematics will extend to higher charge states or heavier elements. The influence of excitation-autoionization generally increases with increasing charge and with increasing mass, and studies possible only on circulating-beam accelerators will greatly extend our knowledge and understanding of this phenomenon. Due to limited ion beam intensities for highly charged ions, correlated two-electron effects have not been isolated in enough cases to establish any patterns at all. Again, the luminosity of the planned circulating beam and the cooler electron gun will make numerous new studies possible.

One ionization path which will be studied using the HISTRAP facility has been designated Resonant-Excitation Double Autoionization (REDA). The initial stage of this ionization process is capture of the free electron into an excited level of the ion, accompanied by excitation of a target ion electron. This highly excited ion can stabilize by radiation (a dielectronic recombination event) or by throwing off two excited electrons for a net ionization event (REDA). The two electrons may be emitted either simultaneously in a correlated event or sequentially. The REDA process was first predicted, in 1981, to contribute significantly to ionization but was clearly observed for the first time only in 1988 [Mu88]. The first observation of REDA at ORNL is shown in Fig. 3.1-3 in ionization of U^{13+} [Gr88]. The width of the feature on the left corresponds to our predicted energy resolution, implying that a single resonance may account for the feature. With the resolution of the cooler electron gun, the peak would be about a factor of ten times higher and narrower than that observed here. The feature on the right could most likely also be resolved in more detail with a brighter ion beam and better electron beam resolution. The systematics of this phenomenon are unknown, but indications from the few existing measurements are that higher charged and heavier ions may exhibit more and larger REDA features.

3.1.2 Ion-Atom Collisions

The discussions above have dealt with processes in which the ion beam was confined to the ring and the interacting species did not disturb the vacuum. For experiments involving atomic targets, we must

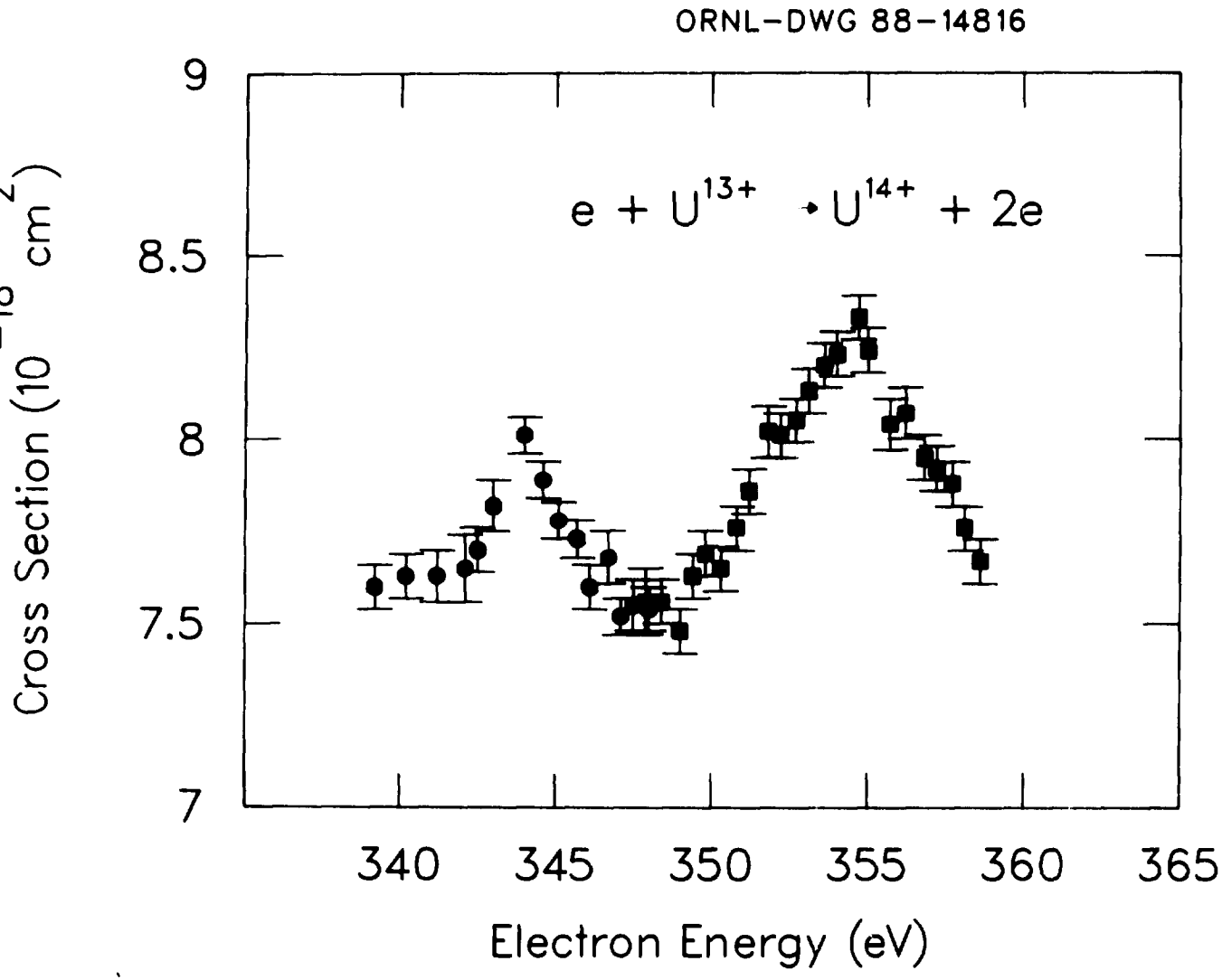

Fig. 3.1-3 Ionization cross section for U^{13+} versus electron energy.

be able either to introduce gas into the ring in the form of a differentially pumped cross beam or to extract the stored beam. Moreover, to obtain the appropriate center-of-mass energies, we must either be able to vary the ion beam energy or be able to merge an accelerated atom (neutralized ion) beam.

The advantages obtained in HISTRAP are again those of emittance and luminosity. Beams of very high charge state ions available from tandem accelerator injection can be decelerated and cooled in the ring for low-energy collisions studies.

The high luminosity permits use of very thin targets to achieve reasonable signal levels for low cross-section processes in the presence of sequential high cross-section processes which lead to the same product. An example here is the study of electron pair transfer from He to an energetic highly charged ion. The cross section for single-electron transfer may be 10^3 to 10^4 times greater. To avoid the interference of sequential single capture would require a vanishingly small target length for a single-pass experiment. However, with a target of just 10^{10} atom/cm^2 and a cross section of 10^{-22} cm^2, the ~1-mA beams in the storage ring would give signals of ~6000 cps with insignificant interference from double capture.

Such intensities also make possible measurements of the emission spectra following charge capture into excited states of the circulating ion. By colliding a bare nucleus with a spin polarized atomic target, such as an optically pumped lithium beam, one may prepare and store a spin-polarized hydrogenlike ion beam for subsequent experiments. Here

is another example of the utility of the multicharge storage capability of HISTRAP.

In connection with charge transfer of polarized electrons, it also has been suggested that parity violation might be observed in an experiment where one measures the polarization of the radiative electron capture photon in coincidence with the electron spin direction.

Generation of Very Low-Energy Multicharged Ion Beams

It has been demonstrated that fast MeV/nucleon, multicharged ions colliding with neutral target atoms can create multicharged recoiling target ions with high probability. These recoiling target ions have very little kinetic energy, $\lesssim 1$ eV, and can be used for further experimentation. The recoils are generally extracted from the collision region, charge and energy analyzed, and used in further collision studies in the keV energy region. Thus far, hammer beams, MeV/nucleon beams have been supplied by many accelerators, ranging from EN tandem Van de Graaffs to the UNILAC at GSI. The advantage of the HISTRAP for such experimentation lies in the intense currents of the stored ions available for use as "hammers." If the cross section for multiple target ionization is much greater than the charge-changing cross section of the projectile ion, the individual projectile ion may be recycled in the ring to create many target recoils. The energy loss in these collisions may be recovered by the electron beam cooler. If one has multicharge storage capability, charge-changing collisions of the "hammer" ion will not destroy its utility as long as its charge state, q, can be accommodated in the ring. Therefore, if one injects the ion

into the ring at its most probable equilibrium charge value, it will be useful as a hammer until it leaks out through collisions which take it outside the Δq acceptance of the ring.

Estimates by the Heidelberg group indicate that intensities of 10^9 bare recoil Ar ions per second would be produced from a 10^{11} atom/cm^2 target by 10^{10} iodine ions circulating at 8 MeV/nucleon. Such intensities of very low-energy Ar^{18+} have never been approached in the past and would open new possibilities for experimentation: differential scattering, crossed beams with the ECR multicharged ion beams, etc.

To handle even a target thickness of 10^{11}/cm^2 without destruction of the vacuum will require, for noncondensible species, narrowly collimated nozzle beams and differential pumping. Since the physics of multiply charged ions is independent of the neutral atomic outer shell configuration, the target atom, which is to be used as a multiply charged ion projectile, could equally well be of a condensible element to ease the pumping requirements. For example, a directed atomic beam of titanium could be condensed easily after passage through the stored beam region and then participate in the pumping via getter action.

3.1.3 Ion-Ion Collision Experiments

The availability of two separate injection systems on HISTRAP makes possible an interesting and unique opportunity for the study of ion-ion collisions. Here we would inject an ion beam with a given M/q, where M is the mass of the ion having charge q, from the ECR-RFQ injector, accelerate it to a kinetic energy E, and then inject another ion species

from the Holifield tandem. The condition for the simultaneous storage of two ion beams is

$$(E_1/E_2) = (M_2/M_1)(q_1/q_2)^2 \ . \qquad (3.1\text{-}7)$$

Within the merged beams, collisions would take place with relative energy

$$E_r = k\mu\ (B\rho)^2\ [(q_1/M_1) - (q_2/M_2)]^2 \ , \qquad (3.1\text{-}8)$$

where μ is the reduced mass and $B\rho$ the magnetic rigidity of the system. A continuous range of E_r is obtained by varying E_1 and suitably adjusting E_2 and B. As an example, consider the collision $Cl^{13+} + Cl^{14+}$. We inject Cl^{13+} from the RFQ at 250 keV/amu, accelerate to 34.5 MeV, and then inject Cl^{14+} at 50 MeV from the HHIRF tandem. The relative collision energy is then 78 keV. Acceleration of the Cl^{13+} to 297 MeV followed by injection of Cl^{14+} at 345 MeV gives a relative energy of 900 keV. For the case of equal magnetic rigidity as described above, the beams are merged over the entire circuit around the ring.

Because of the larger momentum aperture of HISTRAP, we are not limited to colliding beams of equal rigidity. Two beams with $B\rho_1 = \alpha\ B\rho_2$ where $1.0 < \alpha < 1.08$ can be simultaneously stored. The relative collision energy where the beams overlap in parallel is

$$E_r = k\mu\ (B\rho_1)^2\ [(q_1/m_1) - \alpha(q_2/m_2)]^2 \ . \qquad (3.1\text{-}9)$$

For $\alpha > 1.04$, the two beams can be completely separated in the dispersive legs of the ring. Using this mode permits us to collide beams of identical charge and mass.

For experiments of this type, as for those involving colliding beams, good emittance is necessary. Although the two beams are at

different velocities, cooling can be achieved by changing the electron beam velocity to accommodate each beam separately. A competing process, such as capture from background gas, should be relatively suppressed because of the decreased cross section at high velocity in the laboratory system. Studies of charge transfer, ionization, and other collisional phenomena in ion-ion systems have been very strongly circumscribed in the past. The only study extant on multicharged ion-ion collisions was reported from ORNL [Ki87]. It involved a reflected beam geometry and is possible only for symmetric collisions in a very limited range of charge states and energy. The capabilities of the HISTRAP system will do much to open this area to investigation.

3.1.4 Spectroscopy

Precision Spectroscopy of One- and Two-Electron Ions

The objective of work in this area is to achieve rigorous tests of single-particle quantum electrodynamics over a wide range of nuclear charge and to study specific two-electron correlations and level shifts.

Experiments at various accelerators around the world have used beam foil spectroscopy, low energy recoil ions, and decelerated ion beams for these measurements. Problems of Doppler width and "spectator" electrons, a second electron captured into some outer orbit which perturbs the inner energy levels, have limited the accuracy of the measurements. Using presently available methods, the decelerated, totally-stripped ion beam is the most promising. But even here the potentialities are limited by Liouville's theorem since the deceleration leads to an

increased angular width, which mitigates the Doppler width gain from deceleration.

Cooled stored beams offer great advantages here. The precise energies of the beam are known, and the emittance can be very highly refined. The ions can be decelerated and the attendant increase in angular width can be removed by electron beam cooling. To perform such experiments, a beam of bare nuclei is formed. The nuclei are allowed to capture an electron into an excited state from some target. The precision spectroscopy is then done on the radiative decay photons. For the highly charged ions in question, these photons are in the X-ray region.

With HISTRAP, the experiment could be carried out either with a decelerated cooled extracted beam passing through a thin gas target or with the stored beam at higher velocities. With the stored beam, one would use a very thin gas target or, possibly, the merged electron beam itself as a target. In the latter case we can estimate the signal from the radiative recombination rate τ_{RR}; for 10-MeV/nucleon $^{35}Cl^{17+}$ the $\tau_{RR} \sim$ 10-100 sec. With 10^9 stored ions this corresponds to $\sim 10^7$/sec. Since the recombination cross section is proportional to 1/n, about half of the beam will recombine into $1 < n \lesssim 10$ with about a quarter going directly into the desired $n = 2$. Moreover, since the cycle time is $\sim 10^{-6}$ sec, all of those ions which have captured an electron will have relaxed so that spectator effects are cancelled. It is estimated that a precision in Lamb shift measurements of 10^{-4} may be possible using stored cooled beams.

High Resolution Laser Spectroscopy of Ions

HISTRAP could be an excellent source for high resolution linear and nonlinear laser spectroscopic studies of ions. One arm of the ring could be used as a common path for collinear laser and particle beams. The laser beam could provide either a traveling wave field (for linear spectroscopy or a standing wave field for nonlinear spectroscopy, such as saturation or two-photon absorption spectroscopy.

The finite line widths of spectral lines limit the ultimate precision attainable in high resolution measurements. The major cause of line broadening for atoms or ions in rare-field media is the first-order Doppler effect. The compression of the longitudinal velocity distribution of the ions in the ring, resulting from kinematic bunching and electron cooling, could reduce considerably the size of this contribution in a collinear laser-particle beam arrangement. The first-order Doppler effect could be eliminated entirely by using, for example, two-photon absorption spectroscopy.

If first-order Doppler broadening is eliminated or sufficiently reduced, the residual line width will be determined primarily by the finite time available for the spectroscopic measurement. In effect, this time is the duration of the coherent interaction between a particle and the electromagnetic field. This time interval may be determined in a given experiment by either the transit times of particles through the interaction region, the duration of the optical field if the laser is operated in the pulsed mode, or the radiative lifetime of the upper and lower levels of the transition. In a single interaction region the line

width will be determined by the shortest of these times. However, the restriction set by the uncertainty principle can be overcome by the use of a quantum interference method based on the interaction of the particle with two or more temporally separated interaction regions. One essentially obtains narrow interference fringes within the profile determined by a single interaction region. The situation is entirely analogous to the Young's slit experiment in optics. The central fringe is always centered at the transition frequency, and its width decreases inversely with the number of interaction regions employed. In the case of the ring, one could visualize the particles interacting with a collinear laser field situated in one arm of the ring on every orbit of the ring. In principle, this should narrow the resonances considerably. The arrangement would produce results like the multiple-slit interference pattern obtained with a diffraction grating. Of course, it is essential that the phase difference between successive interaction regions remains fixed coherent.

One application of the precise determination of the absolute transition frequencies of simple ions could be in testing the theory of special relativity to high accuracy. For example, the measurement of second- and higher-order Doppler shifts could test the time-dilation factor of relativistic kinematics. The Michelson-Morley experiment could be repeated by testing for the isotropy of space to the speed of electromagnetic waves. This could be done using two or more arms of the ring to make high resolution spectroscopic measurements.

Many single-charged ions have E1 transitions which may be pumped by presently available lasers. With multicharged ions most E1 transitions have too high an energy to be pumped. An exception would be fine structure levels in hydrogenic ions. However, there are a number of M1 transitions available in this frequency range which, with presently available laser intensities, could be used in the ring experiments.

3.2 Molecular Ion Spectroscopy

Studies of the structure of simple molecular ions is a rapidly growing field. For example, the number of molecular ions which have been studied by infrared laser spectroscopy has increased from 1 in 1980 to 14 in 1984 to 55 in 1988 [La88]. Presently, the ions are studied in gas discharges or by Doppler tuning an ion beam velocity to a laser frequency in a merged-beam system. This latter approach has the advantages of (1) unambiguous identification of the ions in the beam, (2) high degree of spatial control, and (3) sub-Doppler resolution due to kinematic compression. In a sense, this is similar to the single-pass merged electron-ion beam experiments described in the section on recombination. Here again the luminosity and immersion time available in a ring system may do much to increase the sensitivity and precision of the experiments. In the ring system, the molecular ionic target would be exposed many times to the stimulating photon field during the lifetime of an excited state. In effect, the merging of the ion beam with a photon beam in one leg of the ring is equivalent to a Ramsey separated resonator experiment.

One great problem in the study of molecular ions is the unknown and often "hot" internal energy distribution introduced during their formation in the ion source. A great additional benefit which is obtained in a storage ring is the ability to allow time for the radiative decay of internal excitation (IR active modes).

Molecular ions cannot be injected from the Holifield tandem, and because they are singly charged, they cannot be handled by the RFQ which has a M/q range of 2 to 6. If we wish to use the synchrotron action in the ring for acceleration, we must have at least 20 keV/nucleon injection energy. To achieve molecular ion capability, another injector, for example, a single-ended 3-MV Van de Graaff, would be required for injection of molecular ions with masses up to 150. At mass 150, the molecular ions could be accelerated up to 2 MeV/nucleon.

3.2.1 Molecular Ion – Electron Collisions

Stored molecular ions cannot be cooled by electron interaction because of the large cross sections for dissociative recombination,

$$AB^+ + e \rightarrow A + B \qquad (3.2\text{-}1)$$

Cooling via laser interactions can, however, be accomplished. Here again the electron beam in the cooler is an effective apparatus for the study of low-energy molecular ion – electron collisions.

These collisions are important in atmospheric physics and combustion physics. For example, the reaction

$$H_3O^+ + e \rightarrow H_2 + OH \qquad (3.2\text{-}2)$$

is the primary ion loss mechanism in flames. Capture can occur into vibrationally excited molecular-ion Rydberg states which decay rapidly

by dissociation. These processes, therefore, display sharp resonances. Resonances also occur in dissociative excitation collisions,

$$\begin{array}{l} AB^+ + e^- \rightarrow [AB^+]^* + e \\ \qquad\qquad\quad \downarrow \\ \qquad\qquad\quad A + B^+ \ . \end{array} \tag{3.2-3}$$

Both of these processes could be studied with well-defined ground vibrational state molecular ions by observing the attenuation of the stored beam as a function of electron energy.

3.2.2 Laser "Cooling" of Ion Beams

If a laser beam, directed counter to an ion beam, is tuned for resonant absorption by the ion, the ion will be decelerated. This occurs because the absorption of the directional momenta of the incident photons is followed by an isotropic distribution of the re-emitted photons. If there is a distribution of velocities in the ion beam, the deceleration will only take place for those ions which are not Doppler-shifted out of resonance with the laser beam. Thus, for example, by tuning the laser or ion beam velocity so that resonance is achieved for the higher velocity particles, the distribution can be squeezed towards the lower velocity edge and cooling is achieved. With singly charged ions, where dipole allowed transitions (E1) are accessible with ordinary lasers, cooling times are of the order of 10 msec.

Laser cooling of stored molecular-ion beams could also be accomplished by pumping low-lying vibronic states. For multicharged ions, E1 transitions require photons which are too high in energy for presently available lasers. However, transitions between, for example, M1 transitions in intercombination states of highly charged ions, do

fall into the visible region. Although oscillator strengths may be 10^4 lower than for E1 transitions, saturation is still achievable. An example is exciting the Ni VIII ground state, $3d^3\ {}^4F_{3/2}$, to $3d^3\ {}^4P_{1/2}$ via an M1 transition with an excitation energy of 23,261 cm^{-1}, which is well within range of optical lasers. The limitation here is in the relaxation time of the excited state which may exceed the transit time around the ring. If this were the case, suitable laser beam modulation would have to be employed. The interplay between Doppler shift and the precision with which a given intercombination line is known would permit, on the one hand, a precise calibration of the beam energy or, on the other, precise spectroscopy of the ionic system.

3.3 Condensed "Crystalline" Beams — The Cooling Process

The "cooling process," the process by which the emittance and momentum spread of the beam is reduced, is in itself an interesting area for fundamental investigation. The "cooling" process proceeds through Coulomb scattering of cold electrons from "hot" ions. To see this in a simple manner, imagine a volume filled with perfectly stationary electrons, assume T_e = 0°K, which is moving in the laboratory system with a velocity exactly equal to the average velocity of a group of positively charged ions. Ions with velocity components exactly equal to the electron group velocity will be unaffected, but ions with any remaining velocity in any direction will be slowed by Coulomb scattering. In the ring, the ion beam passes through a freshly supplied cold electron beam region on each pass and should ultimately reach the electron "temperature."

The actual temperature distribution of a beam of electrons accelerated from a cathode at temperature T_c is "flattened" in space. The transverse temperature of the beam $T_\perp$ is equal to T_c, kT_c = 0.1-0.2 eV, but because the beam is accelerated to an energy E, the longitudinal temperature $T_\parallel$ is decreased to

$$kT_\parallel = 1/8\ (kT_c)^2/E\ , \qquad (3.3\text{-}1)$$

so that, in principal, a 1-keV electron beam can reach a temperature of $T_\parallel \sim 10^{-2}$°K.

If such cooling can actually be achieved, it is possible that a "crystallization" of the ion beam could occur. In the reference frame of the ion beam center, an individual beam particle rotates in a small circle, with about 100-μm diameter, because of the strong focussing transverse betatron oscillation. To minimize their potential energy, the ions would order themselves with a fixed interionic distance in the longitudinal dimension. As the density is increased, the repulsive forces increase and the ions can no longer be packed in a string. Instead, they form into a helical array and with further increasing density, they form helices within helices. The result of calculations [Ha88] for such configuations are shown for T = 0°K in Fig. 3.3-1. In Fig. 3.3-2, we show the results of adding thermal motion in a molecular dynamics calculation [Ra87]. The lower portion of Fig. 3.3-2 shows the high degree of order within one of the helical layers.

The methods of detection of structure have been discussed and two rings presently under construction, Heidelberg and Aarhus, have the production of crystallized beams as a priority [Pt88]. The crystallized

ORNL-DWG 88-15966

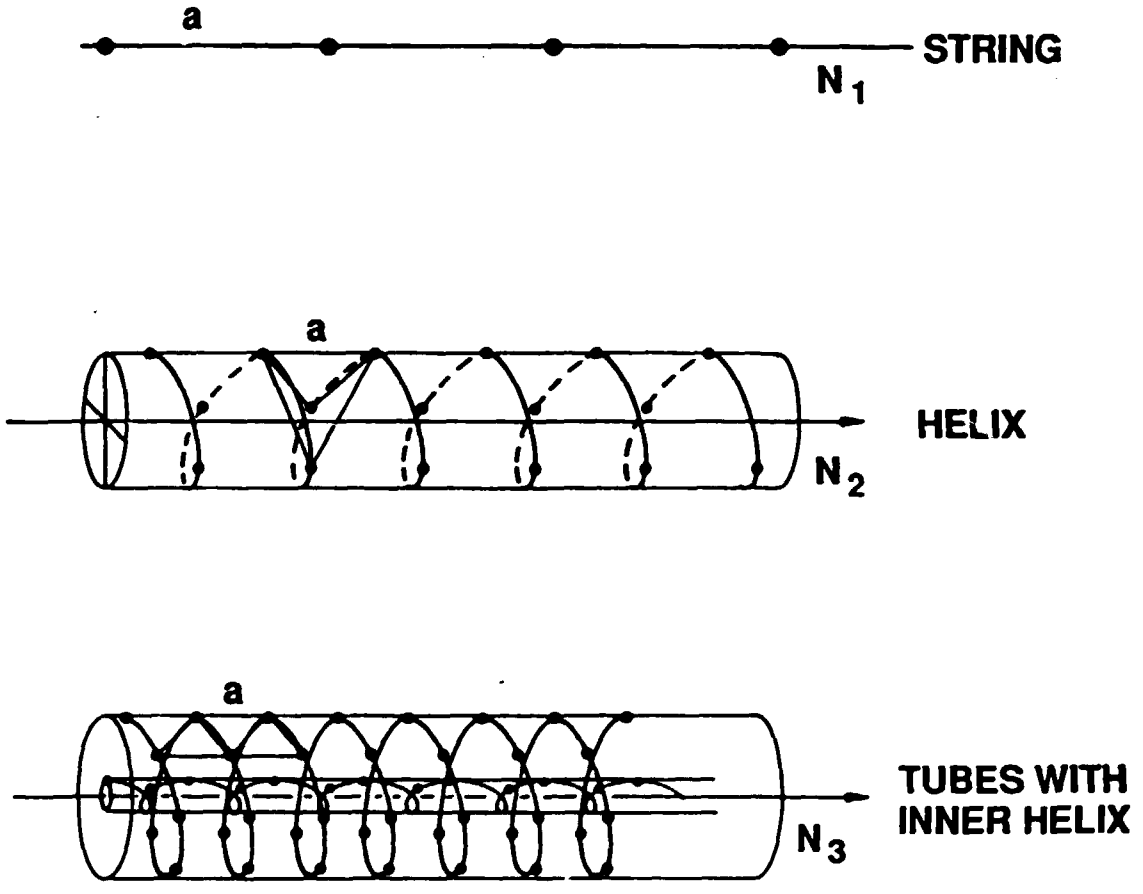

Fig. 3.3-1 Schematic drawing of beam crystals at a temperature of 0°K. With increasing number density, the crystals move from a string to a helix to concentric tubes.

ORNL-DWG 88-15965

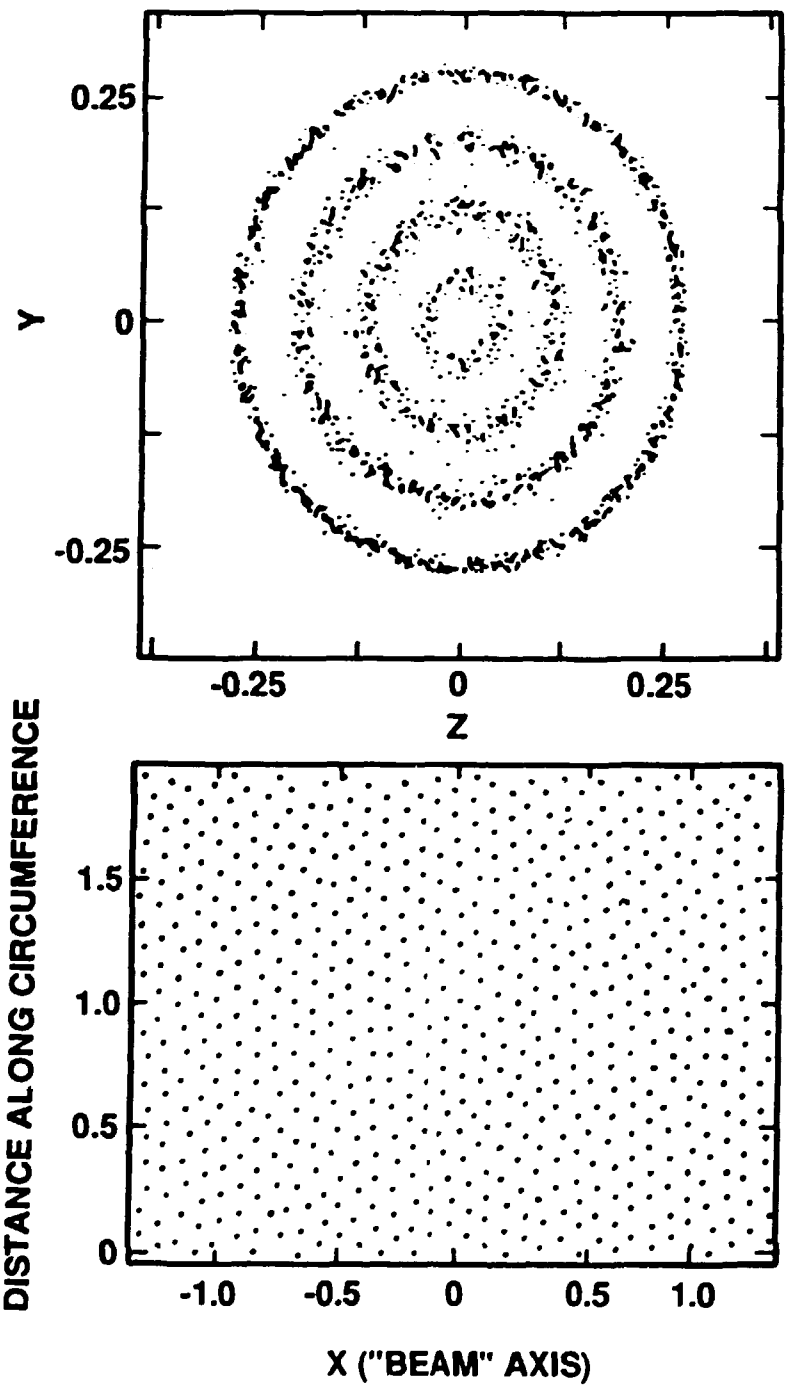

Fig. 3.3-2 The upper part of the figure shows the results of a Molecular Dynamics calculation with 2000 ions in the cell. The ion coordinates are projected onto the Y-Z plane perpendicular to the beam direction X. The lower part of the figure shows the distribution of ions in the outermost shell on the surface of the shell.

beams are the two-dimensional analog of the ordered structures which have recently been observed in ion traps. If such beams can, in fact, be formed, many interesting properties follow. On the practical side, for example, only adiabatic collisions between beam particles can occur because of the order in the crystal. Intrabeam scattering is eliminated for the same reason. Questions relating to this new solid's structure include its lattice "phonon" spectrum, the coherence lengths in lattice oscillations, and the nature of phase transitions.

3.4 Nuclear Physics with HISTRAP

The availability of ion beams with masses exceeding A = 12 and energies in the range of 20 to 80 MeV/nucleon would provide a major new tool for nuclear physics research at the Holifield Heavy Ion Research Facility and provide the United States with heavy ion beams of uniquely high quality. Only two U.S. facilities have been constructed that can provide beams in this energy range; the K800 facility at Michigan State and the K500 facility at Texas A&M University. Neither facility is in full operation yet. The heavy ion beams from HISTRAP will be "cooled," and therefore characterized by low emittance and extremely high energy resolution. Both the energy resolution and emittance will be significantly better than that of the beams from the Michigan State and Texas A&M facilities. There are a significant number of important experimental programs that are ideally suited to, and often require, the higher quality beams from HISTRAP. The existence at HHIRF of major experimental research devices such as the Spin Spectrometer, the high-resolution Broad Range Spectrograph, the BGO Compton suppression system,

the HILI detector for charged particles, and the soon to be completed large array of BaF_2 photon detectors ensure immediate utilization of the new beams from HISTRAP. We briefly describe below a few of the areas of research that would be enhanced by the existence of the HISTRAP beams.

3.4.1 Giant Resonances

The discovery and systematization of new classes of giant resonances during the past decade has had a profound influence on the field of nuclear structure physics. However, present studies have been limited largely to the observation of gross properties such as energy, width, and strength of the isoscalar, non-spin-flip resonance. This limitation has been imposed not by research interest but by the characteristics of the available beams from present accelerators. The use of heavy ion beams at HHIRF has led to the study of the microscopic nuclear structure of the giant resonances through the measurement, for the first time, of the gamma-ray decay of the resonances. These experiments were made possible by the large cross sections with which heavy ions from the HHIRF excite giant resonances. Much larger giant resonance excitation cross sections, with much better resonance peak-to-continuum ratios, can be achieved with the 50-82 MeV/nucleon beams that will be provided by HISTRAP than with lower-energy heavy ions or with medium energy, 100-500 MeV, light ions. This has been demonstrated recently in exploratory experiments, using 84-MeV/nucleon ^{17}O beams, by an ORNL-led collaboration working at the French facility GANIL [Be88a, Be88b].

Figure 3.4-1 shows spectra from the reaction $^{208}Pb(^{17}O,^{17}O')^{208}Pb$ for 84-MeV/nucleon ^{17}O ions (solid curve) and 22-MeV/nucleon ^{17}O ions (dashed curve). The two curves are normalized to one another in the unstructured region of the spectrum near 40 MeV of excitation energy. The benefits of the higher incident energy is apparent; the resonance cross sections are much larger as is the ratio of the peak strength to continuum strength. Such large cross sections make detailed photon decay studies possible for most nuclei. Furthermore, the new beams would provide cross sections 100 times larger than we now obtain for isovector resonances, making this new class of giant resonances amenable to systematic study for the first time. The extremely high quality of the heavy-ion beams from HISTRAP, together with the unparalleled gamma-ray detection facilities provided by the Spin Spectrometer and the BaF_2 array at HHIRF, will greatly enhance these studies compared to those we have carried out earlier at HHIRF and GANIL.

The biggest effect of the HISTRAP beam energies will, however, be on studies of the giant dipole resonance (GDR). The large resonance peak in Fig. 3.4-1 is dominated (~2.5b/sr) by the GDR — with the next most significant contribution being the isoscalar giant quadrupole resonance (~0.7b/sr). Systematic studies of gamma decays of the GDR to low-lying excited states will become feasible. Recent nuclear structure calculations make definite predictions on these branches which could easily be tested with the Spin Spectrometer and BaF_2 array.

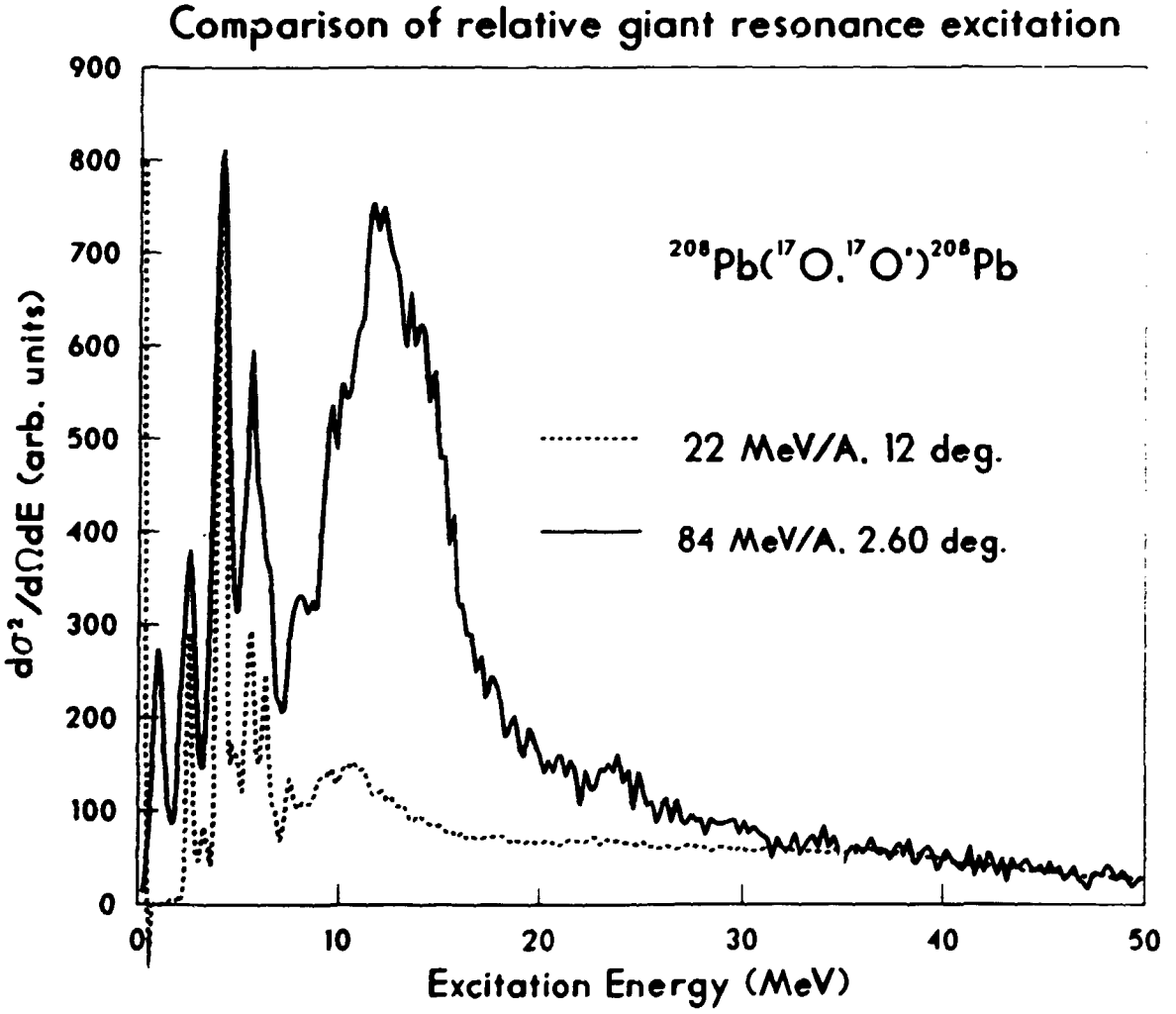

Fig. 3.4-1 Comparison of nuclear giant resonance excitations at 22 MeV/nucleon and 84 MeV/nucleon.

3.4.2 Nuclear Collision Dynamics

Studies of the behavior of nuclear matter under conditions of extreme temperature and density are in the forefront of nuclear physics research. Such studies will eventually lead to the development of an equation of state for nuclear matter which holds the key to our understanding of nuclear phase transitions to new forms of nuclear matter. We know that compressed or rapidly spinning nuclear matter is effectively produced in energetic nucleus-nucleus collisions. Increasingly extreme conditions can be attained in these collisions by raising both the relative velocity and the size of the colliding nuclei.

The availability of heavy-ion beams from HISTRAP with energies up to 80 MeV/nucleon will be a major asset in studies of nuclear collision dynamics. It is expected that the way in which colliding nuclei interact changes dramatically when the relative energy of the nuclei is raised above ~25 MeV/nucleon. At the energies currently available from the HHIRF, collisions are governed by nuclear mean field effects. As bombarding energies increase into the regime which will be made available by HISTRAP, nucleus-nucleus collisions are increasingly dominated by nucleon-nucleon collision effects. At incident energies exceeding 20 MeV/nucleon, colliding nuclei move past each other in a time shorter than the time it takes the disturbance to propagate throughout the colliding partners. This can give rise to interesting phenomena such as the propagation of shock waves in nuclear matter and intense localized heating of nuclear matter. The exact nature of the onset and extent of phenomena such as shock waves and localized heating

depends upon fundamental nuclear properties such as the compressibility of nuclear matter and the momentum distribution of individual nucleons in the colliding nuclei.

Investigation of these interesting phenomena will require experiments capable of nearly complete characterization of all the products of nuclear reactions. Such measurements become progressively more difficult as the number of final fragments from nucleus-nucleus collisions increases. With the HILI multidetector system currently in operation at HHIRF, we can carry out such measurements taking advantage of the unique high quality of the high energy HISTRAP beams. The HILI detector provides complete coverage of all angles forward of 20° using over 200 detectors for light fragments ($Z < 10$) and 4 detectors for large complex fragments ($Z > 10$). This detection system will be particularly effective with energetic heavy beams from HISTRAP colliding with lighter target nuclei where the large forward momentum provided in the laboratory frame kinematically focuses the reaction products into a forward cone. This will allow for measurements of, for example, individual energy spectra of all complex fragments gated by energy loss, momentum transfer, or other information characterizing the reaction.

3.4.3 The Giant Dipole Resonance in Hot Nuclei

The study of giant dipole resonances built on excited states has been pursued vigorously for several years, but efforts have concentrated on extraction of nuclear shapes — at relatively low excitation with temperatures $T \lesssim 2$ MeV. It is extremely interesting and important to carry out systematic studies of the GDR in very hot systems; $T \sim 4$ MeV

up to the maximum temperature which nuclei can support. It is possible that the GDR can be used as a probe of the nuclear shape, even at these high temperatures; however, of more interest is the study of the GDR itself. Can we observe shifts in the mean resonance energy and loss of collective dipole strength in the resonance peak as the nuclear temperature is raised? Is GDR strength redistributed to lower energy, near the unperturbed $1\hbar\omega$ energy, as the temperature is increased? Can the GDR be used as a probe for investigating the liquid-vapor phase transition in nuclei? All of these questions can be addressed using beams available from HISTRAP. The needed measurements will require very sophisticated experiments with nearly complete event characterization. The equipment available at HHIRF, including the Spin Spectrometer, the Dwarf Ball and Wall, the BaF_2 array, and gas heavy-ion detectors provide a capability for these investigations that far exceeds those available at any other medium-energy facility in the U.S.

3.4.4 Nucleus-Nucleus Bremsstrahlung

The facilities available at HHIRF will make us uniquely able to exploit the higher-energy heavy-ion beams to be produced by HISTRAP for study of hard (>25 MeV) photons in nucleus-nucleus collisions, that is, bremsstrahlung-photons. A large body of inclusive data is now available which suggests but does not yet confirm, that above ~50 MeV/nucleon, neutron-proton first-collision models are appropriate for description of the hard photon spectrum. At lower energies multiple collision effects, also referred to as thermal effects, may be

important. If this situation is to be clarified, systematic exclusive measurements are required. The combination of detector systems at HHIRF which can be brought to bear on this problem is unique, and can provide almost complete event characterization. For example, the BaF_2 array is an ideal tool for γ-γ correlation studies of hard photon production, which can in principle provide information on the degree of coherence in the production of hard photons. Data obtained with such a high degree of exclusivity will enable us to make a significant contribution to the field.

4.0 ACCELERATOR FACILITIES

4.1 General Synchrotron Considerations

A synchrotron consists of dipole, quadrupole, and sextupole magnets arranged in a ring. This arrangement is called the lattice. The dipole magnets bend the beam by 360° to form a closed orbit; the quadrupole magnets focus the beam about this closed orbit; and the sextupole magnets make this focusing somewhat independent of magnetic rigidity. Ions travel inside a vacuum chamber around the ring guided by the bending and focusing forces of these magnets. To confine the ions in the vacuum chamber as they are accelerated or decelerated, the strength of the magnetic field (B) is varied according to the linear momentum per nucleon (P) of the ion:

$$B\rho = AP/Qe, \qquad (4.1\text{-}1)$$

where ρ is the bending radius of the magnet and, Q is the charge number of the ion and A is the ion mass number. The acceleration or deceleration is achieved by applying an alternating electric field whose frequency is synchronized with the revolution frequency of the ion. The maximum ion energy is determined by the maximum bending power of the dipole magnets and by the mass and charge of the ion. For the proposed $B\rho$ = 2.67-Tm ring, the maximum energy is 82 MeV/nucleon for ions with Q/A = 1/2, 11 MeV/nucleon for $^{238}U^{43+}$ ions, and 22 MeV/nucleon for $^{238}U^{60+}$ ions.

For a given magnetic field, the orbit of ions with the design energy and no transverse velocity is a closed curve called the central orbit. Ions with the same energy but with nonzero transverse velocity

oscillate around the central orbit as a result of the focusing magnetic forces. This transverse motion relative to the central orbit is known as betatron motion. It is usually described in terms of a periodic amplitude $\beta(s)$ and a phase $\phi(s)$:

$$x = \sqrt{\varepsilon_x \beta_x(s)} \sin(\phi_x(s) + \phi_{x0}) ;$$

$$y = \sqrt{\varepsilon_y \beta_y(s)} \sin(\phi_y(s) + \phi_{y0}) ; \qquad (4.1\text{-}2)$$

$$\text{and} \quad \phi_x(s) = \int_0^s \frac{ds'}{\beta_x(s')} ;$$

where x, y are the horizontal and vertical displacements from the central orbit, s is the distance along the central orbit, and ε_x and ε_y are the ion emittances. The number of oscillations in one revolution around the ring is the tune of the betatron motion, and is given by

$$\nu_x = \frac{1}{2\pi} \oint \frac{ds'}{\beta_x(s')} . \qquad (4.1\text{-}3)$$

The design tunes for HISTRAP are $\nu_x = 2.309$ and $\nu_y = 2.274$.

For a given lattice design, the betatron-functions are obtained by solving the equations of motion. The maximum betatron motion is limited by the size of the vacuum chamber, which is usually limited by the aperture of the dipole and quadrupole magnets. The corresponding maximum emittance is the acceptance of the synchrotron. HISTRAP has a horizontal acceptance of about 200π mm-mrad and a vertical acceptance of about 60π mm-mrad. Usually, the injected beam has an emittance (ε) smaller than the acceptance (A) of the ring, and it is possible to inject several turns (A/ε) of beam before the full acceptance is filled. The number of ions (N) that can be injected in a ring is given by

$$N = dAIC/\epsilon/v, \qquad (4.1\text{-}4)$$

where I is the intensity, C is the ring circumference, v is the beam velocity at injection, and d is a dilution factor since multiturn injection usually is not 100% efficient. In principle, it is possible to fill both the horizontal and vertical phase space by multiturn injection. However, only one dimension has been used in existing accelerators, and considerable dilution is usually encountered. More than 35 turns of beam can be injected from the HHIRF tandem into HISTRAP. In addition to the beam intensity limit caused by synchrotron acceptance and injected beam emittance, there is a space charge limit due to the action of the electric and magnetic field of the beam on itself. Ion beams from the tandem with a new pulsed magnetic-cusp plasma sputter ion source will be able to fill HISTRAP to its space charge limit.

Ions with momentum-to-charge ratios (P/Q) different from the design value will oscillate around a different central orbit. In general, the central orbit of ions with larger momentum or lower charge has a larger average radius. This deviation $\Delta x(s)$ is described by a dispersion function $\eta(s)$ from which the displacement of the central orbit can be obtained as

$$\Delta x(s) = \eta(s) \frac{\Delta(P/Q)}{P/Q}, \qquad (4.1\text{-}5)$$

where $\Delta(P/Q)$ is the deviation of P/Q from the design value. Usually, a small dispersion function is desirable because it increases the amount of deviation in P/Q that can be accommodated in the ring. The design mode for HISTRAP has dispersion equal to zero in all four straight sections and a maximum dispersion of 1.6 m in the quadrupoles. The

magnet apertures are large enough so that HISTRAP can hold $\Delta(P/Q)/PQ = \pm 0.04$.

In addition to the limit on the beam intensity due to the synchrotron acceptance and beam emittance, there are limits due to the electric and magnetic field produced by the beam itself. The repulsive space charge force introduces a defocusing effect and reduces the tune of the betatron motion. Since the strength of this force varies according to the radial position of the particle in the beam, it produces a distribution of tune reduction. The number of particles, N_{SC}, needed to produce a tune shift, $\Delta\nu$, is

$$N_{SC} = \varepsilon\beta^2\gamma^3 \frac{A}{Q^2} B_f \Delta\nu \; 2.72 \; 10^{18} \; , \qquad (4.1\text{-}6)$$

where ε is the unnormalized emittance of the synchrotron beam assuming $\varepsilon_x = \varepsilon_y$ in units of π meters, $\beta = v/c$, γ is the Lorentz factor, and B_f is the bunching factor. Notice that for injection at low energy, N_{SC} is proportional to kinetic energy. As the beam is accelerated, $\varepsilon\beta\gamma$, the normalized emittance, is invariant, and thus N_{SC} is proportional to the velocity. The A/Q^2 dependence means that particles with higher charge states cause larger tune shifts. If the tune shift results in a resonance condition, the transverse motion will be unstable. To avoid resonances, the $\Delta\nu$ value is usually limited to less than 0.08. For HISTRAP, $\varepsilon_x = 200\pi$ mm-mrad $\neq \varepsilon_y = 60\pi$ mm-mrad, in which case an effective emittance of 110π mm-mrad can be used in Eq. 4.1-6.

Another collective effect, the microwave instability, is caused by the coherent interaction of the beam with the beam pipe. The limit on particle number, the Keil-Schnell limit, is given by

$$N_{ks} = \left(\frac{\Delta P}{P}\right)^2 \beta^2\gamma^3 \frac{A}{Q^2} \frac{R|\eta|}{g} 6.65\ 10^{17}, \qquad (4.1\text{-}7)$$

where ΔP is the FWHM of the momentum spread, R is the mean radius of the ring, η is the frequency slip factor, and g is a geometric factor with a value of about 3.0. Notice that the same $\beta^2\gamma^3$ A/Q^2 factor appears as in the space-charge limit. Theoretical study indicates that a catastrophic loss of beam may not occur if the number of ions exceeds the Keil Schnell limit. Instead, a tail will be developed in the momentum distribution which can stabilize the beam. The existence of this stabilization mechanism is an open question.

4.2 HISTRAP Design

4.2.1 Lattice Design

The main design criteria for HISTRAP are listed in Table 4.2-1. These criteria determine the basic lattice, layout, and location of the ring. As listed in Table 4.2-1, the ring will be used to accelerate, decelerate, and store heavy ions, and in particular, to decelerate highly-charged very-heavy ions down to low energies. The maximum bending power is set at 2.67 Tm, corresponding to a K = 340 cyclotron. This allows relatively high-energy atomic physics experiments to be performed, but does not make the bending power a significant cost factor in the ring design. One straight section must have at least a 3.5-m free space between valves to hold the electron beam cooler, and another equally long straight section to be kept free of accelerator apparatus and used for circulating beam experiments with fixed targets, merged

Table 4.2-1. Design Criteria for HISTRAP

- Accelerate, decelerate and store heavy ions
- Maximum bending power of $B\rho$ = 2.67 Tm
- Electron beam cooling
- In-ring circulating beam experiments with

  Fixed targets
  Merged electron beams
  Merged photon beams
  Crossed ion beams

- Store multiple charge states with $\Delta Q/Q = \pm 4\%$
- Inject from the HHIkF 25 MV tandem
- Inject from dedicated ECR/RFQ source
- Slow extraction system for external experiments

photon beams, and crossed ion beams. Merged ion-electron beam measurements will be done with the electron beam cooler in a mismatched velocity condition. In addition to these space requirements, circumference is also needed for an rf system, an injection septum, and a future slow extraction system to feed external beam lines. The dipoles must be of "C design" to accommodate merged photon beam experiments.

Perhaps the most difficult and most interesting requirement in Table 4.2-1 is the momentum aperture of ±4%. This will provide HISTRAP the unique capability of storing beams with charge states separated by ±4%. This will allow, for example, ^{238}U ions with charge states between 60+ and 65+ to be simultaneously stored in a stable configuration. Finally, HISTRAP must be located to utilize two injectors: the existing HHIRF tandem accelerator and a dedicated ECR source and RFQ linac. The

location of HISTRAP is shown in Fig. 2.1-3. This location, between the new atomic physics annex and the old south annex, and next to the tandem magnet room, is ideal. HISTRAP will be injected from the HHIRF tandem in a very simple way with an optimum-length beam line.

The ring lattice must meet the above requirements and, in addition, the arrangement of the quadrupole magnets should produce beta functions which are small in the magnetic elements. However, the electron beam cooler provides some limits on the beta functions. In the cooling section, the minimum value of β is limited by the upper limit of the cooling time because a small β gives a large angular divergence which takes longer to cool. On the other hand, the minimum angular divergence of the beam attainable by cooling is limited by the angular divergence of the electron beam due to thermal motion. Since the emittance $\epsilon = \theta^2\beta$, a smaller emittance can be reached if the cooling section has a small beta function. A value of $\beta \sim 10$ m gives an optimal cooling rate for a 50 MeV/nucleon beam, an emittance of 40π mm-mrad, and an electron thermal temperature of 0.1 eV.

Moreover, it is desirable to have the beam nondispersed in the straight sections used for cooling, rf, and experiment. The requirement of holding several charge states simultaneously means the maximum value of the dispersion function has to be small. Also, it is important that quadrupoles be placed in dispersed sections so that the sextupoles for chromaticity correction can be placed nearby. In addition, the horizontal and vertical beta function should be different at the proposed sextupole locations.

The values of the tunes of the synchroton must be chosen to avoid resonances, especially the structure resonances. A 1/3 integer resonance horizontal slow extraction system is plannmed for the future. Therefore, the horizontal tune has to be near a third integer number not corresponding to a structure resonance. Finally, it is preferable to have the horizontal and vertical tunes differ by zero or an integer amount in order to have a large resonance-free space around the operating point.

In addition to long straight sections, additional space for correction magnets, bump magnets for injection, vacuum equipment, and beam monitoring devices must be provided in the ring. Since space is at a premium, the tradeoff between circumference and aperture is the important consideration. As the circumference increases, the magnet size increases. Finally, the lattice has to be reasonably tolerant to magnet strength and alignment errors, so that only a small aperture allowance is needed for closed-orbit distortion and beta function variations.

The proposed lattice shown in Fig. 2.1-1 meets these requirements. Each 90° bending quadrant consists of a quadrupole triplet between two 45° dipole magnets. In addition, each quadrant has reflection symmetry about its midpoint. The straight section length is an important parameter and was chosen to be four meters long. Three of the straights are used for cooling, future extraction, and in-ring experiments, respectively. The fourth straight section is used for both injection and the rf cavity.

The straight sections are made nondispersive by making each quadrant, consisting of three quadrupoles and two 45° dipoles, a 90°

achromatic bend. The quadrupole triplet comprises focusing (F) – defocusing (D) – focusing (F) quadrupoles in the horizontal plane. This arrangement minimizes the dispersion in the quadrupole magnets. The horizontal and vertical tunes of the ring were chosen to be near 7/3. At the design tune these are $\nu_x = 2.3088$ and $\nu_y = 2.2744$, which avoids structure resonances and facilitates extraction by excitation of the third integer resonance.

The two values of the tune and the requirement of having non-dispersed straights impose three conditions. With the length of the long straights fixed at 4 m and the dipole magnet lengths fixed at 1.309 m, there are only four lattice parameters which can be varied to satisfy these three conditions. These parameters are: the strength of the two types of quadrupole magnets, the distance between the F and D quadrupoles S_{QQ}, and the distance between the F quadrupole and the dipole S_{QD}. This allows only one free parameter which can be used for the adjustment of beta functions. Figure 4.2-1 shows the change of the lattice functions as the distance between the quadrupoles is varied. The horizontal beta function β_x is insensitive to this parameter, but the vertical beta function β_y is quite sensitive. The value of $S_{QQ} = 0.7$ m is chosen because it gives a smallest overall β_y function in the dipole magnets. The variation of the quadrupole gradients with S_{QQ} is shown in Fig. 4.2-2. The β functions and the dispersion function η_x are shown in Fig. 4.2-3 for 1/8 of the lattice. The lattice parameters are listed in Table 4.2-2. This lattice meets all the design requirements and requires the minimum number of quadrupole magnets.

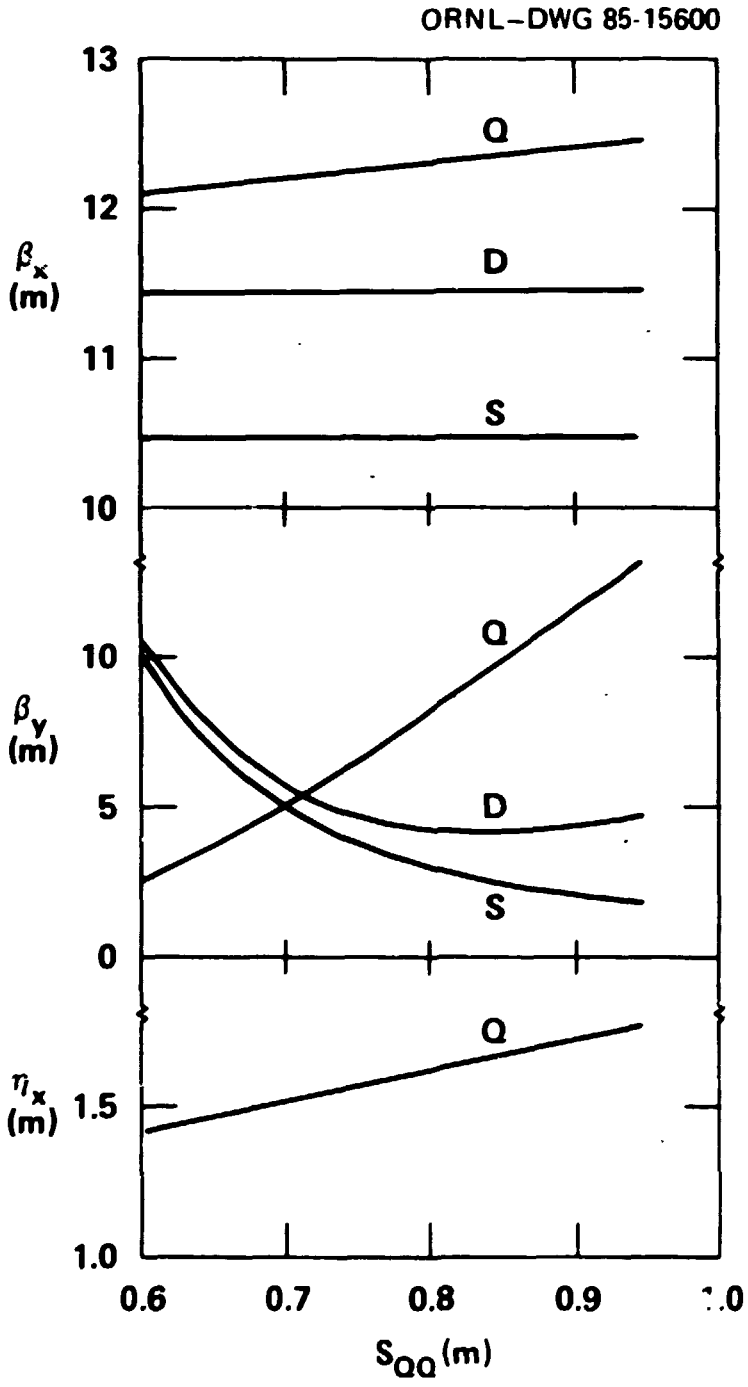

Fig. 4.2-1 Variation of the maximum lattice functions with quadrupole spacing S_{QQ} between Q_F and Q_D. The maximum values of the beta functions and dispersion in the quadrupoles (Q), dipoles (D), and in the long straights (S) are shown. The other lattice parameters S_{QD}, Q_F, and Q_D are varied in order to keep $\nu_x = 2.3088$, $\nu_y = 2.2744$, and $\eta_x = 0$ in the long straight sections.

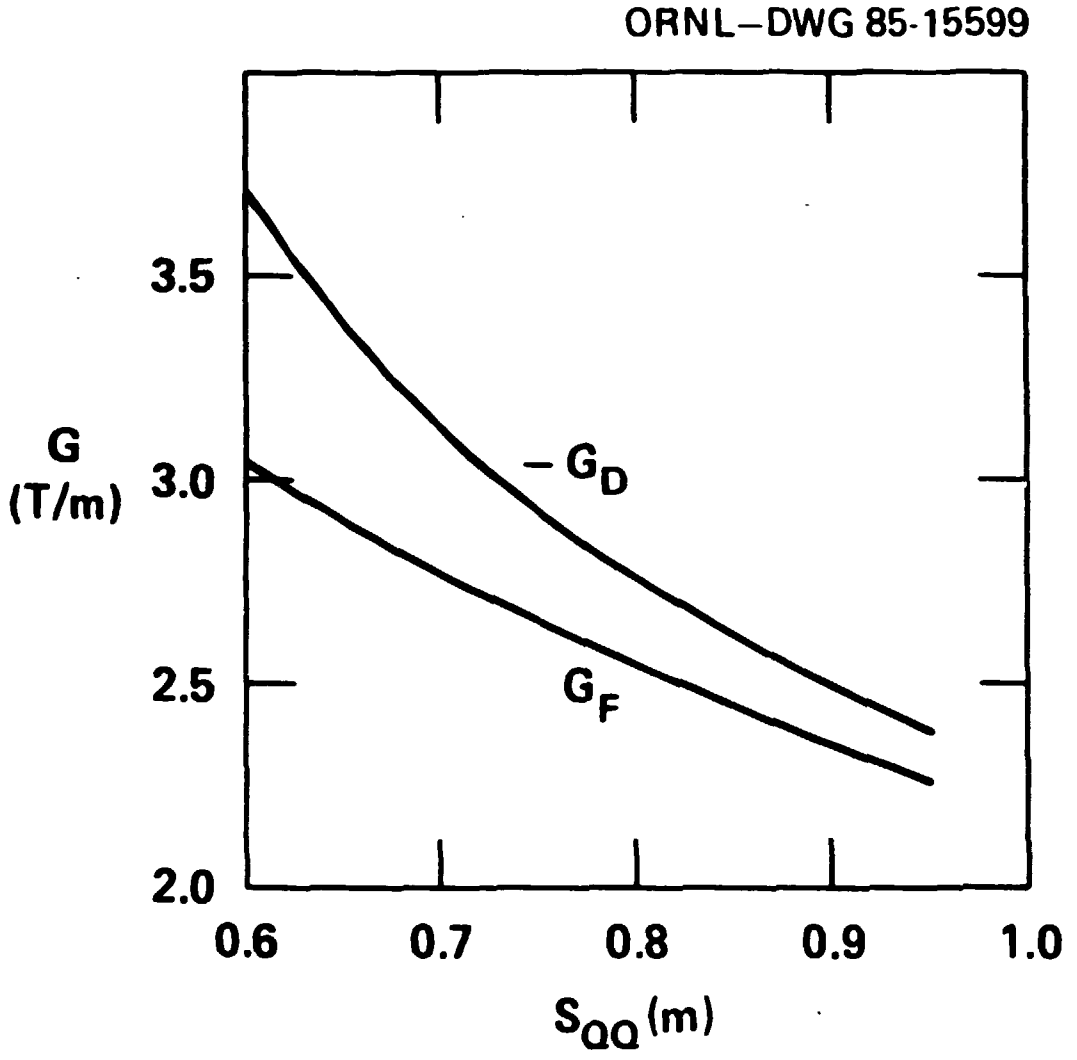

Fig. 4.2-2 Change of the quadrupole gradients as the distance S_{QQ} is varied. The values of the gradient are for $B\rho$ = 1.5 Tm.

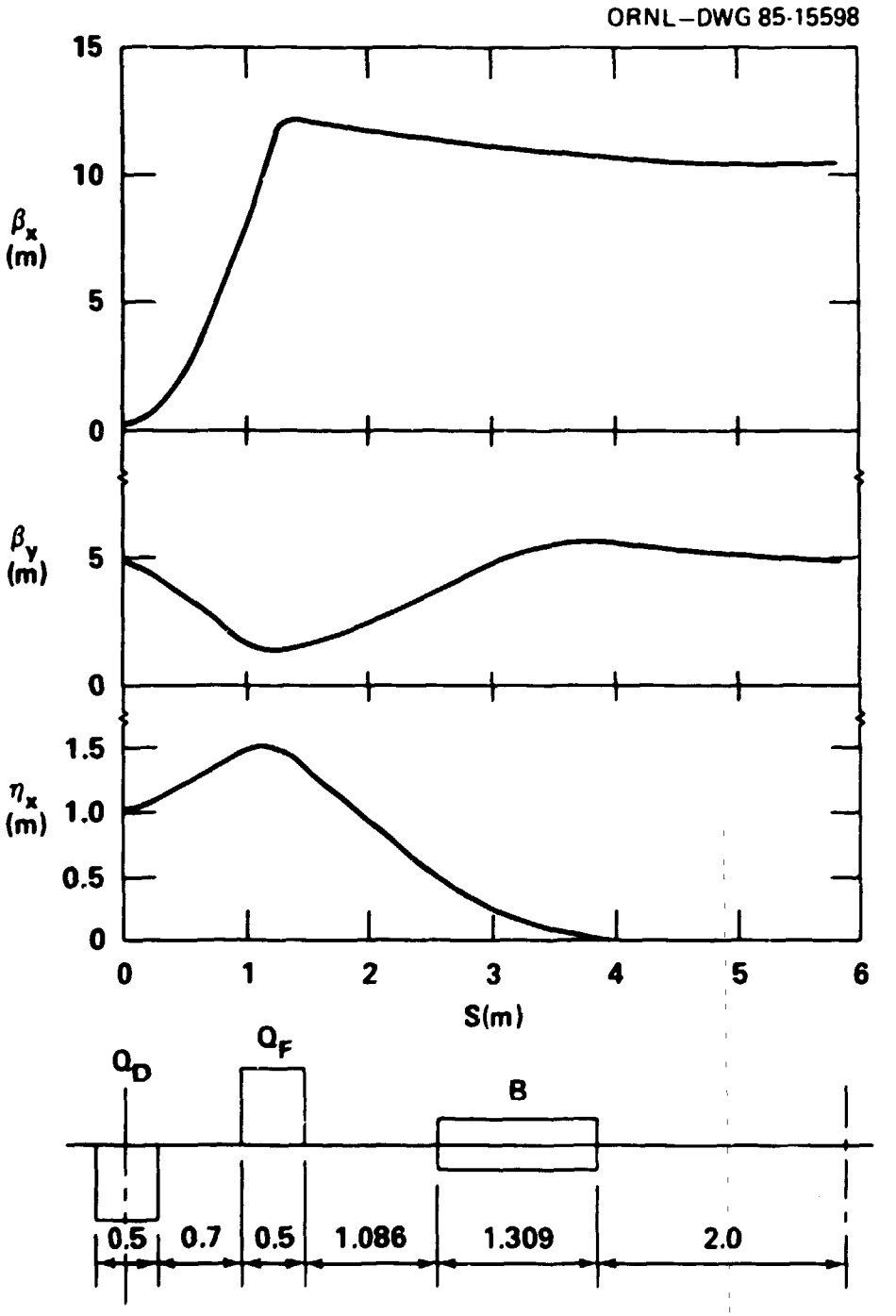

Fig. 4.2-3 Lattice functions for 1/8 of the circumference of HISTRAP.

Table 4.2-2. Parameters of the HISTRAP lattice

Magnetic rigidity	$B\rho$ = 2.67 Tm	
Circumference	C = 46.757 m	
Long straight (4)	ℓ_S = 4.0 m	
Dipole (8)	ρ = 1.666 m	
	θ = 45°	
	ℓ_D = 1.309 m	
Quadrupole (12)	ℓ_Q = 0.5 m	
Q_F (8)	G_F = 4.930 T/m	
Q_D (4)	G_D = -5.569 T/m	
Tune	ν_x = 2.308	ν_y = 2.274
Chromaticity	ξ_x = -6.184	ξ_y = -1.524
Transition gamma	γ_t = 6.69	
Beta function		
Dipole	$\hat{\beta}_x$ = 11.4 m	$\hat{\beta}_y$ = 5.7 m
Quadrupole	$\hat{\beta}_x$ = 12.2 m	$\hat{\beta}_y$ = 5.[illegible] m
Straight	β_x = 10.5 m	β_y = 4.[illegible] m
Dispersion function		
Dipole	$\hat{\eta}_x$ = 0.49 m	
Quadrupole	$\hat{\eta}_x$ = 1.51 m	
Straight	η_x = 0 m	

In order to hold several charge states of the same beam in the storage mode, it may prove necessary to cancel the chromaticity by using higher multipole magnets, and in particular, sextupole magnets. Since all the quadrupoles are in dispersive regions, this cancellation could be achieved locally by placing a sextupole magnet next to each quadrupole magnet. These sextupoles are shown on all sketches and engineering drawings of HISTRAP and are contained in the cost estimate. The extraction system is also shown on all sketches and engineering drawings of HISTRAP, but the hardware is not contained in the cost estimate.

4.2.2 Injection Parameters and HISTRAP Performance

The maximum energy per nucleon and the maximum circulating and extracted beam currents that can be expected from HISTRAP are strongly dependent on the parameters of the heavy ion beams injected into HISTRAP. In general, the most energetic beams do not correspond to the most intense beams. The maximum energy per nucleon depends on the maximum bending power of HISTRAP, which is 2.67 Tm, and the maximum injected charge state. This information is summarized in Table 4.2-3 and graphed in Figure 4.2-4. HISTRAP will have two injectors: the HHIRF tandem injector and the dedicated ECR/RFQ injector. These injectors are described in detail in Sections 4.3 and 4.4, respectively. For each injector, two cases are listed: a high-current case and a high-energy (high-charge-state) case.

The highest charge states and the highest energies will be achieved with tandem injection. The high-current case assumes tandem operation at 22 MV with foil strippers in both the tandem terminal and the HISTRAP

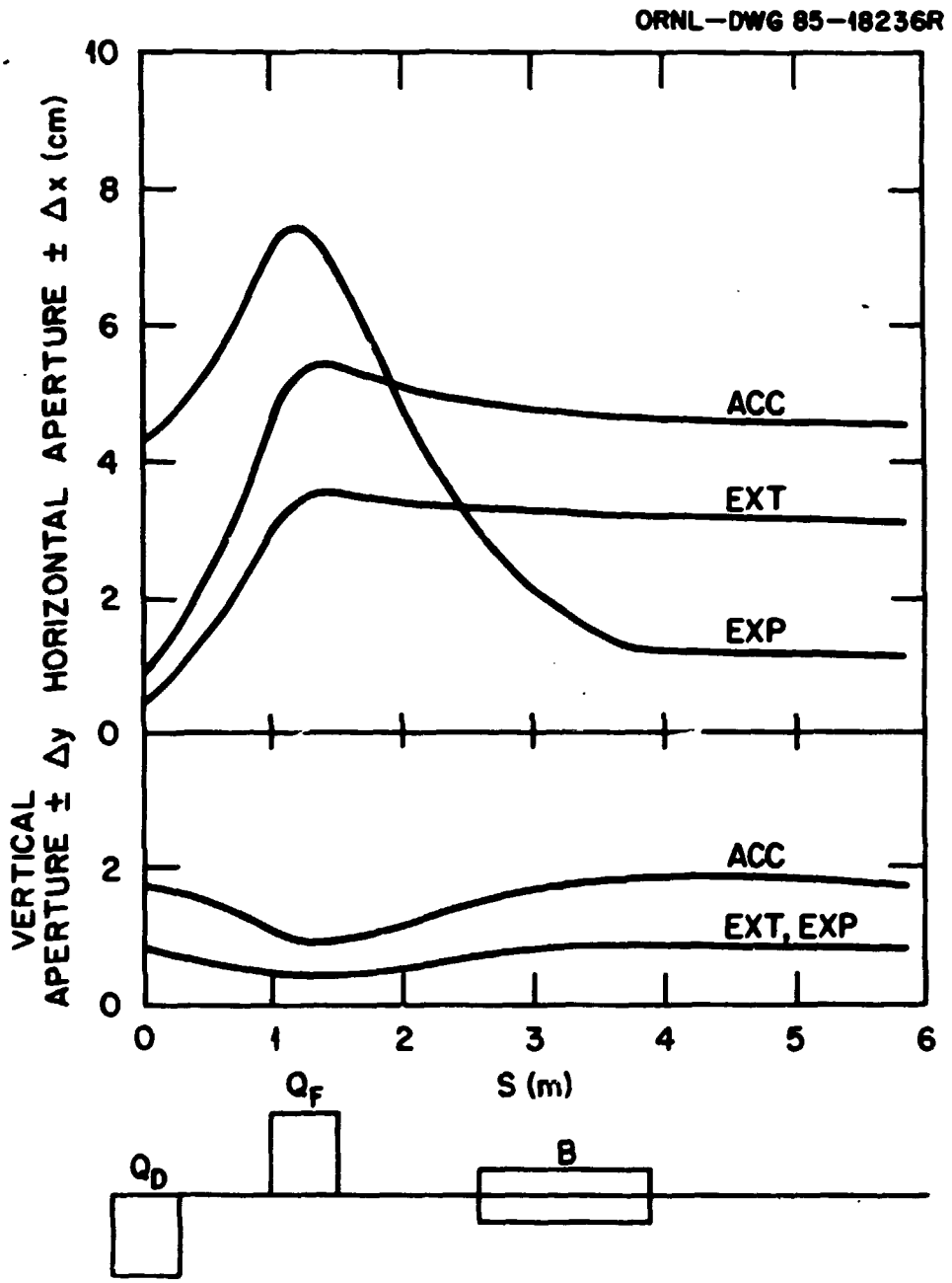

Fig. 4.2-4 The horizontal and vertical aperture requirements for acceleration (Acc), extraction (Ext), and experiment (Exp).

Table 4.2-3. Expected charge states and resulting maximum energy per nucleon for both tandem and ECR/RFQ injection of HISTRAP. Both high-current and high-energy cases are listed.

ION	TANDEM INJECTION				ECR/RFQ INJECTION			
	High-Current		High-Energy		1 PμA		1 PnA	
	Q	E/A	Q	E/A	Q	E/A	Q	E/A
^{12}C	6	82.2	6	82.2	6	82.2	6	82.2
^{16}O	8	82.2	8	82.2	8	82.2	8	82.2
^{32}S	15	72.7	16	82.2	12	47.1	14	63.6
^{40}Ca	18	67.1	20	82.2	13	35.6	16	53.5
^{58}Ni	24	57.1	27	71.7	15	22.7	20	40.0
^{79}Br	27	39.4	32	54.8	17	15.8	23	28.8
^{127}I	36	27.2	42	36.8	21	9.3	30	19.0
^{150}Nd	38	21.8	44	29.1	22	7.4	33	16.5
^{197}Au	40	14.1	48	20.2	24	5.1	39	13.4
^{238}U	43	11.1	51	15.6	25	3.8	41	10.1

injection line. The most probable charge states are assumed at both strippings. Fully stripped ions with Q/A = 1/2 will have a maximum energy of 82.2 MeV/nucleon. Uranium ions will be injected into HISTRAP in the 43+ charge state, giving a maximum energy of 11.1 MeV per nucleon. The high-energy case assumes tandem operation at 25 MV with beam currents about a factor of 20 less than the high-current case. This reduction in current and gain in energy results from taking charge states higher than the most probable charge state. In the tandem terminal, a higher charge state having about 50% intensity of the most probable charge state is chosen; and at the injection foil, a higher charge state having about 10% intensity of the most probable charge state is

chosen. Fully stripped ions up to chromium can be obtained. Uranium 51+ ions will give a maximum energy of 15.6 MeV/nucleon.

The dedicated ECR source and RFQ preaccelerator will produce lower charge states, but will always be available for HISTRAP injection. Two cases are listed in Table 4.2-3: a high-current, 1-pμA case and high-energy, 1-pnA case. Figure 2.1-2 summarizes the energy per nucleon results as a function of mass for the various injection options.

Both the circulating particle currents and extracted particle currents that can be expected from HISTRAP are directly proportional to the number of ions which can be stored in HISTRAP under stable conditions. As discussed in Section 4.1, the number of ions that can be stored in HISTRAP must be less than the space charge limit, N_{sc}, and perhaps less than the Keil-Schnell limit, N_{ks}. Both of these limits are directly proportional to the ion energy. In addition, the space charge limit is directly proportional to the beam emittance, and the Keil-Schnell limit is proportional to the square of the relative beam energy spread.

Tables 4.2-4 and 4.2-5 list both the space charge limit and the Keil-Schnell limit of HISTRAP for ions injected from the ECR/RFQ source operated in both the high-current and high-energy modes. These limits are valid at the injection energy of 0.25 MeV/nucleon with a beam energy spread of 1% and with HISTRAP acceptances of $\varepsilon_x = 200\pi$ mm-mrad and $\varepsilon_y = 60\pi$ mm-mrad. A transmission of 40% is assumed to account for losses in the RFQ and injection line. The number of ions which actually can be injected into HISTRAP with the ECR/RFQ injector is emittance-limited for both the high-energy case and the high-current case. In particular, the

Table 4.2-4. Properties of high-current beams, 1 puA, from the ECR/RFQ at nine-turn injection

Beam	Charge	E/A (MeV/ nucleon)	ΔP/P (%)	N_{inj}	N_{sc}	N_{ks}
^{12}C	6	0.25	0.5	$1.5\ 10^{8}$	$2.1\ 10^{9}$	$7.4\ 10^{9}$
^{16}O	8	0.25	0.5	$1.5\ 10^{8}$	$1.6\ 10^{9}$	$5.5\ 10^{9}$
^{32}S	12	0.25	0.5	$1.5\ 10^{8}$	$1.4\ 10^{9}$	$4.9\ 10^{9}$
^{40}Ca	13	0.25	0.5	$1.5\ 10^{8}$	$1.5\ 10^{9}$	$5.2\ 10^{9}$
^{58}Ni	15	0.25	0.5	$1.5\ 10^{8}$	$1.7\ 10^{9}$	$5.7\ 10^{9}$
^{79}Br	17	0.25	0.5	$1.5\ 10^{8}$	$1.8\ 10^{9}$	$6.1\ 10^{9}$
^{127}I	21	0.25	0.5	$1.5\ 10^{8}$	$1.8\ 10^{9}$	$6.4\ 10^{9}$
^{150}Nd	22	0.25	0.5	$1.5\ 10^{8}$	$2.0\ 10^{9}$	$6.9\ 10^{9}$
^{197}Au	24	0.25	0.5	$1.5\ 10^{8}$	$2.2\ 10^{9}$	$7.6\ 10^{9}$
^{238}U	25	0.25	0.5	$1.5\ 10^{8}$	$2.4\ 10^{9}$	$8.4\ 10^{9}$

Table 4.2-5. Properties of high-energy beams, 1 pnA, from the ECR/RFQ at nine-turn injection

Beam	Charge	E/A (MeV/ nucleon)	ΔP/P (%)	N_{inj}	N_{sc}	N_{ks}
^{12}C	6	0.25	0.5	$1.5\ 10^{5}$	$2.1\ 10^{9}$	$7.4\ 10^{9}$
^{16}O	8	0.25	0.5	$1.5\ 10^{5}$	$1.6\ 10^{9}$	$5.5\ 10^{9}$
^{32}S	14	0.25	0.5	$1.5\ 10^{5}$	$1.0\ 10^{9}$	$3.6\ 10^{9}$
^{40}Ca	16	0.25	0.5	$1.5\ 10^{5}$	$1.0\ 10^{9}$	$3.5\ 10^{9}$
^{58}Ni	20	0.25	0.5	$1.5\ 10^{5}$	$0.9\ 10^{9}$	$3.2\ 10^{9}$
^{79}Br	23	0.25	0.5	$1.5\ 10^{5}$	$1.0\ 10^{9}$	$3.3\ 10^{9}$
^{127}I	30	0.25	0.5	$1.5\ 10^{5}$	$0.9\ 10^{9}$	$3.1\ 10^{9}$
^{150}Nd	33	0.25	0.5	$1.5\ 10^{5}$	$0.9\ 10^{9}$	$3.1\ 10^{9}$
^{197}Au	39	0.25	0.5	$1.5\ 10^{5}$	$0.8\ 10^{9}$	$2.9\ 10^{9}$
^{238}U	41	0.25	0.5	$1.5\ 10^{5}$	$0.9\ 10^{9}$	$3.1\ 10^{9}$

ECR/RFQ will produce a beam with an emittance of about 12π mm-mrad; consequently, about 9 turns of this beam can be injected into the HISTRAP. As listed in Tables 4.2-4 and 4.2-5, this corresponds to 1.5 x 10^8 ions for the high-current case and 1.5 x 10^5 ions for the high-energy case, respectively.

Finally, the expected HISTRAP beam current performance with ECR/RFQ injection is summarized in Table 4.2-6. Values for the high-current case are listed without parentheses and values for the high-energy case are listed in parentheses. The stored ion numbers have been converted to in-ring circulating currents in particle μA after acceleration to the full energy at Bρ = 2.67 Tm. Time averaged extracted currents in particle pA which would be available in external beam lines are also listed, assuming a cycling rate of 0.4 Hz.

Table 4.2-6. Full-energy properties of high-current (high-energy) beams from the dedicated ECR/RFQ injector

ION	CHARGE	MeV/A	CIRCULATING pμA	EXTRACTED ppA (0.4Hz)
^{12}C	6 (6)	82.2 (82.2)	61 (.061)	1.0 (1.0 10^{-3})
^{16}O	8 (8)	82.2 (82.2)	61 (.061)	1.0 (1.0 10^{-3})
^{32}S	12 (14)	47.0 (63.6)	47 (.054)	1.0 (1.0 10^{-3})
^{40}Ca	13 (16)	35.6 (53.5)	40 (.050)	1.0 (1.0 10^{-3})
^{58}Ni	15 (20)	22.7 (40.0)	33 (.044)	1.0 (1.0 10^{-3})
^{79}Br	17 (23)	15.8 (28.8)	28 (.037)	1.0 (1.0 10^{-3})
^{127}I	21 (30)	9.3 (19.0)	22 (.031)	1.0 (1.0 10^{-3})
^{150}Nd	22 (33)	7.4 (16.5)	19 (.029)	1.0 (1.0 10^{-3})
^{197}Au	24 (39)	5.1 (13.4)	16 (.026)	1.0 (1.0 10^{-3})
^{238}U	25 (41)	3.9 (10.1)	14 (.022)	1.0 (1.0 10^{-3})

Because of the higher injection energy, the highest circulating and extracted currents will be obtained with tandem injection. The number of ions at the tandem injection energy for the HISTRAP space-charge limit and Keil-Schnell limit are listed in Table 4.2-7 for the high-current case. The $\Delta P/P$ values resulting from straggling in a 200-$\mu g/cm^2$ carbon stripping foil are used for the tandem beam. At these energies, the Keil-Schnell limit is less than the space-charge limit. So, if the Keil-Schnell limit is valid, the relative momentum spread of the beam would have to be increased to about 0.3% for stable storage.

Recent advances in negative ion source technology and, in particular, the pulsed cusp-source work of Alton et al, [Al88b] will allow HISTRAP to be filled to the space-charge limit with tandem injection.

Table 4.2-7. Properties of beams from the tandem for HISTRAP injection for the high-current case

Beam	Charge	E/A (MeV/ nucleon)	$\Delta P/P$ (%)	N_{sc}	N_{ks}
^{12}C	6	12.8	0.018	$10.7\ 10^{10}$	$4.8\ 10^{8}$
^{16}O	8	11.0	0.021	$69.0\ 10^{9}$	$4.2\ 10^{8}$
^{32}S	15	7.6	0.031	$27.5\ 10^{9}$	$3.6\ 10^{8}$
^{40}Ca	18	6.6	0.035	$20.0\ 10^{9}$	$3.4\ 10^{8}$
^{58}Ni	24	5.3	0.04?	$13.6\ 10^{9}$	$3.3\ 10^{8}$
^{79}Br	27	3.9	0.053	$10.8\ 10^{9}$	$4.1\ 10^{8}$
^{127}I	36	2.8	0.070	$7.0\ 10^{9}$	$4.6\ 10^{8}$
^{150}Nd	38	2.4	0.079	$6.2\ 10^{9}$	$5.3\ 10^{8}$
^{197}Au	40	1.9	0.098	$6.0\ 10^{9}$	$7.8\ 10^{8}$
^{238}U	43	1.7	0.110	$5.6\ 10^{9}$	$9.4\ 10^{8}$

Table 4.2-8 summarizes the resulting circulating and extracted beam currents, assuming HISTRAP is filled to the space-charge limit at injection. With 22-MV tandem operation, the most probable charge states for the terminal and injection foil, 35-turn injection, a 40% tandem transmission, and 20% rf loss, the required instantaneous injection current from the tandem would be in the order of one mA. The exact injector currents are listed in the table. Circulating particle currents from 38 pmA for light ions to 0.9 pmA for uranium ions will be

Table 4.2-8. Injection, circulating, and extracted beam currents at maximum energy for high-current tandem injection. HISTRAP will operate with about a 0.4-Hz repetition rate; 1.6 Hz could be possible. The currents are calculated assuming HISTRAP will be filled to the space charge limit.

ION	CHARGE	MeV/A	INJECT* PmA	CIRCUL. PmA	EXTRACTED PnA 0.4 Hz	1.6 Hz
^{12}C	6	82.2	2.8	37.6	6.8	27.4
^{16}O	8	82.2	2.1	27.8	4.4	17.7
^{32}S	15	72.7	1.8	10.0	1.8	6.9
^{40}Ca	18	67.1	1.7	7.5	1.3	5.1
^{58}Ni	24	57.1	1.6	4.7	0.87	3.5
^{79}Br	27	39.3	1.6	3.1	0.69	2.8
^{127}I	36	27.2	1.2	1.7	0.45	1.8
^{150}Nd	38	21.8	1.1	1.4	0.40	1.6
^{197}Au	40	14.1	1.1	1.1	0.38	1.5
^{238}U	43	11.1	1.3	0.9	0.36	1.4

* 22-MV tandem
Most probable charge states
35-turn injection
40% tandem transmission
20% rf loss

available. This corresponds to impressive circulating heavy ion electrical currents; 225 mA for ^{12}C ions and 35 mA for uranium.

Extracted currents depend on the repetition rate, which is limited by magnet power supply cost. Table 4.2-8 lists extracted currents for two repetition rates. This proposal contains funds for power supplies which can cycle the magnets at about a 0.4 Hz repetition rate. The extracted beam current could be increased by about a factor of four by increasing the repetition rate to 1.6 Hz. This would require a substantial investment in power supplies. A 1.6-Hz repetition rate requires a dB/dt of 5.5 T/s, which is near the technological limits for conventional laminated magnets and metallic vacuum chambers.

4.2.3 Choice of Aperture

The size of the beam is determined by the amplitude of the betatron function $\beta(s)$, the dispersion function $\eta(s)$, displacement of the beam for extraction, and the expected closed-orbit distortion after correction. From the known lattice functions, the aperture requirements can be calculated for a given beam emittance ε, momentum and charge deviation $\frac{\Delta(P/Q)}{(P/Q)}$, extraction displacement X_{ext}, beta function at the extraction point β_{ext}, and closed-orbit errors ΔXeq according to:

$$R(s) = \sqrt{\varepsilon\,\beta(s)} + \eta(s)\left(\frac{\Delta P}{P} - \frac{\Delta Q}{Q}\right) + X_{ext}\sqrt{\frac{\beta(s)}{\beta_{ext}}} + 2\sqrt{6}\,\frac{\Delta Xeq}{\sqrt{\beta}}\sqrt{\beta(s)} \qquad (4.2\text{-}3)$$

It is obvious that during different phases of the operation, such as acceleration, cooling, and extraction, the aperture requirements are different. We have studied three cases: (1) acceleration, (2) extraction of cooled beam, and (3) experiments with stored cooled beam with

several charge states. The parameters used are listed in Table 4.2-9. The aperture requirements are shown in Fig. 4.2-4. In the quadrupole magnet Q_F, the beam has the largest horizontal size, which is about ±8 cm. This is dictated by the requirement of holding beams of charge state 4% above and below the central beam. In the bending magnet, the beam needs an aperture ±5 cm in the horizontal and ±2 cm in the vertical plane. In addition to the beam aperture, the aperture of the magnets includes space for beam pipe and insulation, beam pickup devices, shims and clearance, etc.

Table 4.2-9 Values of parameters used in the aperture calculations

		ε (π mm-mrad)	$\Delta P/P$	$\Delta Q/Q$	X_{ext} (m)	β_{ext} (m)	$\frac{\Delta X_{eq}}{\sqrt{\beta}}$ † ($\sqrt{m}$)
Acceleration	x	200	0.0035	0	0	0	0.000011
	y	60	0.0035	0	0	0	0.000034
Extraction	x	13	0.001	0	0.02	10.5	0.000011
Cool beam	y	13	0.001	0	0	0	0.000034
Experiment	x	13	0.001	0.04	0	0	0.000011
Cool beam	y	13	0.001	0.04	0	0	0.000034

† After correction

4.2.4 Closed Orbit and Focusing Errors

Random errors in the dimensions, field strengths, and positions of the ring magnets will cause two types of effects: (1) a distortion of the closed orbit, and (2) a deviation of the focusing strength from the

design value. These effects have been studied using the computer program SYNCH.

The deviation of the closed orbit from the design orbit is the result of (1) random errors in the integrated dipole strengths, (2) random rotational errors of the dipole magnets around the beam axis, and (3) random alignment errors of the quadrupoles transverse to the beam. The root-mean-square (rms) deviations due to the rms errors of all the magnets are calculated to be:

dipole strength errors

$$\Delta X = 3.18\sqrt{\beta_x}\ \Delta B/B$$

dipole rotational errors

$$\Delta Y = 2.43\sqrt{\beta_y}\ \Delta\theta$$

quadrupole position errors

$$\Delta X = 3.69\sqrt{\beta_x}\ \Delta x$$

$$\Delta Y = 2.66\sqrt{\beta_y}\ \Delta y$$

where ΔX and ΔY are the rms displacements of the closed orbit from the design orbit in the x and y directions, respectively, and where $\Delta B/B$, $\Delta\theta$, Δx, and Δy are the rms errors in the integrated relative dipole strength, dipole rotational angle, and the horizontal and vertical quadrupole alignment. All the distances and beta functions are measured in meters, and angles in radians.

For typically achievable tolerances of $\Delta B/B = 5\cdot10^{-4}$, $\Delta\theta = 2\cdot10^{-4}$ rad, and $\Delta x = \Delta y = 0.15$ mm, closed orbit errors given by

$$\Delta X = 16.9\cdot10^{-4}\sqrt{\beta_x}$$

$$\Delta Y = 6.2\cdot10^{-4}\sqrt{\beta_y}$$

are obtained. This gives rms closed orbit errors of ΔX = 5.3 mm and ΔY = 1.4 mm for the beta function values of 10 m and 5 m, respectively.

Random focusing errors are produced by (1) random nonzero gradients in the dipole magnets and (2) random errors in the integrated quadrupole strengths. These errors change the tune and the amplitude of the betatron motion. The rms errors due to dipole gradient errors from all the dipoles are given by:

$$\Delta\nu_x = 1.103\ \Delta G/B$$

$$\Delta\nu_y = 0.407\ \Delta G/B$$

$$\Delta\hat{\beta}_x/\hat{\beta}_x = 4.79\ \Delta G/B$$

$$\Delta\hat{\beta}_y/\hat{\beta}_y = 2.57\ \Delta G/B$$

where $\Delta G/B$ is the rms value of the dipole gradient normalized to the dipole field measured in m^{-1}, $\Delta\nu_x$ and $\Delta\nu_y$ are the rms errors in x and y tunes, respectively, and $\Delta\hat{\beta}_x/\hat{\beta}_x$ and $\Delta\hat{\beta}_y/\hat{\beta}_y$ are the rms fractional errors in the maximum values of the x and y beta functions respectively. The rms errors from gradient errors of all the quadrupoles are given by:

$$\Delta\nu_x = 1.13\ \Delta G/G$$

$$\Delta\nu_y = 0.56\ \Delta G/G$$

$$\Delta\hat{\beta}_x/\hat{\beta}_x = 7.55\ \Delta G/G$$

$$\Delta\hat{\beta}_y/\hat{\beta}_y = 2.18\ \Delta G/G$$

where $\Delta G/G$ is the rms error in the integrated quadrupole strength. To keep tune changes less than 0.001 from these errors, the $\Delta G/B$ and $\Delta G/G$ errors must be kept less than one part in 10^3. These criteria should be easily met with standard magnet manufacturing techniques. For these values, the errors in the beta functions are negligible.

4.2.5 Tracking Studies of the HISTRAP Lattice

Extensive tracking studies have been done on the HISTRAP design lattice using the LIE3 option of MAD [Is85]. These studies were performed to determine if the sextupole strengths required for chromaticity correction would produce harmful nonlinear effects. The studies showed that for the reference design mode, the dynamic aperture remains larger than the physical aperture when the sextupole strengths are tuned to produce zero chromaticity.

In addition, investigations of the possible orbit displacements and instabilities due to magnet imperfections in the proposed lattice have been carried out by tracking studies. The low-order errors considered to date include edge angle distortions of the dipole magnetic fields, dipole tilt errors, quadrupole displacement errors, first order errors of the dipole and quadrupole field gradients, and finally, a systematic sextupole error in the dipole magnets. These studies were performed with the sextupole strengths adjusted to give zero chromaticity.

Of these, the most significant errors arise from possible systematic errors in the edge angles of the dipole magnets. In the design lattice, the rectangular dipole ends make an angle of 22.5° with the central trajectory. Differential saturation and other effects could reduce this angle to 21.5°, which is equivalent to introducing effective quadrupole magnets at the dipole ends, giving tune shifts in the order of 0.2. More importantly, about 0.2 m of dispersion is introduced to the nondispersed straights, which is unacceptably large for some of the proposed experiments involving multiple charge states. It is possible to re-tune the lattice to the original tunes and dispersions by

introducing a quadrupole at either the entrance or exit of each dipole and adjusting appropriately the strengths of the main focusing (QF) and defocusing (QD) quadrupoles and the new trim quadrupole (QT). Also, the chromaticity of the lattice is changed, so the sextupole strengths must change. Listed below are the original normalized and integrated quadrupole and sextupole strengths and the new strengths which reproduce the original lattice properties with 21.5° dipole angles. The possibility of producing this trim quadrupole strength with dipole pole face windings is being investigated.

	Original Lattice	Re-tuned Lattice
Edge	22.5°	21.5°
QF	0.925 m^{-1}	0.932 m^{-1}
QD	-1.044 m^{-1}	-1.061 m^{-1}
QT	0.0	0.042 m^{-1}
SF	0.482 m^{-2}	0.541 m^{-2}
SD	-1.760 m^{-2}	-2.132 m^{-2}

The stability of particles in the above re-tuned lattice was studied. A systematic sextupole error in the dipole magnets with a normalized strength of -0.55 m^{-3} was also included. A 17-cm horizontal by 5-cm vertical rectangular quadrupole aperture and a 9.4-cm by 5.0-cm dipole aperture were assumed. We further assumed a horizontal emittance of 200π mm-mrad, and a vertical emittance of 80π mm-mrad. Particles were "injected," equally displaced in the vertical and horizontal directions, and tracked for 400 turns.

In all cases where DP/P exceeded 0.05 in absolute value, the particles were lost on the "edge" of the dipole aperture. For all particles studied in the ±5% momentum range, the orbit trajectories were dynamically stable until they hit the dipole "edge." Listed below are

the maximum displacements for which particles remained within the magnet apertures as a function of momentum error, in units of normalized displacements, where σ_x is 4.58 cm, and σ_y is 1.62 cm.

DP/P	$\sigma_x = \sigma_y$
-0.05	0.3
-0.04	0.6
-0.03	0.7
-0.02	0.7
-0.01	0.8
+0.01	0.8
+0.02	0.7
+0.03	0.6
+0.04	0.5
+0.05	0.3

Thus, the aperture is the restrictive feature of the lattice, as opposed to the dynamic stability of the orbits for the ±5% momentum range. In all cases, the limiting factor was the horizontal aperture of the dipoles.

Finally, a study of the dipole corrector strengths needed for closed orbit correction was made. The rms error assumptions were:

Dipoles:	
Tilt angle	0.0002 rad
Relative strength error	0.0005
Relative quadrupole gradient	0.001
Quadrupoles:	
Transverse displacement errors	0.15 mm
Relative gradient errors	0.001

All the above errors were assumed to be randomly distributed over the lattice magnets using the option TGAUSS(1) in MAD. Twenty runs were made with different random error distributions to study the magnitude of the closed-orbit distortions, and for each run the MICADO option in MAD

was used to select dipole corrector strengths which minimized the closed-orbit distortions. Eight horizontal and eight vertical correctors were used. The horizontal correctors were placed at the dipole entrances to model the dipole backlog winding correction capability. The vertical correctors were placed in the F sextupoles located between the dipoles and F quadrupoles. Beam position monitors were placed in all twelve quadrupoles.

For the 20 runs, the average rms horizontal displacement in the beam position monitors was 5.5 mm, and in the vertical direction, the average rms displacement was 1.0 mm. The required rms horizontal corrector strength ranged in value between 0.21 and 0.68 mrad. The maximum individual corrector strength was 1.61 mrad. In the vertical direction, the rms corrector strengths ranged between 0.18 and 0.58 mrad with maximum strength for a single corrector of 0.97 mrad. In all cases, the dipole correctors reduced the closed-orbit errors to less than 0.1 mm.

4.2.6 Electron Beam Cooler Considerations

The toroidal and solenoidal magnetic fields of the EBC will be a major perturbation on the orbits of the circulating ions in HISTRAP. These perturbations require correction. HISTRAP, like many other rings, will operate with nearly equal tunes to take advantage of the large resonance-free region near the tune space diagonal. Consequently, the excitation and compensation of the $\nu_x = \nu_y$ resonance, which couples the two transverse motions, is important. Without compensation, beam would be lost through coherent transverse emittance oscillations between the

two transverse planes, and the design tunes may not be achievable. For HISTRAP, this would be particularly severe since the horizontal acceptance is much larger than the vertical acceptance. Because of this, the strengths of the coupling contributions have been estimated, positions for correction skew quadrupoles have been identified, and skew quadrupole strengths for compensation have been calculated.

Solenoid magnet fields, solenoid end fields, quadrupole tilts, dipole tilts, and beam-linking currents all contribute to coupling; however, in HISTRAP, the 1.0-m-long solenoid of the EBC dominates all other sources of coupling when operated at 0.2 T for maximum rigidity beams. Following the formalism of Guiguard [Gu78], this coupling can be compensated to zero by a pair of skew quadrupoles positioned symmetrically about the EBC straight in either pair of the short straight sections between the dipoles and F quadrupoles, as shown in Fig. 4.2-5. These empty positions have horizontal and vertical betatron phase-advance differences of ±37.3° and ±40.4°. In either pair of positions, integrated and normalized skew quadrupole strengths, $\ell B'/B\rho$, of about 0.01 m^{-1} are required for compensation. This is about 1% of the main quadrupole strength. Coupling correction for the EBC should not be a problem in HISTRAP.

The EBC also gives large dipole kicks to the circulating ions. These kicks occur in the bending toroids which guide the smooth solenoidal magnetic field onto the direction of the circulating ions. To minimize these effects, the EBC will be mounted in a vertical plane so that the dipole kicks occur in the horizontal plane, which has the largest aperture. In addition, the backleg windings of the adjacent

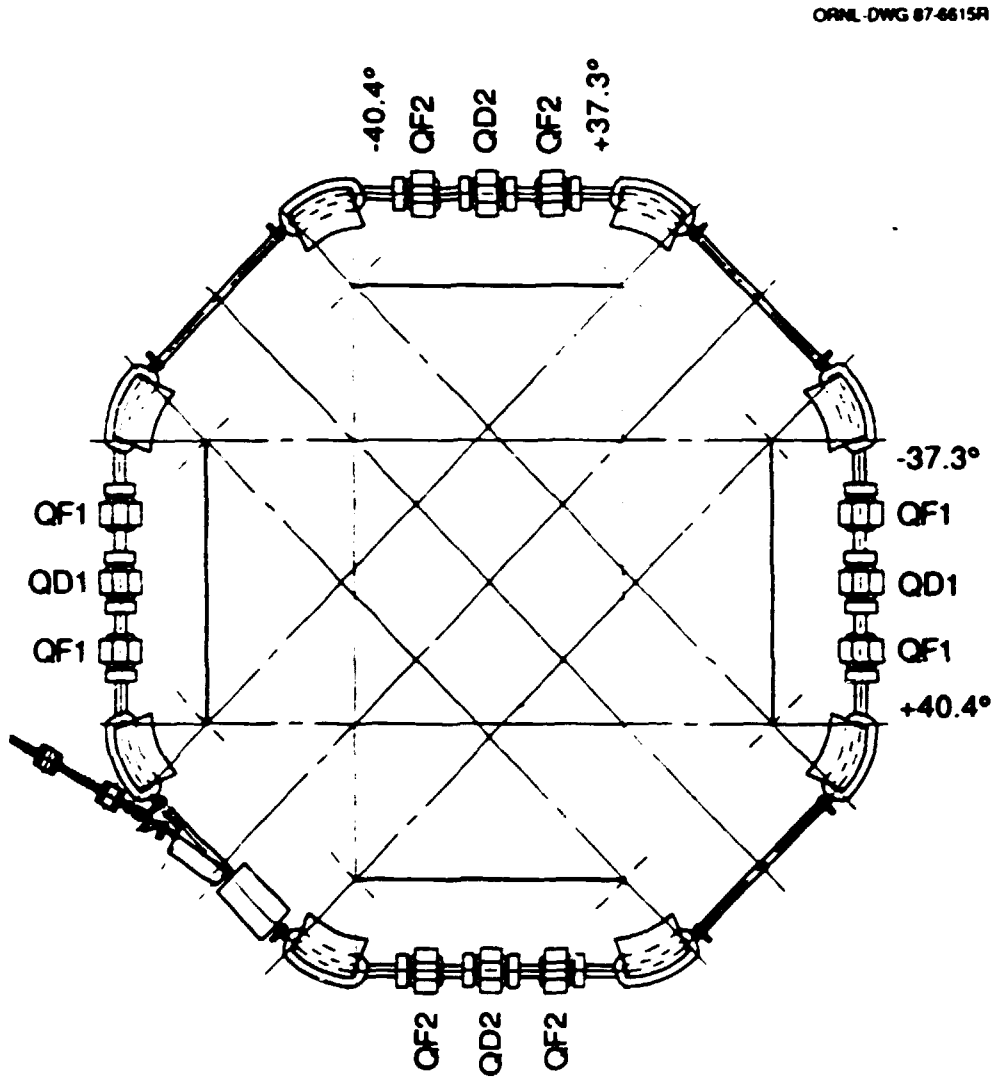

Fig. 4.2-5 HISTRAP lattice showing the quadrupole families, QF1 QD1 QF2 QD2, required for operation in a twofold symmetric mode with four nondispersed straights. Also shown are the symmetric positions about the cooler straight section for skew quadrupole placement. These positions have horizontal and vertical phase-advance differences of ±37.3° and ±40.4°.

dipoles can be used for horizontal correction. The dipole kicks from the toroids are estimated to be in the order of 0.010 radians. The resulting perturbation on the closed orbit can be compensated with 0.004 radian backleg winding corrections and a pair of 0.014 radian dipole correctors positioned close to and symmetric about the EBC.

4.2.7 Phase Space Stacking for HISTRAP Injection

A preliminary investigation of emittance dilution from beam stacking in horizontal phase space has been made. The design mode of HISTRAP was used assuming an ideal beam and no magnet errors. A single kicker magnet was placed in the lattice in the short straight section between the dipole and the quadrupole triplet. With the kicker so placed, a large distortion of the closed orbit occurs at the middle of the 4-m straight section essentially opposite the kicker magnet. In this study, the kicker magnet, which introduced a deflection of 0.05 radians in the closed orbit, produced a bump of radius 3.38 cm in the center of the 4-m straight. The horizontal acceptance of HISTRAP is limited by the ±5.50 cm of good field in the dipole magnets. The maximum closed orbit displacement produced in any dipole by this same kicker magnet is 3.57 cm, and the amplitude of the beta function in the dipole is 12.59 m. Consequently, with the full kicker strength the acceptance of the lattice is 30π mm-mrad.

A zero-width septum was assumed in the center of the 4-m straight at a radius of 4.7 cm from the equilibrium orbit. An assumed tandem beam with an emittance 2π mm-mrad, a beta function of 3.0 meters, and an alpha function of zero was injected at 4.95 cm from the machine center.

Test ions were distributed approximately uniformly on the perimeter of this beam and each ion was then tracked through one turn. At the end of each turn, the kicker strength was reduced so that the closed orbit deflection was reduced by the ratio of the radius of the closed orbit at injection to the number of ion bunches injected. At the end of the injection, the closed orbit was at the normal equilibrium orbit. At each step, the beta function of the lattice was changed to the value appropriate for the corresponding kicker value, and the beam acceptance was increased to the appropriate value. The beta function and the closed-orbit radius vary roughly linearly with the kicker strength and a linear approximation was used. After each turn, those ions which were not inside the septum radius were discarded.

Since the lattice has a tune near one-third, the closed orbit should shrink by the diameter of the injected beam after every third turn. In this case, the injected beam diameter was 0.49 cm so that approximately 3 x (3.38cm/0.49cm) = 21 turns should be stackable in HISTRAP with no losses to the septum. Indeed, the tracking calculations show that 18 turns can be stacked with no losses. Cases stacking more than 18 turns were also studied. For these, ions were distributed roughly uniformly over the horizontal phase space of the injected beam and tracked. In a typical case, if 500 test ions were distributed in an injected bunch, and all ions tracked for 35 turns, then 98.5% of the injected particles survived. It remains an open question as to how much ion loss to the septum can be tolerated, and effects of finite septum length and thickness must be considered. It seems very reasonable for preliminary estimates of HISTRAP beam currents to assume that almost all

ions will survive for a 35-turn injection. Fig. 4.2-6 shows the phase-space profiles of the injected bunches for this case.

4.2.8 Other Lattice Operating Modes

The HISTRAP lattice shown in Fig. 4.2-5 was optimized for multiple-charge-state operation and consists of four 4-m-long straight sections connected by 90° achromatic bends. The achromatic condition and the design tunes of $\nu_x = 2.309$ and $\nu_y = 2.274$ were met by adjusting the focusing and defocusing quadrupole strengths and the dipole-quadrupole separation distance. This reference design mode is fourfold symmetric, with four dispersionless straights, and has two quadrupole and two sextupole families.

Other, more flexible, modes of operating this lattice are also possible. In particular, this proposal calls for power supplies and bussing for six quadrupole families and eight sextupole families. This will allow HISTRAP to be operated in any twofold symmetric lattice mode, with up to six quadrupole tuning parameters, to meet various conditions desired by the experimentalists. Twofold or fourfold symmetric lattice solutions exist with other straight-section dispersions and beta functions. As an example, Fig. 4.2-7 shows the tune space for all operating modes of the HISTRAP lattice, including the reference design mode, with four dispersionless straight sections. Third, fourth, and fifth order sum resonances and the second order difference resonance are shown. The numbers in Fig. 4.2-7 are the integrated and normalized strengths of the strongest quadrupole, always defocusing, required in the lattice.

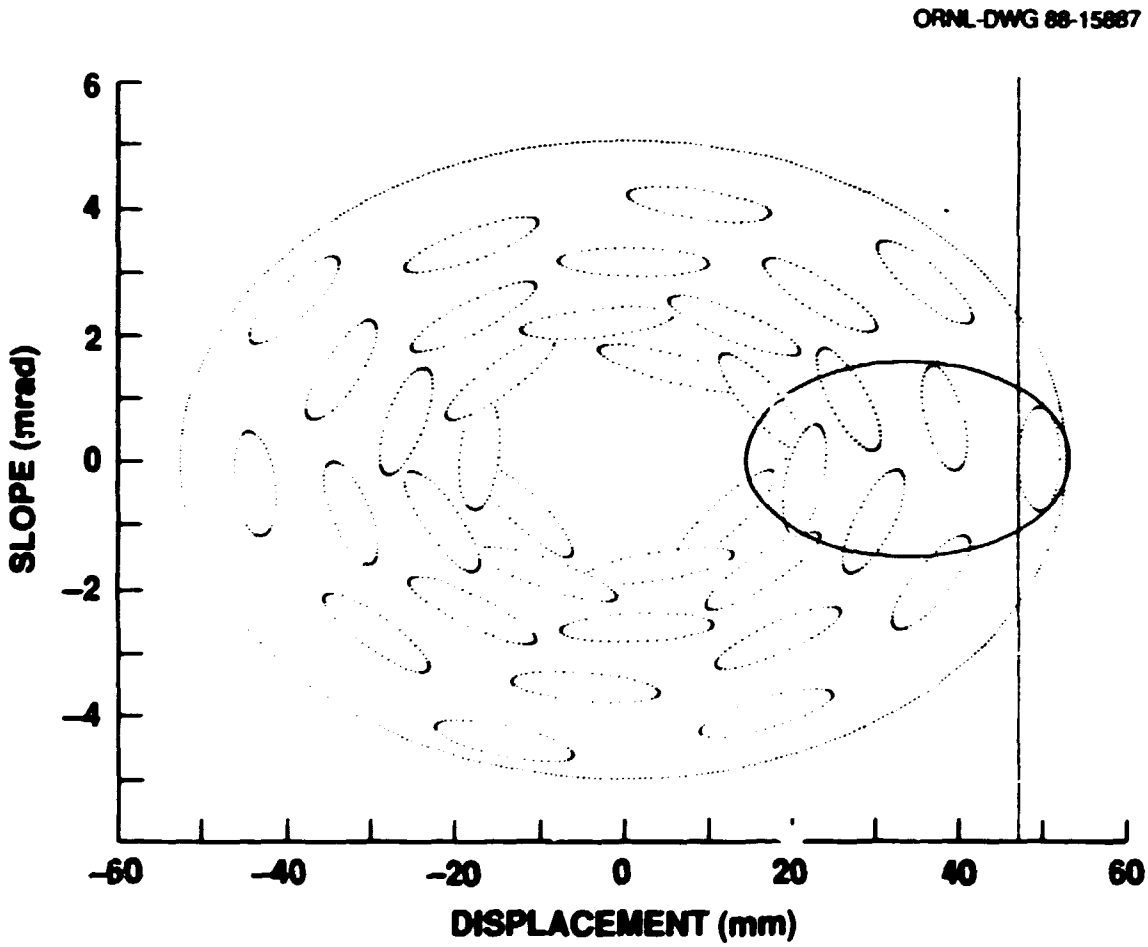

Fig. 4.2-6 Phase space distribution of 35 turns of ions injected in a perfect HISTRAP lattice. The solid vertical line shows the position of the injection septum. The two large ellipses represent the acceptance of the lattice at injection, kicker on, and after injection, kicker off. The emittance of the injected beam is 2 π mm-mrad with a beta function of 3.0. The initial acceptance of the machine is 30 π mm-mrad, and the final acceptance is 265 π mm-mrad.

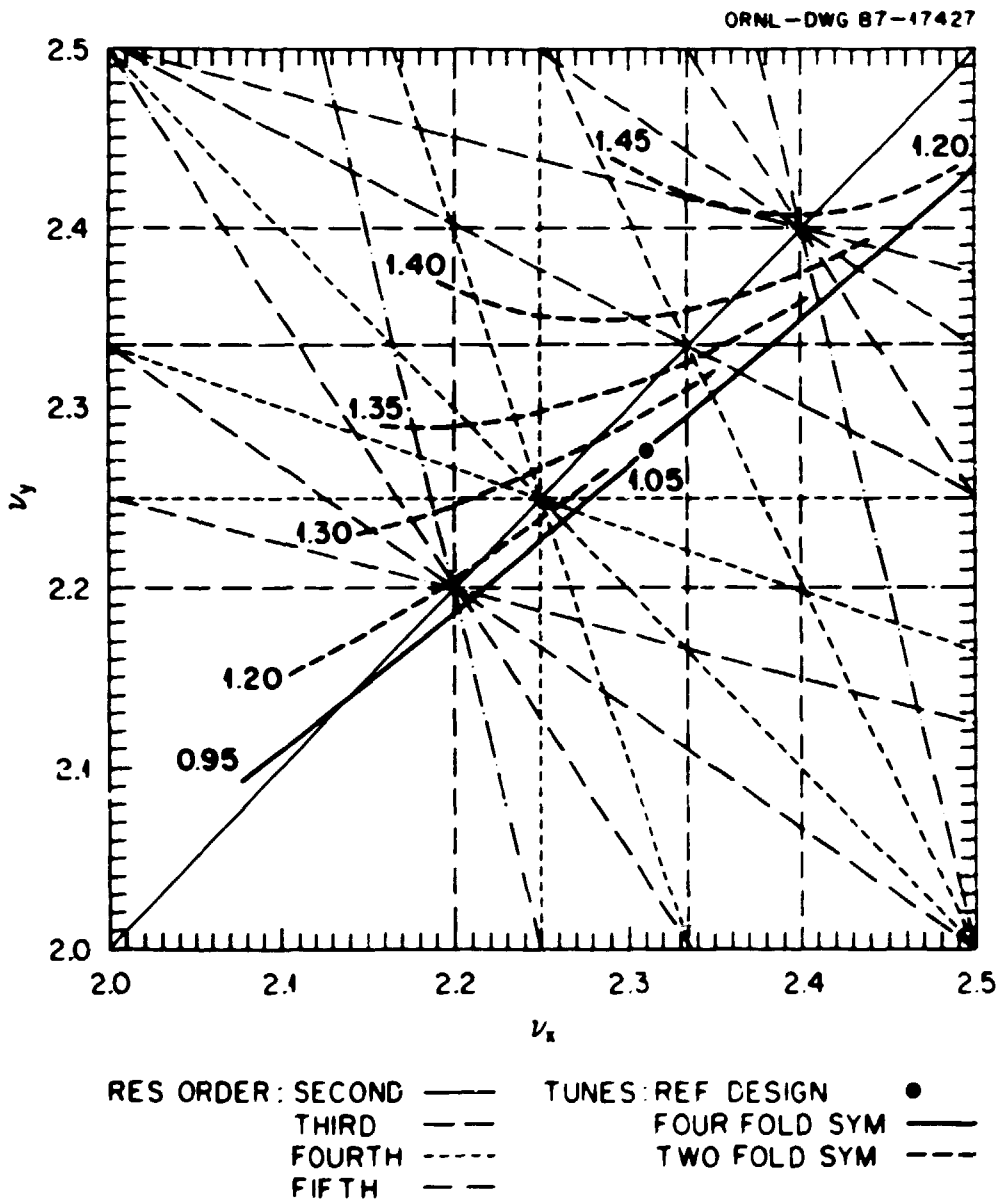

Fig. 4.2-7 Tune space of HISTRAP lattice operated in a mode with all four straight sections dispersionless. The numbers in the figure are the normalized and integrated strength of the strongest quadrupole in the lattice.

Fourfold symmetric solutions with four nondispersed straights require quadrupole strengths such that QF1 = QF2 = QF and QD1 = QD2 = QD. These solutions are shown as the heavy line in Fig. 4.2-7. The strength of QD varies from 0.95 m^{-1} to 1.20 m^{-1}. The HISTRAP reference design operating point, with the QD strength = 1.05 m^{-1} and the QF strength = 0.93 m^{-1}, is shown as the heavy solid point. The tune space above this line is also available for stable operation with twofold symmetry, simply by setting the quadrupole families of Fig. 4.2-5 such that QD1 ≠ QD2 and QF1 ≠ QF2. This region of tune space is indicated by the heavy dashed lines. A maximum integrated and normalized quadrupole strength of 1.37 m^{-1} is desirable and is the specification for HISTRAP.

Another very interesting set of lattice solutions is shown in Fig. 4.2-8. For these solutions, the lattice was again allowed to be twofold symmetric with the design mode tunes and, as shown, the quadrupoles were divided into the three families QF1, QD, and QF2. Again, with QF1 = QF2 = 0.93 m^{-1} and QD = 1.05 m^{-1} the lattice operates in the fourfold symmetric mode with four nondispersed straight sections. If the strength of QF1 is reduced, then dispersion can be introduced into the straight sections if needed by the experimentalists. One pair of straight sections S_1 will have positive dispersion, whereas the other pair S_2 will have negative dispersion. The beta functions and dispersions shown in Fig. 4.2-8 all occur at the design tunes of ν_x = 2.309 and ν_y = 2.274. Consequently, dispersion can be introduced as desired into the straight sections while the ion beam is circulating in HISTRAP. These studies show that the HISTRAP lattice can provide a variety of

ORNL-DWG 88-15589

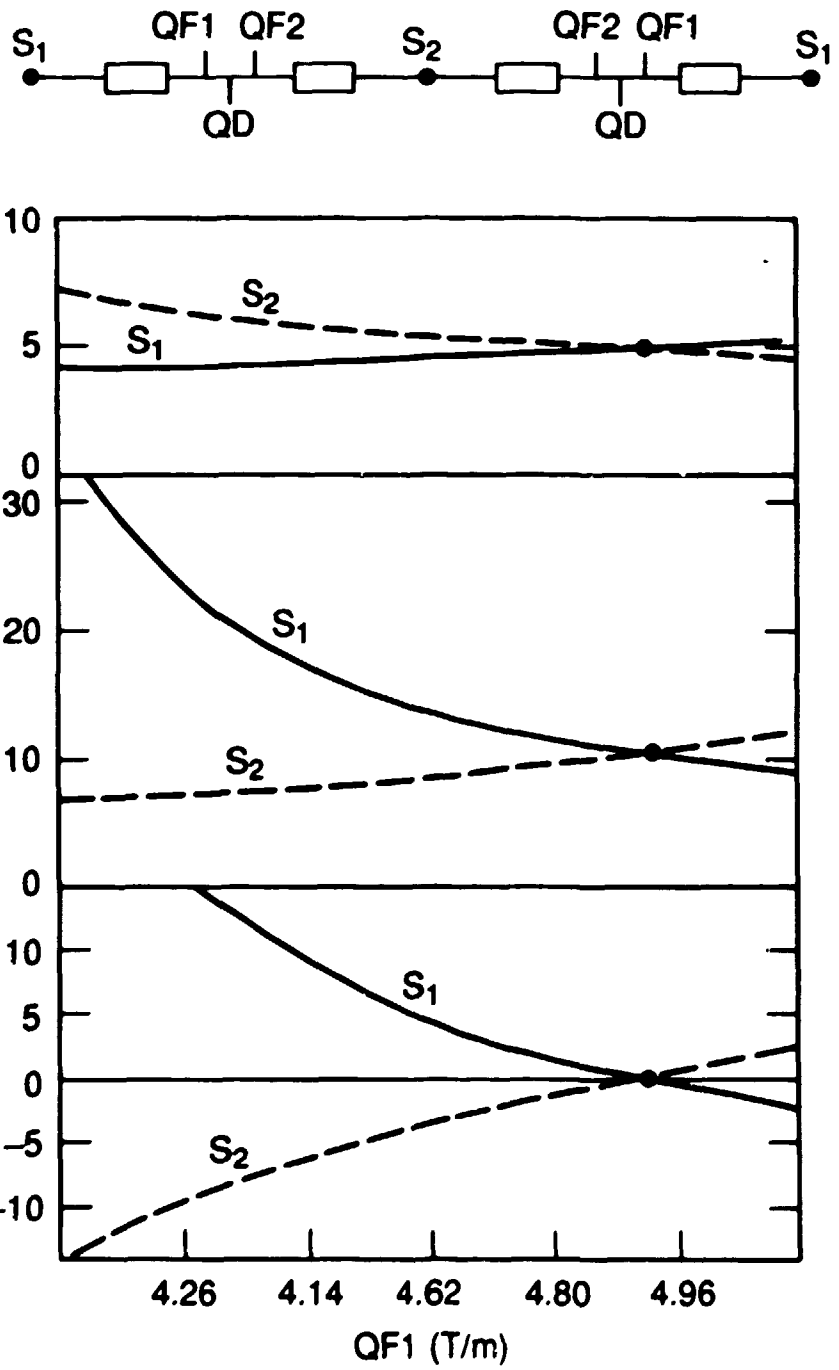

Fig. 4.2-8 Beta functions and dispersions in the center of straight sections S_1 and S_2 as a function of the quadrupole strength QF1. These lattice solutions all occur with the design tunes so they can be adjusted with beam circulating in HISTRAP.

beam conditions for in-ring experiments, and contains considerable flexibility in the choice of the tune operating point.

4.3 HHIRF Tandem Injector

4.3.1 HHIRF Tandem Accelerator

The existing HHIRF tandem accelerator shown in Fig. 4.3-1 is perhaps the best injector in the world for a small synchrotron/cooler/storage ring. This tandem is a model 25URC accelerator provided by the National Electrostatics Corporation. The accelerator, which is insulated with pure SF_6 at pressures up to 0.7 MPa, has been designed to operate at terminal potentials up to 25 MV with analyzed beam intensities up to 1 pμA averaged over time. The accelerator pressure vessel, which is approximately 30 m high and 10 m in diameter, houses a column structure 18.9 m high (excluding the high voltage terminal) of which 16.5 m was initially insulator. The accelerator has a vertical folded configuration. The column structure is equipped with five dead sections, three quadrupole lenses, three sets of steerers, and a second stripper located in the upper major dead section. Each dead section is equipped with vacuum pumps. The accelerator uses a CAMAC-based digital control system in which virtually all control and monitoring information is transmitted on six-bit serial highways.

During normal operation, negative ions are produced on a 500-kV injector platform, accelerated to ground potential, and mass analyzed with a 90° injector magnet. After acceleration to the terminal, the ions pass through either a gas or foil stripper and are again charge and mass analyzed with the 180° terminal bending magnet. After acceleration

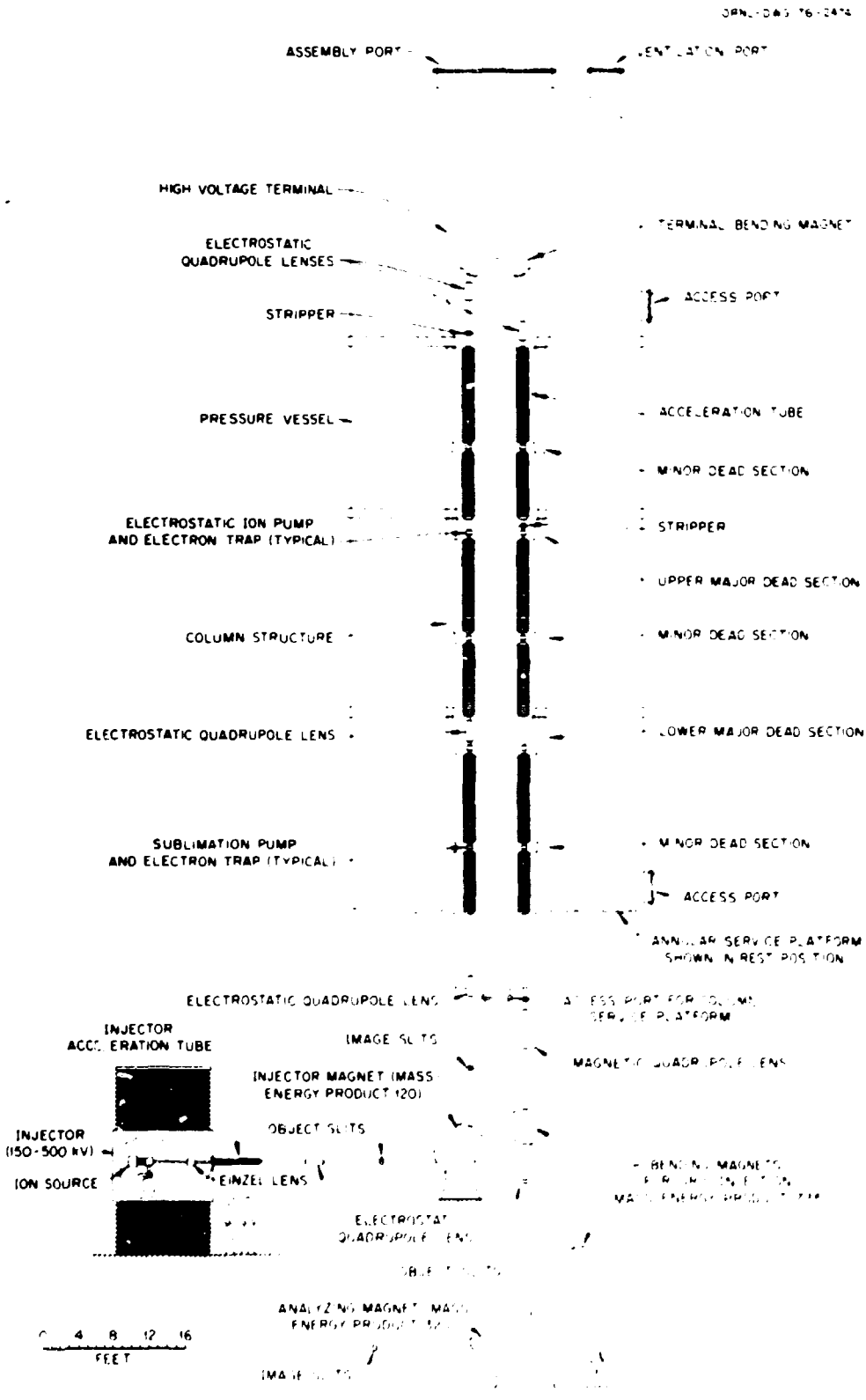

Fig. 4.3-1 Schematic view of the HHIRF tandem accelerator. This tandem has produced beam for an experiment with a terminal voltage of 25 MV, and is perhaps the best injector in the world for a small heavy-ion synchroton.

to ground, the positive ions are deflected either into the ORIC injection line, with a special set of bending magnets, or into tandem experimental beam lines with a rotating 90° vertical energy analyzing magnet having a mass energy product of 320. Table 4.3-1 is a list of isotopes accelerated by the tandem and delivered for scheduled experiments.

Table 4.3-1. HHIRF beams provided for scheduled experiments

BEAM	MAX. ENERGY (MeV)	MODE*	BEAM	MAX. ENERGY (MeV)	MODE*
^{1}H	25	T	^{49}Ti**	235	T
^{7}Li	128	T,C	^{50}Ti**	250	T
^{9}Be	158	C	^{51}V	216	T
^{10}B	168	C	^{52}Cr	230	T
^{11}B	169	T,C	^{56}Fe	842	T,C
^{12}C	300	T,C	^{58}Ni	1010	T,C
^{13}C**	67	T	^{60}Ni	228	T
^{16}O	405	T,C	^{63}Cu	189	T
^{17}O**	381	C	^{65}Cu	290	T
^{18}O**	352	T,C	^{64}Ni**	290	T
^{19}F	190	T	^{74}Ge	306	T
^{24}Mg	178	T,C	^{76}Ge	305	T
^{25}Mg	132	T	^{79}Br	1000	C
^{26}Mg**	160	T	^{81}Br	604	C
^{27}Al	196	T	^{78}Se	320	T
^{28}Si	333	T,C	^{80}Se	285	T
^{29}Si	150	T	^{82}Se	295	T
^{30}Si	264	T	^{90}Zr	395	T
^{32}S	725	T,C	^{93}Nb	276	T
^{34}S**	155	T	^{107}Ag	374	T
^{36}S**	123	T	^{109}Ag	733	C
^{35}Cl	692	T,C	^{116}Cd**	499	C
^{37}Cl	187	T	^{112}Sn**	570	C
^{40}Ca	227	T	^{116}Sn**	684	T,C
^{44}Ca**	201	T	^{120}Sn	240	T
^{48}Ca**	200	T	^{150}Nd**	760	C
^{45}Sc	200	T	^{197}Au	591	T
^{46}Ti**	280	T	^{238}U	119	T
^{48}Ti	581	T,C			

* T = Tandem alone; C = Coupled mode.
** Beam provided with separated isotope probe sample.

Tandem accelerators usually produce dc beams, while synchrotron injection requires tightly-pulsed beams. High-intensity, pulsed $^{16}O^-$ beams were injected into the HHIRF tandem in order to evaluate operation in a pulsed mode [A186c]. For these tests, a pulse length of 100 μs, a repetition rate of 8 Hz, and an average pulse amplitude of 100 μA were chosen. A terminal potential of 14.1 MV was used with a 6-μg/cm^2 carbon terminal foil stripper. Examples of the 300-KeV $^{16}O^-$ injected beam and the 99-MeV $^{16}O^{6+}$ accelerated beam are shown in Fig. 4.3-2. No evidence of voltage instabilities or terminal voltage droop were detected during these tests. However, the transmission of the pulsed component of the beam was observed to be slightly lower than that of the dc component, perhaps indicating the presence of space-charge effects which are expected during low-velocity transport of intense negative ion beams in the injector. We also noted that transport of pulsed beams through the injector and to the accelerator required a slight increase of lens potentials over those required for transport of dc beams. The absence of any observable detrimental effects during operation of the HHIRF tandem accelerator with intense pulsed ^{16}O beams indicates that the tandem accelerator can be used effectively as a synchrotron injector.

The original acceleration tubes have been replaced with tubes of a compressed geometry design. In this design, which utilizes a modified National Electrostatics Corporation high-gradient, 17-cm-long tube section, the 3-cm-thick heatable aperture assembly provided as part of the original installation was replaced with an aperture assembly of essentially zero length. This change has had two beneficial effects: The first is that seven tube sections were installed in the space

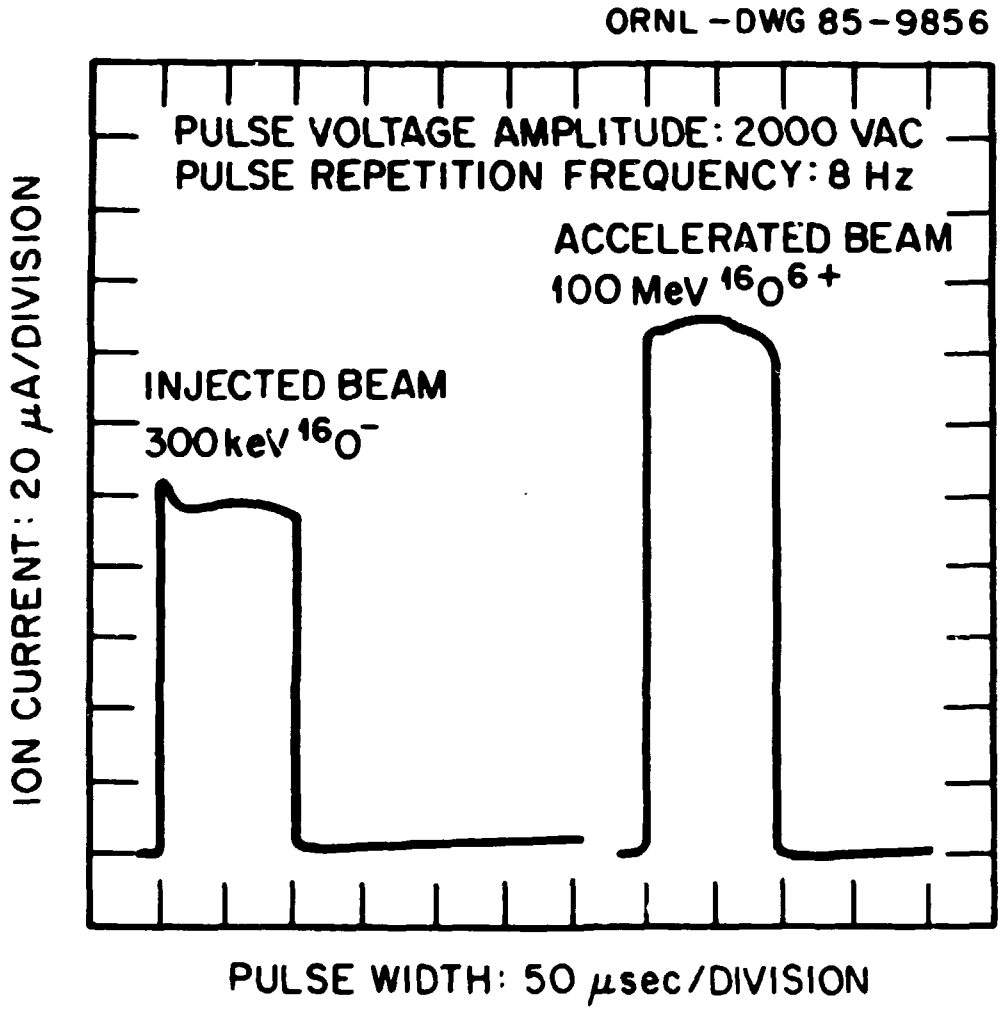

Fig. 4.3-2 Current waveforms of pulsed ^{16}O beams inejcted into and accelerated by the HHIRF tandem accelerator.

previously occupied by six, thus increasing the effective insulator length per unit column length by a factor of 7/6 = 1.17. The second is that removal of the high-current feedthroughs, which are an integral part of the heatable aperture assembly, removes a source of vacuum leaks in the accelerator.

By October 1987, all the old tubes had been completely replaced. In September 1988, the tandem voltage was stable at 25.5 MV and a 225-MeV oxygen beam was used for an atomic physics experiment. A terminal voltage of 25.0 MV was required for this beam. The HHIRF tandem has achieved the highest voltage of any electrostatic accelerator in the world, is operated as a national users' facility, is used to inject a circular machine (the ORIC cyclotron), and is ideal for HISTRAP injection. The high voltage will allow the highest possible charge states to be injected into HISTRAP. In addition, the HHIRF has profited from a broad-based and aggressive development program for negative ion sources.

4.3.2 Pulsed Negative Ion Sources

Several different negative ion sources based on the sputter principle and capable of producing pulsed beams have been developed at ORNL and elsewhere. Recently, a significant advancement has been made in the technology of pulsed negative ion sources by ORNL and the National Laboratory for High Energy Physics in Japan. In particular, a multicusp magnetic field plasma source was used to generate milliamperes of negative ions [Al88b]. All of these sources utilize cesium to enhance the probability for negative ion formation. They can be categorized according to the means for producing the positive ion beam used in the

sputter process. These sources either utilize direct surface ionization of cesium vapor for positive ions as it comes in contact with a hot, high-work-function surface, or they utilize a plasma to form positive ions. In either case, the positive ions are accelerated against a negatively biased probe containing the material of interest. During the sputter process, a fraction of the particles ejected from the sample will be ionized negatively.

Sources Based on Direct Surface Ionization

The positive ion currents achievable in sources which utilize direct surface ionization can attain values up to the space charge limit of the particular electrode configuration. For such sources, the perveance K of the electrode configuration can be measured or calculated by solving Poisson's equation. The perveance is a function of the geometry of the electrode system or plasma/sputter probe interface. Since we assume that the negative ion current increases in proportion to the positive ion current, the perveance is a convenient measure for comparing ion sources.

The sample material for cw beams is mounted on a 1-to-5-kV negatively biased probe. Sputtering of the negatively biased sample material is usually effected by positive cesium ions which are formed by direct surface ionization during collisions with a hot high-work-function ionizer. Four negative ion sources based on direct surface ionization of cesium have been used at ORNL. The sources differ only in the geometry of the ionizer, its spacing in relation to the negatively biased sample, sample exit aperture spacing, and the aperture size. Sources equipped with spherical [Al85], ellipsoidal [Al87a, Al88a] and

cylindrical geometry ionizers [Al86a] were designed and developed at ORNL, whereas the General Ionex Corporation Model 860 negative source was developed at the University of Pennsylvania [Mi83]. These sources have perveances of 2 x 10^{-9}, 17 x 10^{-9}, 57 x 10^{-9}, and ~ 60 x 10^{-9} x [$A/V^{3/2}$], respectively. The cylindrical geometry ionizer source shown in Fig. 4.3-3 has been described in detail in Ref. Al86a and the emittance and brightness characteristics of the source have been reported in Refs. Al88a, Al87a, and Al87b. Average normalized emittance data for all these sources operated in the dc mode are summarized in Fig. 4.3-4 as a function of percent of negative ion beam intensity.

The negative ion source must be pulsed for synchrotron injection. Typical pulse widths and repetition rates needed for HISTRAP injection are about 100 μs and a few Hz, respectively. The peak beam currents desirable for injection are on the order of several milliamperes and exceed dc ion beam intensities available from most sources. However, it is known from previous work at BNL [Th83] and ORNL [Al86c] that such pulsed-beam intensities may be possible for a limited number of elements with high electron affinities and that such beams can be injected into tandem accelerators without detrimental effects. A schematic electrical diagram of the power supply arrangement used during testing of these sources is shown in Fig. 4.3-5. The source housing is biased positive relative to the sample probe by superposition of the pulse generator and a dc power supply. With this arrangement, the pulsed and dc beam components can be controlled independently.

The dependence of peak beam intensities on pulsed voltage amplitude is shown in Fig. 4.3-6. The negative ion yields increase linearly for

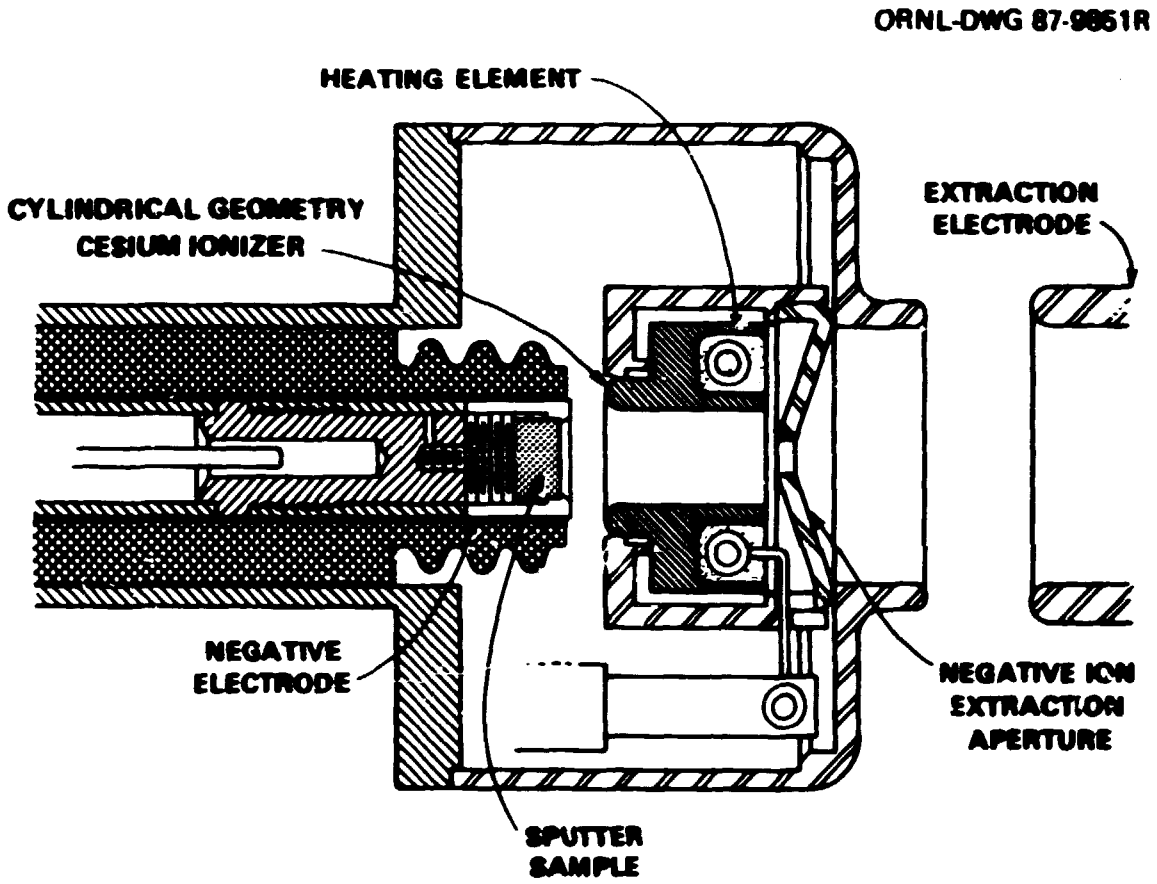

Fig. 4.3-3 Schematic drawing of the ion formation and extraction region of the negative ion source equipped with a solid tungsten cylindrical geometry cesium ionizer.

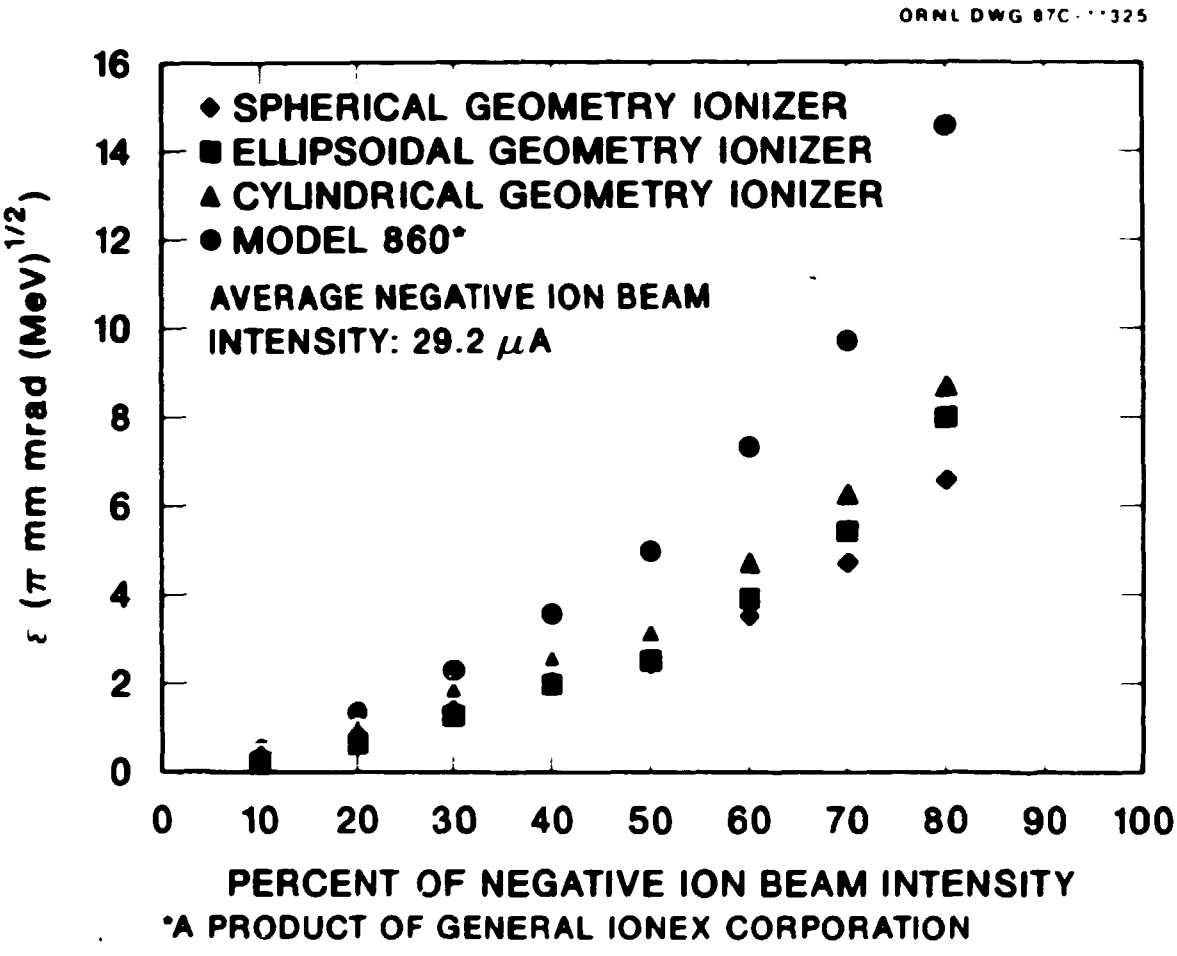

Fig. 4.3-4 Average normalized emittance ε versus percent total dc negative ion beam for the negative ion sources equipped with spherical, ellipsoidal, and cylindrical geometry cesium surface ionizers, and the Model-860 negative ion source.

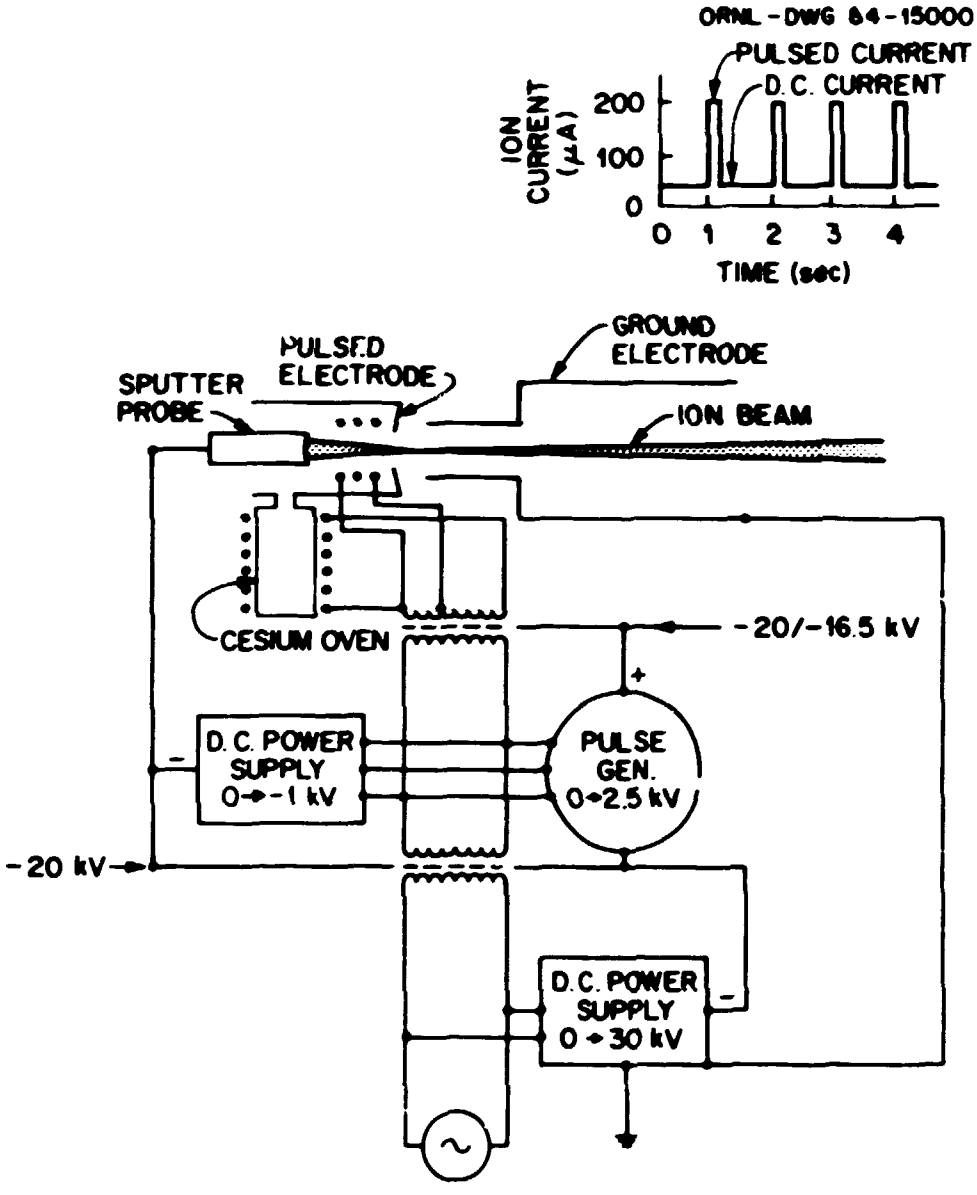

ION SOURCE TO PROVIDE CONSTANT D.C. NEGATIVE ION CURRENT WITH SUPERPOSED CURRENT PULSES AT 1 Hz AND 100 μsec WIDE (SIMPLIFIED POWER SUPPLY ARRANGEMENT)

Fig. 4.3-5 Electrical diagram of the power supply arrangement used during pulse testing of negative ion sources.

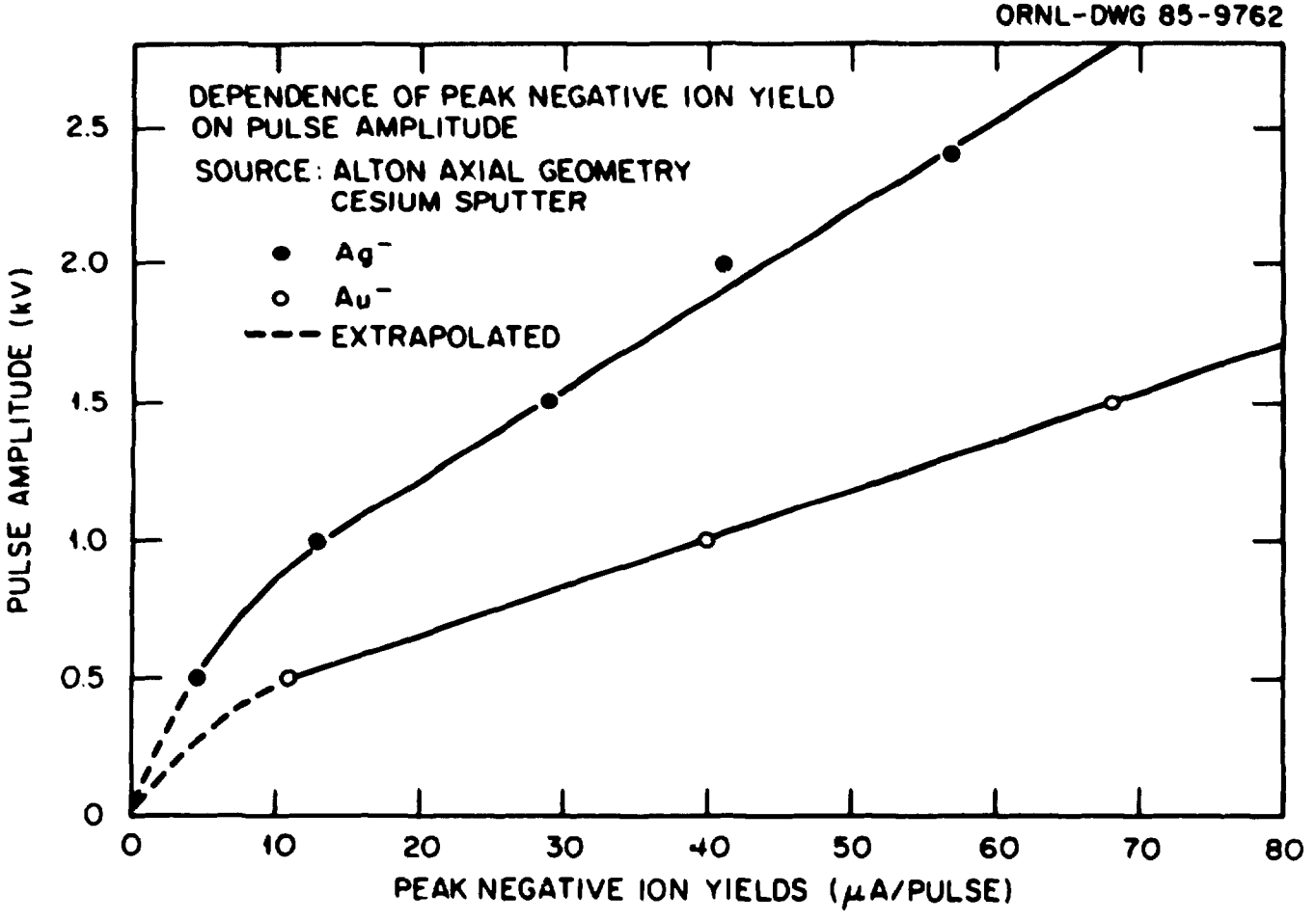

Fig. 4.3-6 The dependence of peak negative ion yields on pulsed voltage amplitude.

peak voltages above 400 V. From these results, much higher yields can be expected with increased output voltages. However, the negative ion yield will ultimately reach a maximum and begin to decrease with further increases in voltage. The pulse shape and amplitude of negative ion beams were found to be independent of repetition rate between 1 and 56 Hz and of pulse width between 10 and 230 μs.

Examples of Au^-, Cu^-, and Ni^- spectra measured under these conditions are shown in Fig. 4.3-7. The pulse generator was operated at 1.2 kV with a pulse width of 100 μs and a repetition rate of 10 Hz. The emittances of these ORNL sources are larger for pulsed operation than for cw operation. Figure 4.3-8 displays emittance versus percent of negative ion beam for the cylindrical ionizer geometry source for pulsed operation. The emittances of the ellipsoidal geometry ionizer and Model-860 sources are similar. Pulsed emittance contours, particularly in the x-direction, exhibit considerably more structure than do their dc counterparts. Emittances for the 80% contour levels for maximum ion beam intensities was found to be 14π mm-mrad $(MeV)^{1/2}$ regardless of species and type of source. The data in Fig. 4.3-8 clearly suggest an intensity dependent effect. These emittances of pulsed negative ion beams are found to be factors of 1.6 for the cylindrical geometry ionizer source, 1.75 for the ellipsoidal geometry ionizer source, and ~ 1.0 for the Model-860 sources, times larger than those measured previously for dc beams.

Plasma Sputter Negative Ion Sources

The plasma-type pulsed sources are capable of milliamperes of current because a large sputter probe containing the material of

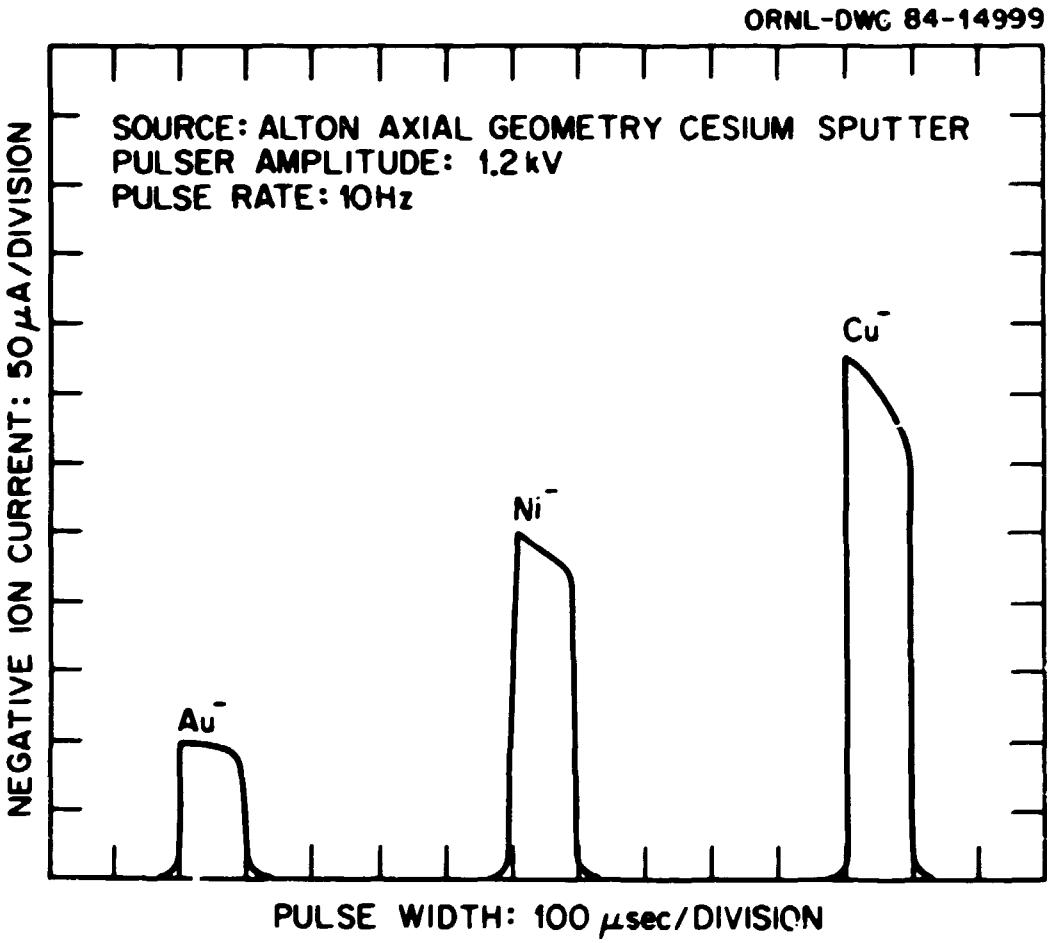

Fig. 4.3-7 Waveforms of negative ion beams produced by the cylindrical ionizer geometry source operated in the pulsed mode.

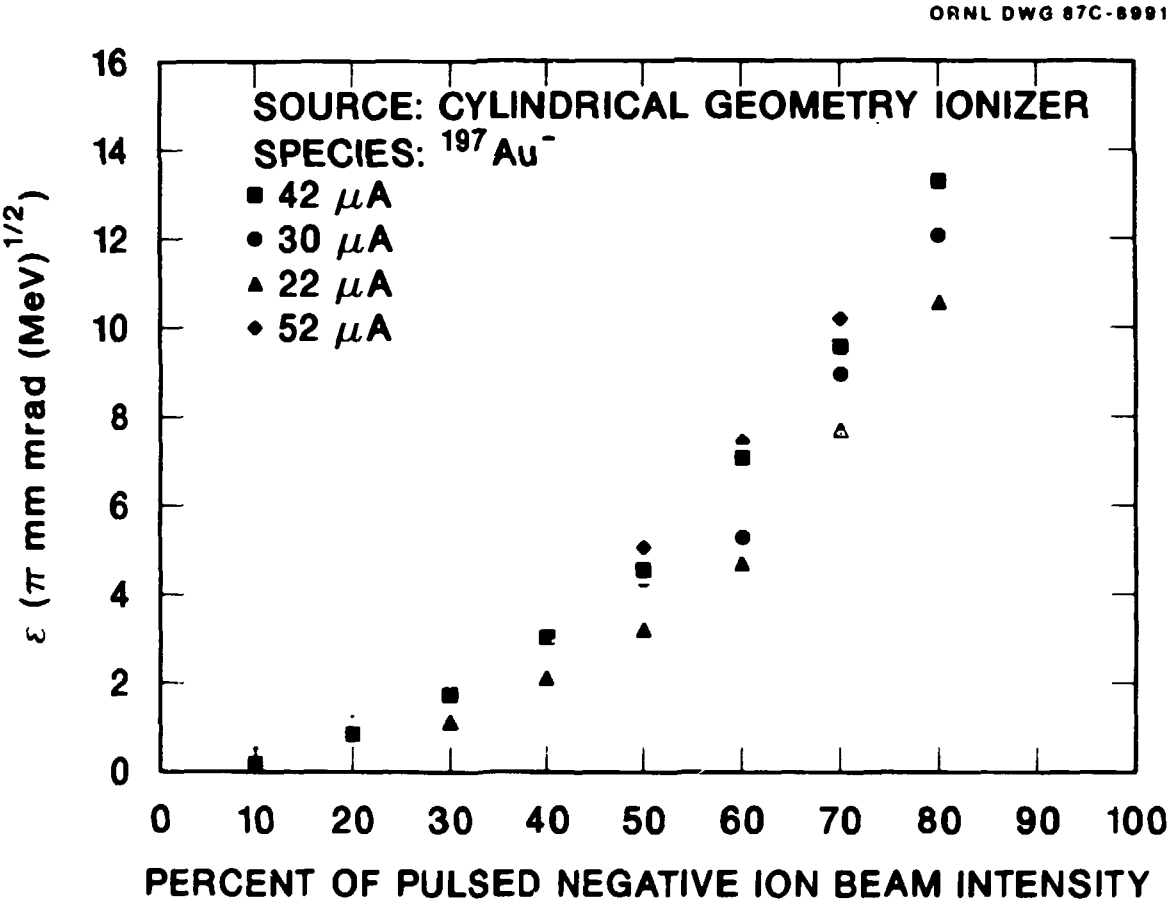

Fig. 4.3-8 Normalized emittance versus percentage pulsed negative ion beam intensity for various peak $^{197}Au^-$ negative ion currents extracted from the cylindrical geometry ionizer source.

interest can be used and uniformly sputtered. This characteristic makes it possible to take advantage of the large area spherical geometry optics formed between the sputter probe and the plasma sheath interface surrounding the probe. Negative ions created in the process are accelerated and focused through the plasma to a common focal point which is usually chosen as the ion exit aperture.

Two sources based on the plasma sputter principle have been investigated. The first source [Al86b] shown schematically in Fig. 4.3-9 embodies some of the principles associated with the radial geometry source developed by Tykesson and Andersen [Ty76]. A weak magnetic field of 150 G produced by a lightweight permanent Al Ni-Co magnet is used to collimate the primary electron beam, which is thermonically emitted by a tantalum filament located at the end of the ionization chamber. The electron beam produces an approximately uniform plasma by collisional impact with neutral cesium vapor introduced into the chamber from the externally mounted oven. Auxiliary discharge support gas, usually Ar, is introduced into the chamber by means of a standard leak valve to supplement the cesium vapor. Chemically active gases may also be used to make negative ions from the gas itself or from chemical combination with the sputter probe material. The sputter sample is typically a 10-mm-diameter cylinder with a concave spherical emission surface of radius 15 mm which is maintained at about 1000 V negative to the discharge chamber. This particular concept is among the most prolific and universal of sources based on the sputter principle, producing useful intensities of both atomic and molecular ion species. This source has demonstrated the capability of producing cw beams of

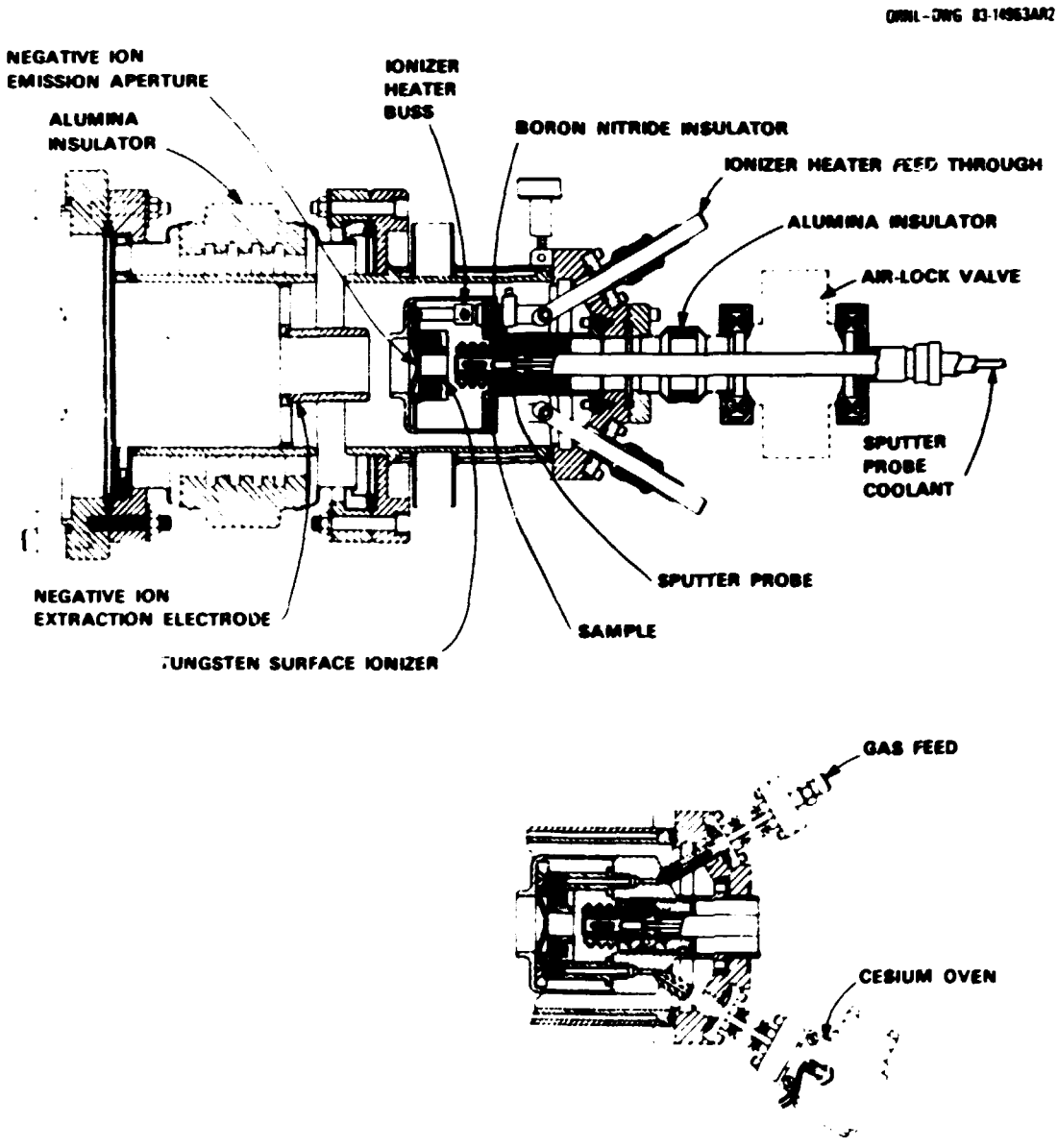

Fig. 4.3-9 Schematic drawing of the radial-geometry plasma-sputter negative ion source.

almost every element at intensities up to a few hundred μA. Although the source has not been evaluated extensively for pulsed operation, it is expected to produce intensities equal to or greater than those from cesium sputter sources.

The multi-cusp magnetic field plasma surface source, routinely employed for the production of high-intensity pulsed H^- ion beams at LAMPF (Yo84) and at the National Laboratory for High Energy Physics [Mo87] has recently been modified and tested for use as a high-intensity pulsed-mode heavy negative ion source [Al88b]. This work has led to a dramatic increase in pulsed negative currents that can be obtained.

The source, modified for heavy negative ion generation, is shown schematically in Fig. 4.3-10. For heavy ions, a high-density plasma discharge, seeded with cesium vapor, was produced by pulsing the discharge voltage of two series connected LaB_6 cathodes maintained at 1450°C. For this application, the negatively biased spherical geometry probe was made of the material of interest. In order to produce higher beam intensities at a given probe voltage, a chemically inert discharge support gas was used. Cesium was introduced into the discharge from an external oven operated typically at a temperature of 214°C. The sheath surrounding the negatively biased sputter probe was maintained at about 500 V negative to the housing and served as the acceleration gap and lens for focusing the ion beam through the 18-mm-diam exit aperture space. With pulsed-mode operation at low duty factors, the LaB_6 cathodes exhibited very little erosion after many hours of operation. With the combined long lifetimes of the sputter probe, LaB_6 cathodes, and low

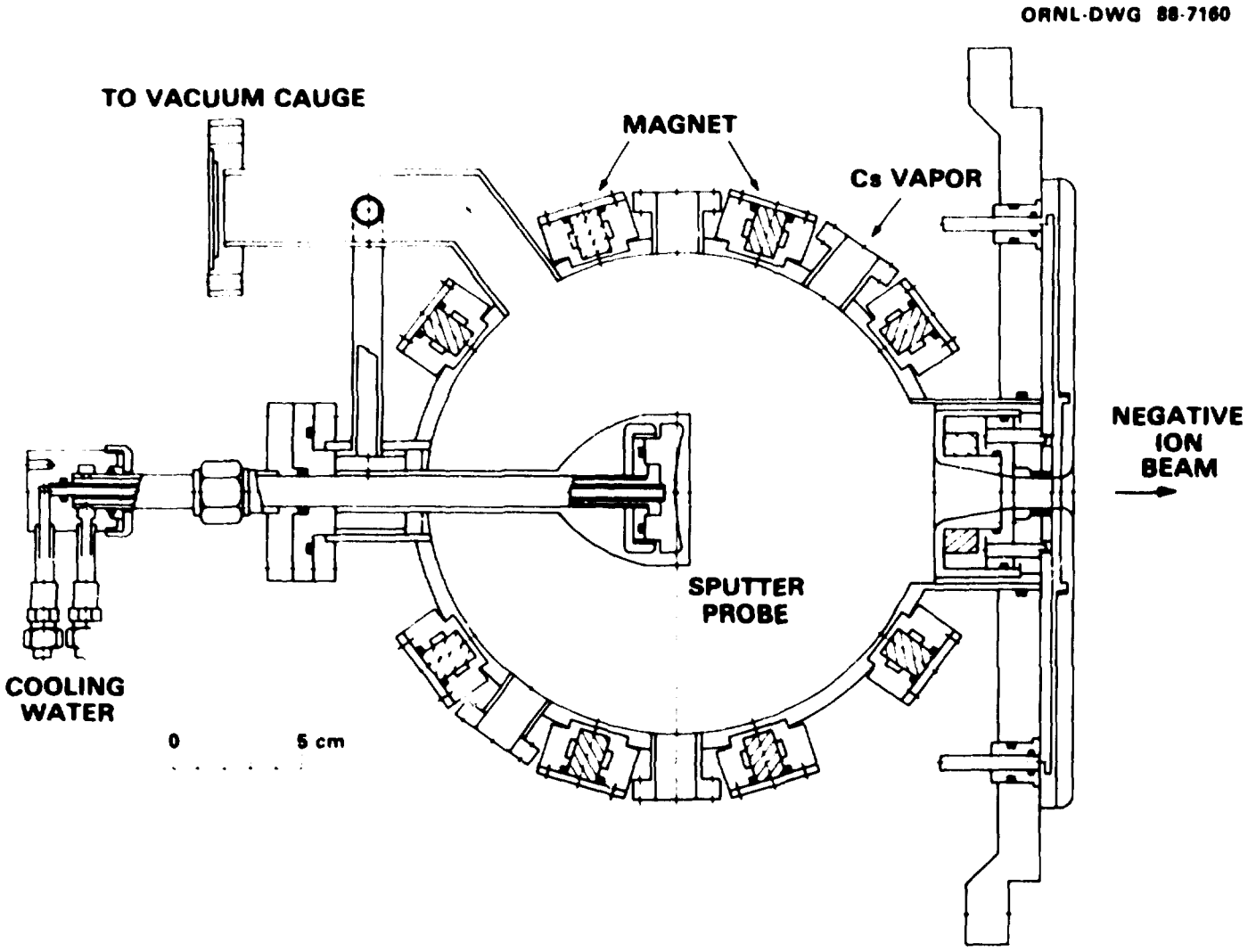

Fig. 4.3-10 Schematic drawing of the high-intensity cusp-field plasma-sputter negative ion source.

cesium consumption rate, the source can operate stably for a few thousand hours without maintenance.

This source holds considerable promise for use with tandem accelerator pulsed injection applications. In particular, Table 4.3-2 is a partial list of total beam intensities obtained from pulsed operation of this source. It is important to appreciate that the peak negative ion beam intensities are frequently 100 times or more greater than those from the earlier sources. Examples of nickel beam emittances versus percent total pulsed negative ion beam are shown in Fig. 4.3-11 with peak pulse intensities of 2.5 and 6.0 mA. The emittances are seen to increase in proportion to the ion beam intensity, as expected from space charge considerations. At the 80% contour level, the emittance values

Table 4.3-2. Total heavy negative ion peak beam intensities from the high-intensity plasma sputter negative ion source

Sputter Probe	Sputter Probe Voltage (V)	Geometry	Total Peak Beam Intensity (mA)	Species (%)
Ag	937	Spherical	6.2	Ag^-(91)
Au	437	Spherical	10.3	Au^-(73)
Bi	937	Spherical	2.7	Bi^-(6);O^-(42)
C	937	Spherical	6.0	C^-(36);C_2^-(58)
Co	937	Spherical	6.0	Co^-(85)
Cu	438	Sphrical	8.2	Cu^-(77)
CuO	438	Flat	4.5	Cu^-(40);O^-(60)
GaAs	937	Flat	3.7	As^-(20);As_2(52)
GaP	937	Flat	1.8	P^-(44)
Mo	438	Spherical	30.0	O^-(67)
Ni	438	Spherical	5.0	Ni^-(87)
Pd	937	Spherical	7.6	Pd^-(69)
Pt	937	Spherical	8.1	Pt^-(71)
Si	937	Spherical	6.0	Si^-(75)
Sn	937	Spherical	3.6	Sn^-(67)

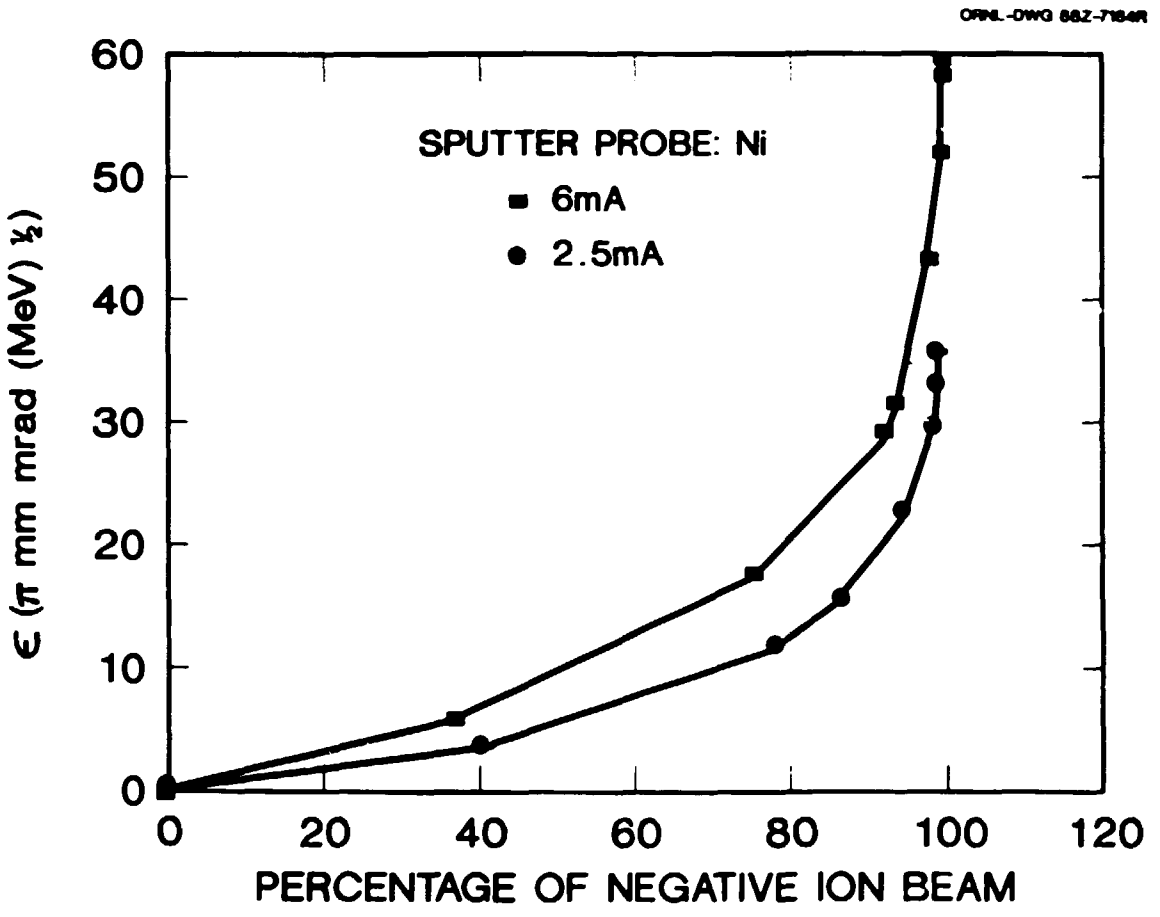

Fig. 4.3-11 Normalized emittance ε versus percent total pulsed negative ion beam for the high-intensity cusp-field plasma-sputter negative ion source.

are comparable to those from other sources. This source is capable of filling HISTRAP to the space charge limit and represents a major step forward for pulsed, negative heavy-ion-beam technology.

4.3.3 Tandem Injection of HISTRAP

HISTRAP will be injected with beam from the HHIRF tandem with a straightforward extension of an existing atomic physics experimental beam line, which is optically identical to the first section of the HISTRAP injection line. The tandem feeds experimental beam lines through a 90° vertical bending magnet, which has a maximum bending power of 2.6 Tm, and which can be rotated to the appropriate beam line as needed. Tandem injection into HISTRAP will require rotating this energy-analyzer magnet to this new injection line as shown in Fig. 4.3-12. This energy-analyzer magnet produces a double waist at which image slits are used to control the tandem voltage and hence beam energy. Typical beam parameters at this waist are listed in Table 4.3-3. It is convenient and natural to use this double waist as the starting point for the optical design.

The injection line was divided into three functional sections: a stripping section, an achromatic section, and a matching section. The optical elements for these sections are listed in Table 4.3-4. The beam envelope as calculated with TRANSPORT is shown in Fig. 4.3-12. The three sections are connected to each other, to the tandem, and to HISTRAP at double waists. The total length of the line is 23 m.

The stripping section transports the beam with unit magnification in both planes from the double waist at the tandem slits, through the

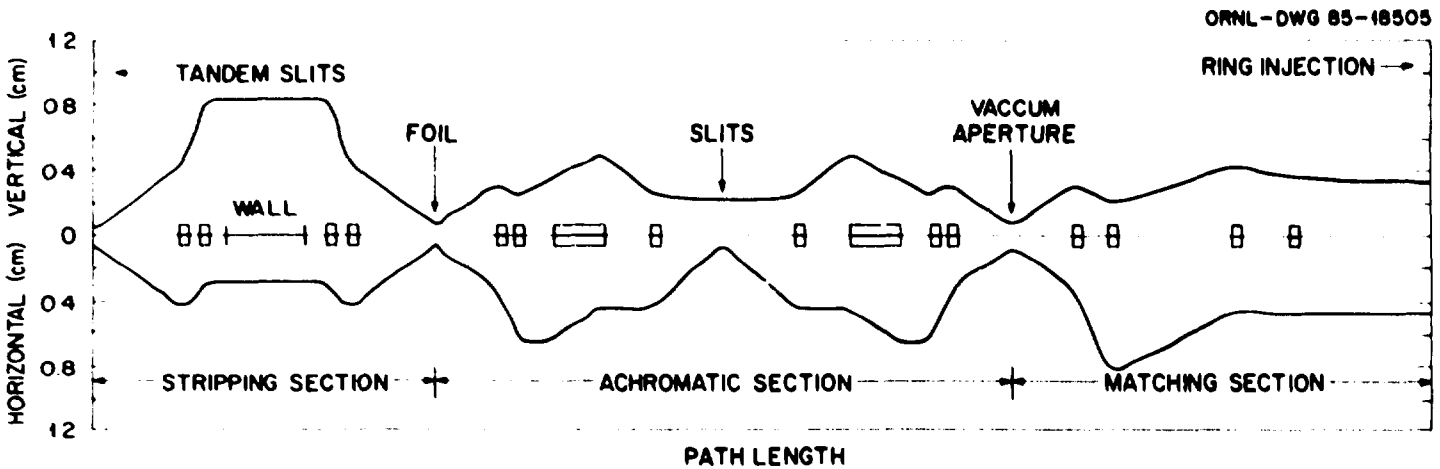

Fig. 4.3-12 Beam envelopes for the transfer line from the image double waist of the 90° energy analyzer magnet to the ring injection point.

Table 4.3-3. Some typical beam characteristics along the injection line

Double Waist of 90° Energy-Analyzer Magnet
$B\rho$ = 2.36 Tm
Beam diameter = 1.5 mm
$\varepsilon_x = \varepsilon_y = 2.3\pi$ mm-mrad
$\beta_x = \beta_y = 0.25$ m
$\alpha_x = \alpha_y = 0$
$\Delta E/E = \pm 0.01\%$
Vacuum pressure 1 x 10^{-8} torr
Immediately after Stripping Foil
$B\rho$ = 1.0 Tm
$\varepsilon_x = \varepsilon_y = 2.5\pi$ mm-mrad
$\Delta E/E = \pm 0.10\%$
At HISTRAP Injection
β_x = 10.5 m and variable
α_x = 0 and variable
β_y = 4.8 m
α_y = 0
Vacuum pressure 1 x 10^{-12} torr

Table 4.3-4. Elements of tandem injection line

Element	L(m)	B(T) or B'(T/m)	Element	L(m)	B(T) or B'(T/m)
Stripping Section ($B\rho$ = 2.3 Tm)					
1 drift	1.20		20 drift	0.98	
2 quad	0.20	+22.5	21 quad	0.20	+4.1
3 drift	0.15		22 drift	0.85	
4 quad	0.20	-17.3	23 44° exit angle		
5 drift	1.96		24 46° bend	0.80	1.00
6 quad	0.20	-17.3	25 drift	0.50	
7 drift	0.15		26 quad	0.20	+7.2
8 quad	0.20	+22.5	27 drift	0.15	
9 drift	1.20		28 quad	0.20	-8.2
			29 drift	1.00	
Achromatic Section ($B\rho$ = 1.0 Tm)			**Matching Section ($B\rho$ = 1.0 Tm)**		
10 drift	1.00		30 drift	1.00	
11 quad	0.20	-8.2	31 quad	0.20	-8.0
12 drift	0.15		32 drift	0.15	
13 quad	0.20	+7.2	33 quad	0.20	+6.4
14 drift	0.50		34 drift	2.00	
15 46° bend	0.80	1.00	35 quad	0.20	-2.2
16 44° exit angle*			36 drift	0.80	
17 drift	0.85		37 quad	0.20	+0.5
18 quad	0.20	+4.1	38 drift	2.56	
19 drift	0.98				

*Exit angle is with the beam relative to the pole edge.

The stripper foil is located after drift 9. The charge-state selection slits are located after drift 19. The achromat image and vacuum baffle are located after drift 29.

concrete shielding wall, to a double waist image point. A charge-state stripping foil is placed at this image waist, where beta values are 0.25 m in both planes. A 350-MeV Au beam with an emittance of 2.3π mm-mrad traversing a 10-$\mu g/cm^2$ foil at this location would have its radial emittance increased by about 10%. As listed in Table 4.3-3, the beam would have its relative energy spread increased from about 1×10^{-4} to about 1×10^{-3}. Before this foil, energy dispersion is negligible. After this foil, energy dispersion is not negligible. For this stripping section two strong quadrupole doublets were used, one on each side of the concrete wall. This section of the injection line presently exists.

The achromatic section transports the nondispersed beam from the stripping-foil double waist, through a 92° bend, to produce a nondispersed double waist with unit magnification in both planes. This section is mirror symmetric about its midpoint, at which charge-state-selection slits are located. At these slits, the beam has a double waist with a dispersion of 1.31 m, giving horizontal half distances of 0.7 mm and 33 mm for $\Delta E/E = 0.001$ and $\Delta Q/Q = 0.025$, respectively. A 2.3π mm-mrad beam has a horizontal half-width of 0.6 mm and a vertical half-width of 1.5 mm. The image double waist of the achromat provides an ideal location for a vacuum separating aperture. A 2.3π mm-mrad beam has a diameter of 1.5 mm at that point. Removal of unwanted charge states at the center of this achromatic section is important, since only about 20% of the ions for a very heavy beam entering this section will have the correct charge for injection.

The matching section transports the beam from the vacuum-aperture double waist to the injection double waist at the center of a straight

section in the ring. The beam is matched to the lattice parameters listed in Table 4.3-3, with the four quadrupole singlets listed in Table 4.3-4. The quadrupole spacings listed allow the beam parameters to be tuned somewhat at injection. This entire beam line is just one solution using only first-order optics. The beam is confined everywhere along the injection line to a diameter of less than 2.0 cm. Standard three-inch-bore ORIC quadrupoles can be used.

The desire for the largest possible beam current in the synchrotron requires a maximum filling of the ring acceptance. This will be achieved by multiturn injection using a slow orbit bump in the horizontal plane. A full $\varepsilon = 200\pi$ mm-mrad beam at the center of a dispersion-free straight section has a horizontal half-width of 46 mm. The electrostatic septum will inject the $\varepsilon = 2.5\pi$ mm-mrad beam from the tandem about 50 mm radially outward from the equilibrium orbit. At the start of injection, the equilibrium orbit will be moved radially outward to the septum by a set of slow bump magnets. This orbit bump is then continuously reduced until the beam is centered about the unperturbed equilibrium orbit at the end of injection. The time of the orbit bump needs to be variable from about 2 to 200 μs, depending on the injection conditions.

Some parameters for the multiturn injection hardware are listed in Table 4.3-5. An electrostatic septum and up to four bump magnets may be required. The septum bends the beam by 15° with a 75-keV/cm electric field. It has a 1.0-cm-wide gap, a 4.5-m radius of curvature, and requires a 75-kV bias supply. The septum has been sized to inject an $\varepsilon = 2.5\pi$ mm-mrad beam from the tandem. Beams from the RFQ will be

Table 4.3-5. Injection elements in ring

Bump Magnets	
Number	4
Effective length	15 cm
Maximum field	800 gauss
Gap	7 cm
Good-field width	10 cm
Fall time	2-200 μs
Septum	
Length	1.3 m
Bend angle	15°
Radius of curvature	4.5 m
Horizontal aperture	1.0 cm
Vertical aperture	2.4 cm
Voltage	75 kV
Gradient	75 kV/cm

brought to a focus, as they may have a larger emittance. The electrostatic septum will introduce a 0.30-m uncompensated horizontal dispersion into the beam at injection, which corresponds to a radial width of ±0.15 mm for $\Delta E/E = \pm 0.1\%$. This dispersion is negligible.

The slow injection bump can be made with four kicker magnets located between the F sextupoles and dipoles. Kicks of 7 and 10 mrad from the magnets upstream of the septum produce an $x = 54$ mm and $x' = 0$ bump at injection, whereas kicks of 8 and 10 mrad from the two magnets downstream of the septum return the beam to the unperturbed equilibrium orbit. These kickers are arranged to preserve the fourfold symmetry of the ring and are capable of producing a slow bump in any straight section. There is no obvious advantage in arranging the kickers symmetrically about the injection point. The requirements for the four

kickers are rather modest. Other solutions with fewer kickers are probably possible.

4.4 ECR/RFQ Injector

HISTRAP will also be injected with an ion beam extracted from an electron cyclotron resonance multicharged-ion source, accelerated by a compact radio frequency quadrupole linac, and merged into the tandem injection line downstream of the second bending magnet of the achromat. The ECR source, beam transport, and RFQ subsystems of this injector are discussed below.

4.4.1 ECR Ion Source

The ion source which will be built for HISTRAP is an upgrade of the existing ORNL ECR ion source [Me85, Me87] which has been in operation since March 1984. This ion source has reliably produced ion beams over a wide range of atomic species and charge states for a large variety of atomic physics experiments [Me88]. The salient features of the ORNL ECR source are shown in Fig. 4.4-1. The source consists of two stages. In the main stage, electrons are confined in a minimum-B configuration and heated by resonant absorption of 10.6 GHz microwaves. Subsequent collisions of these energetic electrons with source gas atoms produce ions of very high charge states. The minimum-B structure is produced by a superposition of an axial mirror field and a radial hexapole field. Three conventional water-cooled solenoids are used to produce the axial mirror field. The hexapole field is produced by a compact [Ha80] assembly of $SmCo^5$ permanent magnets positioned around the cylindrical

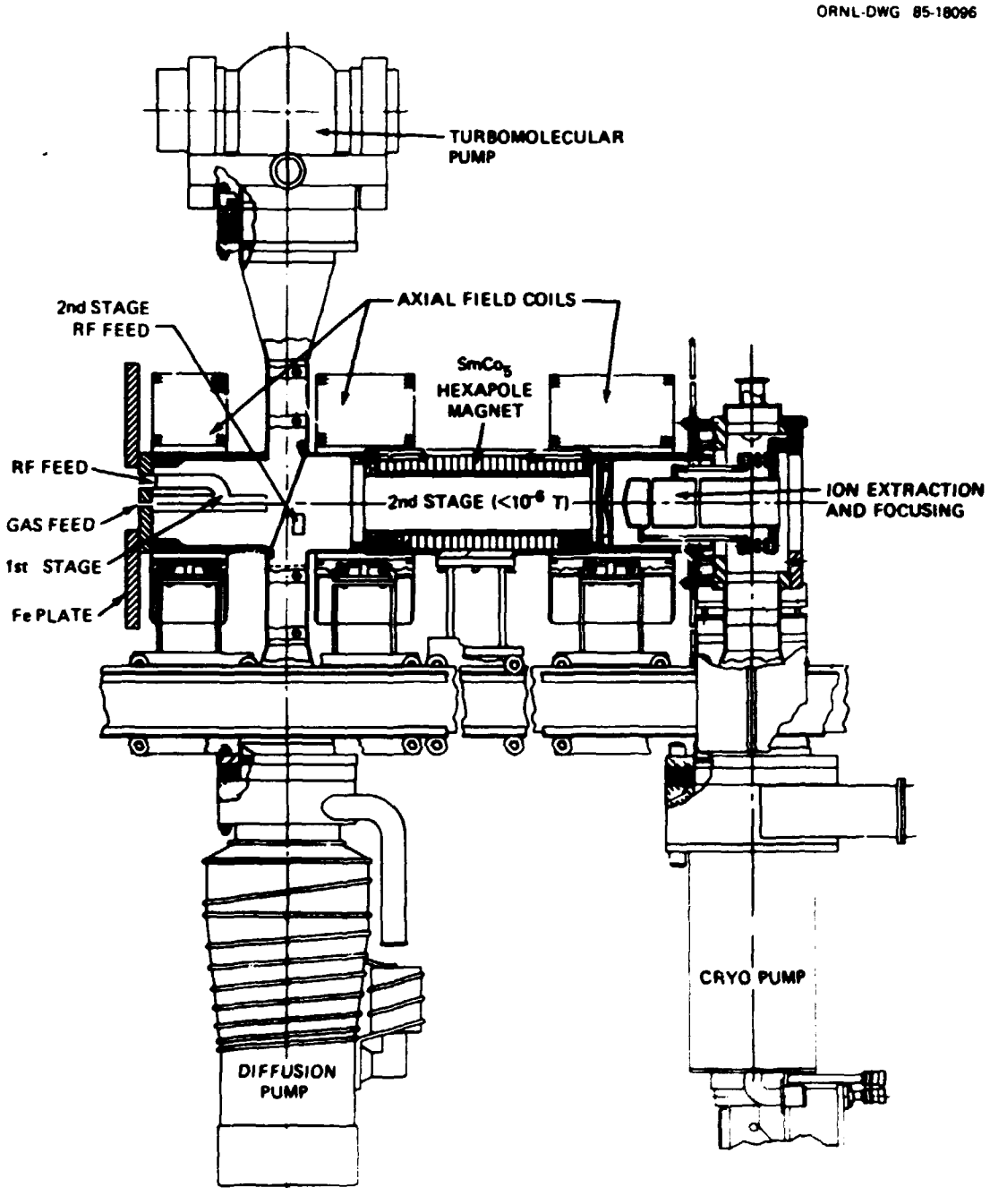

Fig. 4.4-1 Schematic drawing of the existing ORNL 10.6-GHz ECR ion source which has produced a wide variety of highly charged ions for atomic physics measurements.

vacuum wall of the main stage. Cooling of the permanent magnet assembly is achieved by water circulation through the voids created between the cylindrical vacuum wall and the duodecagon defined by the placement of the $SmCo^5$ bars. The injector stage operates also in electron cyclotron resonance mode at 10.6 GHz, and serves as a source of ions and electrons to "fuel" the main stripper stage. Microwave power to the first stage is obtained from the same 10.6 GHz supply providing power to the main stage by means of a low-insertion-loss variable power divider.

The mechanical design of the source features ease of assembly and access. The source divides into three sections, each of which is separately supported by, and can be rolled freely on, precision tracks. The three solenoidal field coils are supported by a similar track structure, and can be moved freely about to expose otherwise inaccessible source parts during source disassembly, or to change the axial mirror ratio in the main stage while the source is fully assembled.

The ECR source also has the capability of metal ion production, using a solid sample feed technique in which a metallic vapor is created from a thin foil sample heated by insertion into the main stage plasma edge. The foil is clamped to the end of a lever arm that can be rotated about a pivot. Rotation of the sample into the plasma edge is achieved via a mechanical linkage to a linear motion feedthrough located on the second stage microwave feedthrough flange. Table 4.4-1 summarizes representative ion currents attainable with the existing 10.6-GHz ECR source. As can be seen, beams of total extracted intensity of about 1 pnA have been obtained for Au^{33+}.

Table 4.4-1. Representative 10.6 GHz ORNL ECR source beam currents (electrical μA); 10-12 kV source voltage

	^{16}O	^{40}Ar	^{56}Fe	^{58}Ni	^{84}Kr	^{127}I	^{129}Xe[a]	^{181}Ta	^{197}Au
+1	400	110	10						
+2	300	120	*						
+3	170	90	20						
+4	100	75	*						
+5	83	*	23	3	20				
+6	50	65	25	5	25				
+7	2.5	73	*	7	26				
+8	0.1	105	*	12	27				
+9		45	20	20	33		5.0		
+10		*	10	17	31	8	4.5	12	25
+11		3.0	5	*	33	10	3.5	*	27
+12		0.7	*	5	40	14	3.5	12	21
+13			2	3	23	18	3.2	12	18
+14			*	1	21	20	2.5	12	*
+15			1.5	0.5	15	18	1.5	12	18
+16				0.15	5	*	1.2	12	15
+17				0.03	1	10	1.0	11	12
+18					*	*	0.6	8	10
+19					0.25	3	0.6	5	7
+20						2	0.5	3.5	5
+21						*	0.25	2	5
+22						0.5	0.12	1.8	4
+23								*	3
+24								1.5	2.5
+25							0.08	1.0	*
+26							0.05	*	0.9
+27								0.4	0.4
+28								0.1	*
+29								0.05	0.1
+30									0.015[b]
+31									0.005[b]

*Indicates m/q degeneracy with contaminant beam.
[a]5 x 5 mm slits.
[b]2 x 2 mm slits.

An upgraded version of the existing ORNL ECR source will be used for HISTRAP. This is very similar in overall mechanical design to the 10.6-GHz ORNL ECR source, will operate at 14.5 GHz, and will feature an iron return yoke for the axial magnetic field coils. The 14.5-GHz HISTRAP ECR source is shown schematically in Fig. 4.4-2, and its operating parameters are summarized in Table 4.4-2. Use of an iron flux return circuit will give about a 20% increase in axial magnetic field intensity; the increased power dissipation associated with the remaining 20% increase in axial magnetic field required to attain a closed ECR surface at 14.5 GHZ can be handled easily by the cooling capacity reserves designed into the present coils. The permanent magnet hexapole structure can also be easily upgraded for 14.5-GHz operation by replacing the original $SmCo_5$ material with Nd-Fe-B magnets, which will produce about 40% higher peak magnetic fields.

The use of a higher microwave frequency is expected to significantly increase extracted beam currents, especially for charge states above the peak of the extracted charge state distribution. The scaling of ECR source performance with microwave frequency in the region of 10-20 GHz has been experimentally verified at Grenoble [Ge88]. The dashed lines in Fig. 4.4-3 show the expected charge-state trend vs atomic mass number of the ionic species for two different beam intensities at 14.5 GHz. These expected performance curves are based on recent measurements on the 14.5-GHz MINIMAFIOS source at Grenoble [Ge88] for ion beam production from a wide range of elements, including Ta and Pb. For comparison, Fig. 4.4-3 also shows the corresponding curves as solid lines describing the performance of the present 10.6-GHz ECR source.

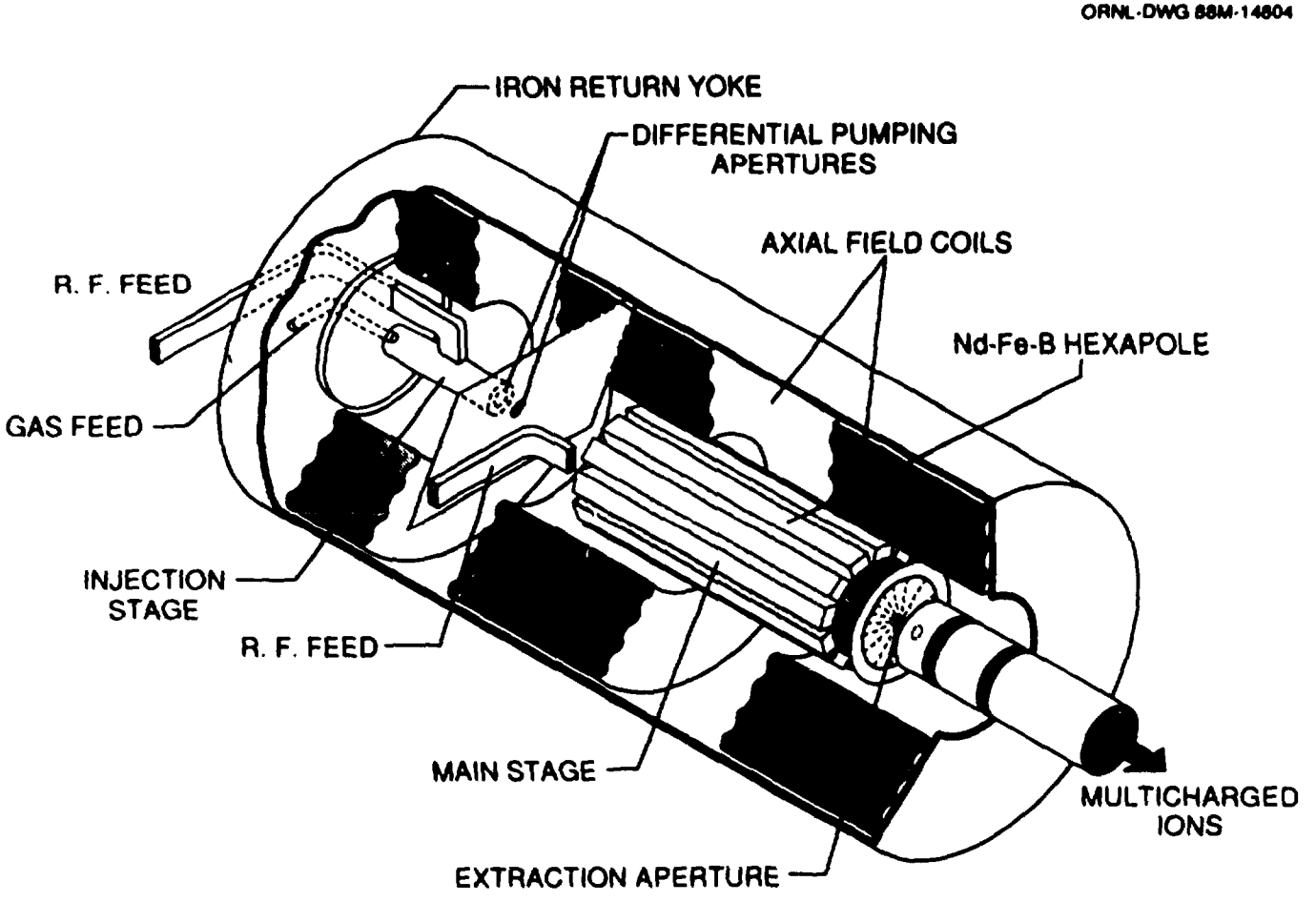

Fig. 4.4-2 Cutaway drawing of the 14.5-GHz ECR ion source which is planned for HISTRAP.

Table 4.4-2. 14.5-GHz HISTRAP ECR source parameters

Microwaves	
First stage 14.5 GHz	50-100 W
Second stage 14.5 GHz (2.5 kW max)	20-1500 W
Magnetic Fields	
Mirror ratio	1.6
Hexapole field at vacuum wall	5.8 kG
Field in extraction plane	6.5 kG
Field in first stage	around B_{res} for 14.5 GHz
Total solenoid power	100 kW
Vacuum (operating condition)	
First stage	10^{-3}–10^{-4} torr
Second stage (1×10^{-7} torr base)	$1\text{-}6 \times 10^{-6}$ torr
Extraction	1×10^{-7} torr
Dimensions	
Solenoids ID	18 cm
Solenoids OD	40 cm
Hexapole ID	9.5 cm
Hexapole length	33 cm
Vacuum wall ID second stage	8.6 cm
Anode aperture	0.8 cm
Extraction aperture	1.0 cm
Extraction gap	2.6 cm

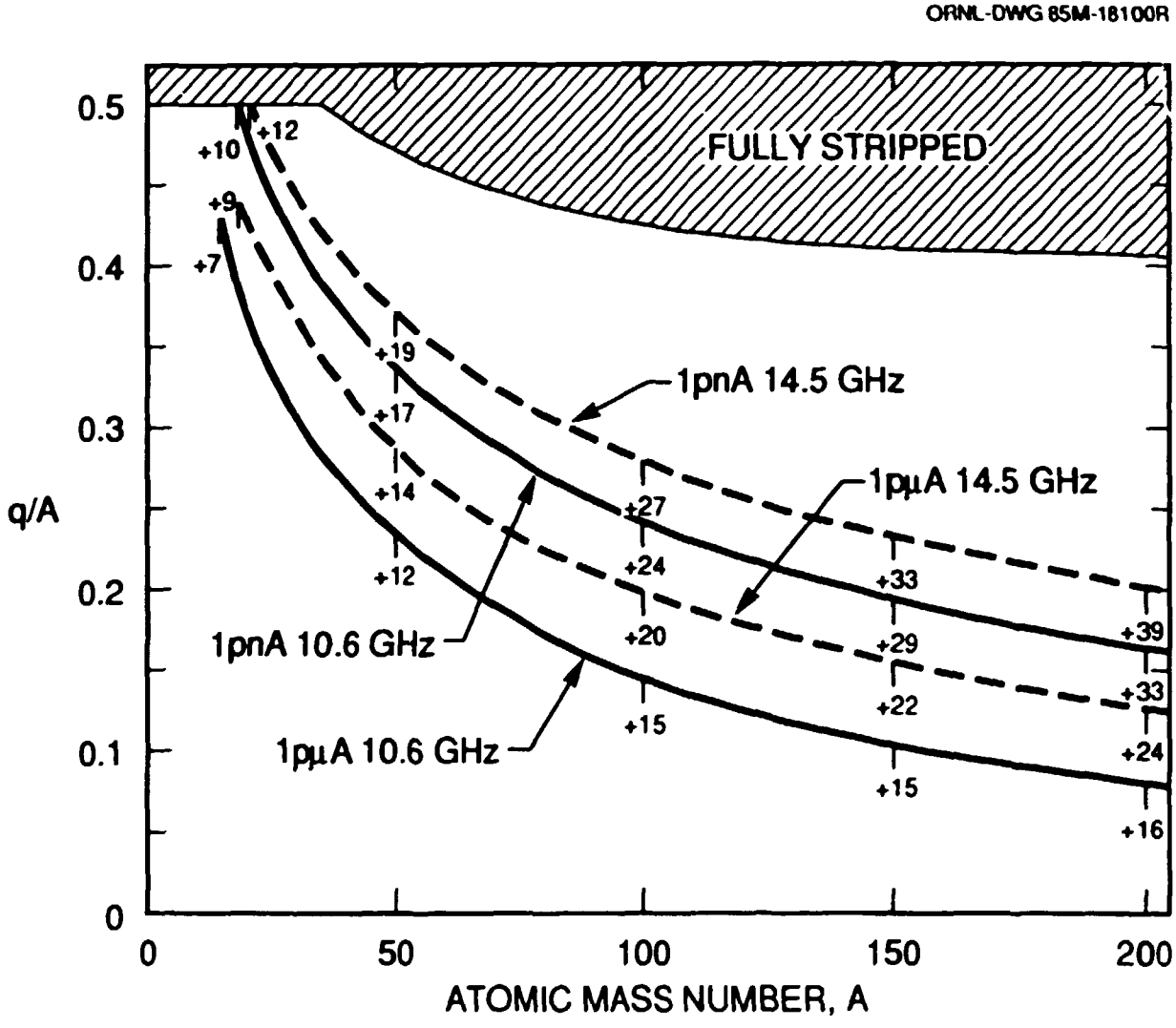

Fig. 4.4-3 Expected charge states as a function of atomic mass number for two different beam intensities for the planned 14.5-GHz HISTRAP ECR source, dashed lines. The solid lines are corresponding curves for the existing 10.6-GHz ECR source.

The expected performance at 14.5 GHz for Au ions is shown in Fig. 4.4-4 by the dashed line; charge state distributions for Au and other metallic beams obtained with the 10.6-GHz ECR source are also shown for comparison. As can be seen, a beam intensity of about 400 enA is expected for the design ion Au^{33+} from the 14.5-GHz HISTRAP ECR source.

4.4.2 Beam Extraction and Transport

Figure 4.4-5 shows the beam tranport system immediately following the ECR source. Ion extraction from the ECR source is accomplished by a three-element extraction electrode, the first two elements of which can be biased independently for ion focusing and prevention of electron backstreaming. The position of the anode and the extraction electrode, as well as the extraction gap itself, can be varied by the use of shims. An electrostatic unipotential lens operated in "accel" mode images the extracted beam onto the entrance slit of a stigmatic 90° magnetic charge analyzer having a 40-cm radius of curvature. The entrance slit assembly is located about 100 cm downbeam of the source anode; object and image distances for the 90° magnet are 80 cm. Retractable Faraday cups located immediately after the entrance and exit slits are used to measure total extracted beam currents, and charge-selected beam intensities, respectively. Both entrance and exit slit assemblies feature independently adjustable horizontal and vertical slit jaws on which current can be measured. A second electrostatic unipotential lens, located downbeam of the charge analyzer exit slit and immediately before the entrance to the RFQ, serves to produce the strongly converging beam required at the start of the RFQ vane structure. An electrostatic

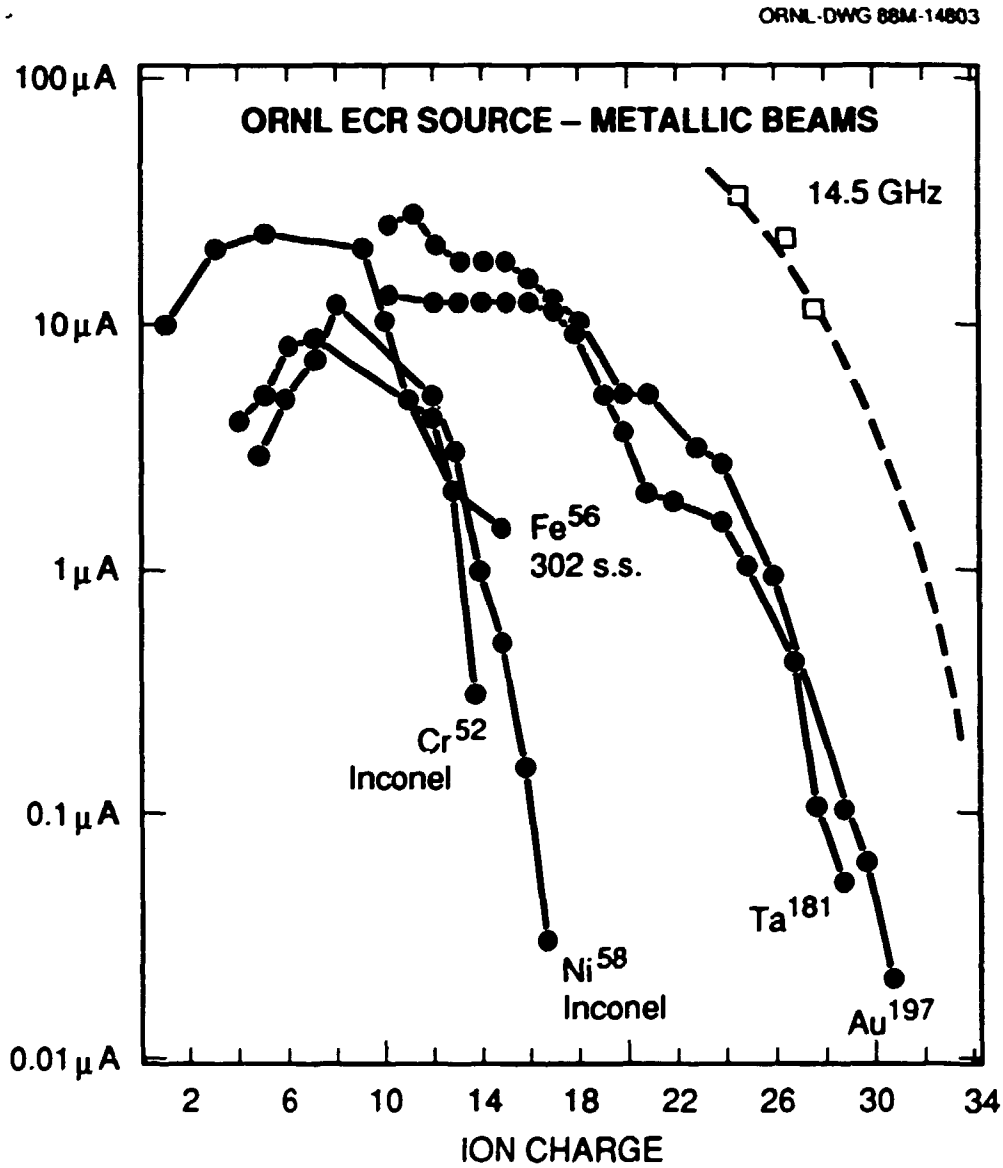

Fig. 4.4-4 Expected performance of the planned 14.5-GHz HISTRAP ECR source for Au ions (dashed lines) compared with present performance of the 10.6-GHz ECR source for Au and other metallic beams (solid lines).

ORNL Photo 8247-84

Fig. 4.4-5 Existing ORNL 10.6-GHz ECR source and beam transport line. The HISTRAP 14.5-GHz ECR source and injection line will be similiar.

quadrupole located between the exit slit assembly and the einzel lens is included to "trim out" any asymmetries introduced by the 90° charge analyzer. A calculated beam envelope from the exit of the ECR source to the entrance of the RFQ accelerator is shown in the upper panel of Fig. 4.4-6.

A calculated beam envelope for the line between the RFQ and the tandem injection line is shown in the lower panel of Fig. 4.4-6. The strongly diverging beam exiting the RFQ is focused by a magnetic quadrupole lens onto the entrance aperture of a double gap debuncher located 110 cm down beam. The debuncher is used to match the longitudinal emittance of the accelerated ion beam to the longitudinal acceptance of HISTRAP. The debuncher is calculated to reduce the ion beam momentum spread from an initial value of 1.0% to 0.3%, well below the maximum momentum acceptance of the ring. A second magnetic quadrupole lens 50 cm down-beam of the debuncher, together with the magnetic quadrupole lens used as a trimmer immediately following the second 45° bending magnet of the tandem injection line, will serve to produce a suitable double waist at the required location.

4.4.3 RFQ Accelerator

The RFQ accelerator is a new and unique kind of linear accelerator based on an idea of Kapchinskii and Teplyakov [Ka70] that is ideally suited for accelerating low-energy ion beams. Compared to conventional linear accelerators, such as the magnetically focused drift-tube linac, the RFQ accelerator is significantly less complex. Since the accelerating electric fields in the RFQ are also used for radial focusing,

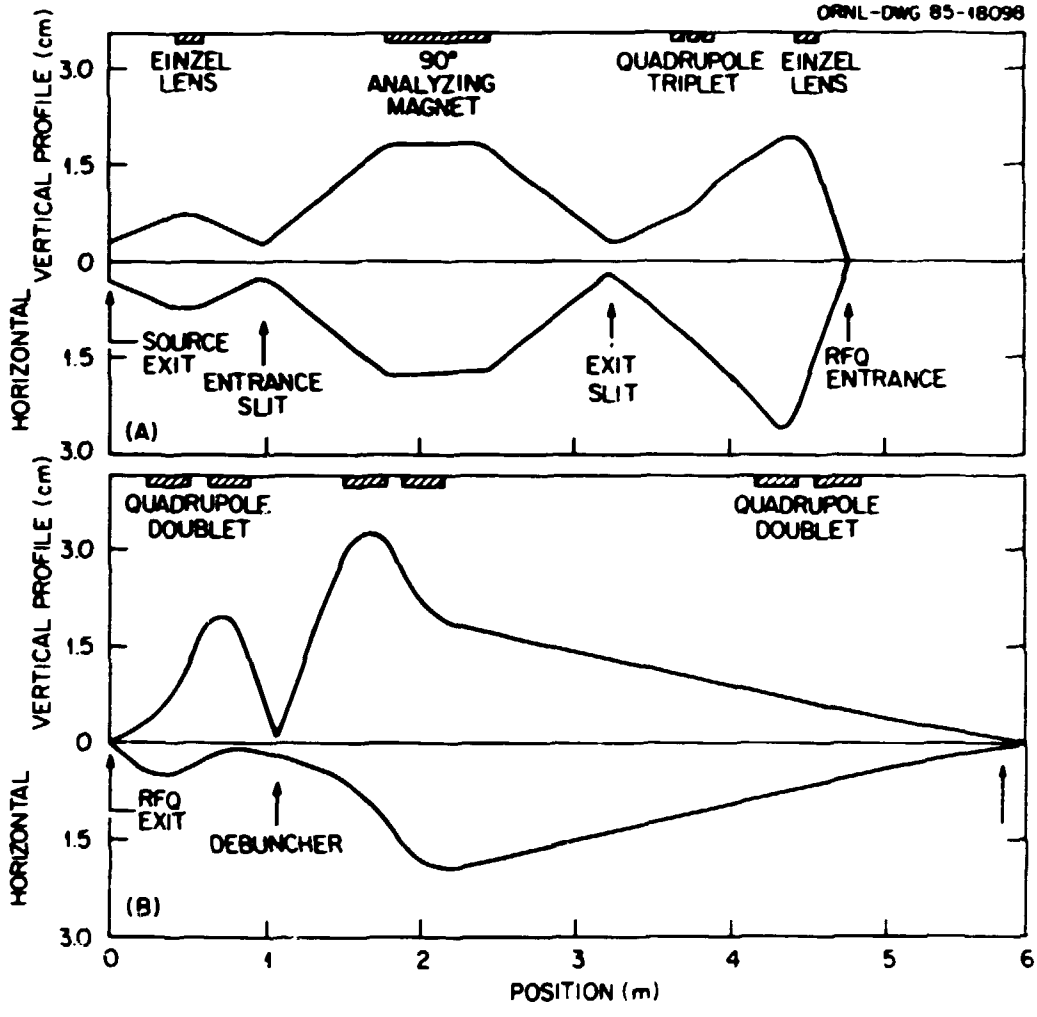

Fig. 4.4-6 Calculated beam profiles between (A) the ECR source and RFQ entrance and (B) the RFQ exit and tandem injection line.

the need for external magnetic focusing is eliminated. In addition, the injector energy requirement is lowered, since the electric focusing force is velocity independent. Moreover, since the RFQ accelerator is self-bunching, complex rf cavity bunchers and complicated low-energy beam transport systems are not required.

The RFQ structure is basically a right cylindrical resonant cavity containing four vanes arranged symmetrically around the beam axis. When excited in the TEM210 mode, adjacent vane tips have equal voltages of opposite sign. This transverse quadrupole field is focusing in each plane during half of the rf cycle, and defocusing during the other half, giving the structure the properties of an alternating-gradient focusing system with a strength independent of particle velocity. To generate a longitudinal accelerating field, the vane tips are modulated, the phase of the vane tip modulation in one plane being shifted by 90° relative to that in the orthogonal plane. The period of the modulations is tailored such that the longitudinal electric field has a spatial harmonic whose phase velocity matches the beam velocity as it varies along the machine during the acceleration process. The magnitude of the accelerating field is controlled by the depth of the modulations cut into the vane tips.

An RFQ is presently being used as an injector for SATURNE II in France, and RFQ R&D programs exist at GSI and Frankfurt in Germany. In the United States, RFQ accelerators have been built at Los Alamos Scientific Laboratory and Lawrence Berkeley Laboratory. A newly completed RFQ is being used to inject polarized protons into the AGS at Brookhaven National Laboratory. We note that LBL has designed and built

two presently operational heavy ion RFQ accelerators, one as part of an upgrade of the Bevatron local injector [St85], and one as a preaccelerator for use at the CERN Linac I [Go85]. The fact that both RFQs met or exceeded their design specifications, and have operated with a minimum of required maintenance, speaks to the considerable expertise LBL has in the design and fabrication of heavy ion RFQs. The conceptual design for the present RFQ was arrived at in collaboration with the LBL RFQ group.

Figure 4.4-7 shows a cross sectional view of the proposed RFQ, illustrating many of the mechanical design features. Primary reference fiducial flats will be precision ground onto four sides of the thick-walled, copper-plated steel rf cavity. Each vane will be supported by cylindrical mounting plugs with two critical engagement surfaces whose separation will determine the radial position of the pole tip relative to the cavity. Transverse vane position will be determined by shims located between the flats on the vane mounting plug and one of the jacking bars. These bars run down the length of the structure and will be keyed into the cavity. Thermal stabilization of the structure will be maintained by a water tube that is captured in this keyway by the jacking bar.

The vanes, like the cavity, will be made of copper-plated mild steel. The vanetip modulations will be cut using a numerically controlled milling machine. During the same set up, fiducial notches will be machined to provide an accurate surface from which the location of the complex pole-tip surface can be referenced. A canted helical spring made of silver-plated, precipitation-hardened Be-Cu alloy will be

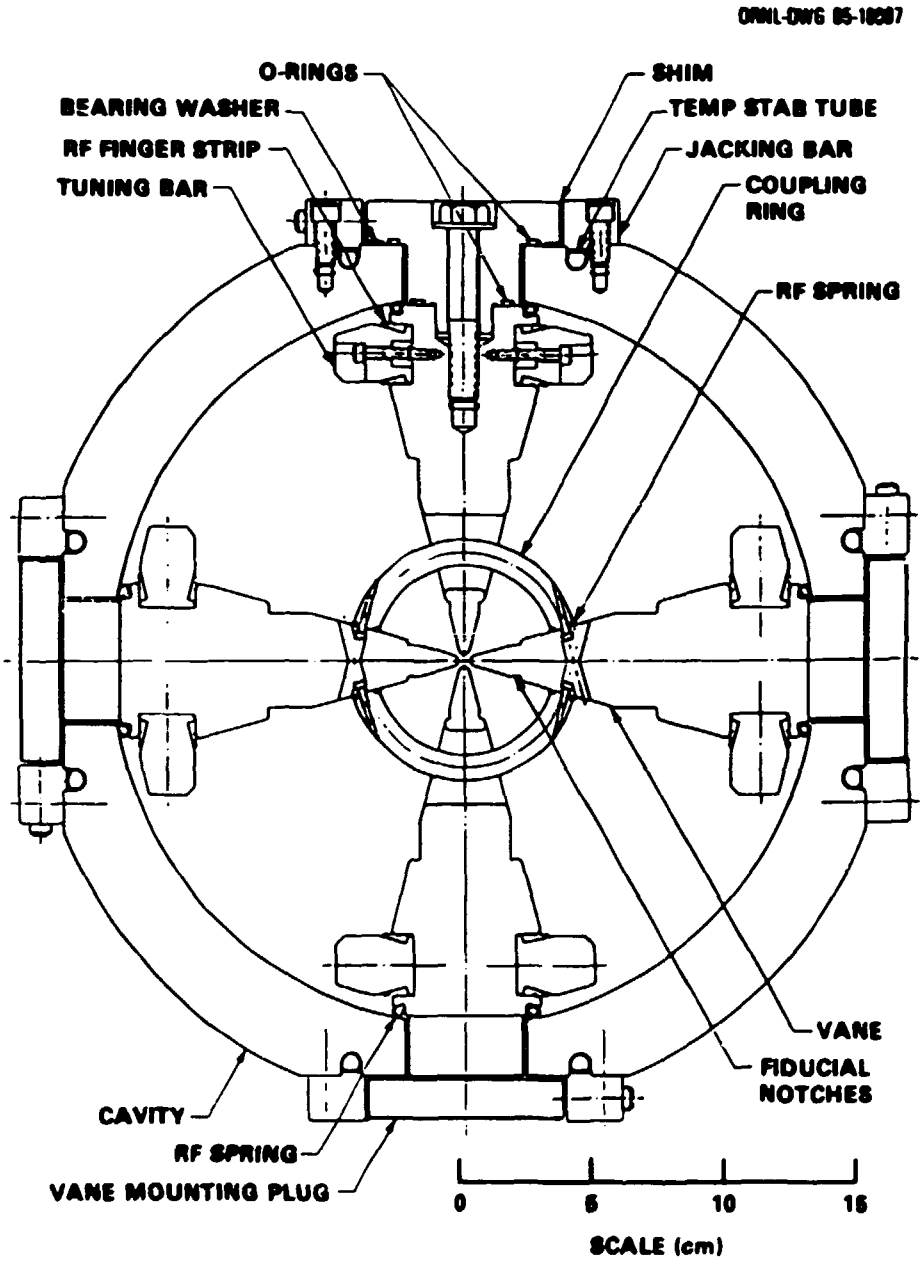

Fig. 4.4-7 Cross sectional view of the RFQ linear accelerator.

used for the main rf joint between the vanes and the cavity. Vane coupling rings will be used to ensure azimuthal field stabilization and balance. These rings form a low-impedance connection between diametrically opposite vanes, providing a strong coupling between the quadrants to locally equalize the quadrant field amplitudes.

The rf cavity will be loop-driven via a circular port near the longitudinal center. A block diagram of the rf electrical system is shown in Fig. 4.4-8. Six monitoring loops per quadrant will permit sampling of the H-field near the cavity wall. Each quadrant will be pumped through a radial port using commercially available cryopumps.

Table 4.4-3 summarizes the design parameters of the proposed RFQ. The 5-keV/nucleon injection energy requires a 30-kV ECR source potential, which is attainable without the use of a high voltage platform. The anticipated duty factor of <0.1% is not expected to give thermal management problems vis-a-vis the 30-kW peak power required. By reducing the field gradient below that required for the $^{197}Au^{33+}$ design ion, ions of lower mass-to-charge ratio can also be accelerated. After suitable conditioning of the accelerator, it is expected that all ions in the range $2 < m/q < 6$, which includes all fully stripped light ions of mass > 4, can be accelerated.

Simulation results for the proposed RFQ, summarized in Table 4.4-4, show the design to have very high capture efficiency and negligible emittance growth. The longitudinal emittance of the accelerated beam is sufficiently small that the maximum momentum spread constraint imposed by the storage ring can be satisfied easily by use of a modulator after the RFQ. The transverse phase space ellipse orientations on the input

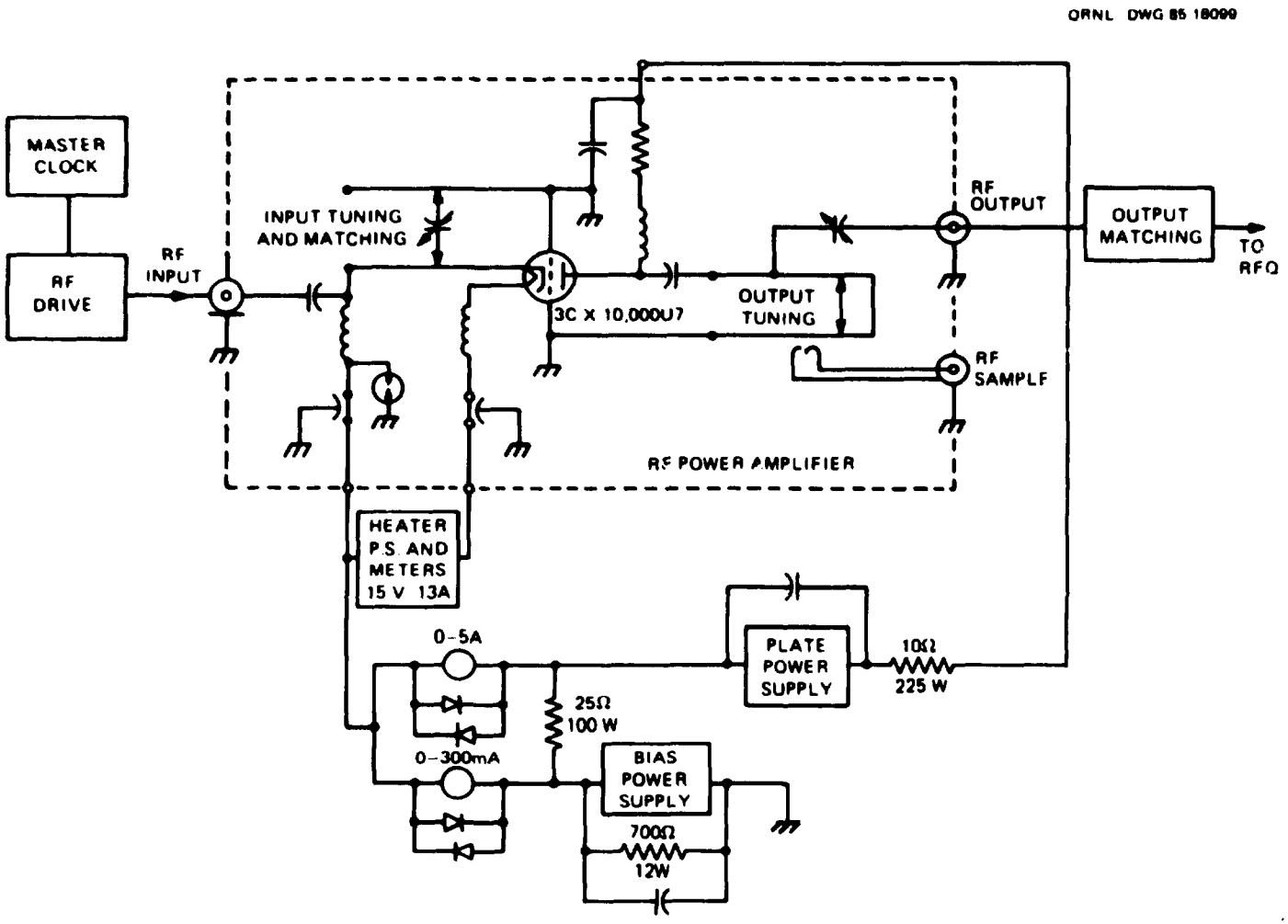

Fig. 4.4-8 Block diagram of the RF electrical system for the RFQ accelerator.

Table 4.4-3. Summary of RFQ linac parameters

Design ion	$^{197}Au^{+33}$
Frequency	228 MHz
Input energy	5 keV/nucleon
Output energy	251 keV/nucleon
Vane length	236.6 cm
Average bore radius (r_0)	1.42 mm
Maximum surface field	28 MV/m
Vane-vane voltage	29 kV
Peak rf power	30 kW
Cavity radius	13.7 cm

Table 4.4-4. Summary of RFQ simulation results

Unnormalized acceptance:	79π mm-mrad
Input phase space ellipse parameters:	β_x = 0.025 m α_x = 0.95 β_y = 0.025 m α_y = 0.95
Output phase space ellipse parameters:	β_x = 0.055 m α_x = 1.1 β_y = 0.055 m α_y = -1.2
Output energy:	251 keV/nucleon
Output energy spread (90%):	±5 keV/nucleon (±2%)
Output phase spread (90%):	±22°
Emittance growth:	0%
Theoretical transmission:	98%

and output ends of the RFQ indicated by the simulation pose no ion optic problems as discussed in the preceding section on beam transport.

The location for the debuncher cavity and the energy spread reduction to be expected were determined by a simulation that involved 500 ions with Gaussian energy and spatial distributions. A sinusoidal energy modulation was imposed at various distances from the RFQ and the energy spreads before and after modulations were compared. Figure 4.4-9 shows the energy spread reduction factor (REDF) and the effective rf voltage (RFKV) required as a function of RFQ-to-modulator distance. This figure shows that the energy spread can be reduced by about a factor of three, and that the modulator location is not very critical. The maximum energy spread reduction factor depends only on the phase spread, while the modulator location is determined by the initial beam energy spread. Since the RFQ energy and phase spread is independent of the particular ion species accelerated, the location and performance of the debuncher should essentially be the same for all ions.

4.5 Synchrotron/Cooler/Storage Ring Systems

4.5.1 Magnet System

The dipole, quadrupole, and sextupole magnet designs are largely determined by the magnetic field strength and aperture requirements. These were discussed in Section 4.2. Table 4.5-1 reviews these requirements and lists the full-width good field and clearance requirements for the dipole and quadrupole magnets. The sextupole requirements are identical to those of the quadrupoles. For these requirements, a very generous allowance of 8 mm was used for closed-orbit errors and other

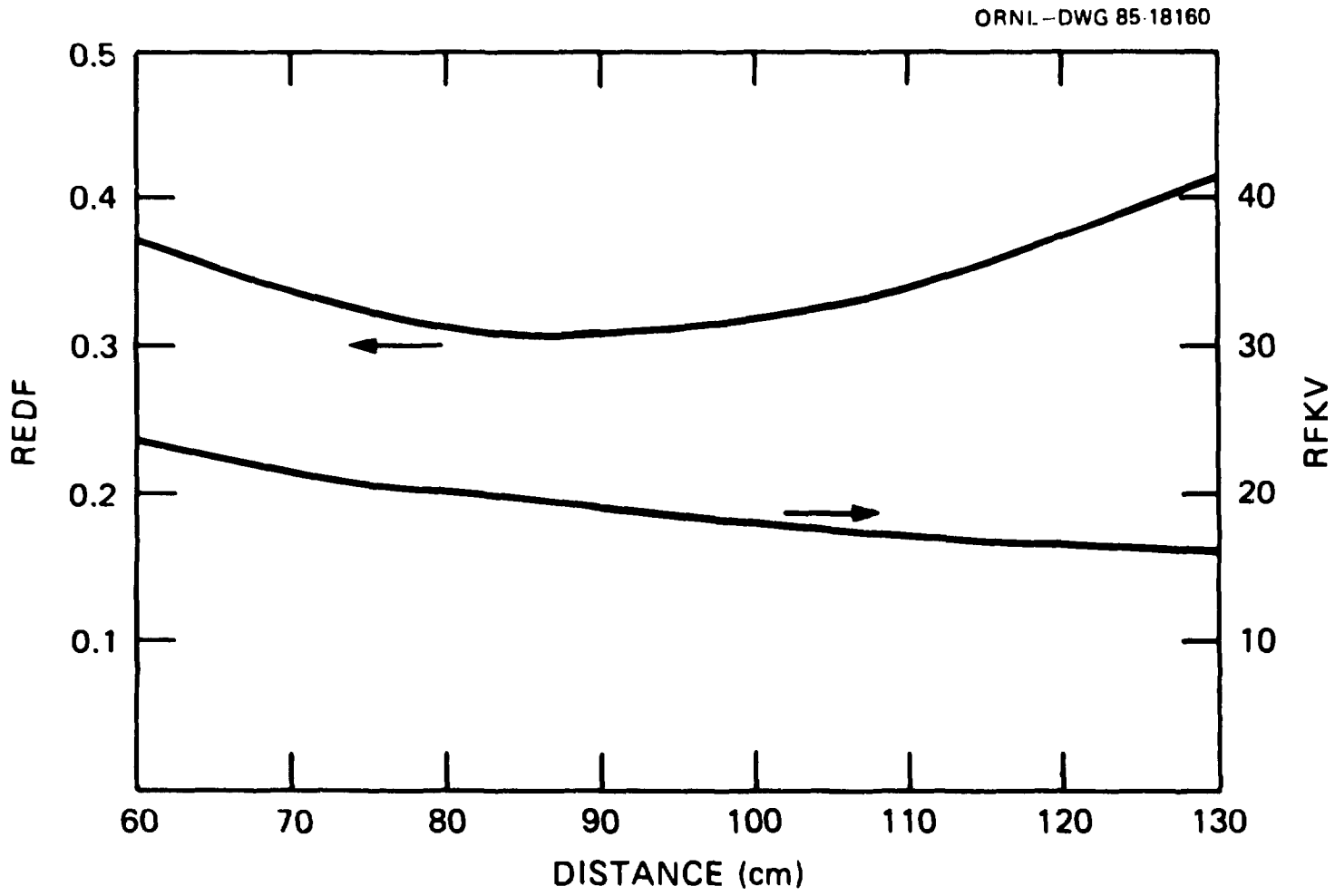

Fig. 4.4-9 Debuncher energy spread reduction factor (REDF) and RF amplitude (RFKV) as a function of distance from the RFQ exit.

Table 4.5-1. Good-field and clearance full-width requirements (mm)

Vertical (Mode A)	Dipoles	F Quads	D Quads
Closed-orbit errors	8	8	8
Betatron oscillations	37	20	35
Beam pipe and insulation	22	22	22
Beam pickups	-	40	40
Shims and clearance	3	1	1
Good field	45	28	43
Clearance	70	91	106

Horizontal MODE =	A[a]	B[b]	A	B	A	B
Closed-orbit errors	8	8	8	8	8	8
Betatron oscillations	96	24	94	26	23	6
Energy dispersion	4	1	11	4	7	2
Charge dispersion	0	40	0	120	0	80
Beam pipe and insulation	22	22	22	22	22	22
Beam pickups	-	-	40	40	40	40
Clearance	1	1	1	1	1	1
Good field	118[c]	80[c]	113	158	38	96
Clearance	141[c]	102[c]	176	221	101	159

[a]Mode A is for the injection of a beam with ϵ_x = 200π mm-mrad and ϵ_y = 60π mm-mrad and $\Delta P/P$ = 0.35% (full width).

[b]Mode B is for storing multiple charge-state cooled beams with $\Delta Q/Q$ = ±4%, $\Delta P/P$ = 0.10%, and ϵ = 13π mm-mrad in both planes.

[c]Includes secant 22.5° factor for parallel end construction.

margins. In principle, the dipole correctors should reduce the closed-orbit errors to less than 1 mm.

Dipoles

A 7.0-cm dipole vertical gap is required: 4.5 cm for betatron motion and closed-orbit errors, and an additional 2.5 cm for beam pipe,

bakeout insulation, and shims. The maximum dipole horizontal good field is required to inject a full 200π mm-mrad beam and is 11.0 cm. This good field requirement is increased to 12.0 cm to accommodate the secant 22.5° factor from the parallel end design. This is the worst case for dipole aperture.

The dipoles are illustrated in Fig. 4.5-1. They will be of a "C" type construction to accommodate merged ion-laser beam experiments. In addition, "C" type construction allows easy access to the vacuum chamber. Because of the 12.7-cm sagitta, the dipoles will be continuously curved to follow the central trajectory. For simplicity of construction, the magnet ends and all laminations will be parallel, requiring 22.5° beam entrance and exit angles. Stress deflection calculations indicate that the gap will close, on average, by a factor of 16×10^{-4} at a 1.6-T excitation. The asymmetry in this deflection is important and will induce a 0.005-T/m quadrupole field. Each assembled dipole will weigh about 11 tons and will have an iron length of 1.230 m to give a magnetic path length of 1.309 m along the central trajectory.

Each dipole magnet will be excited by 40 turns of 4.5 cm x 1.6 cm of Cu conductor with a peak current of 2400 A. At full excitation the magnet will require 30 kW for the resistive loss and contain 43 kJ of stored energy. The design closely follows that used for the BNL VUV light-source dipoles and allows simple racetrack coils to be employed. Table 4.5-2 gives a full listing of the dipole characteristics.

In order to make horizontal steering corrections, the dipoles will require backleg windings with a strength of up to $\Delta B/B \sim 1.0 \times 10^{-2}$. This will require about 40 turns of air-cooled cable carrying 25 A.

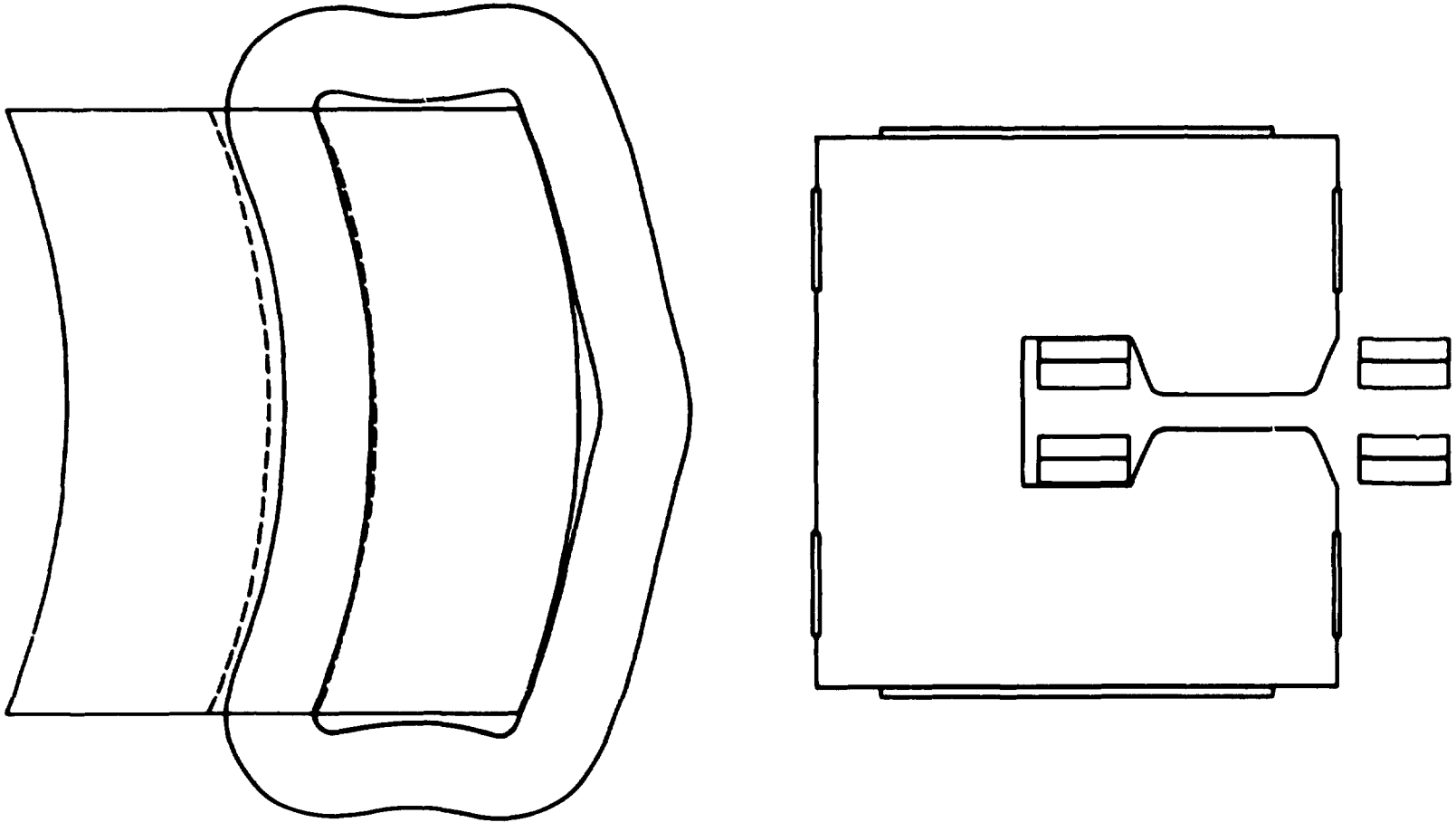

Fig. 4.5-1 Illustration of the HISTRAP dipole magnet. A yoke length of 123.0 cm is needed to give a 130.9-cm pathlength along the central trajectory. The laminations are 110-cm high, 101-cm wide, and have a 7.0-cm gap.

Table 4.5-2. Dipole characteristics

Number	8
Basic Requirements	
Magnetic path length	130.9 cm
Vertical aperture	7.0 cm
Good-field horizontal aperture	12.0 cm
Bending radius	166.7 cm
Bend angle	45.0°
Beam entrance angle	22.5°
Beam exit angle	22.5°
Typical injection field	0.60 T
Maximum field for acceleration	1.60 T
Minimum field for deceleration	0.03 T
Sagitta	12.7 cm
Core Characteristics	
Magnet steel length	123.0 cm
Lamination height	110.0 cm
Lamination width	101.0 cm
Yoke width	40.0 cm
Packing factor	99 %
Core weight	10 tons
Coil Characteristics	
Number of turns	40
Conductor outside dimensions	4.45 x 1.59 cm^2
Cooling-hole inside diameter	0.95 cm
Conductor area	626 mm^2
Average turn length	3.9 m
Cu weight	2100 lb
Water pressure drop	100 psi
Temperature rise	7.4°C
Flow rate	15.6 gpm
Excitation Characteristics	
Peak current	2400 A
Peak current density	3.8 A/mm^2
Coil resistance at 40°C	5 mΩ
I^2R loss for 1.6-T flattop	30 kW
Stored energy of 1.6-T field	43 kJ
Inductance	15 mH

There is some concern that remnant field effects will compromise field quality at low excitation so that the capability to decelerate and store ions will be reduced. One solution to this problem, at least for the dipoles, would be to install pole-face windings. These windings could consist of about 20 turns of 1 mm x 1 mm cable enclosed in a 3-mm-thick

plastic plate. The plate would be installed next to the steel, just outside the vacuum chamber insulation. The cable ends could be constructed to allow any external configuration desired. Currents of up to 5 A per turn would allow appreciable corrections at low excitation. A prototype dipole has been designed with the 3D program TOSCA and fabricated by the FNAL magnet factory. This work is discussed in Section 5.3.

Quadrupoles

The quadrupole aperture requirements also depend on the operating mode. In addition, the aperture requirements for the four D and eight F quadrupoles differ. However, for simplicity, it is assumed that all 12 quadrupoles will be identical. Some of the good-field and clearance considerations are listed in Table 4.5-1. The most stringent requirement occurs for the F quadrupole with the ring operating in the multiple-charge-state-storage mode. In this mode it is assumed that three beams with $\Delta Q/Q$ = -4%, 0%, +4% are stored. Each beam has ε = 13π mm-mrad with $\Delta P/P$ = ±0.10%; some cooling is assumed. Figure 4.5-2 illustrates the F quadrupole aperture requirement for this case. The lower charge-state beam centered at x = +6.0 cm has ε = 13π mm-mrad as stated. The space required for betatron oscillations, momentum spread, and closed-orbit errors is shown. This beam requires a horizontal good-field radius of 8 cm. A field gradient accuracy of ±0.05% out to this radius requires a quadrupole with an 18-cm bore and 15-cm-wide pole tip, as shown. Space for beam pickups, beam pipe, and bakeout insulation is also shown. However, it is important to appreciate that the large bore and pole-tip width are determined by the

ORNL-DWG 85-17488

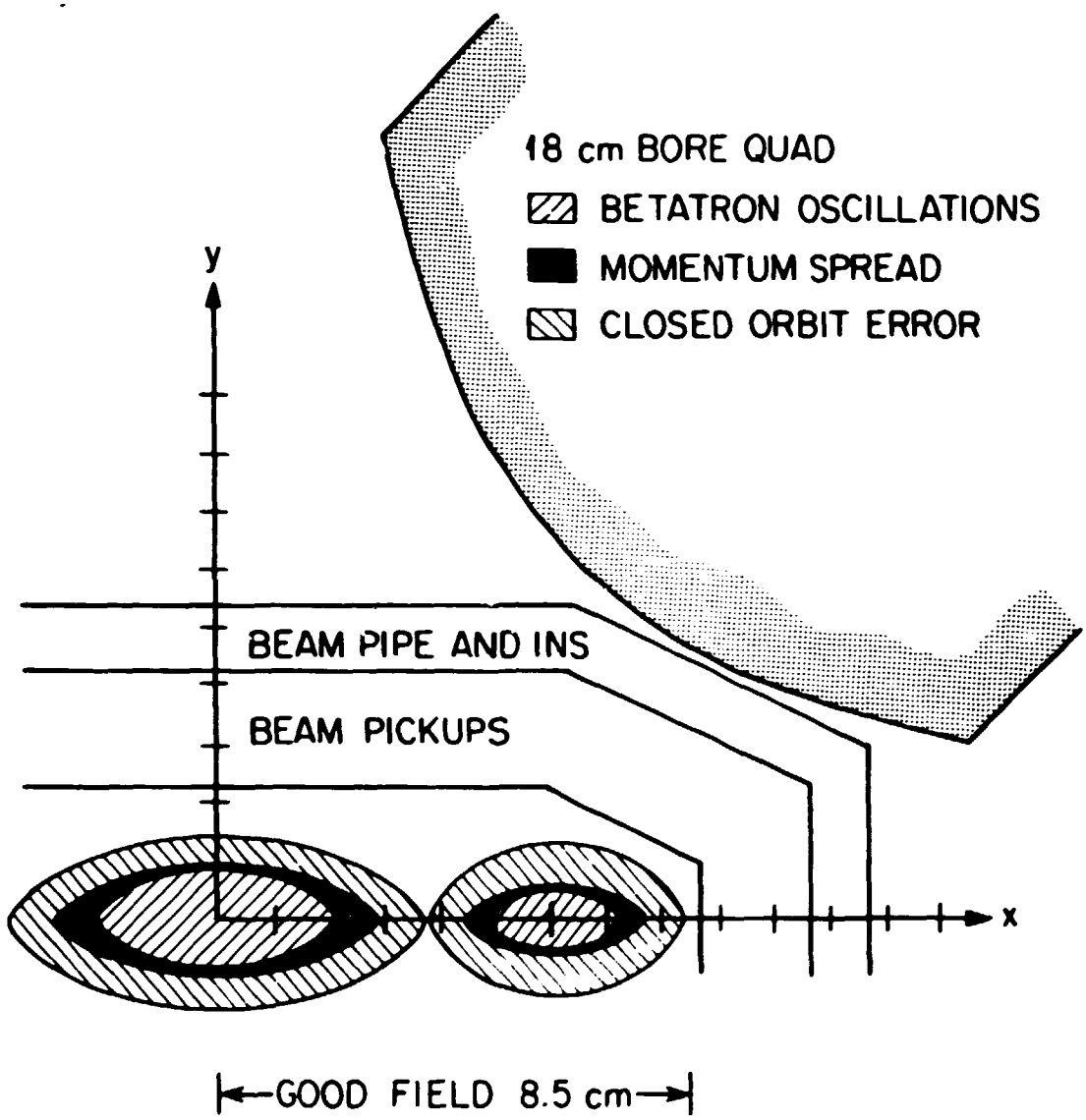

Fig. 4.5-2 Aperture requirement in the F quadrupole. The beam centered at +6.0 cm ($\Delta Q/Q = -4\%$) has $\varepsilon = 13\ \pi$ mm·mrad with $\Delta P/P = 0.1\%$. This beam requires a good field at 8.5 cm which in turn determines the bore of 18 cm and pole-tip width of 15 cm. For comparison, a central beam of $\varepsilon = 40\ \pi$ mm·mrad with $\Delta P/P = 0.3\%$ is also shown.

horizontal good-field requirement. The central beam shown in Fig. 4.5-2 should also have $\epsilon = 13\pi$ mm-mrad with $\Delta P/P = 0.1\%$, but for illustration a beam with $\epsilon = 40\pi$ mm-mrad with $\Delta P/P = 0.3\%$ is shown.

With the design mode at the nominal betatron tunes, the D quadrupoles need to be 13% stronger than the F quadrupoles and require a maximum strength, integrated over the path length, of about 2.8 T. An effective field length of 50 cm requires a gradient near 5.6 T/m and a "pole-tip" field near 5.1 kG. The characteristics of these quadrupoles, with an additional 30% margin to allow considerable flexibility in the choice of the final operating point, are summarized in Table 4.5-3. A very preliminary design of these quadrupoles is illustrated in Fig. 4.5-3, and Fig. 4.5-4 shows a two-dimensional calculation of the gradient uniformity as a function of radius. The pole-tip contour was taken as a hyperbolic curve with straight regions, matched on each end, as shims. These shims were made tangent to the hyperbola at x = 11.03 cm and y = 3.63 cm, and have a thickness of 1.5 mm at the pole-tip ends. These pole tips give a gradient good to $\pm 0.6 \times 10^{-3}$ out to a radius of 9.0 cm for both high and low excitation. The gradient profile for an unshimmed pole is also shown.

Each pole will require a peak current of 265 A for 95 turns. At full excitation, each quadrupole will have a resistive loss of 12.6 kW and a stored energy of 6.0 kJ. As presently designed, the laminations must be assembled into four quadrants. The rectangular pole faces will allow simple racetrack coils to be inserted on each pole. These quadrants will then be assembled into lower and upper halves prior to final assembly around the beam pipe. An effective length of 50 cm will

Table 4.5-3. Quadrupole characteristics

Number	12
Basic Requirements	
Magnetic length	50.0 cm
Bore (inscribed diameter)	18.0 cm
Good-field radius	8.5 cm
Maximum gradient	7.3 T/m
Maximum "pole-tip" field	6.1 kG
Core Characteristics	
Magnet steel length	42.0 cm
Magnet steel height	80.0 cm
Magnet steel width	80.0 cm
Yoke width	10.0 cm
Pole-tip width	15.0 cm
Packing factor	99 %
Core weight	2564 lb
Coil Characteristics	
Number of turns/coil	95
Conductor outside dimensions	0.93 x 0.93 cm^2
Cooling-hole inside diameter	0.52 cm
Conductor area	65.0 mm^2
Average turn length	1.7 m
Total Cu weight	829 lb
Excitation Characteristics	
Peak current	265 A
Peak current density	4.6 A/mm^2
Total coil resistance at 40°C	180 mΩ
I^2R loss for 7.3 T/m flattop	12.6 kW
Stored energy for 7.3 T/m field	6.0 kJ
Inductance	180 mH

require a yoke length of 42 cm. The three-dimensional effects in these quadrupoles will be large. A detailed 3-D design and optimization with some prototype construction will probably be required. Removable end shims with feedback from magnetic measurements will ensure that the required field quality can be obtained.

ORNL-DWG 85-17922

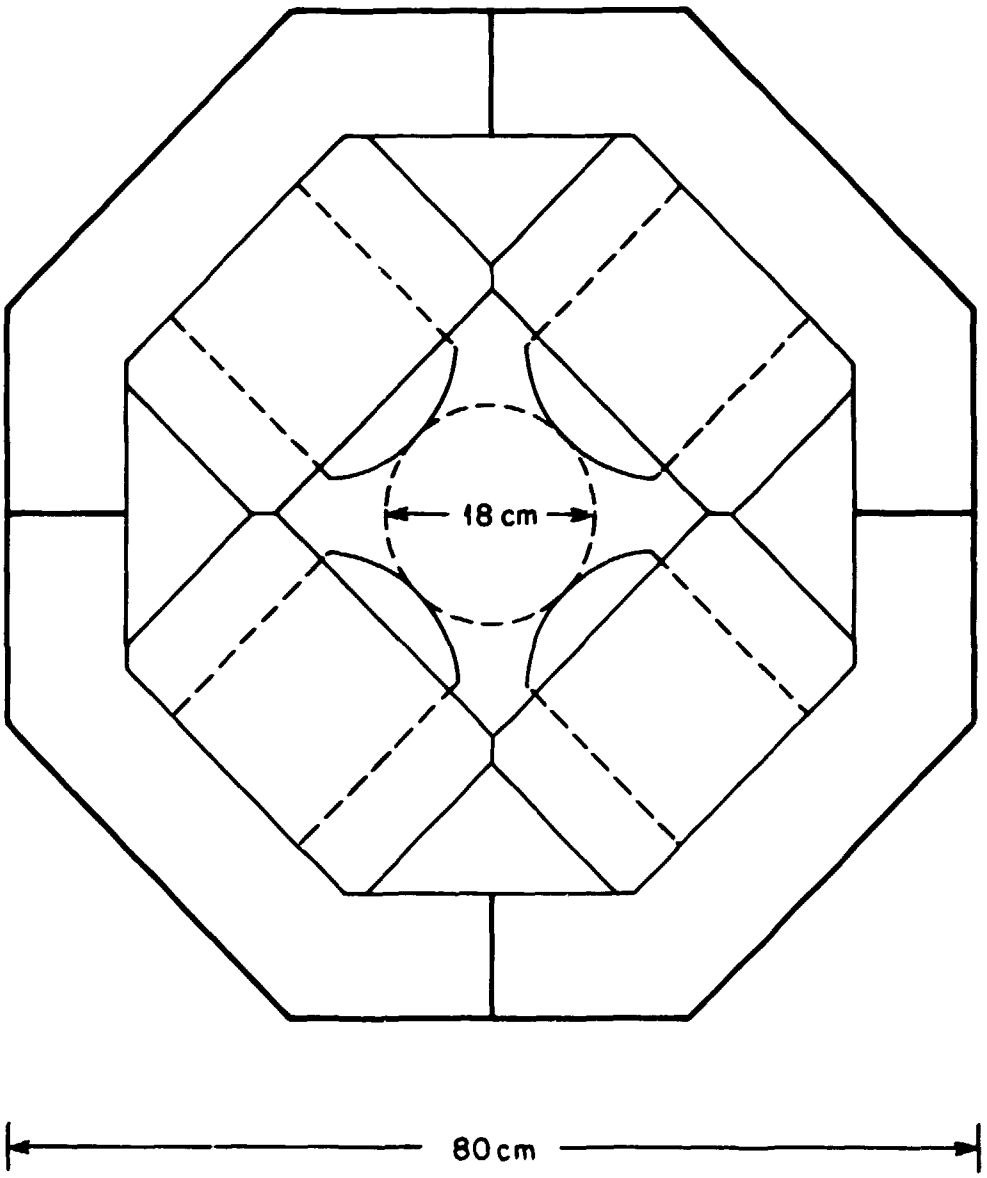

Fig. 4.5-3 Illustration of an 18-cm-bore HISTRAP quadrupole magnet. An effective field length of 50 cm requires an iron core length of about 42 cm.

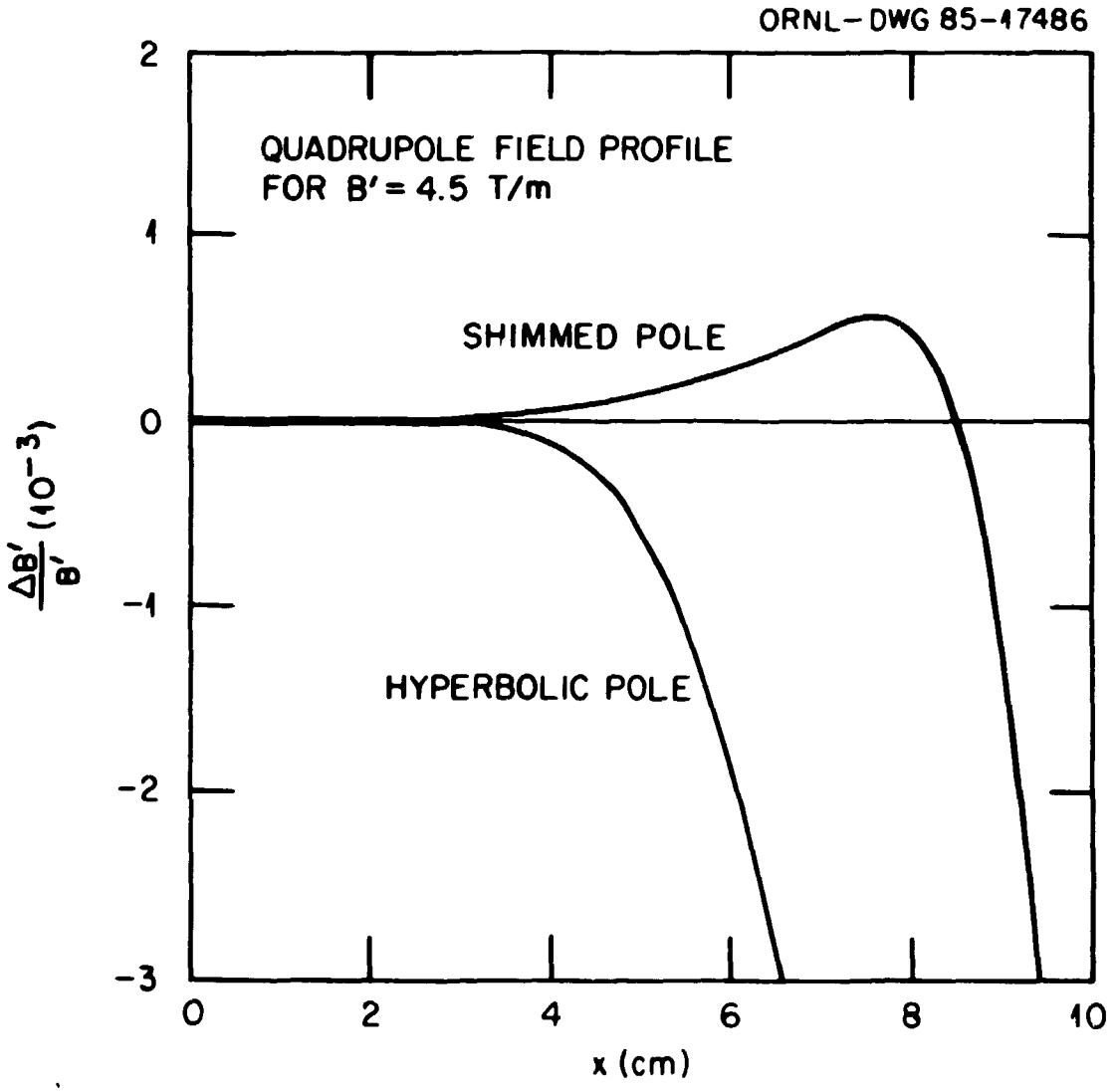

Fig. 4.5-4 Field derivative profile for the HISTRAP quadrupole magnet. A field derivative accurate to $\pm 0.6 \times 10^{-3}$ at a radius of 9.0 cm is obtained at both high and low excitation with 1.5-mm-thick shims.

Sextupoles

HISTRAP has natural chromaticities of $\xi_x = -6.2$ and $\xi_y = -1.5$. The resulting change in horizontal tune for a unit charge change at Q = 25, $\Delta Q/Q = \pm 4\%$, is ± 0.25. If we wish to have $\Delta\nu_x < 0.02$ for all charge states and allow 20% of this spread to be from sextupole error, then we require a sextupole field with a ±2% accuracy. The $\Delta Q/Q = \pm 4\%$ storage mode also requires this accuracy out to a radius of 8.5 cm, as was the case for the quadrupole magnets. The need for a sextupole field accurate to 2% out to a radius of 8.5 cm is a rather severe requirement. Fortunately, the required sextupole field strength is rather low. If the quadrupoles are corrected locally for chromatic effects with sextupoles, the maximum integrated sextupole strength is in the order of $B''L \sim 4$ T/m. Doubling this strength to provide a safety factor requires sextupoles with $B'' = 20$ T/m^2 over an effective length of 40 cm.

A cross section of a sextupole meeting the above needs is shown in Fig. 4.5-5, and its characteristics are listed in Table 4.5-4. The sextupoles have an outside diameter of 60 cm, a bore of 25.5 cm, and a pole-tip width of 5.75 cm. Each pole is wound with 24 turns of the same conductor as used for the quadrupoles. At $B'' = 20$ T/m^2 of excitation, a current of 460 A is needed, giving a resistive loss per magnet of 8.5 kW and stored energy of 1.0 kJ.

Power Supplies

The power supply requirements are dominated by the power converter to drive the dipole magnets. This power converter has been sized at 700 kVA, the approximate level used to drive the BNL NSLS booster dipoles. The requirements for this supply are listed in Table 4.5-5. With the

ORNL-DWG 85-17997

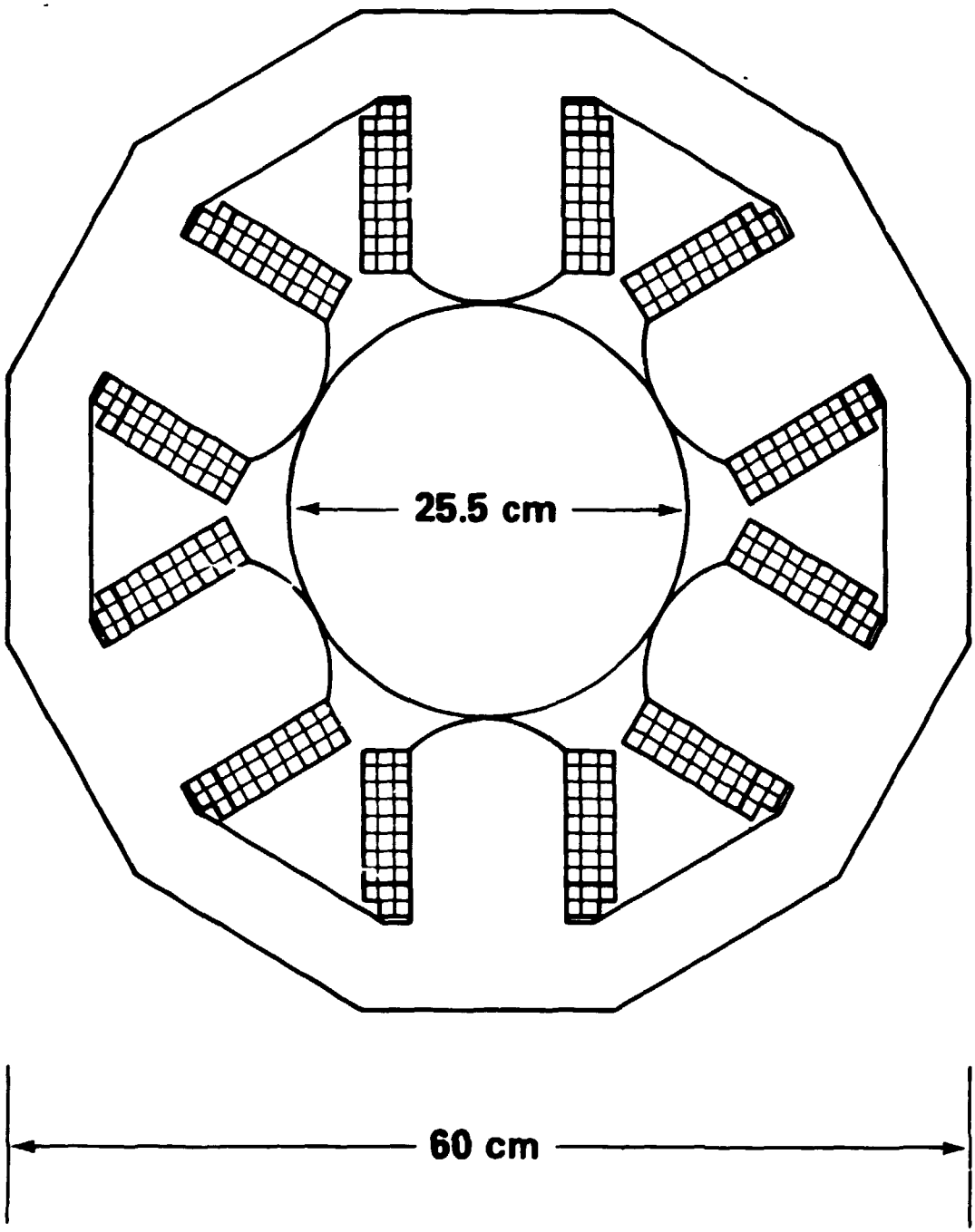

Fig. 4.5-5 Cross section of a 25.5-cm-bore HISTRAP sextupole magnet. An iron yoke length of 30 cm should give an effective field length of about 40 cm.

Table 4.5-4. Sextupole characteristics

Number	16
Basic Requirements	
Magnetic length	~40 cm
Bore (inscribed diameter)	25.5 cm
Good-field radius	8.5 cm
Maximum B"	20 T/m^2
Maximum "pole-tip" field	3.4 kG
Core Characteristics	
Magnet steel length	20.0 cm
Magnet steel height	60.0 cm
Magnet steel width	60.0 cm
Yoke width	5.25 cm
Pole-tip width	9.56 cm
Packing factor	99 %
Core weight	560 lb
Coil Characteristics	
Number of turns/coil	24
Conductor outside dimensions	0.93 x 0.93 cm^2
Cooling-hole inside diameter	0.52 cm
Conductor area	65.0 mm^2
Average turn length	0.84 m
Total Cu weight	155 lb
Excitation Characteristics	
Peak current	460 A
Peak current density	7.0 A/mm^2
Total coil resistance at 40°C	40 mΩ
I^2R loss for 20 T/m^2 flattop	8.5 kW
Stored energy for 20 T/m^2 field	1.0 kJ
Inductance	10 mH

Table 4.5-5. Synchrotron magnet power supplies

Dipoles:	number of supplies	1
	current	2400 A
	voltage	290 V
	resistive load	240 kVA
	inductive load	460 kVA
	total load	700 kVA
	regulation	$\Delta I/I \sim 3 \times 10^{-5}$
	bipolar	
Quadrupoles:	number of supplies	6
	current	265 A
	voltage	210 V
	resistive load	40 kVA
	inductive load	16 kVA
	total load	56 kVA
	regulation	$\Delta I/I \sim 1 \times 10^{-4}$
	bipolar	
Sextupoles:	number of supplies	8
	current	460 A
	voltage	40 V
	resistive load	17 kVA
	inductive load	2 kVA
	total load	19 kVA
	regulation	$\Delta I/I \sim 3 \times 10^{-4}$
	bipolar	
Horizontal Correctors:	number of supplies	8
	current	16 A
	voltage	25 V
	total load	0.4 kVA
	regulation	$\Delta I/I \sim 3 \times 10^{-3}$
	bipolar	
Vertical Correctors:	number of supplies	8
	current	100 A
	voltage	10 V
	total load	1.0 kVA
	regulation	$\Delta I/I \sim 3 \times 10^{-3}$
	bipolar	

eight dipoles connected in series, this 700-kVA supply can drive the inductive load at a rate equivalent to a $\dot{B}$ of the order of 1.7 T/s.

Figure 4.5-6 illustrates various acceleration and deceleration cycles to a maximum dipole field of 1.2 T, assuming a $\dot{B}$ of 1.7 T/s. The top part of Fig. 4.5-6 shows the dipole field for an acceleration cycle with slow extraction to an external beam line. The $\dot{B}$ of 1.7 T/s can ramp the dipoles from the 0.6-T injection level to the 1.2-T level in about 0.45 s. Requiring a 50% experimental duty factor, that is allowing 0.8 s for a slow spill, gives a total cycle time of about 1.6 s. The fill time shown in Fig. 4.5-6 has been lengthened for clarity; the true fill time would be of the order of 1 millisecond. The current, voltage, and power output from the dipole supply over this cycle are illustrated in Fig. 4.5-7. The bottom part of Fig. 4.5-6 shows a typical acceleration cycle for an in-ring experiment with a storage time of one minute. The middle part of Fig. 4.5-6 shows a possible deceleration cycle to a dipole field level of 0.06 T (20 keV/nucleon for $^{197}Au^{40+}$). The time averaged dipole resistive loss for this case would be very small.

Table 4.5-5 also lists the corresponding power supply requirements for the quadrupoles, sextupoles, and dipole correctors. The 12 quadrupoles have been divided into six circuits, and a 10% margin for safety and losses has been included. The 16 sextupoles would be divided into eight circuits. The electrical requirements have been taken directly from Table 4.5-4 without margin, as the sextupoles are designed to have a factor of two reserve in field strength. This margin has been included to allow for uncertainties in the ring chromaticity. These

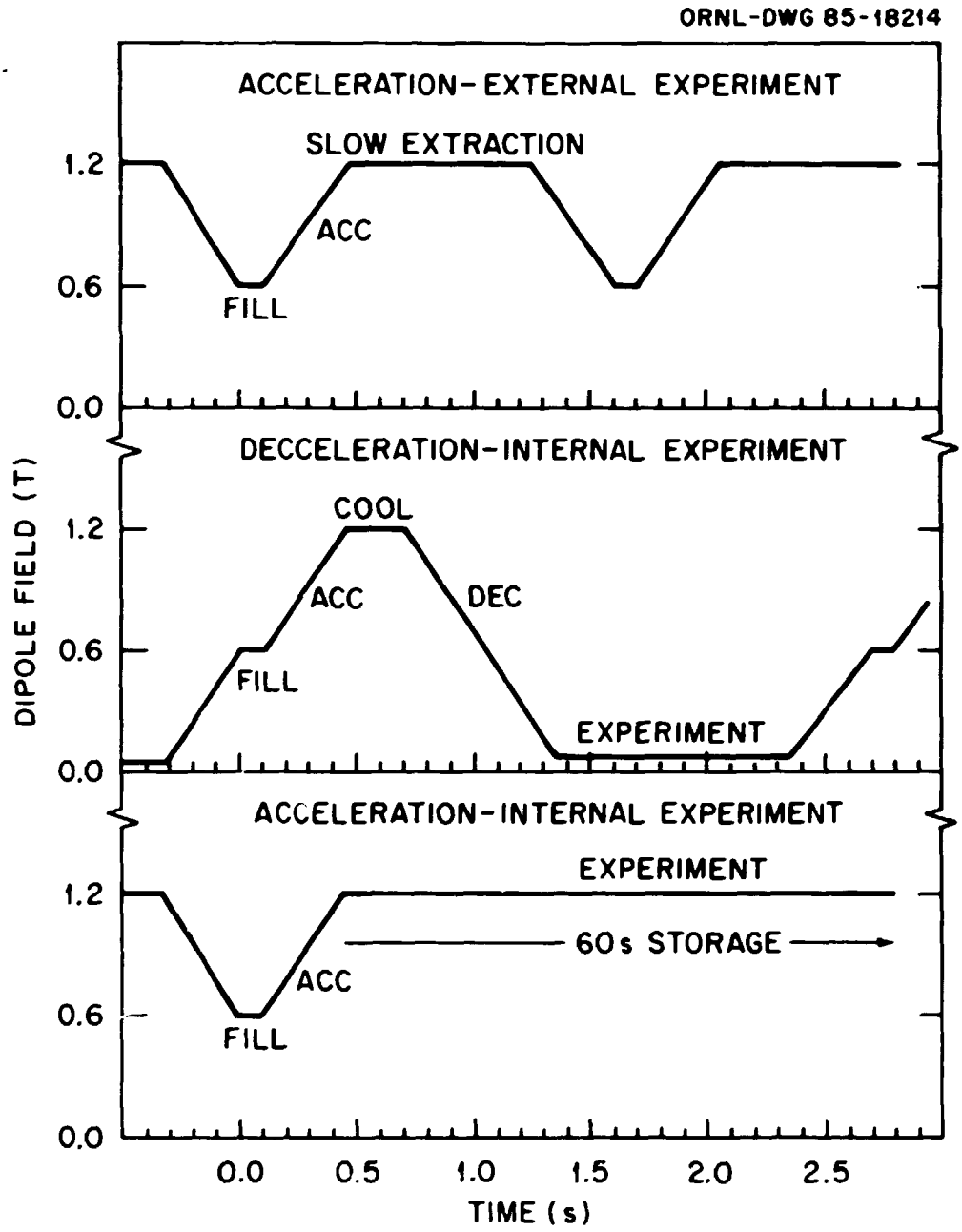

Fig. 4.5-6 Dipole fields levels with time for various possible HISTRAP acceleration and deceleration cycles.

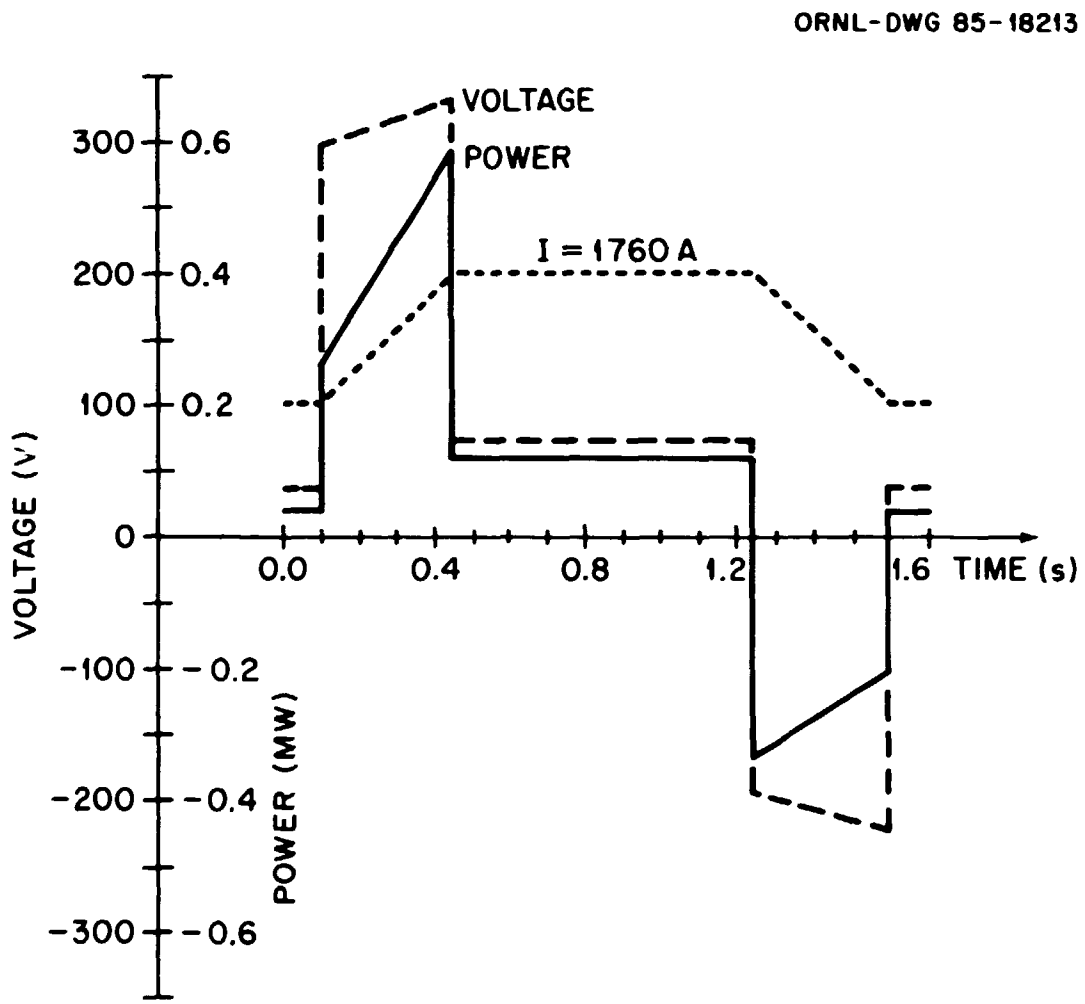

Fig. 4.5-7 The current, voltage, and power requirements for the dipole magnets operated in an acceleration and slow extraction mode.

uncertainties arise from the rather different sextupole strengths predicted by different lattice codes to correct the chromaticity. A careful measurement of the chromaticity will be made as part of the ring commissioning procedure. An approximate estimate of the supplies needed for the dipole correctors has also been listed.

4.5.2 RF System

RF Requirements

A wide-band, ferrite-loaded radio frequency cavity will be used to accelerate and decelerate ion beams in HISTRAP. This rf system must be able to operate over a wide range of frequencies and accelerating voltages. Beams will be injected from either the HHIRF tandem or the dedicated ECR/RFQ injector. Beams will be injected with a variety of charge-to-mass ratios and kinetic energies per nucleon. In addition, the longitudinal phase-space area of the injected beam will depend upon its mass and kinetic energy per nucleon. This is particularly true for post-stripped tandem beams where the stripper foil thickness and resultant induced energy spread depend on the isotope. In contrast, beams injected from the ECR/RFQ will have their longitudinal emittance determined largely by the acceptance of the RFQ and the properties of the debuncher following the RFQ.

The cavity voltage and acceleration phase angle are determined by the desired energy gain per turn and the longitudinal phase space area of the injected beam. The energy gain per turn is given by the equation

$$\Delta E/\text{turn} = (Q/A)\, V \sin\phi_s = \rho C \dot{B} \,, \qquad (4.5\text{-}1)$$

where Q/A is the charge-to-mass ratio, V is the cavity voltage, ϕ_S is the rf phase angle with respect to the beam, ρ is the dipole bend radius in m, C is the ring circumference in m, and $\dot{B}$ is the rate of rise of the dipole field in T/s.

The longitudinal phase space area in eV-sec for an injected beam with energy spread ΔE and circulation frequency f is given by

$$\text{Area} = \Delta E/f = \frac{16N}{h\omega_0}\,\alpha(r)\sqrt{\frac{eV\ (Q/A)(E/A)}{2\pi h\ |\eta|}} \qquad (4.5\text{-}2)$$

where h is the harmonic number, ω_0 is the circulation frequency for an ion moving at the velocity of light, E/A is the <u>total</u> synchronous energy per nucleon, η is the frequency slip factor, $\alpha(r)$ is the usual Symon-Sessler [Bo70] moving bucket factor, and $r = \sin\phi_S$. The factor N was fixed at 0.707 to give a reasonable tradeoff between bucket area margin and cavity voltage. Analysis shows that much of the required cavity voltage is needed to provide bucket area for the injected beam.

The cavity frequency range and voltage were evaluated for eight reference beams and four cases: ring injection from either source, and for both acceleration and deceleration. A tuning range of 13 to 1 in frequency is needed to cover all cases. In order to use the same rf cavity for accelerating light ions, the rf harmonic number must be varied to match requirements for specific cases. Tables 4.5-6 to 4.5-9 list the frequencies, voltages, and synchronous phases for these cases. For these tables, tandem operation at 22 MV was assumed, and the HISTRAP dipoles were ramped at 1.7 T/s to a maximum rigidity of 2.0 Tm.

Several bunching and acceleration simulations have been carried out to illustrate the expected behavior of the longitudinal phase space

Table 4.5-6. Injection from HHIRF Tandem followed by acceleration

Ion species	^{12}C	^{32}S	^{40}Ca	^{58}Ni	^{79}Br	^{127}I	^{197}Au	^{238}U
Charge state	6^+	15^+	18^+	24^+	27^+	36^+	40^+	43^+
Injection energy (MeV/nucleon)	4.0	7.56	6.60	5.31	3.90	2.77	1.90	1.57
Final energy (MeV/nucleon)	47.1	41.5	38.3	32.5	22.3	15.4	7.92	6.28
Harmonic number	1	1	1	1	1	1	1	1
Injection f_{rf} (MHz)	0.592	0.812	0.759	0.682	0.585	0.493	0.409	0.372
Final f_{rf} (MHz)	1.96	1.85	1.78	1.65	1.38	1.15	0.831	0.741
Ratio $(f_{rf})_{final}/(f_{rf})_{injection}$	3.32	2.28	2.35	2.42	2.36	2.33	2.03	1.99
$(\Delta P/P)_{injected}$	10^{-3}	10^{-3}	10^{-3}	10^{-3}	10^{-3}	2×10^{-3}	3×10^{-3}	3×10^{-3}
Bunch area (eV·sec/A)	$1.35\ 10^{-2}$	$1.86\ 10^{-2}$	$1.73\ 10^{-2}$	$1.55\ 10^{-2}$	$1.33\ 10^{-2}$	$2.24\ 10^{-2}$	$2.78\ 10^{-2}$	$2.53\ 10^{-2}$
η	-0.969	-0.961	-0.963	-0.966	-0.969	-0.971	-0.973	-0.974
V_{cavity} (start of ramp) (volts)	266.	328.	318.	305.	294.	469.	697.	668.
ϕ_s (start of ramp) (degrees)	29.9	23.8	24.6	25.7	26.7	16.4	11.0	11.4
ν_s (start of ramp)	$2.11\ 10^{-3}$	$1.75\ 10^{-3}$	$1.84\ 10^{-3}$	$2.0\ 10^{-3}$	$2.28\ 10^{-3}$	$3.54\ 10^{-3}$	$5.29\ 10^{-3}$	$5.68\ 10^{-3}$
$\eta_x \cdot (\Delta P/P)$ (start of ramp) (cm)	0.25	0.22	0.22	0.23	0.23	0.39	0.53	0.54

Table 4.5-7. Injection from HHIRF Tandem followed by deceleration

Ion species	^{12}C	^{32}S	^{40}Ca	^{58}Ni	^{79}Br	^{127}I	^{197}Au	^{238}U
Charge state	6^+	15^+	18^+	24^+	27^+	36^+	40^+	43^+
Injection energy (MeV/nucleon)	4.0	7.56	6.60	5.31	3.90	2.77	1.90	1.57
Final energy (MeV/nucleon)	0.121	0.106	0.098	0.082	0.056	0.039	0.020	0.016
Harmonic number	3	3	3	3	3	4	5	6
Injection f_{rf} (MHz)	1.78	2.44	2.28	2.05	1.75	1.97	2.04	2.23
Final f_{rf} (MHz)	0.310	0.290	0.279	0.256	0.211	0.235	0.212	0.225
Ratio $(f_{rf})_{injection}/(f_{rf})_{final}$	5.74	8.41	8.18	7.98	8.32	8.40	9.62	9.90
$(\Delta P/P)$ after cooling	$1.0\ 10^{-4}$	$1.0\ 10^{-4}$	$1.0\ 10^{-4}$	$1.0\ 10^{-4}$	$1.0\ 10^{-4}$	$1.0\ 10^{-4}$	$1.0\ 10^{-4}$	$1.0\ 10^{-4}$
Bunch area (cooled)(eV•sec/A)	$1.35\ 10^{-3}$	$1.86\ 10^{-3}$	$1.73\ 10^{-3}$	$1.55\ 10^{-3}$	$1.33\ 10^{-3}$	$1.12\ 10^{-3}$	$9.28\ 10^{-4}$	$8.44\ 10^{-4}$
η	-0.969	-0.961	-0.963	-0.966	-0.969	-0.971	-0.973	-0.974
V_{cavity} (start of ramp) (volts)	265.	265.	265.	265.	265.	265.	265.	265.
ϕ_s (start of ramp) (degrees)	30.	30.	30.	30.	30.	30.	30.	30.
ν_s (start of ramp)	$3.65\ 10^{-3}$	$2.64\ 10^{-3}$	$2.83\ 10^{-3}$	$3.16\ 10^{-3}$	$3.69\ 10^{-3}$	$5.06\ 10^{-3}$	$6.84\ 10^{-3}$	$8.24\ 10^{-3}$
$\eta_x \cdot (\Delta P/P)$ (start of ramp) (cm)	0.14	0.10	0.11	0.11	0.12	0.11	0.10	0.10

Table 4.5-8. Injection from the ECR/RFQ followed by acceleration

Ion species	^{12}C	^{32}S	^{40}Ca	^{58}Ni	^{79}Br	^{127}I	^{197}Au	^{238}U
Charge state	6^+	15^+	15^+	19^+	21^+	26^+	33^+	37^+
Injection energy (MeV/nucleon)	0.25	0.25	0.25	0.25	0.25	0.25	0.25	0.25
Final energy (MeV/nucleon)	47.1	31.3	26.8	20.5	13.5	8.05	5.40	4.65
Harmonic number	2	2	2	2	2	2	2	2
Injection f_{rf} (MHz)	0.298	0.298	0.298	0.298	0.298	0.298	0.298	0.298
Final f_{rf} (MHz)	3.93	3.24	3.01	2.65	2.16	1.68	1.37	1.28
Ratio $(f_{rf})_{final}/(f_{rf})_{injection}$	13.2	10.9	10.1	8.86	7.25	5.62	4.61	4.28
$(\Delta P/P)_{injected}$	$5.0\ 10^{-3}$	$5.0\ 10^{-3}$	$5.0\ 10^{-3}$	$5.0\ 10^{-3}$	$5.0\ 10^{-3}$	$5.0\ 10^{-3}$	$5.0\ 10^{-3}$	$5.0\ 10^{-3}$
Bunch area (eV•sec/A)	$1.84\ 10^{-2}$	$1.84\ 10^{-2}$	$1.84\ 10^{-2}$	$1.84\ 10^{-2}$	$1.84\ 10^{-2}$	$1.84\ 10^{-2}$	$1.84\ 10^{-2}$	$1.84\ 10^{-2}$
η	-0.976	-0.976	-0.976	-0.976	-0.976	-0.976	-0.976	-0.976
V_{cavity} (start of ramp) (volts)	419.	459.	476.	507.	562.	646.	723.	757.
ϕ_s (start of ramp) (degrees)	18.4	16.8	16.2	15.1	13.6	11.8	10.6	10.1
ν_s (start of ramp)	$1.43\ 10^{-2}$	$1.51\ 10^{-2}$	$1.54\ 10^{-2}$	$1.59\ 10^{-2}$	$1.68\ 10^{-2}$	$1.81\ 10^{-2}$	$1.92\ 10^{-2}$	$1.96\ 10^{-2}$
$\eta_x \cdot (\Delta P/P)$ (start of ramp) (cm)	1.01	0.98	0.97	0.95	0.93	0.90	0.88	0.87

Table 4.5-9. Injection from the ECR/RFQ followed by deceleration

Deceleration will require, for injection from the ECR + RFQ, a prior acceleration followed by a cooling period, then the deceleration. Accordingly, the rf parameters will be similar to the case of tandem injection followed by deceleration. The principal difference will be in the rf frequency, which is quoted here, always assuming cooling at a kinetic energy of 2 MeV/nucleon.

Ion species	^{12}C	^{32}S	^{40}Ca	^{58}Ni	^{79}Br	^{127}I	^{197}Au	^{238}U
Charge state	6^+	13^+	15^+	19^+	21^+	26^+	33^+	37^+
Injection energy (MeV/nucleon)	2.0	2.0	2.0	2.0	2.0	2.0	2.0	2.0
Final energy (MeV/nucleon)	0.121	0.080	0.068	0.052	0.034	0.020	0.014	0.012
Harmonic number	3	3	3	3	4	5	6	6
Injection f_{rf} (MHz)	1.26	1.26	1.26	1.26	1.68	2.10	2.52	2.52
Final f_{rf} (MHz)	0.310	0.252	0.232	0.203	0.219	0.210	0.211	0.195
Ratio $(f_{rf})_{initial}/(f_{rf})_{final}$	4.06	4.99	5.41	6.19	7.66	9.98	11.93	12.91

in HISTRAP. Results for a tandem-injected $^{197}Au^{40+}$ beam are shown in Figs. 4.5-8 to 4.5-12. For these simulations, 801 ions were tracked. In these figures, NB = number of turns for bunching, NA = number of turns for acceleration, VC = cavity voltage, H = harmonic number, ϕS = synchronous phase angle, EO = MeV/nucleon of synchronous ion, and F = MHz of the cavity.

Adiabatic bunching must be used to avoid beam loss during capture in rf buckets prior to acceleration. This is illustrated in Fig. 4.5-8, which shows the adiabatic bunching of a tandem-injected 1.9-MeV/nucleon $^{197}Au^{40+}$ beam when the rf amplitude is ramped linearly from 0 to 697 volts in 6970 turns. All the beam is captured and the beam phase space area is less than the rf bucket area at the end of the 17-ms bunching operation. The beam was injected with an rms energy spread of 0.15%. Figure 4.5-9 shows that almost all of the beam is captured when the rf phase angle is shifted to 10.9° for acceleration. In these simulations, phase angles are shifted instantaneously for acceleration; in actual practice, the shift will probably be gradual. In any case, the rf cannot be turned off for more than a few microseconds since the beam will completely debunch in 200 to 400 μs under normal conditions. As acceleration occurs, the ratio of the rf bucket area to the beam phase space area remains constant.

Figures 4.5-10, 4.5-11, and 4.5-12 illustrate the bunching, capture, and deceleration of a tandem-injected 2.0-MeV/nucleon $^{197}Au^{40+}$ beam which is assumed to have been cooled to an rms energy spread of 0.02%. The beam is bunched by ramping the rf voltage from 0 to 265.5 volts in 26547 turns. This slower 65-ms bunching is required to keep

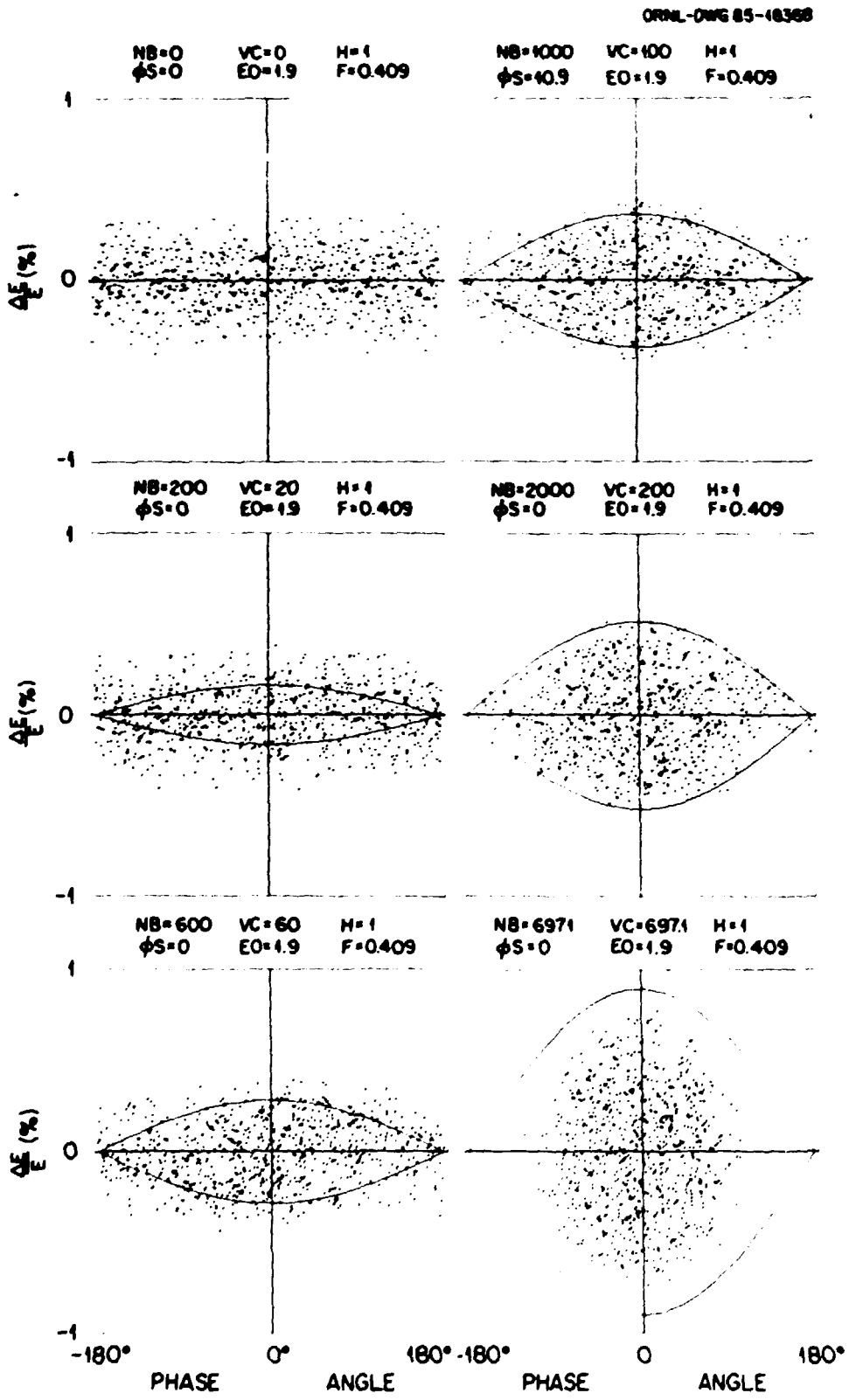

Fig. 4.5-8 Bunching simulation for $^{197}Au^{40+}$ ions with an rms energy spread at injection of 0.15% and an adiabatic voltage turn-on.

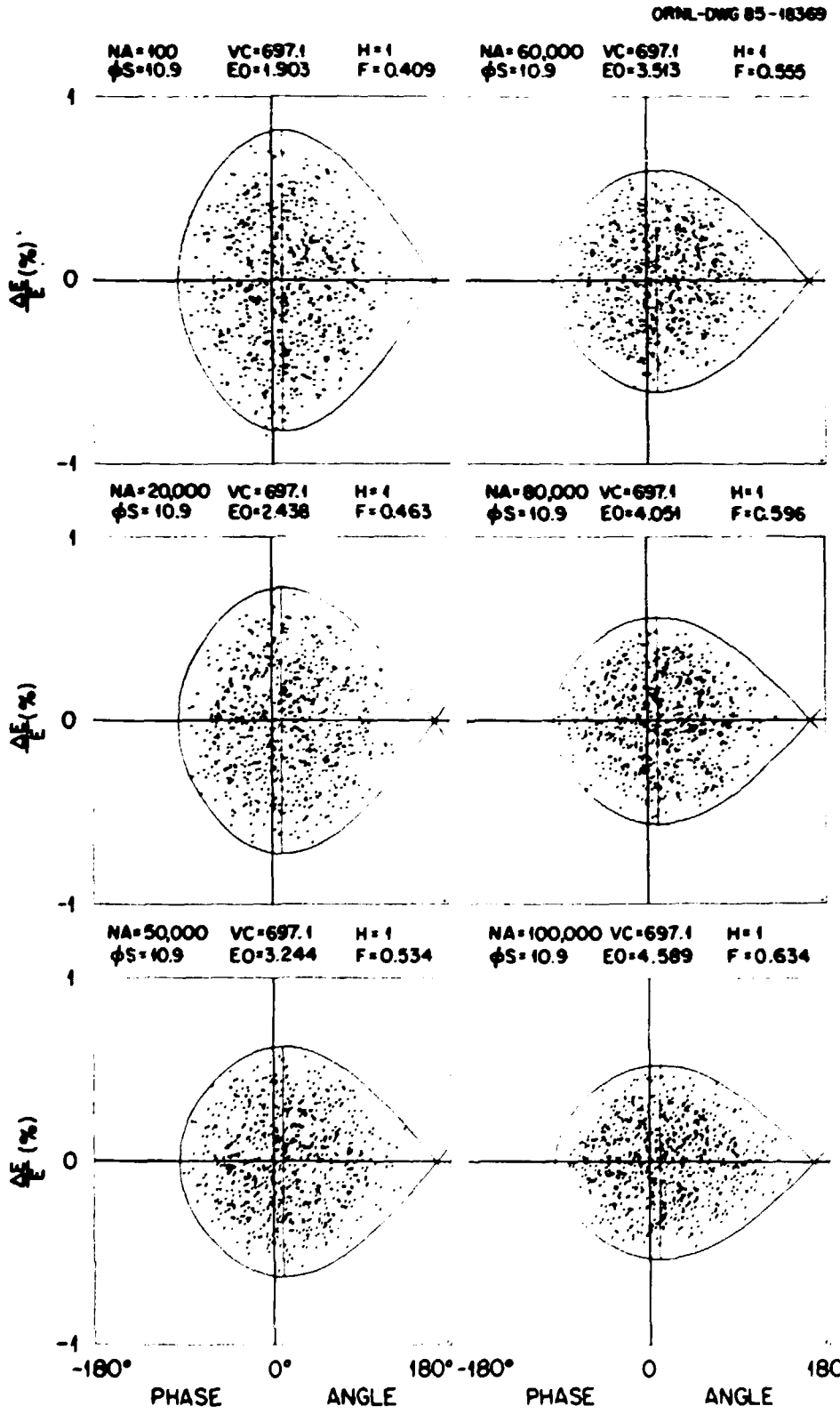

Fig. 4.5-9 Acceleration simulation for $^{197}Au^{40+}$ ions following the adiabatic bunching process of Fig. 4.5-8.

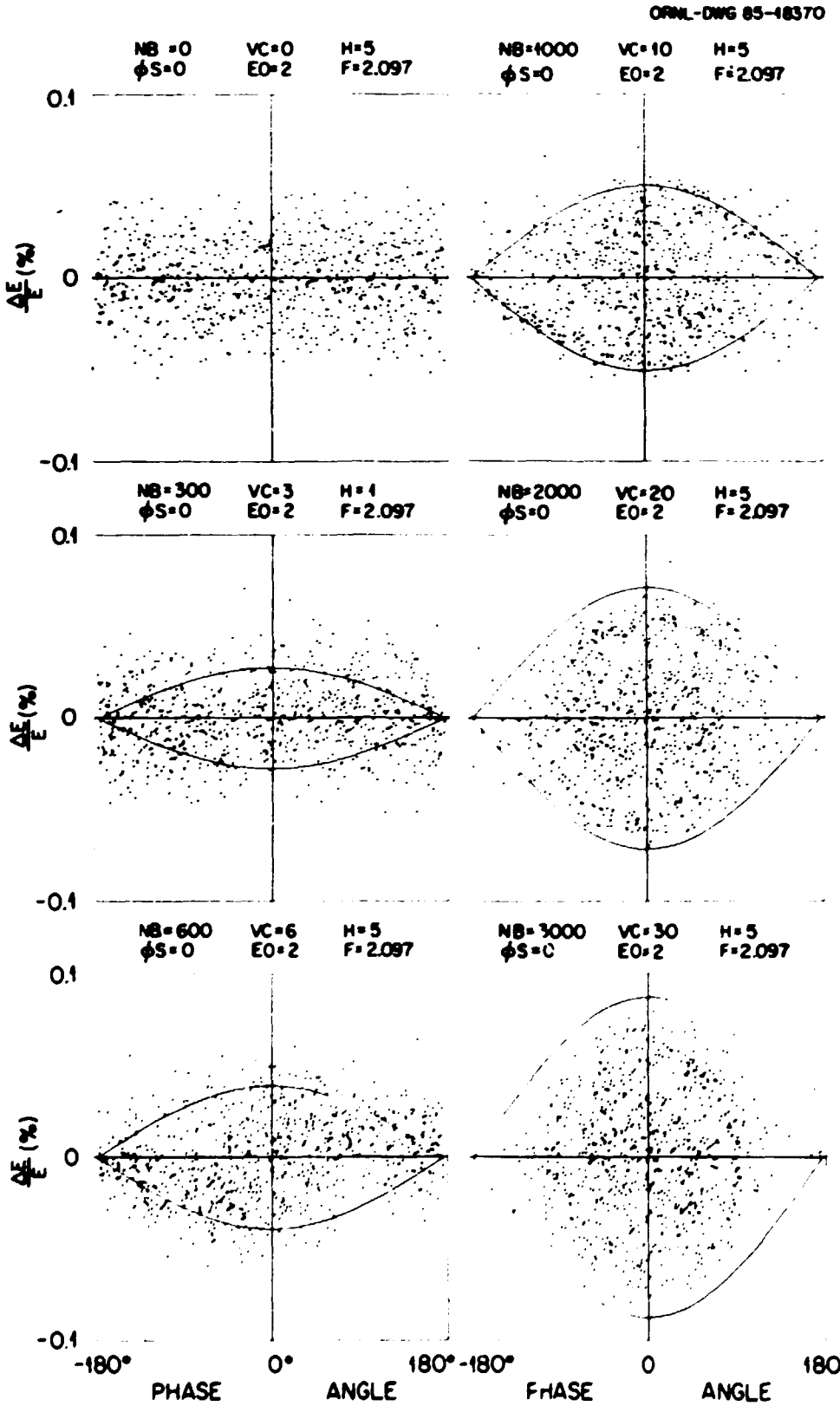

Fig. 4.5-10 Bunching simulation for $^{197}Au^{40+}$ ions with an rms energy spread of 0.02%. This energy spread would be obtained with cooling.

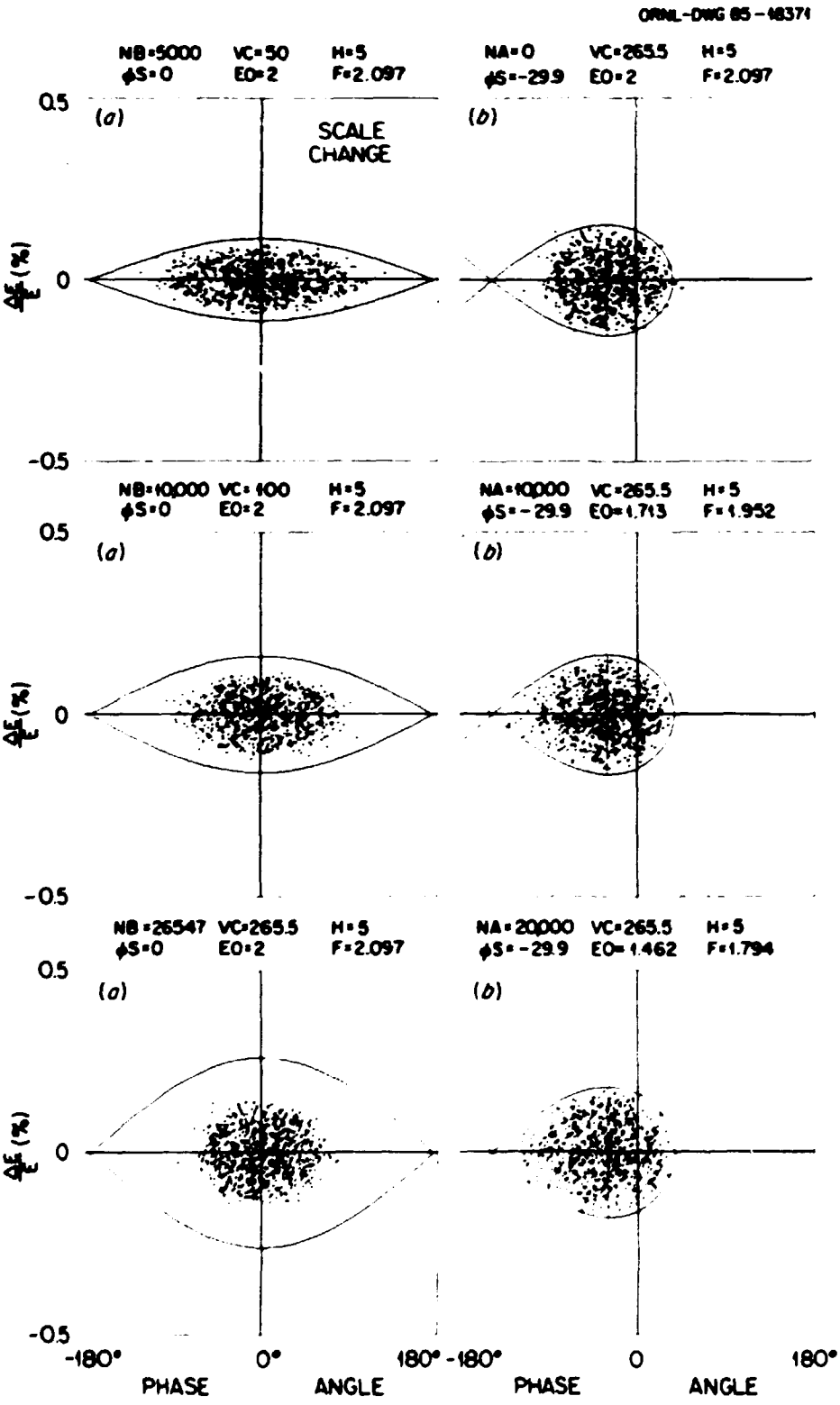

Fig. 4.5-11 (a) Continuation of the bunching of the cooled beam of Fig. 4.5-10. Note the scale change. (b) Deceleration simulation for $^{197}Au^{40+}$ ions following the bunching process of the cooled beam.

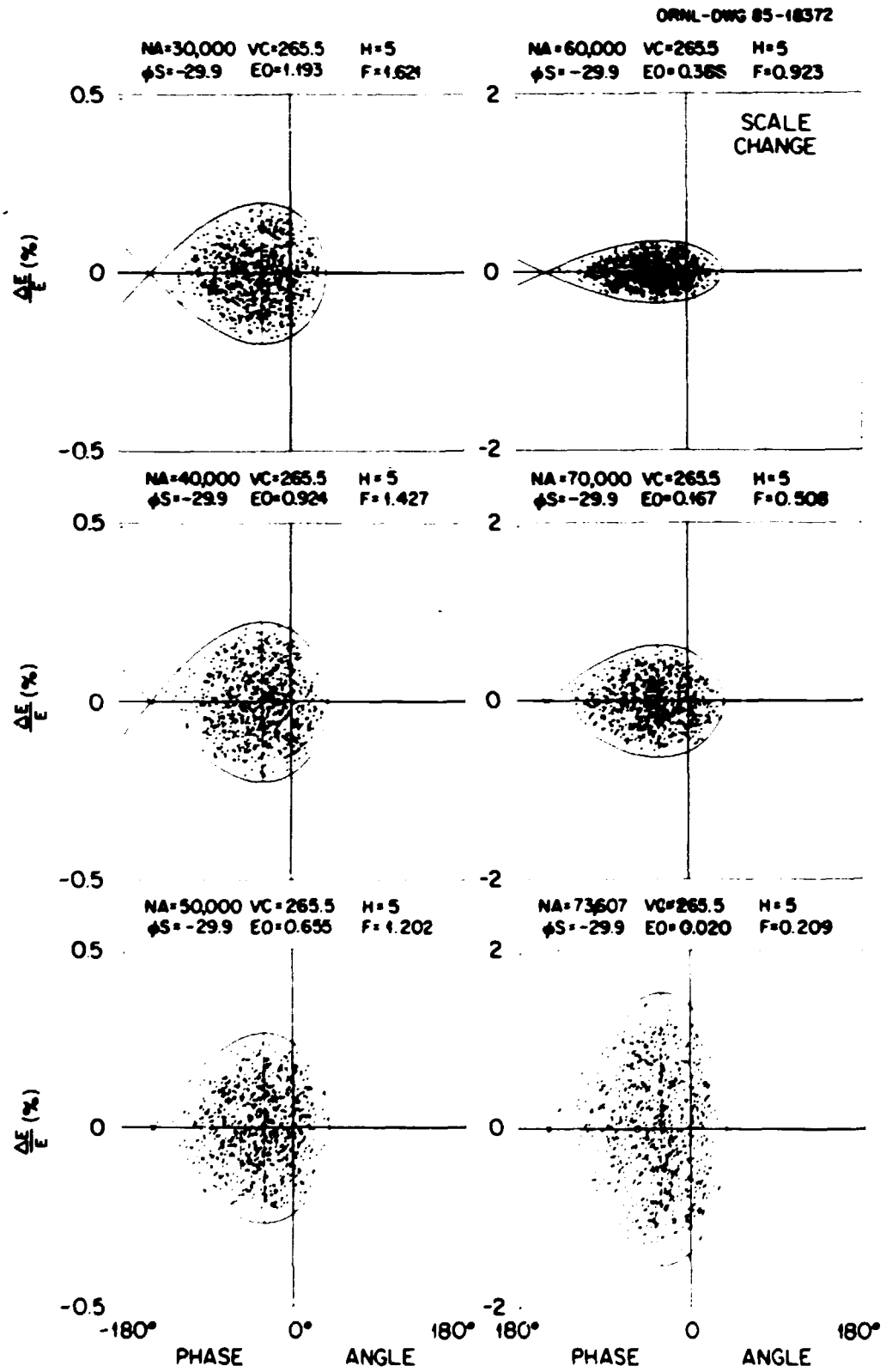

Fig. 4.5-12 Continuation of the deceleration process of the cooled beam of Fig. 4.5-11.

the bucket beam energy spread as small as the initial energy spread in the injected beam. Note that the beam has been allowed to debunch fully during the cooling period. Harmonic number 5 was chosen in order that the cavity frequency be in the range of 0.20 to 2.10 MHz for a full deceleration from 2.0 to 0.020 MeV/nucleon. For all interesting cases, a cavity with a maximum voltage of 2.5 kV per turn operating between 0.2 and 2.6 MHz was adequate. The required rf cavity parameters are listed in Table 4.5-10.

RF Cavity

In order to meet the requirements of Table 4.5-10, a ferrite-loaded, half-wavelength, coaxial resonator was chosen with figure-eight bias windings. This cavity is very similar to the BNL AGS design and the Saclay Saturne design. Since it is desirable to have an rf cavity with a tuning range which can sweep through a 13:1 frequency ratio without switching the acceleration harmonic number, the accelerating system is based upon the use of MnZn ferrite, which is noted for its wide permeability range. This ferrite selection restricts the practical tuning range of the rf system to a maximum frequency of about 3 MHz. An initial set of system parameters which meet the above criteria are listed in Table 4.5-11.

Except for the ferrite, the components of the rf system involve well developed technology. The cavity, rf conductors, and ferrite bias current conductors will be fabricated from copper. The beam tube will be a separable structure of stainless steel with alumina ceramic accelerating gap. The accelerating gap will be part of the beam line and will be connected to the resonant cavity by spring finger contacts. The

Table 4.5-10. HISTRAP rf system requirements

Tuning range	0.2 to 2.6 MHz
Acceleration voltage per turn	2500 volts
Maximum accelerating system length	1.2 meters
Nominal beam tube aperture	0.15 meters

Table 4.5-11. rf cavity characteristics

Peak rf voltage	2500 volts
Tuning range	0.2 to 2.6 MHz
Overall length	1.2 meters
Beam tube ID	0.15 meters
Ferrite rings	
Material	TDK SY7
ID	0.3 meters
OD	0.5 meters
thickness	0.025 meters
number	28
Cooling for ferrite	Water
Ferrite peak power density	200 mW/cc
Total peak rf drive power	20 kW
Ferrite permeability range	8 to 1400
Peak ferrite bias current	3000 ampere turns
Shunt capacitance	6000 pF

beam tube will be wrapped with heater blankets for in situ baking at 300°C each time it is exposed to air. The space between the inner and outer cavity conductors will be filled with 28 30-cm-ID, 50-cm-OD, 2.5-cm-thick ferrite rings. These ferrite rings will be separated by water-cooled copper plates. At full power, the temperature of the ferrite will rise, at most, a few degrees. Water cooling will also be provided on the inner conductors of the cavity to stabilize the cavity temperature whenever the beam tube is being baked at 300°C.

Cavity tuning will be accomplished entirely through magnetically biasing the ferrite inductors with up to five figure-eight windings. These windings can be configured in any parallel or series combination to suppress any parasitic resonances, as needed. The ferrite rings will be TDK type SY7, or equivalent, similar to those fabricated for tests and measurements in the Brookhaven AGS-booster development program. This ferrite has an initial permeability value of about 1800. About 3000 A-turns of bias current is required for tuning the bias permeability to 18, as is required at the upper end of the cavity's frequency range. The resonant structure requires a total of 28 ferrite rings for 2.5 kV. Each ring weighs about 17 kg, and the total ferrite inventory is 476 kg. The peak ferrite power density has been measured by BNL to be about 65 mW/cc, giving at total rf drive power of 5800 W for the HISTRAP cavity. To normalize the frequency to the range between 0.2 and 2.6 MHz will require about 15,000 pF of capacitive loading across the gap.

The rf drive signal will be derived from a programmable sweep frequency signal generator. Reference signals will be a combination of

computer generated information with analog corrections from the main dipole field, intensity sensor, and beam position. The drive signal will be followed by an amplitude modulator and a broadband power amplifier. The amplifier will have to deliver about 6 kW of rf power to the cavity for the full 2.5-kV gap voltage under something less than optimum impedance matching conditions. Therefore, the amplifier and the transmission lines to the cavity should be somewhat oversize and a nominal 10-kW level appears adequate.

The rf system will require a tie-in to the main accelerator control system. The computer will provide some fundamental operation data and control signals for setting sweep frequency span, accelerating voltage, frequency sweep rate, and initial ferrite program. Feedback circuitry will update the control programs so as to track with the dipole field strength resulting from the dipole control program. Feedback from the rf cavity and actual beam position data will fine-tune the rf amplitude and phase as appropriate for beam stability.

Cavity tuning will be accomplished entirely through magnetically biasing the ferrite inductors. The bias power supply will be a commercially built unit with programmable current control. An analog correction signal will be obtained from the phase error between the accelerating gap voltage and the power amplifier output. The bias driver will be a programmable power supply or high power operational amplifier with sufficient bandwidth to permit ramping linearly from zero to full output in less than about 0.5 s. The peak output ratings for a three-turn configuration are a current of 1000 A, a voltage of 50 V, and a nominal power of 50 kW. A ferrite testing program has been initiated

and a prototype rf cavity has been built. This work is discussed in Section 5.2.

4.5.3 Vacuum System

Vacuum Requirements

The vacuum requirement to accelerate, decelerate, and store highly-charged, very-heavy ions is severe. Such ions passing through residual gas can either capture electrons from gas molecules or lose electrons by colliding with gas molecules. Such charge-changing collisions alter the magnetic rigidity of the ion, causing it to be lost. In addition, the ions may undergo multiple small-angle Coulomb collisions with gas molecules, causing an increase in beam emittance and eventual beam loss when the ions can no longer be contained within the HISTRAP acceptance. The greatest loss of beam arises from charge-changing collisions.

Estimates of beam lifetimes in HISTRAP from charge-changing collisions were made using the electron capture cross sections of Schlacter [Sc84] and electron loss cross sections of Alonso and Gould [Al82]. The vacuum requirements resulting from these calculations for a tandem-injected Au^{40+} beam, one of the worst cases, are summarized in Figs. 4.5-13 and 4.5-14. Figure 4.5-13 shows single-electron capture and single-electron loss cross sections for Au^{40+} ions incident on atomic hydrogen as a function of kinetic energy. The straight lines show the electron loss or capture cross sections which give a 90% survival of the beam after a one-second coast at the pressure indicated above the lines. Electron capture is the dominant loss mechanism at low energies. In particular, at 100 keV/A, the capture cross section is 2×10^{-14} cm^2 and

ORNL-DWG 85-17983

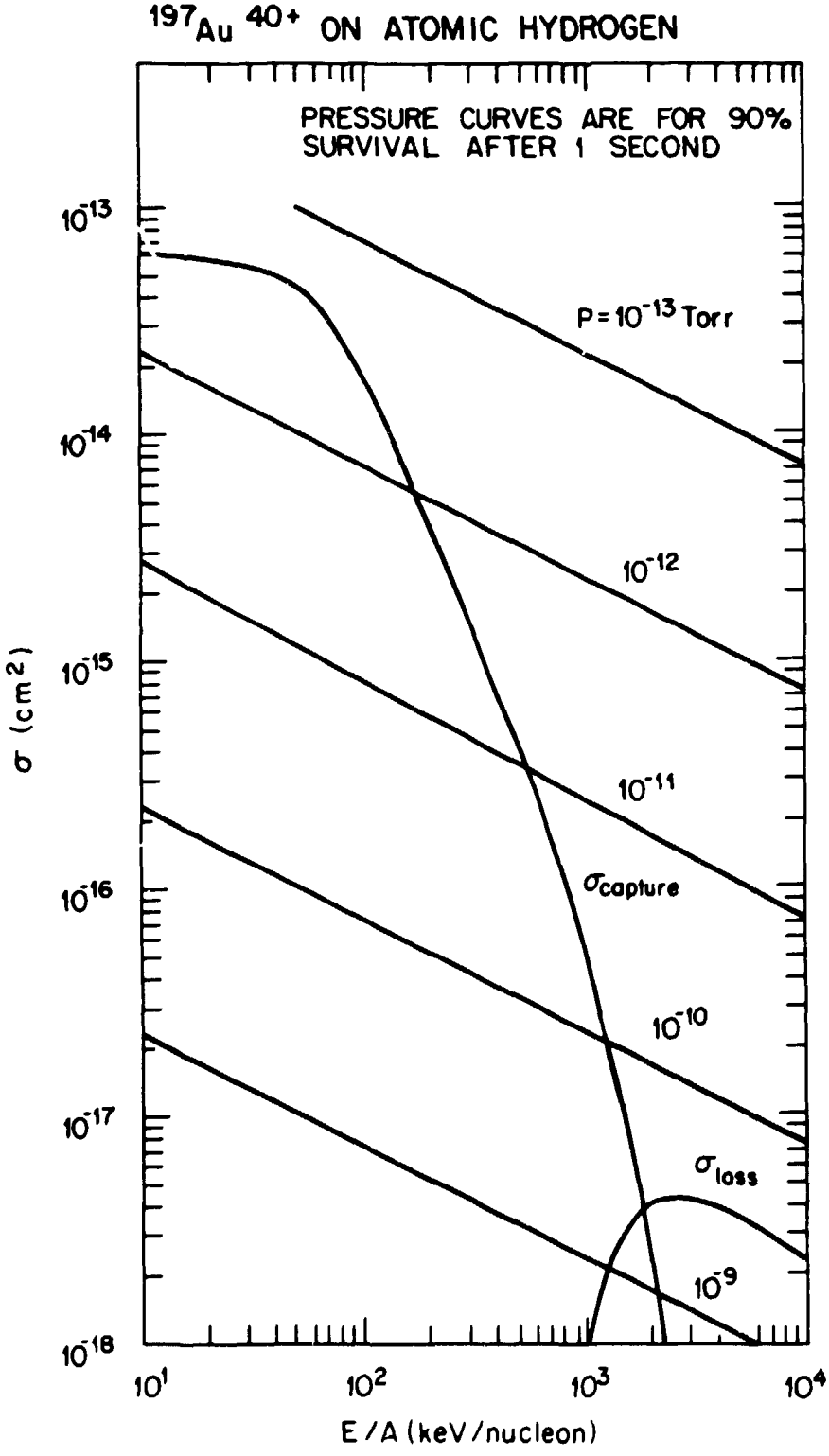

Fig. 4.5-13 Single-electron capture and single-electron loss cross sections for Au ions incident on atomic hydrogen as a function of energy. The straight lines show the total cross section which gives a 90% survival of beam after a one-second coast at the indicated pressures.

ORNL-DWG 85-18504

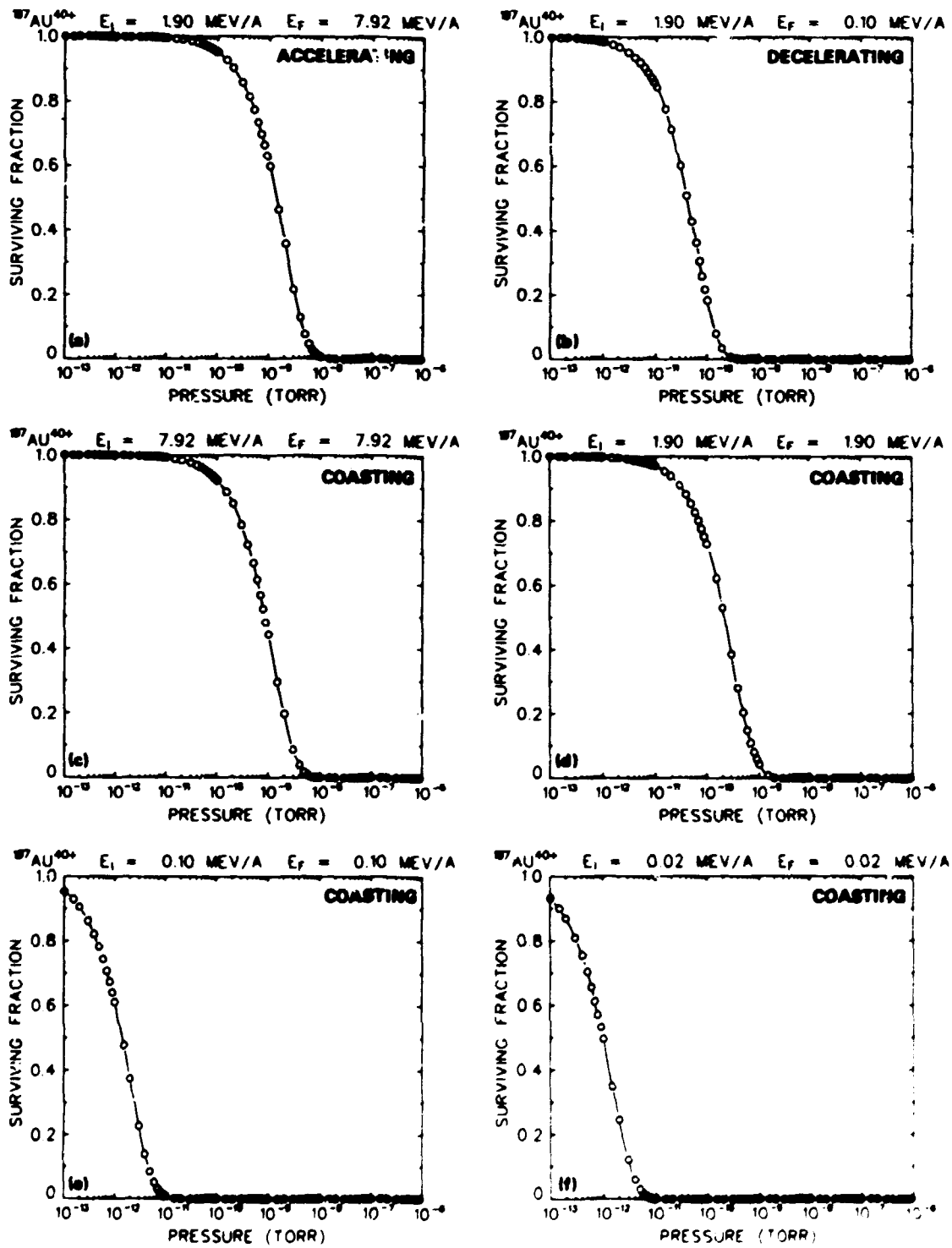

Fig. 4.5-14 The surviving fraction for tandem-injected Au beams as a function of vacuum system pressure for various HISTRAP operating cycles. The residual gas was assumed to be 90% H_2 and 10% N_2. EI and EF are the initial and final kinetic energies per nucleon, respectively.

the Au^{40+} ions would require a vacuum of 2×10^{-12} Torr to have a 90% survival fraction after one second of storage. Figure 4.5-14 shows the survival fraction as a function of HISTRAP chamber pressure for various cycles with Au^{40+} ions in a residual gas of 90% H_2 and 10% N_2. The upper panels are for acceleration from 1.9 to 7.9 MeV/A and for deceleration from 1.9 to 0.10 MeV/A. The remaining panels are for one-second coasts (storage times) at 7.9, 1.9, 0.10, and 0.02 MeV/A. With a vacuum pressure of 1×10^{-12} Torr, about 50% of a coasting 20 keV/A Au^{40+} beam would be lost in one second. For acceleration and storage at high energies, pressures of the order of 5×10^{-10} Torr are acceptable.

Vacuum Hardware

In general, the HISTRAP vacuum system will be conductance limited and will have a conductance similar to that of 10-cm ID pipe. A pressure of 1×10^{-12} Torr can be achieved in a 10-cm-ID beam pipe if (1) the pipe material has a specific outgassing rate of 1×10^{-13} Torr-L/cm^2/s, and (2) the pipe has 1000-L/s pumps placed every 1.5 m along its length. HISTRAP has a circumference of 46.8 m, and under these circumstances, about 32 1000-L/s pumps will be required. The HISTRAP vacuum system will have a total surface area of about 20 m^2.

Vacuum chambers with surface outgassing rates in the order of 1×10^{-13} Torr-L/cm^2/s can be fabricated from 304/316 series stainless steel. These steels contain interstitial hydrogen at a level of a few ppm, which gives rise to an outgassing rate greater than 10^{-12} Torr-L/cm^2/s. This hydrogen outgassing rate can be reduced by an order of magnitude by vacuum firing the chamber at 950°C for about an hour [Ca67]. In addition to reducing the hydrogen outgassing rate, the 950°C

bake provides a completely clean surface, since all hydrocarbons are cracked. Flanges from 316-LN stainless steel are required, to assure sharp knife edges are retained following several high-temperature bakes. All dipole chambers, quadrupole chambers, beam pipes, septa chambers, EBC chambers, etc., will be fabricated from such material. To reduce eddy current effects during fast ramps, dipole chambers with a wall thickness of 0.3 mm will be employed. In addition, a small amount of alumina ceramic will be needed for bump-magnet chambers, rf gaps, torrid gaps, and feedthroughs. Other vacuum materials will be strictly minimized.

The ultrahigh vacuum system must extend along the injection line to the point at which the beam has a double waist. At this point, a vacuum aperture will be installed in order to separate the ring vacuum from beam line vacuum. All components will be designed and tested to withstand a 350°C in situ bakeout. Chambers will be encased in fitted heater blankets of ceramic wool containing embedded heating elements and thermocouples. All flanges will be of the Conflat type with a silver-plated copper gasket. Eight 6-inch, all-metal gate valves are provided to separately isolate the four arcs and four straight sections. In addition, a metal-seal, 4-inch roughing valve is provided in each octant. The roughing system will consist of a three-stage cryosorption pump and a 6-inch cryogenic pump. The use of cryosorption pumps for roughing will eliminate all hydrocarbons. A combination of magnetic sputter ion pumps, titanium sublimator pumps (TSPs), and nonevaporable getter pumps will be used. The TSPs will pump hydrogen and other active gases, whereas the ion pumps at low pressures will be a net source of hydrogen,

but will pump inert gases. The getter strips will be used for space-limited situations. In particular, each octant of the ring will be equipped with about two 60-L/s sputter ion pumps and about four 1000-L/s TSPs. In addition, three 500-L/s sputter ion pumps and fourteen non-evaporable getter pumps with a total speed of 7000 L/s will be used in the electron cooler section. Each ion pump will have its own power supply, whereas only a few power supplies are required for the TSPs.

Measurement of pressures below 10^{-11} Torr is hampered by X-ray emission in standard Bayard-Alpert gauges. Consequently, ionization gauges of the extraction type will be used. Nine of these will be distributed about the ring, each with its own controller. To analyze the contents of the chamber, a residual gas analyzer will be used. Four gauge tubes will be made a permanent part of the ring vacuum system.

The major components of the vacuum system are summarized in Table 4.5-12 Much of the physics program can be carried out with pressures of 10^{-10} to 10^{-11} Torr. Given attention to bakeability, material selection, and use of localized high-speed pumps, the system should experience no particular problems attaining 10^{-11} Torr. The principal difficulty expected in attaining 10^{-12} Torr will be in obtaining materials with the required low outgassing rates. An experimental vacuum program has been started with the construction of an ultrahigh vacuum test stand. This test stand has been used to test chamber materials and treatments, pumps, gauges, and other components. A discussion of this work is given in Section 5.1.

Table 4.5-12. Vacuum system components

Design pressure:	10^{-12} Torr
Design specific outgassing:	10^{-13} Torr L/cm^2/s
In situ baking temperature:	350°C
Major material of construction:	304/316 SS vacuum prebaked at 950°C

Pumps:

32 1000-L/s titanium sublimator pumps in the ring
16 60-L/s magnetic sputter ion pumps in the ring
3 500-L/s magnetic sputter ion pumps in the EBC
14 500-L/s getter pumps in the EBC
1 turbo/cryogenic rough pump cart

Valves:

8 all-metal beam line valves, 6-in. ID
8 all-metal right-angle valves, 4-in. ID

Pressure gauges:

9 extraction ionization gauges
4 residual gas analyzer gauges, 1 controller

4.5.4 Electron Beam Cooling System

Electron Beam Cooling

Ways of improving charged-particle beam quality in storage rings have become of considerable interest. The fundamental quality parameter which describes the beam is the phase-space density. In an ideal situation this density is conserved (Liouville's theorem), but in reality, it decreases due to diffusion-like heating processes such as residual gas scattering. In order to increase storage times and reduce emittances, the phase-space density of the ion beam needs to be increased, which is called "cooling." Cooling is also required prior to deceleration of ions in HISTRAP, since deceleration decreases both the

longitudinal and transverse phase-space densities. This increase in relative momentum spread and emittance will increase aperture requirements, unless the longitudinal and transverse phase-space areas are first decreased.

There are at present two known methods to accomplish phase-space cooling. Electron beam cooling immerses the ion beam in a co-moving, cold electron beam and allows the two beams to come into thermal equilibrium. Because the electron beam is continuously replenished, the ion beam will cool to near the "temperature" of the electron beam. Electron cooling works best for initially-cool, low-emittance beams. Since several amperes of electrons can be generated easily, one is working in a weak beam (ions)-strong beam (electrons) regime, and the cooling rate is independent of the number of ions being cooled.

Stochastic cooling involves sensing the beam position and applying corrective "kicks" to the beam at appropriate places in the lattice. A separate set of pickups and kickers is required for each of the three degrees of freedom: longitudinal, horizontal and vertical. Stochastic cooling works best for hot, diffuse beams. The cooling rate decreases with an increasing number of ions. Given present technology, which allows operation with ~GHz bandwidths, cooling times will exceed 1 second for more than 10^9 ions. Because the ultimate increase in phase-space density for an ion beam is greater using electron cooling, and since the beams to be cooled in HISTRAP are initially rather cool and have numbers of ions in excess of 10^9, electron beam cooling will be used.

Electron beam cooling is accomplished by merging the ion beam with an intense monoenergetic electron beam over a straight section of the circumference of the storage ring. By adjusting the electron velocity to be equal to the mean ion velocity, a situation is created in which, in the common rest frame of the two beams, a recurrent mixing of the "hot ion gas" with the "cold electron gas" takes place. After some time, this mixing reduces the temperature of the ion gas so that the phase-space density of the ion beam is increased. The theoretical explanation of electron beam cooling has been discussed by several authors [Po84, Bu76, Be81], and only the resulting equations are given here. The cooling time is given by,

$$\tau_C = \frac{kAL\beta^4\gamma^5(\theta_e^2 + \theta_i^2)^{3/2}}{\ell j Q^2} , \qquad (4.5\text{-}3)$$

where k is a constant approximately equal to 1.4×10^{12} (SI units); A and Q are the mass (in amu) and charge of the ion; L is the circumference of the storage ring; $\beta = v/c$, $\gamma = (1 - \beta^2)^{-1/2}$; θ_e and θ_i are the divergence of the electron and ion beam; ℓ is the length of the cooling region; and j is the current density of the electron beam. The divergence of the electron beam, θ_e is directly related to the temperature of the electron gun, which is about 800°C. Thus, the transverse temperature, T, of the electron beam equals 800°C or 0.1 eV, and the divergence is given by [Po84, Bu76, Be81],

$$\theta_e = \left(\frac{2T}{m}\right)^{1/2} / c\beta\gamma , \qquad (4.5\text{-}4)$$

where m is the electron mass. The divergence of the ion beam is

determined by the device injecting into the ring and the lattice functions in the cooling region.

Inspection of Eq. 4.5-3 shows that τ_c increases linearly with ion mass and decreases as the square of the ion charge. τ_c also decreases linearly if j or the fraction ℓ/L is increased, so that a long cooling section having a high current density produces the shortest cooling times. The explicit velocity dependence of $\tau_c \propto \beta^4$ in Eq. 4.5-3 is deceptive, since for a space-charge-limited electron gun, $j \propto \beta^3$ and once $\theta_i < \theta_e$ in Eq. 4.5-4, $(\theta_e^2 + \theta_i^2)^{3/2} \propto \beta^{-3}$, which leads to a β^{-2} velocity dependence. The velocity dependence introduced via γ is negligible for these energies. Thus, for the nonrelativistic heavy-ion beams considered here, the cooling time decreases with increasing ion energies so that it is advantageous to cool at the maximum possible kinetic energy in the ring.

Naively, one could think of the cooling process as achieving equal temperatures for the two beams, a condition which may be written as,

$$\theta_i = \left(\frac{m}{A}\right)^{1/2} \theta_e \ . \tag{4.5-5}$$

In practice, the equilibrium ion divergence will be higher because heating mechanisms, such as residual gas scattering, intrabeam scattering, power supply ripple, and misalignment of the ion and electron beams are present. As an example, consider a 10-MeV/nucleon F^{9+} beam with $\theta_i = 3 \times 10^{-3}$ immersed in a 5-keV electron beam with a temperature of 0.1 eV ($\theta_e = 5 \times 10^{-3}$) and $j = 1000\ A/m^2$: Then, for a 1-meter-long cooling section in a 40-m circumference ring, Eq. 4.5-3 predicts a

cooling time of one second and Eq. 4.5-5 predicts an ion divergence of 27 microradians.

HISTRAP Electron Beam Cooler

The electron beam cooling apparatus for HISTRAP shown in Fig. 4.5-15 consists of three major components: the electron gun, the drift region, and the collector. All three are immersed in a solenoidal magnetic field. The 1-meter-long drift region is where the ion cooling takes place. Two identical toroidal magnets with angles of 48 degrees deflect the electron beam onto and away from the ion beam axis. The EBC region is terminated by two UHV valves in order to isolate the remainder of the storage ring, either during maintenance of the EBC apparatus or during startup and testing of the electron gun. The major parameters of the EBC are listed in Table 4.5-13.

The electron gun, shown in Fig. 4.5-16, consists of a flat dispenser-type cathode, a Pierce shield, and a multielectrode anode structure. In the acceleration region of the electron gun, transverse velocities are produced in the electrons due to the focussing action of the anode opening. Since an electron beam in the drift region with minimum transverse velocities is desired, an anode structure which produces "resonant focusing," where the transit time through the anode lens equals exactly one cyclotron period, is selected [Ru77]. This procedure can eliminate the transverse velocity spread caused by acceleration, although the transverse velocity spread caused by the thermal effects of the cathode remains. The cathode and Pierce shield structure is attached to a bellows so that the position of the structure can be adjusted relative to the anode.

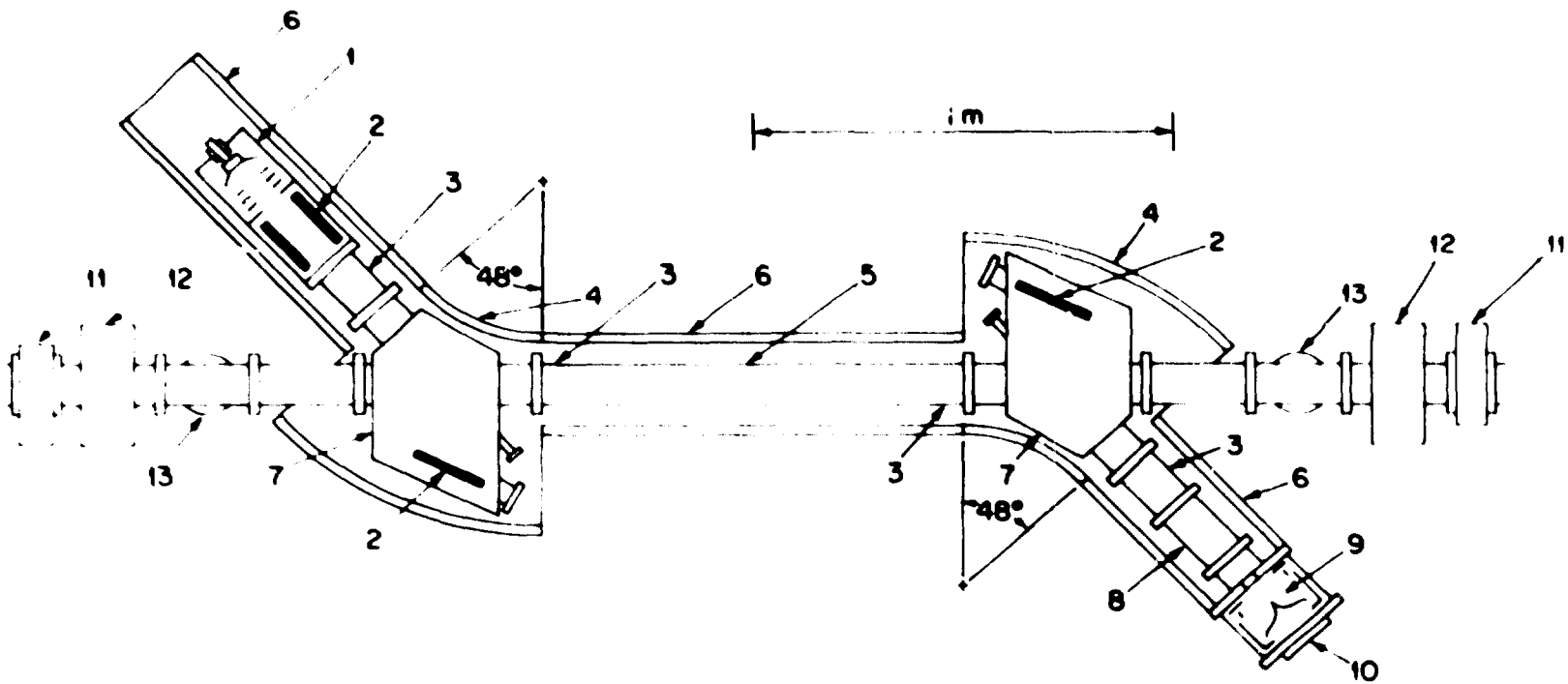

Fig. 4.5-15 The electron beam cooling system showing the location of: 1. electron gun, 2. NEG pumps, 3. pick-up station, 4. toroid, 5. central drift tube or interaction region, 6. solenoid, 7. toroid chamber, 8. collector drift tube, 9. collector, 10. pump port, 11. valve, 12. correction dipole, and 13. pumping station.

Table 4.5-13. Parameters of the electron cooling system

Length of the cooling region	1.00 m
Cathode diameter	5 cm
Electron beam diameter	5 cm
Acceleration	resonant
Deceleration in collector	nonresonant
Electron energy, maximum (minimum)	60 keV (1 keV)
Electron current loss	< 1%
Beam current, maximum (minimum)	5 A (10 mA)
Magnetic field, maximum (minimum)	0.2 T (0.02 T)
Magnetic field stability, $\Delta B/B$	5×10^{-5}
High voltage stability, $\Delta V/V$	5×10^{-6}
Toroid deflection angle	48 degrees
Toroid bending radius	0.5 m
Magnetic field alignment to the ion axis	$<2 \times 10^{-4}$ rad

Contiguous with the electron gun chamber is a section of beam pipe containing an assembly of six nonevaporative getter pumps and a pickup station to monitor the electron beam. This pickup station consists of a cylinder sectioned into four quadrants, coaxial with the electron beam axis. The pickups determine the position of the beam and, with the appropriate microwave diagnostics, the transverse velocity spread of the electrons. The fields in the toroids are adjusted so that, on the axis of the electron beam, the field is the same as in the solenoidal

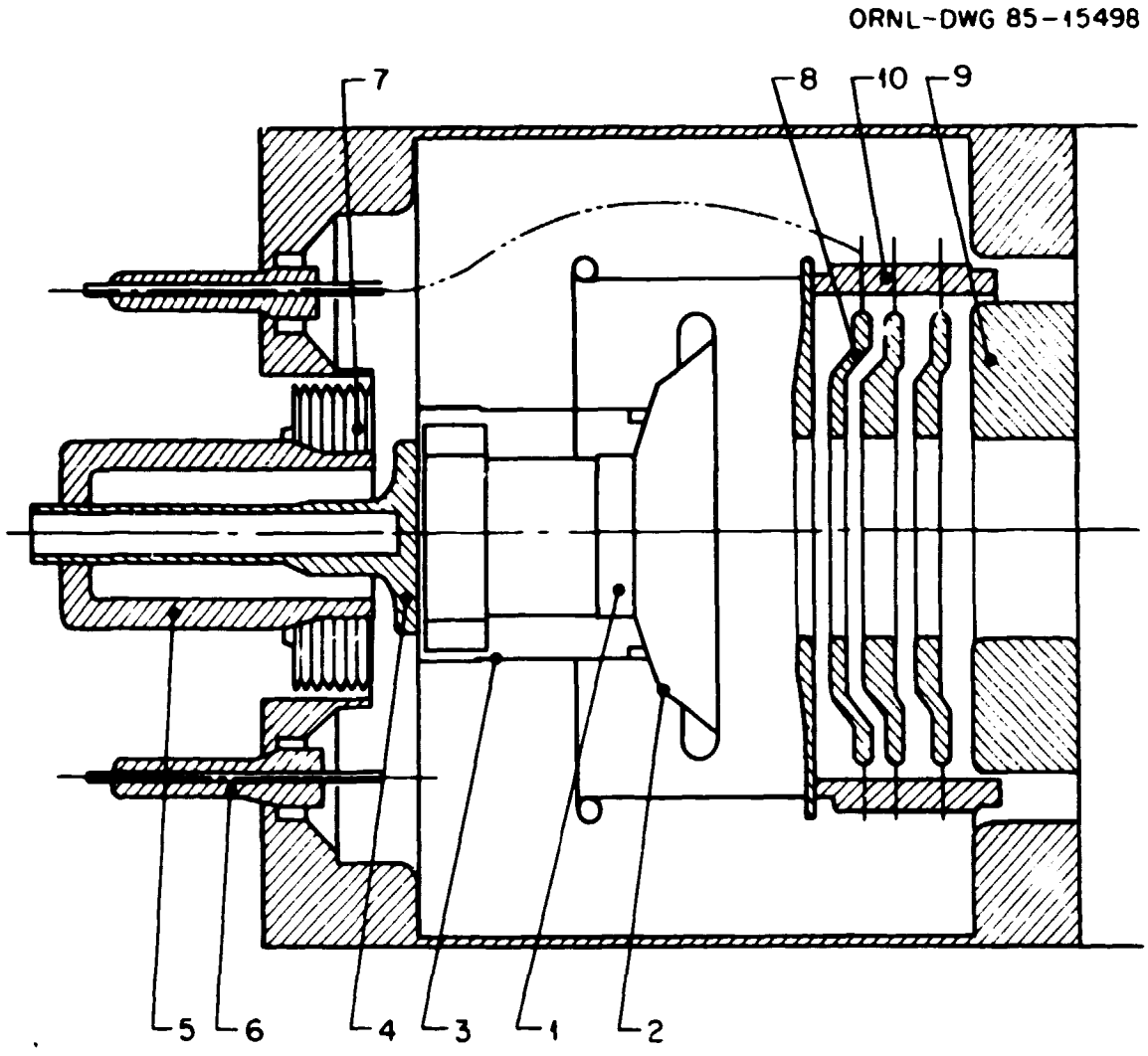

Fig. 4.5-16 The electron gun (LEAR-CERN design) showing the location of: 1. cathode, 2. Pierce shield, 3. heat sink, 4. gas-cooled base, 5. cathode feedthrough, 6. anode feedthrough, 7. bellows, 8. and 9. anodes, and 10. anode support.

regions. Small trim coils are necessary at the toroid-solenoid interfaces in order to make the fields as smooth as possible.

The drift region requires a solenoidal magnetic field uniform to 50 ppm in space and time in order to produce the shortest cooling times and the lowest ultimate divergences of the ion beam. After construction and assembly of the solenoid and vacuum chamber, the field must be mapped and any inhomogeneities eliminated by the installation of trim coils. The Hall probe mapping system, built to measure the HISTRAP prototype dipole magnet field (described in Section 5.3) will be used for this task. The drift region also contains two pickup stations and a coaxial grounded cylinder which surrounds the electron beam. After all the power supplies for the solenoid, toroid, and trim magnets are adjusted to produce the desired field, the power supplies will be computer controlled and ramped together. The magnetic field and the electron energy will be programmed to track each other and the energy of the ion beam.

After being deflected from the ion axis by the second toroid, the electron beam enters the collector region, shown in Fig. 4.5-17. Here the electrons are decelerated by electric fields, and the magnetic field is decreased to allow the electron beam to expand and strike the surface of the collector. The electrons are decelerated to an energy of 3 keV or less, and thus the power requirements of the high-voltage power supply are greatly reduced. Figure 4.5-18 shows the required electrical connections. In addition, lowering the energy of the electrons decreases the outgassing rate when they strike the collector surface.

ORNL-DWG 85-15499

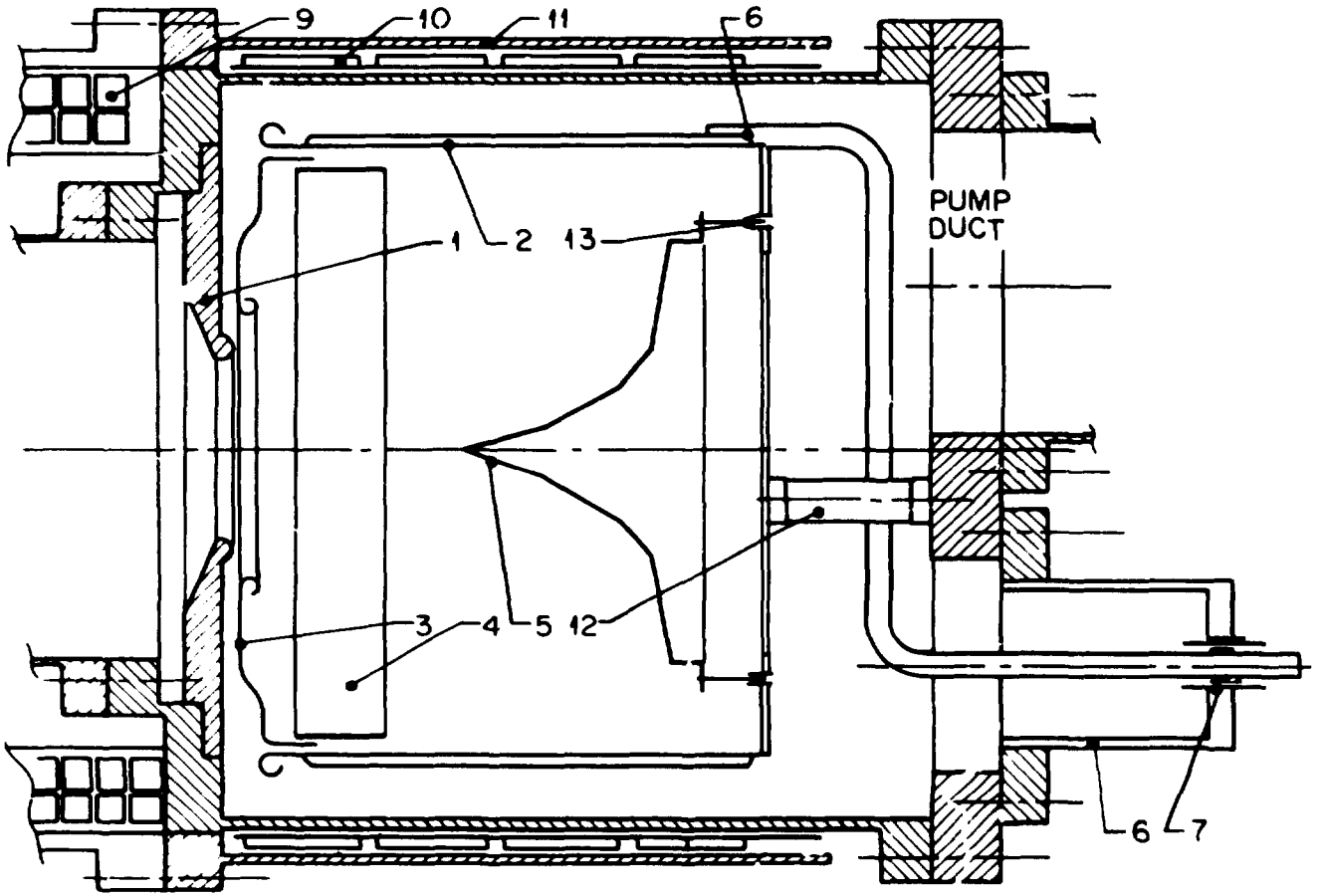

Fig. 4.5-17 The collector (LEAR-CERN design) showing the location of: 1. magnetic shunt, 2. collector, 3. repeller, 4. mesh, 5. tungsten spike, 6. feedthrough, 7. feedthroughs, 8. collector cooling, 9. solenoid, 10. collector correction coil, 11. flux return, and 12. and 13. alumina stand-offs.

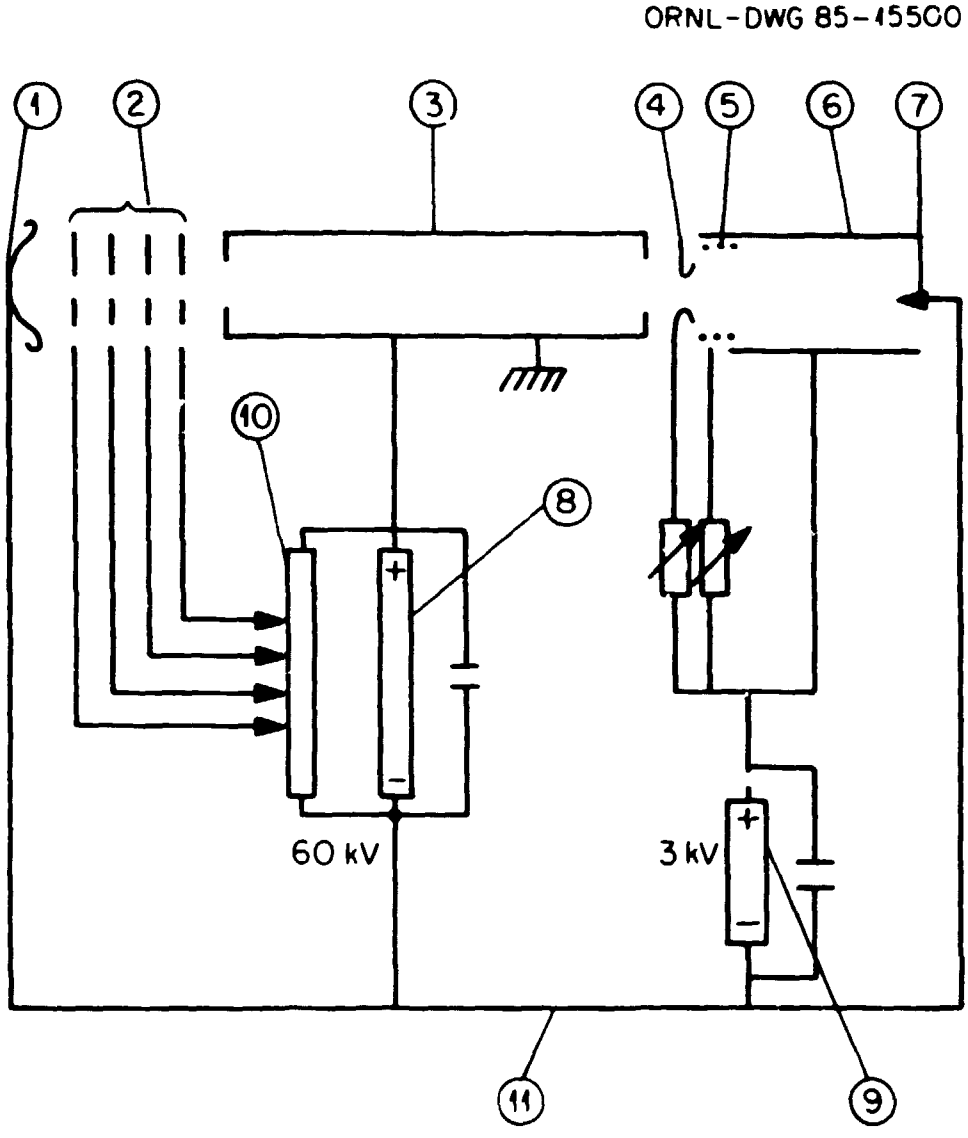

Fig. 4.5-18 Electrical schematic showing the connection to: 1. cathode, 2. anodes, 3. drift tube, 4. repeller, 5. mesh, 6. collector, 7. tungsten spike, 8. anode power supply, 9. collector (recycle) power supply, 10. anode potential divider, and 11. high-voltage Faraday cage common.

This section also provides pumping access for a 500-L/s sputter-ion pump and a roughing port.

The vacuum in the EBC system must be of the same order as the vacuum in the storage ring. There are two main sources of outgassing: (1) the gun region due to the operation of a heated cathode and (2) the collector region due to electrons striking the surfaces. To combat the first, an assembly of six NEG pumps, having a total surface area of 0.15 m^2 and a pumping speed of 3000 L/s, will be placed in a chamber adjacent to the gun region. To minimize the second, the electrons will be decelerated, and a 500-L/s sputter-ion pump will be attached to the collector region. Four 2000-L/s NEG pumps will be placed in each toroid vacuum chamber. The entire system will be bakeable to 350°C. In a similar 40 keV, 4 A, 5-cm-diam beam apparatus at CERN [Ha85], pressures in the mid 10^{-12} Torr range in the cooling region and the toroid chambers have been achieved.

The magnet fields of the EBC which guide the electron beam are a major perturbation to the orbits of the circulating ion beam. For stable operation in the smallest possible aperture, these perturbations must be corrected. First, because HISTRAP will operate with nearly identical horizontal and vertical tunes, the EBC solenoid will couple the corresponding betatron motions. This coupling will be compensated with a pair of weak skew quadrupoles located symmetrically with respect to the EBC straight section. Second, the ion beam will receive up to a 0.01-radian dipole kick in each of the two 48° toroids. The EBC cooler will be placed in a vertical plane so that these kicks occur in the horizontal plane, which has the largest aperture. This orbit distortion

can then be compensated for with the backleg windings of the adjacent dipole magnets and the special set of EBC dipole correctors.

The gun assembly, collector assembly, and solenoid/toroid structures can be brought into initial operation independent of the ring. Field maps can be made, gun operation tested, and vacuum performance studied at various gun currents in an off-line setup. Initial tests of the gun's operation with beam could be made in a single-pass setup on an existing HHIRF beam line. After installation into HISTRAP, a series of tests will be made. These include the effect of the electron beam on the machine tune and lattice functions, the rate of beam loss due to electron capture by the ions, the ability of the gun power supplies to track the main ring dipole field, and the effect of the gun on ring vacuum. After these tests, the cooling performance of the system will be measured for various beams at various energies. Cooling rates and ultimate emittance will be measured for a variety of operating conditions. The ability of the system to cool the ion beams during an acceleration cycle will also be tested. If this proves useful, the overall duty factor of the ring can be increased over present estimates.

An ORNL staff member has spent six months at CERN collaborating on the design and construction of the electron cooling system for the Low Energy Antiproton Ring at CERN. This work is described in Section 5.5.

4.5.5 Beam Instrumentation System

The beam instrumentation system of HISTRAP will initially consist of five individual diagnostic subsystems which have overlapping

components. The diagnostics are: (1) a slit/scintillator system, (2) an electrostatic pickup system, (3) a beam current transformer system, (4) a Schottky noise pickup system, and (5) a beam shaker to measure beam transfer functions.

Slit/Scintillator System

During commissioning of the ring, and possibly during injection of new beams, isolated movable four-jaw slits with beam current meters and TV-viewed insertable scintillator/Faraday cup assemblies will be used. The slits and the Faraday cups will be copies of systems presently in use at the HHIRF. Because these systems are incompatible with full-ring operation, the slits/scintillators will be withdrawn in normal use. After commissioning, these will no longer be necessary and will be removed.

Electrostatic Pickup System

Closed-orbit information will be obtained from beam position monitors (BPMs) based on electrostatic pickups. The electrostatic pickup system will measure the path of the bunched beam through each of the 12 quadrupoles. Figure 4.5-2 shows that there will be space in each quadrupole for both horizontal and vertical pickups. This space exists because of the large quadrupole bore required to maintain good field for the ±4% momentum aperture. In addition, one pickup each will be placed in at least two of the straight sections in order to measure dispersion. The horizontal and vertical positions of the bunch will be sensed by pickups cut at an angle on two opposite faces. The horizontal pickup will have an angular cut in the vertical plane and the vertical pickup

will have an angular cut in the horizontal plane. Between the pickups, and extending from the end of each pickup outward, grounded electrodes of the same cross section may be needed to act as scrapers and field shapers and to eliminate cross-talk between the horizontal and vertical pickups.

The signals at the vacuum feedthroughs must be amplified immediately to provide the best signal-to-noise ratio. The FET preamps will be designed with feedback loops so as to simulate electronically a thermal cold source with 15 dB of amplification. The amplifier will be designed to be switchable to provide 14, 36, and 64 dB of amplification. Signals proportional to beam position within the pickups will be obtained by taking the difference of the signals and dividing by their sum. The BPMs will be experimentally calibrated with a current-carrying wire prior to their installation in the ring.

Beam Current Transformer System

Beam current transformers are used for three different functions: measuring the longitudinal charge distribution in a bunched beam, measuring the total current in a bunched beam, and measuring the total current in an unbunched beam. The first two functions are measured in a straightforward manner with a toroid of high magnetic permeability. The beam pulse passing through the toroid forms a transformer primary and a signal wire around the toroid provides the secondary. After suitable amplification and calibration, the shape of the output gives the longitudinal charge distribution and the area gives the total current. Measuring the current of an unbunched beam requires a so-called dc current transformer (DCCT) which consists of two matched toroids of

high-magnetic permeability through which the beam passes. The bipolar output of a frequency generator drives the two coils into opposite saturations. A coil common to both toroids is connected to the feedback loop of an amplifier. When a beam particle passes through the toroids, the time difference in saturation is sensed by the feedback loop, resulting in a signal proportional to the dc current. A short section of ceramic beam pipe is required at the location of the beam toroid and DCCT.

Schottky Noise System

The electrostatic pickup system will provide the most reliable and precise method of measuring bunched beam position in the ring. However, when the beam is coasting unbunched, the normal electronics will not be able to distinguish between signal and noise. However, as Schottky recognized, there is no such thing as a line of charge; a beam is a sequence of charged particles. By using narrow bandwidth preamplifiers which have their control frequency centered at multiples of the particle revolution frequency, and amplifying those signals with conventional electronics, it is possible to plot the position of each particle in frequency space. By sweeping the frequency positions of all particles, the position of the beam will be measured. In principle, the pickups and most of the electronics are the same for the Schottky systems and the electrostatic pickup systems; only the electrical substitution of preamplifiers and a frequency analyzer are required. A few locations in the ring, perhaps a few of the electrodes in the D quadrupoles, will be used for both horizontal and vertical Schottky pickups.

Beam Shaker System

The beam shaker is used to measure the stability of the beam orbit and the effect on the beam of the wall impedance. The technique uses the electrostatic pickup or Schottky noise systems in the conventional manner to measure the beam response. A frequency generator, which has positive and negative outputs of up to 20 volts, is attached to an extra pair of either horizontal or vertical pickup electrodes. The frequency generator is set to oscillate at a harmonic of the betatron frequency, which forces the beam to oscillate at that frequency and allows the study of beam stability. It is also possible to measure horizontal-vertical coupling by shaking the beam in one plane and measuring the response in the other plane.

4.5.6 Control System

The HISTRAP control system is presently envisaged to be modeled after the one used at the CERN LEAR ring. The hardware and operational requirements for the LEAR ring are very similar to those of HISTRAP. The LEAR system has benefited from many years of experience at CERN with control systems for the linac, PS, ISR, SPS, and now SP$\bar{P}$S and LEP. It has also been adopted as the model control system for the small atomic physics rings at Aarhus, Stockholm, and Heidelberg. Thus, the possibility exists for substantial control system collaboration among these groups and HISTRAP.

Control System Hardware

The control system for the ring must be able to control the various devices with time-dependent setting with accuracies listed in Table

4.5-14. Accuracies are given in terms of the number of bits that a digital system would need to provide. Also listed in the table are devices with settings which remain fixed throughout a cycle. The architecture of the HISTRAP control system is shown in Fig. 4.5-19. The control console is based on a high-end work station. Dedicated displays are provided for alarms, radiation, and safety status. Control processing is distributed at about eight nodes. Processing is further distributed by the availability of intelligent subsystems providing conversions to engineering units and alarm limit checking. Special purpose devices, such as function generators, are to be embedded in the equipment to be controlled. Presently, VMEbus hardware has the best commercial availability, the design of the LEP control system is based on VMEbus, and it is expected that most of the control system hardware will be VME based. However, use of other open standard bus systems, such as CAMAC, GPIB, and possibly FASTBUS, will be dictated by the availability of commercial instrumentation. It is planned to use the existing VAX 11/750 in service at the EN tandem Van de Graaff at ORNL as the host computer for the HISTRAP control system. Considerable ancillary hardware is on hand for that system, including two large disk drives, a tape drive, a line printer, and two color graphics terminals with plotters. A VAX 11/785 in the ORNL Physics Division will also be accessible via an ethernet link.

Control System Software

One data base manager (DBM) program will have overall responsibility for interfacing to specific user programs and to the hardware

Table 4.5-14. Required control accuracies for major apparatus

	Bits accuracy	Number	Time varying*	Time critical*
Ring dipole magnetic field	16	1	X	
Ring quadrupole magnetic fields	16	6	X	
Ring sextupole magnetic fields	12	8	X	
Ring H correctors' fields	12	8	X	
Ring V correctors' fields	12	8	X	
Ring bump magnet fields	12	4		X
Injection electrostatic septum field	12	1		
RF system voltage	16	1	X	
RF system frequency	16	1	X	
RF system phase	16	1	X	
Injection line dipole fields	12	2		
Injection line quadrupole fields	12	18		
Injection line steerer fields	12	14		
Negative ion source extraction voltage	12	1		X
Negative ion source extraction pulse width	12	1		
ECR source extraction voltage	12	1		X
ECR einzel lens voltage	12	2		
ECR electrostatic quadrupole triplet	12	2		
ECR 90° magnet field	12	1		
RFQ voltage	12	1		X

Table 4.5-14 (continued)

	Bits accuracy	Number	Time varying*	Time critical*
Debuncher voltage	12	1		X
EBC gun voltage	16	1	X	
EBC recycle voltage	12	1	X	
EBC solenoid magnets	16	3	X	
EBC toroid magnets	16	2	X	
EBC filament supply	12	1		
EBC trim coil currents	12	7	x	

*Time varying refers to any parameter which will need to be ramped, usually to track the ring dipole field.
Time critical refers to other parameters which must be set to their values only for a short time and at a specific point in the ring cycle.

This list does not include the myriad of other items to be monitored by the control system, such as magnet or power supply water flow, coil temperature, valve status, vacuum pressure, pump status, power supply interlock status, slit position, Faraday cup position and current, Hall probe or $\dot{B}$ coil fields, ECR magnet fields or microwave settings, and such. All the above parameters must be set by the control system. A method of reading back to check settings is implicit for all of the parameters listed. The tandem control computer is assumed to handle all tandem settings, of which there are several hundred. At present, over 500 control points have been identified, of which over 120 require "active setting."

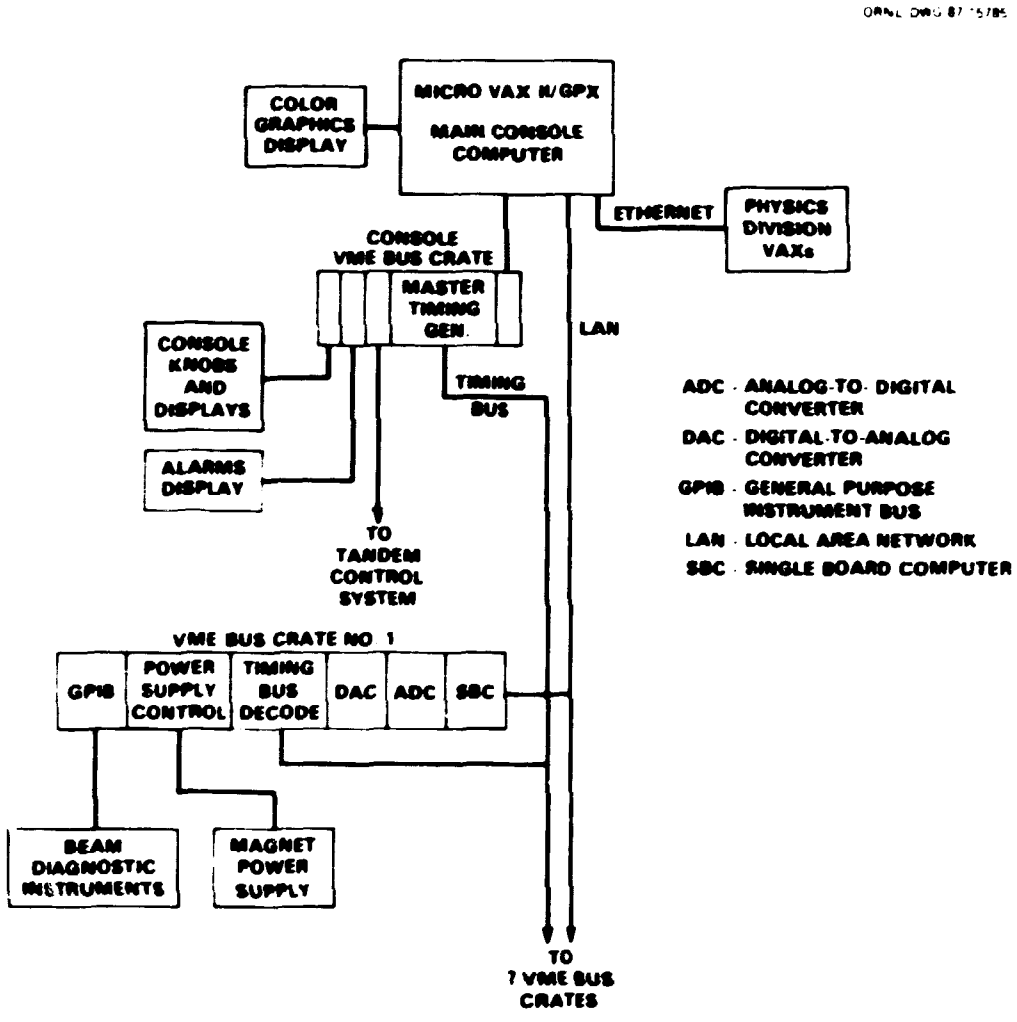

Fig. 4.5-19 Conceptual design for the HISTRAP control system. A prototype control system consisting of the MicroVAX and VME crate has been assembled and was used initially to control the vacuum test stand.

device drivers themselves. High level programs, such as the COMFORT program for extraction of Twiss parameters, and the associated orbit, tune, and chromaticity programs, will all reside on the host VAX and will be invoked as needed by the DBM. It is the responsibility of the DBM to keep track of all parameters, modules, and their locations. The DBM must also know when the requested parameter must be obtained from hardware or whether it must be obtained by running a program, where that program may, itself, need to ask several questions of the CAMAC hardware.

In keeping with the LEAR philosophy, as much programming will be done in PASCAL and FORTRAN 77 as possible. Assembler language will be reserved for final hardware-related routines and low-level programs. It is planned to use as much of the LEAR software as possible to save the many work years of effort needed to develop a control system and data base architecture from scratch.

4.5.7 Future Extraction System

Atomic physics experiments will initially be performed with internal targets, merged electron or photon beams, or crossed ion beams. An important future upgrade for HISTRAP is the addition of an extraction system for external-target experiments. This section outlines a straightforward third-order resonant extraction system to provide slow, uniform beam spills over a time interval of the order of a second for external-target experiments. Four additional elements would be required: one trim quadrupole to provide fine control of the tune, one extraction sextupole to establish a separatrix and drive the resonance,

and electrostatic and magnetic septa to extract the beam. The approximate requirements for these elements are listed in Table 4.5-15. These elements are shown in all the figures and engineering drawings of HISTRAP. This initial extraction study indicates that all these elements can be located in a single straight section.

The extraction sextupole will add the third harmonic imbalance for extraction. This sextupole is located in a nondispersive straight. Since the beam will be driven at the $\nu_x = 7/3$ resonance, only one extraction sextupole is required if it has a 13° phase advance with respect to the electrostatic septum entrance. These conditions can be met by separating the septum entrance and sextupole by 2.4 m symmetrically about a straight section center. This single sextupole will then provide the necessary separatrix with the correct orientation for extraction and will not affect the chromaticity correction due to its placement in a nondispersive section.

With a 2.67-Tm beam, the extraction sextupole must have an integrated strength of 9.0 T/m to provide a growth rate of 1.0 cm in three turns for a septum located 6.0 cm from the equilibrium orbit. To initiate the slow spill, a trim quadrupole with integrated strength of 0.15 T is required to adjust the tune as needed. Horizontal position control can be obtained, if needed, with the dipole backleg windings and bump magnets. In order to keep all the extraction apparatus in a single straight section, the trim quadrupole has been placed near the electrostatic septum entrance.

The electrostatic septum is 1.1-m long and operates at 133 kV with a 1.0-cm gap. A septum thickness of 0.13 mm gives an extraction

Table 4.5-15. Elements required for slow extraction at 2.67 Tm

Extraction Sextupole	
B"	40 T/m^2
Magnetic length	30 cm
Good field radius	6 cm
Bore	16 cm
Pole-tip field	2.6 kG
Number of turns	20
Current	200 A
Total voltage	~20 V
Trim Quadrupole	
B'	1.2 T/m
Magnetic length	20 cm
Good field radius	6 cm
Bore	16 cm
Pole-tip field	800 G
Number of turns	20
Current	20 A
Total voltage	~10 V
Electrostatic Septum	
Length	1.1 m
Radius of curvature	25 m
Horizontal aperture	1.0 cm
Vertical aperture	3 cm
Gradient	130 kV/cm
Voltage	130 kV
Magnetic Septum	
Field	0.73 T
Effective Length	70 cm
Vertical aperture	5 cm
Septum thickness	2 cm
Number of turns	10
Current	3200 A
Coil resistance	5.3 mΩ
DC voltage	17
Resistive loss	50 kW

efficiency of 98.5%. This septum, together with a 25-cm drift, produces a 3.5-cm separation between the extracted and orbiting beams at the magnetic septum entrance. This septum has a width of 2.0 cm, so some room is allowed for bakeout insulation. The magnetic septum is rather straightforward; the main concerns are simplicity and power consumption. The magnetic septum provides a 23.7-cm separation between beams at the start of the sextupole and 110 cm from the straight section center. The final extraction angle is 13.6°. There are other perhaps simpler systems; however, this scheme is operationally simple, has all the apparatus contained in a single straight, and demonstrates that there is ample room in HISTRAP for a future slow-extraction system.

5.0. HISTRAP HARDWARE DEVELOPMENT

Although HISTRAP in some ways is a rather conventional synchrotron, its small size, desired flexibility, and beam cooling capability lead to some very challenging hardware requirements. Three of the most challenging technical problems are (1) the requirement of achieving a vacuum throughout the ring in the order of $1C^{-12}$ Torr; (2) the design and operation of a very-broad-band, ferrite-loaded rf acceleration/deceleration cavity; and (3) the three-dimensional design, fabrication, and field mapping of a prototype laminated dipole magnet. The ORNL Director's R&D Fund has supported research and development in these three critical areas.

In addition, capital reserves were used to assemble a prototype control system which was initially used to control the vacuum test stand, and a Physics Division staff member participated in the optimization and operation of the LEAR electron beam cooler. This work has demonstrated ORNl ability to achieve the desired performance capabilities for HISTRAP and will allow a rapid start in the construction of HISTRAP. The details and results of these developments are described below.

5.1 HISTRAP Vacuum Test Stand

5.1.1 Design

HISTRAP has a total circumference of 46.8 m. The aperture requires 15-cm-diam vacuum pipes in the straight sections and similar chamber areas in the bending and focusing sections, giving a total vacuum

chamber surface area in the order of 20 m^2. The conductance of the vacuum chamber in the bending and focusing sections is expected to be similar to that of 10-cm-diam pipe. HISTRAP requires a pressure in the order of 10^{-12} Torr to be able to decelerate highly charged, very heavy ions down to low energies. An average pressure of 2×10^{-12} Torr can be achieved in a 10-cm-diam beam pipe with 1000-L/s pumps periodically spaced every 1.75 m, if the vacuum chamber material has a specific outgassing rate of less than 1×10^{-13} Torr L $cm^{-2}s^{-1}$. In order to test components and procedures to achieve pressures in the order of 10^{-12} Torr, a vacuum test stand has been built and operated.

Figure 5.1-1 is a sketch of the 3.5-m-long vacuum test stand which approximately models one-sixteenth of the HISTRAP vacuum chamber and was constructed from 10-cm-diam beam pipe. The two titanium sublimation pumps (TSPs) are mounted from tees which are separated by 1.75 m. The two end flanges are separated from the TSPs by one-half of the separation between pumps. A Varian 60-L/s Starcell sputter ion pump (SIP) is used to pump noble and heavy gases. Two Leybold-Heraeus extractor ion gauges are used for low-pressure measurements. One extractor gauge on the end flange is meant to approximate the maximum expected pressure midway between the pumping tees in a periodic system, whereas the other extractor gauge is meant to give a minimum pressure at a pumping tee. In addition, the other end flange holds a VG DX200 residual gas analyzer (RGA) to determine the composition of the residual gas. The system is roughed through a VAT all-metal, right-angle, 10-cm valve, and all components are bakeable to at least 250°C.

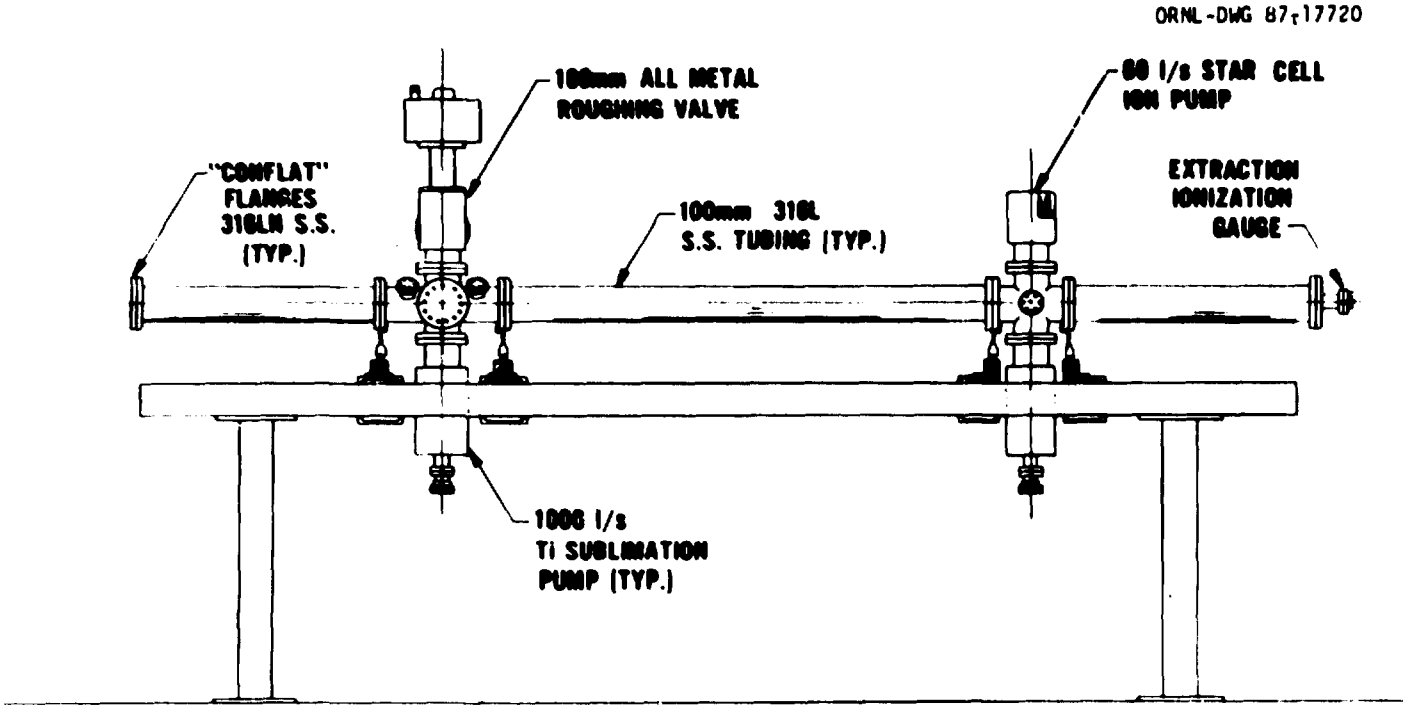

Fig. 5.1-1 UHV vacuum test stand which models one-sixteenth of the HISTRAP vacuum system. The stainless steel chambers were initially vacuum baked at 950°C and are covered with heater blankets for in situ bakes at 300°C. The system is roughed with a crysorption pump followed by a cryopump.

5.1.2 Chamber Processing and Assembly

The vacuum system components were fabricated from 316L stainless steel tubing and 316LN "ConFlat" flanges following procedures used at CERN [Po84, Po87] and BNL [Sk87]. All welds were TIG without filler rod and were either inside welds or full penetration welds. Parts were then leak checked with a mass spectrometer leak detector having a sensitivity of $< 1 \times 10^{-10}$ scc/s of He. The vacuum chambers were initially cleaned by vapor degreasing with perchlorenthylene, water rinsed, dipped in Metex alkaline solution, and rinsed in deionized water. Following the above cleaning, the components were baked in a clean vacuum furnace for two hours at 950°C at a pressure of less than 1×10^{-4} Torr. The cooling rate was carefully controlled to prevent grain boundary precipitations. After cooling, the parts were capped with blank flanges and copper gaskets for transportation and storage.

The assembly of the components was done under controlled clean conditions. Parts were handled only with gloves, white nylon over latex, and the people handling any internal surfaces such as gaskets and gauges were not allowed to handle tools or bolts. The copper gaskets were silver plated to reduce oxidation and sticking during baking. The complete assembly was leak checked using the RGA and helium. The chamber was covered with fourteen Briskheat heating blankets for in situ baking up to 300°C. The temperature was read with 27 type-E thermocouples attached to the chambers and flanges.

5.1.3 Control Hardware and Software

Figure 5.1-2 shows a block diagram of the control system hardware for the vacuum test stand, which is a subset of that proposed for the full HISTRAP. Control is by DEC MicroVAX II/GPX computer and all control input/output functions are provided by VMEbus interfaced by a Performance Technologies, Inc. Model PT-VME903A QBUS-VMEbus adapter. The analog input consists of an Analogic Corp. Model ITG1300 analog input and master control module and two Model ITG1301 expansion modules. Inputs are the 27 thermocouples and two chart recorder outputs of extractor gauge controllers. The system does cold junction compensation and linearization of the thermocouple inputs and provides temperatures with a resolution of ~ 0.3°C. A Force Computers, Inc. Model ISIO-2 intelligent serial I/O module provides readout and control for an ion gauge controller, an ion pump controller, and the RGA. The digital input/output is an Acromag, Inc. Model 9480 module, which controls a contactor supplying all heater blanket power and 14 solid-state relays for the individual heater blankets.

The MicroVAX runs with the Micro VMS operating system. The software in FORTRAN is divided into four classes of processes: (1) monitor/operator interface, (2) data logging, (3) hardware interface driver, and (4) heater control. The monitor/operator interface provides real-time plots of pressure and average temperature versus time and also a real-time plot of temperature versus thermocouple. The data-logging process records all temperatures, pressures, and heater power every 10 minutes. The hardware interface processes transfer data between the VME modules and the shared data commons. These processes perform any

ORNL DWG 88-12586

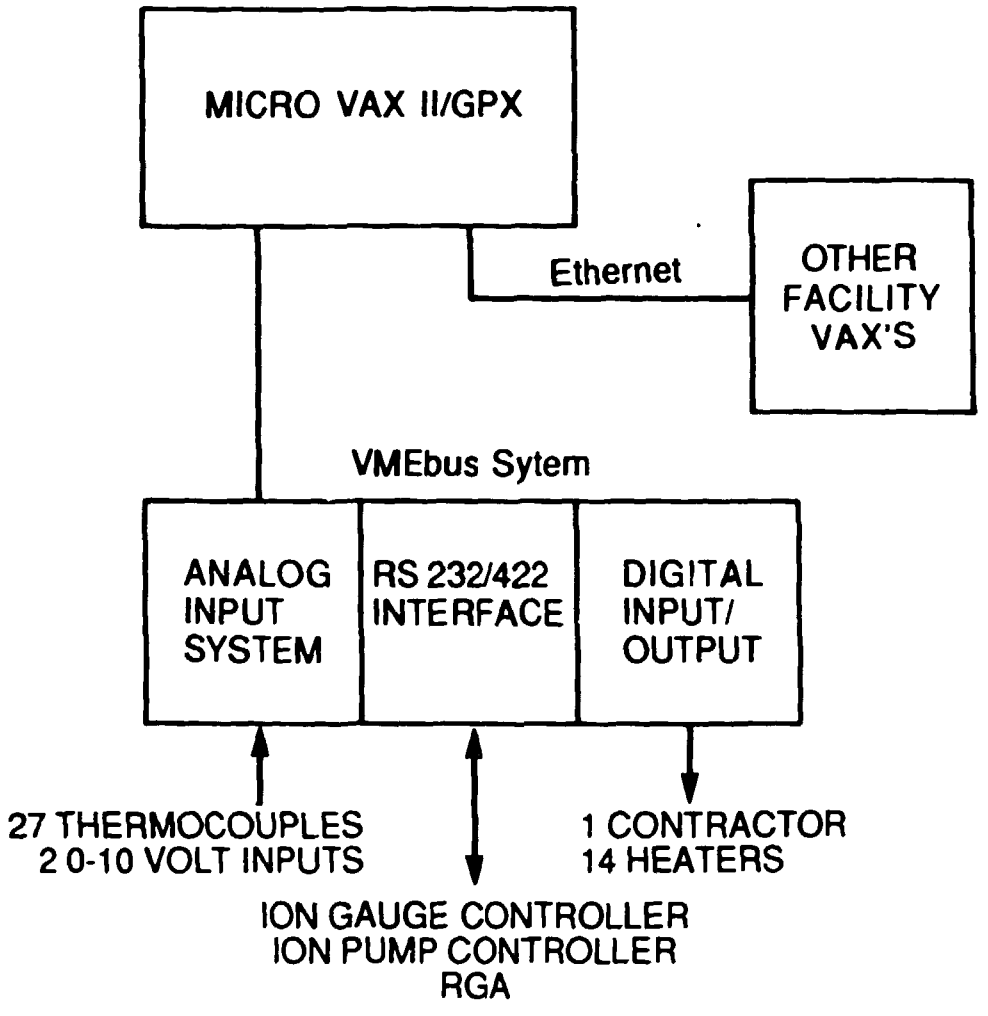

Fig. 5.1-2 Block diagram of the control system hardware for the vacuum test stand.

translations required by the hardware devices and are the only processes which do direct I/O to the VME modules. The heater control processes implement a standard PID controller function. There are separate temperature setpoint and controller parameters for each heater blanket. Required heater power is calculated every 30 seconds. During bakeout, a process monitors the control temperature for each heater and the system pressure. About 2 kW of power is needed to bake the system at 250°C.

5.1.4 Results and Discussion

To eliminate all sources for oil contamination, the roughing system consists of three stages of liquid-nitrogen-cooled sorption pumping, followed by an Air Products 20-cm-diameter closed-cycle gaseous helium cryopump. The cryopump is isolated from the sorption pumps and the UHV system by all-metal valves. The sorption pumps rough the system and the cryopump to 3×10^{-3} Torr.

Figure 5.1-3 shows pressure and temperature profiles as a function of time for a system bakeout cycle. The pressure shown is that measured at the tee containing the roughing valve. After roughing to a pressure of 3×10^{-8} Torr, the chamber temperature was increased to 100°C at a rate of 30°C per hour. The temperature hold at 100°C during heat-up was to check the heating control system and would not be typical of a bakeout cycle. With only the cryopump pumping on the system, the temperature was raised to 250°C and held for 48 hours. During the 250°C bake, the pressure decreased to 3×10^{-8} Torr. Some components which did not have a 250°C upper temperature limit were heated to 300°C.

During cool-down, the temperature was held fixed at 120°C while the TSPs, ion gauges, and RGA were degassed and the SIP was turned on.

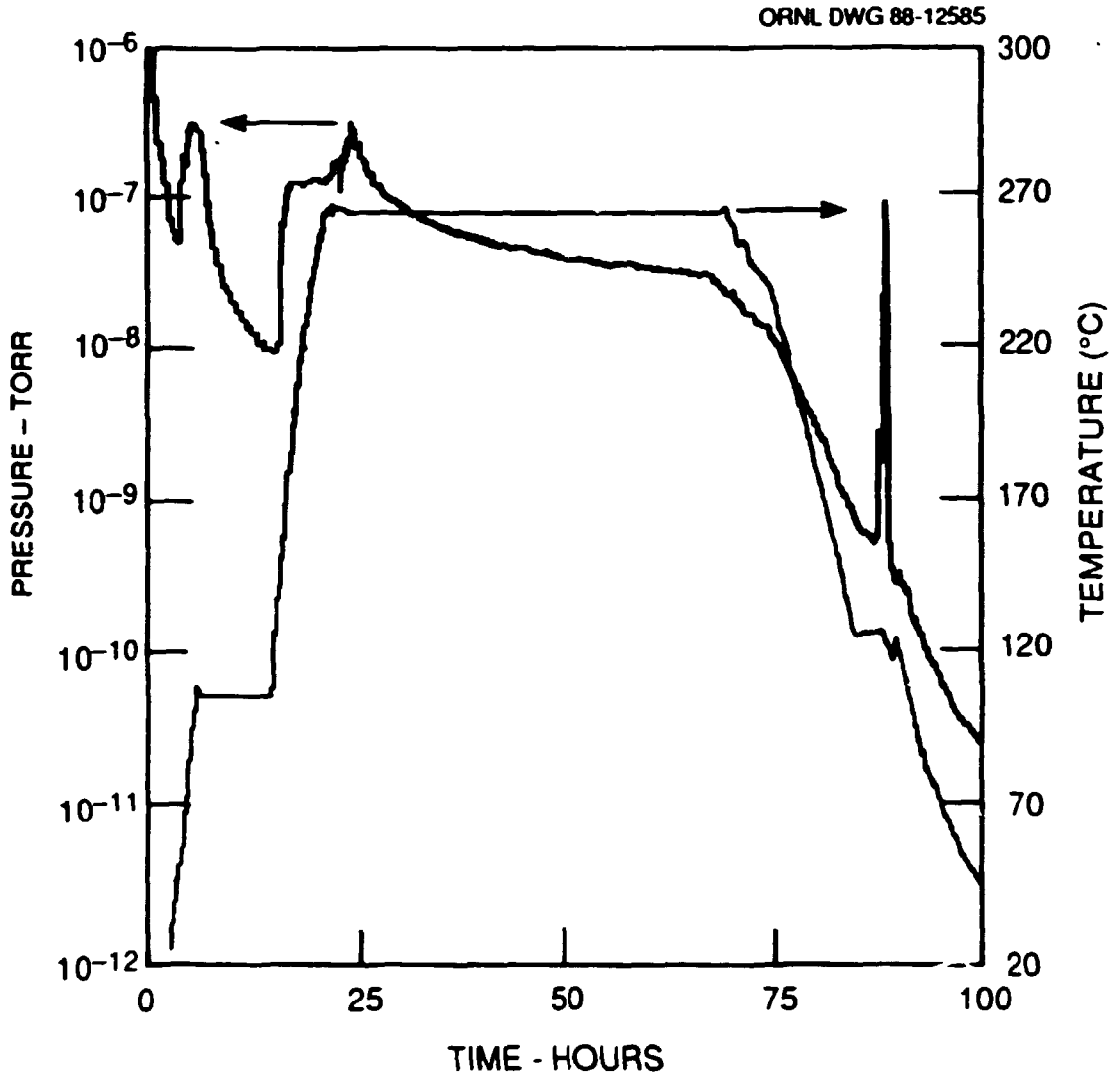

Fig. 5.1-3 Pressure and temperature profile as a function of time for a bakeout cycle of the vacuum test stand. After a pumpdown cycle of one week, a pressure of 4×10^{-12} Torr was obtained.

Cooling down then continued to ambient room temperature and a pressure of 2×10^{-11} Torr was obtained. The titanium sublimators were each flashed for four minutes at 47 A and after the pressure recovered to 2×10^{-11} Torr, the all-metal valve to the cryopump was closed. The remainder of the pump-down was with the TSP and SIP and, after one week, an ultimate pressure of 4×10^{-12} Torr was achieved. The calculated outgassing rate of the stainless steel for this pressure is 4×10^{-13} Torr L $cm^{-2}s^{-1}$ and an average pressure of 8×10^{-12} Torr is calculated for the equivalent periodic system.

The vacuum firing of the stainless steel at 950°C and the in situ 300°C bakeout produce residual outgassing rates which allow for the use of reasonable pump sizes and pump spacing for obtaining pressures on the 10^{-12} scale. The use of a cryopump for roughing during bakeout and cool-down provides a contamination-free method, with high pumping speed, of producing pressures of 2×10^{-11} Torr before the final pumping with the TSP and SIP. This should markedly extend life of the titanium filaments and reduce the time required to reach operating pressure. It is clear from this work that the gauges themselves may be the main source of residual gas at these pressures. Figure 5.1-4 shows a photograph of the assembled vacuum test stand. This work was reported at the American Vacuum Society Meeting at Atlanta (Jo88).

5.2 Prototype rf Acceleration/Deceleration Cavity

A prototype rf cavity intended to meet the HISTRAP acceleration and deceleration requirements of Table 4.5-10 was designed, constructed, and tested. Estimated characteristics of the cavity are listed in Table 4.5-11. The cavity is a half-wave, ferrite-loaded configuration with a

ORNL Photo 4688-88

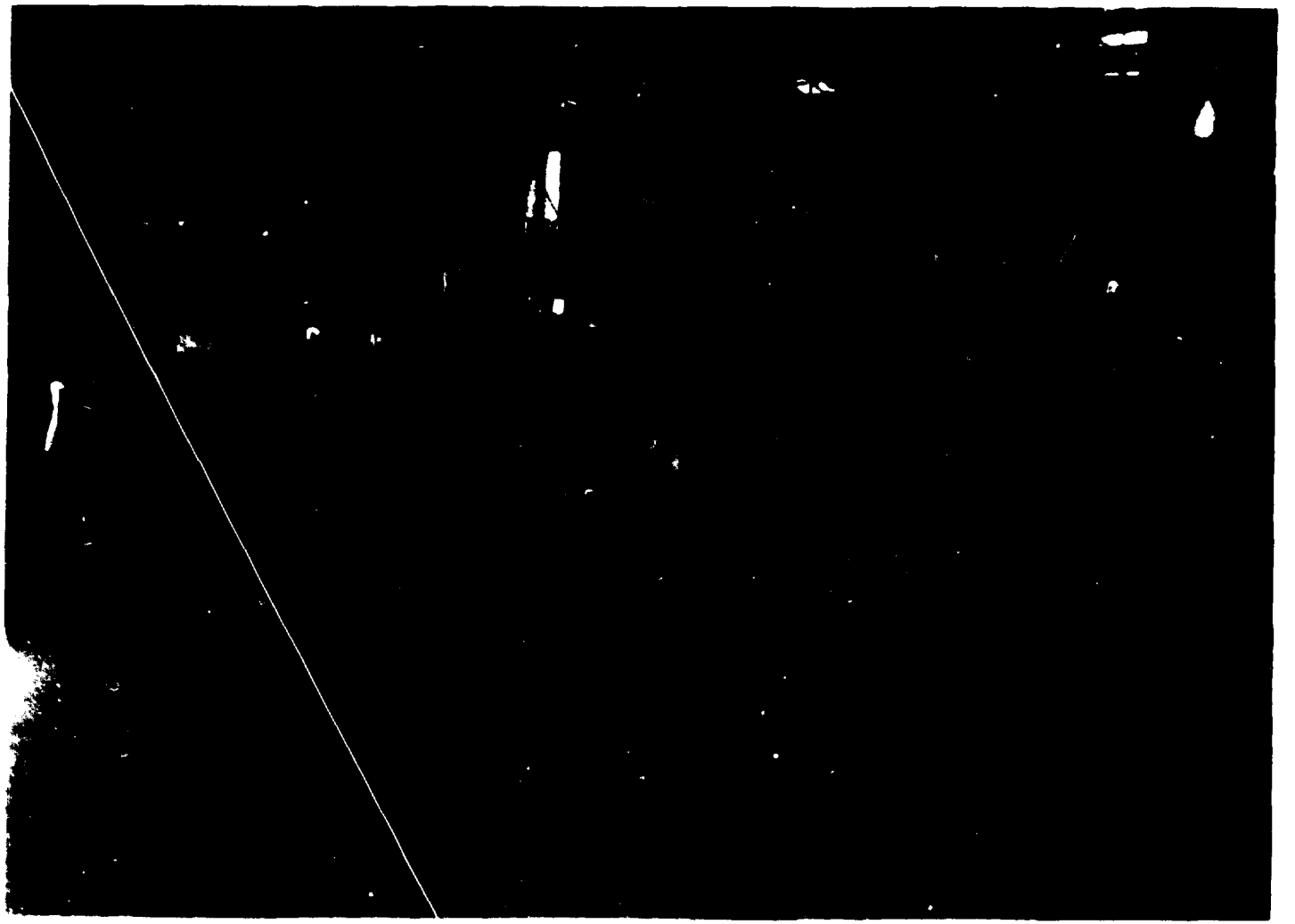

Fig. 5.1-4 Photograph of the assembled vacuum test stand.

single accelerating gap. Tuning is accomplished through application of dc bias current to a set of "figure eight" bias windings. A cross-section view of the cavity is shown in Fig. 5.2-1, and an assembled view is shown in Fig. 5.2-2.

The center conductors of the cavity are mechanically separate from the high-vacuum beam line which contains a ceramic-insulated accelerating gap. Spring-loaded contact fingers provide electrical contact between the cavity high-voltage electrodes and the beam line. These fingers are retractable so that the beam line can be thermally isolated from the cavity structure during the vacuum back-out process.

The complete rf cavity will contain 28 ferrite rings, 14 on each half, which are separated by water-cooled annular copper disks. The ferrite-copper stacks in each half of the cavity are supported by fiberglass end plates which are joined by several steel-lead screws. The prototype cavity is only partially loaded with 16 ferrite rings. The partial load is sufficient for testing and measuring the tuning and power dissipation characteristics of the configuration. Approximately twice as much gap capacitance and rf drive power is required for operating the prototype cavity under the conditions required of the complete cavity.

Ferrite bias is provided through six independent winding segments, three on each ferrite stack. Each segment is a water-cooled copper bus with termination outside the cavity. Outside bus connections are used for completing each "figure eight" winding. All three windings may be operated in series, parallel, or other arrangement as may be found suitable for obtaining appropriate bias levels while avoiding rf

ORNL-DWG 87-17429

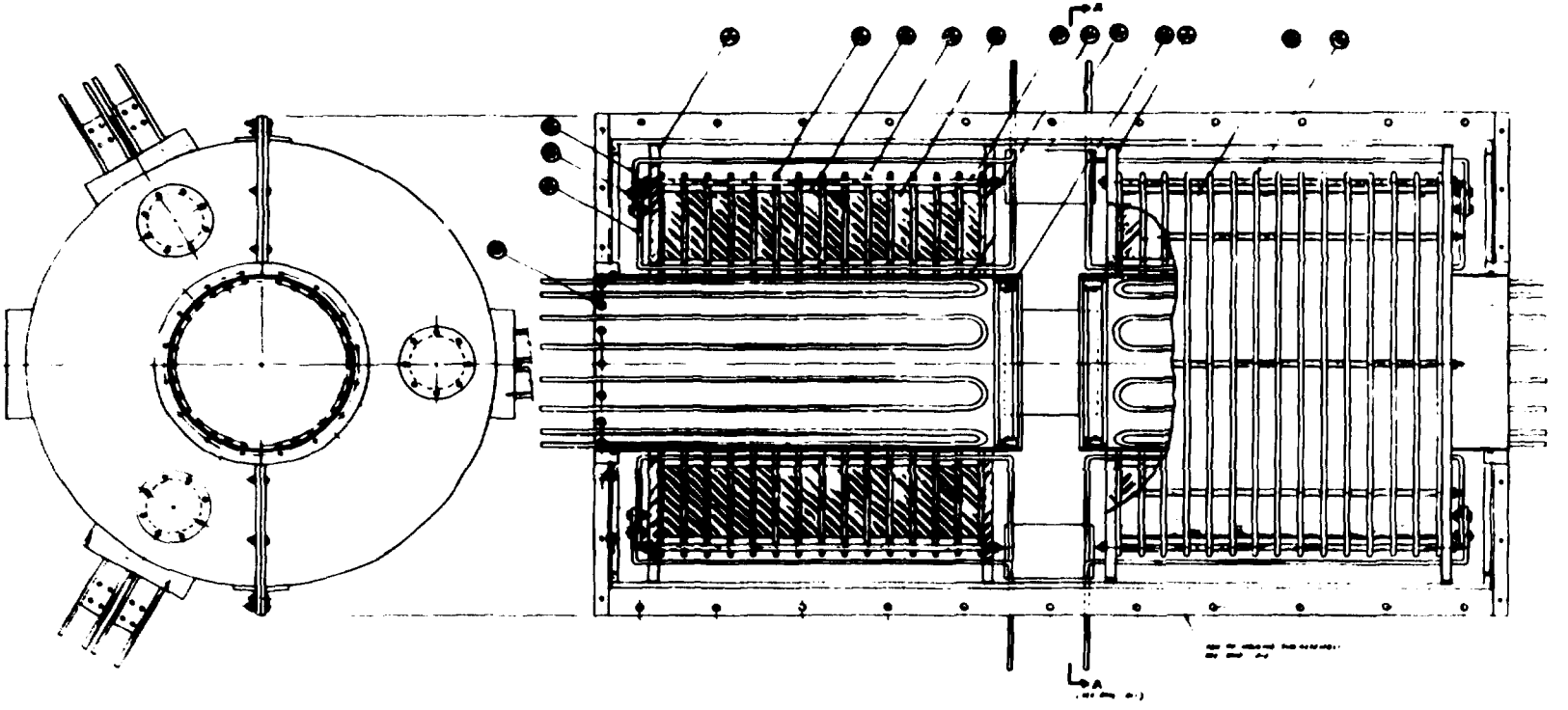

Fig. 5.2-1 Interior view of the proposed HISTRAP rf cavity. The cavity will contain up to 28 2.5-cm-thick ferrite disks. The disks will be separated by 0.6-cm-thick water-cooled plates.

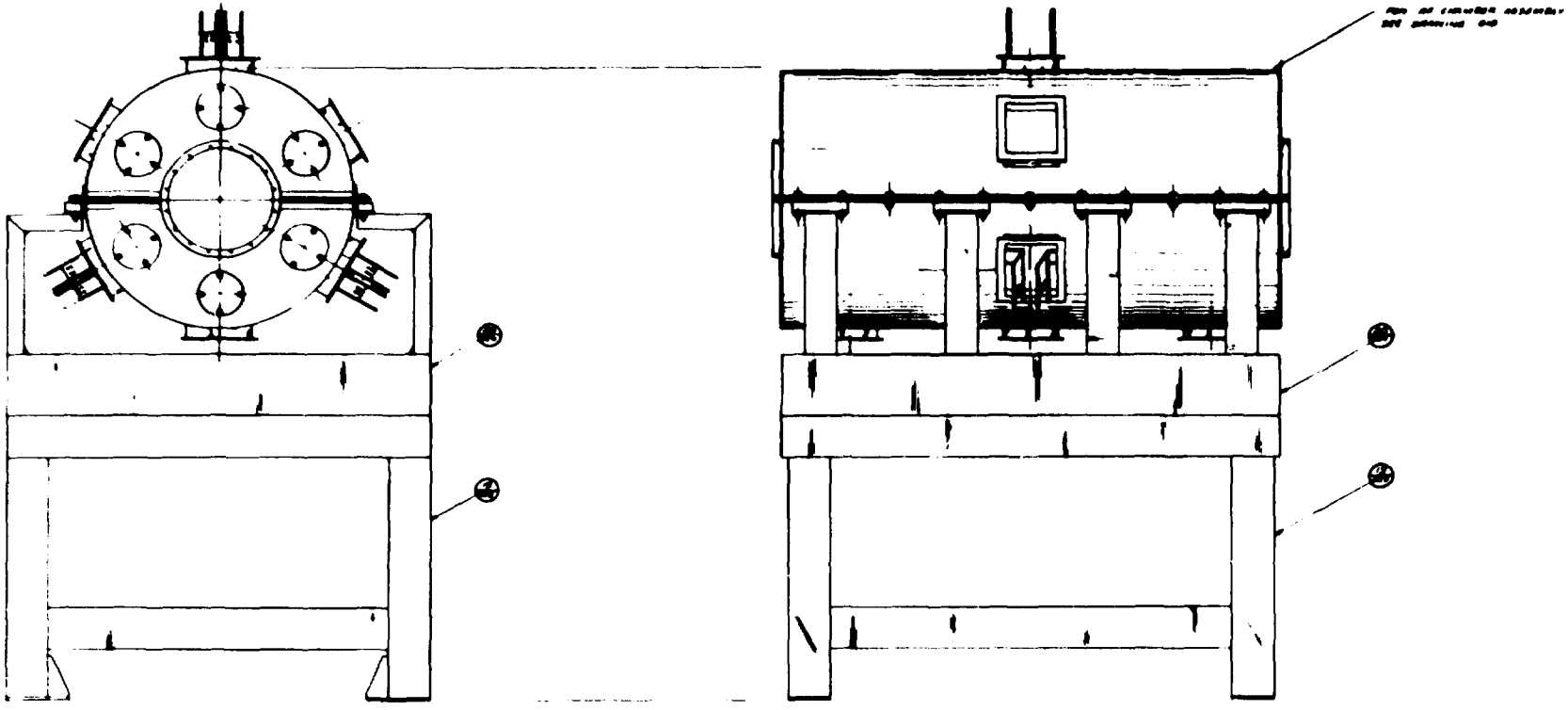

Fig. 5.2-2 Exterior view of the HISTRAP prototype rf cavity. The cavity will have a length of about 120 cm and will be assembled about a 15-cm-diameter S.S. beam pipe containing a 2.5-kV ceramic gap.

parasitic modes. The prototype is operating with the three windings in series, and a 1000-A dc power supply is sufficient to swing the relative permeability over a 200 to 1 tuning range.

The ferrite rings were individually tested to measure relative permeability as a function of dc bias and rf excitation. Values of remnant permeability and power dissipation were found as listed in Table 4.5-11. Efforts to measure tuning characteristics were unsuccessful due to intrinsic inductance in the test apparatus. Full cavity tests with all 16 available rings in the prototype cavity were quite successful with a demonstrated tuning range of 250 kHz to 3.0 MHz, using a dc bias excitation increment of 0 to 2000-A turns. The actual tuning range of the complete cavity will run within the specified limits when the ferrite load is increased to 28 rings.

Test results are shown in Fig. 5.2-3 and Fig. 5.2-4. The very low values of "Q" are especially interesting, since it will be possible to drive the cavity to frequencies substantially below resonance on the low end of the tuning range. This provides some possible extension to the tuning range, and will provide much needed tuner damping in the low-frequency region where slight increments in ferrite bias cause a huge change in resonant frequency. The shunt resistance is nearly constant with respect to frequency at about 80 ohms. Consequently, the cavity will operate comfortably with a balanced drive connected across the accelerating electrodes.

A photograph of the cavity is shown in Fig. 5.2-5. The several ports in the center area are used for access to the bias winding leads and the rf power drive connections. The prototype cavity is driven by a

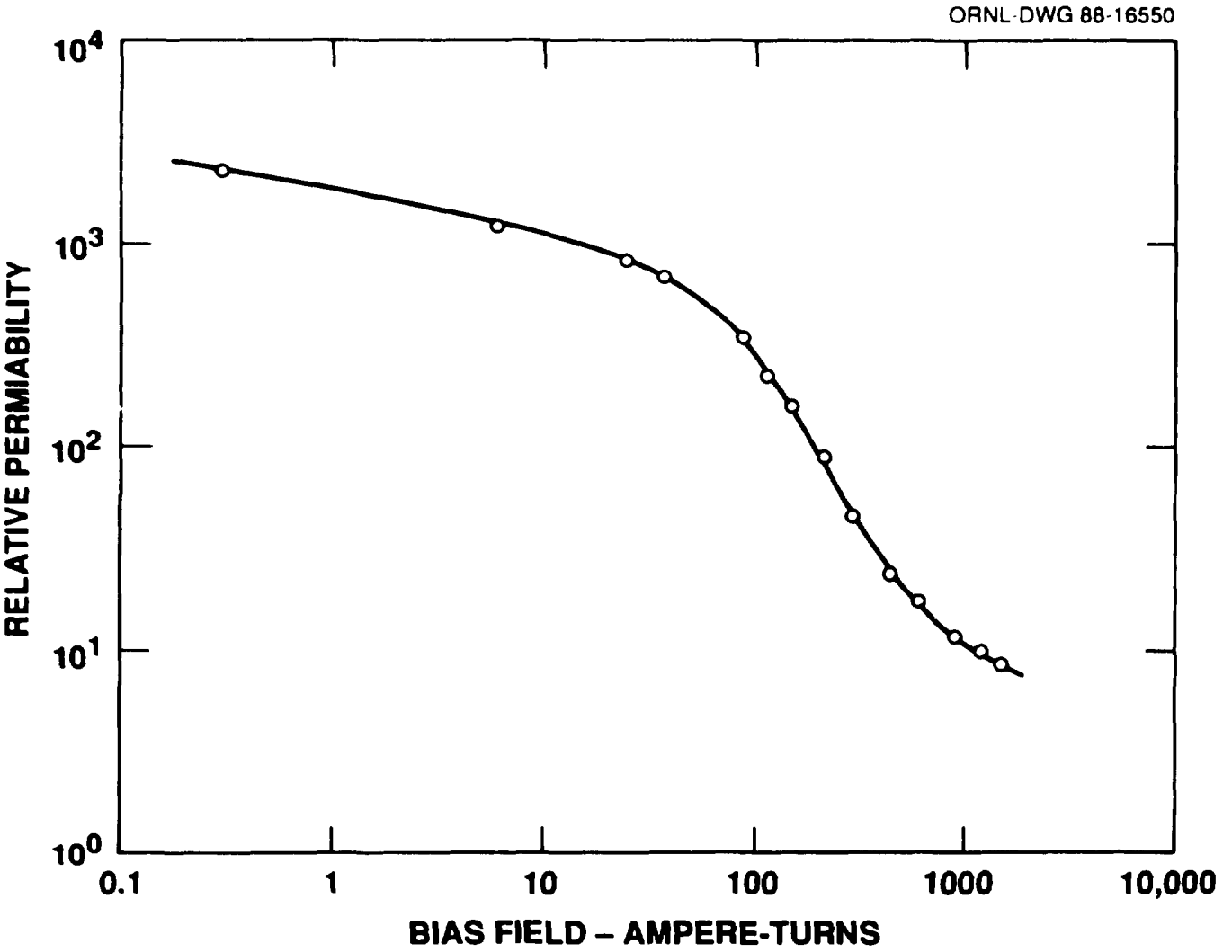

Fig. 5.2-3 Relative permeability of the SY7 ferrite as a function of dc excitation on a log-log scale.

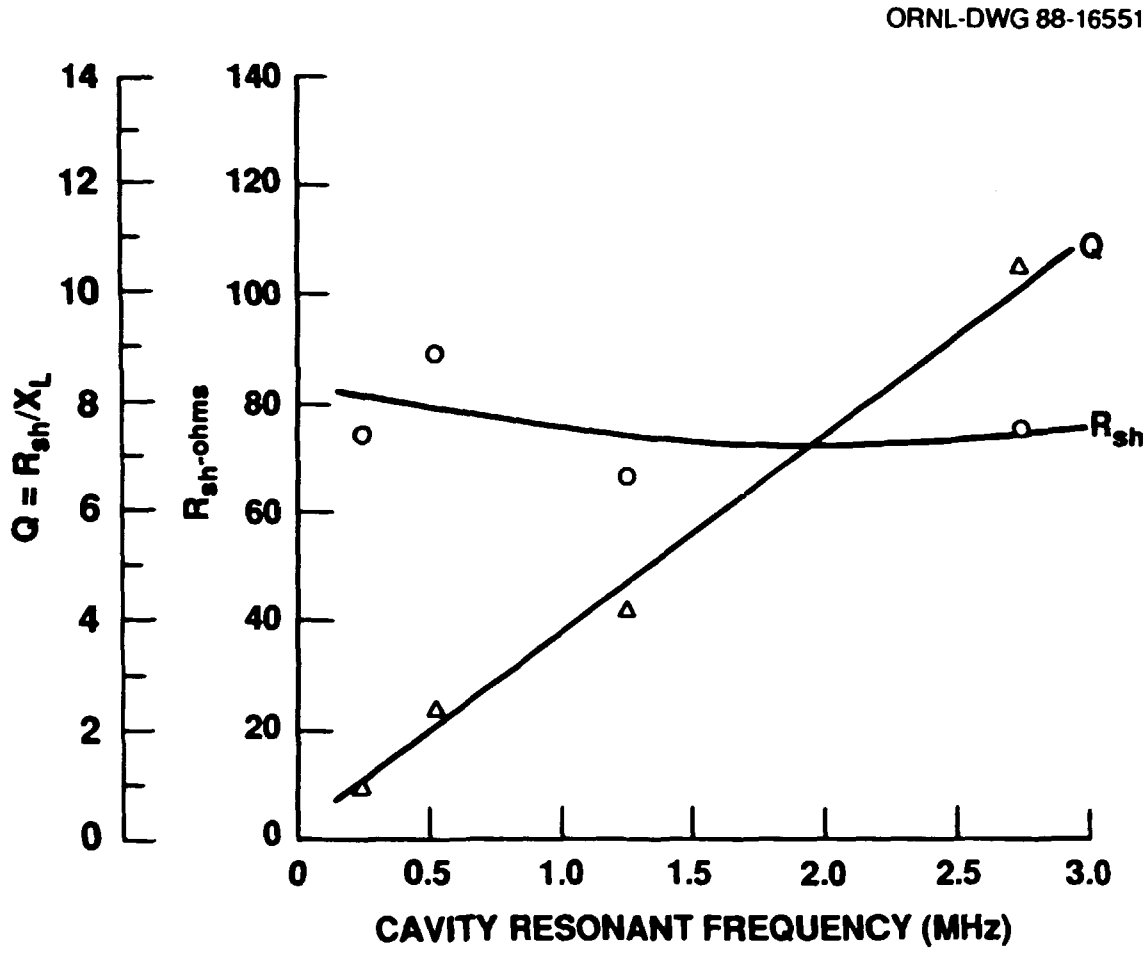

Fig. 5.2-4 Cavity "Q" and shunt resistance as a function of frequency.

ORNL Photo 10257-88

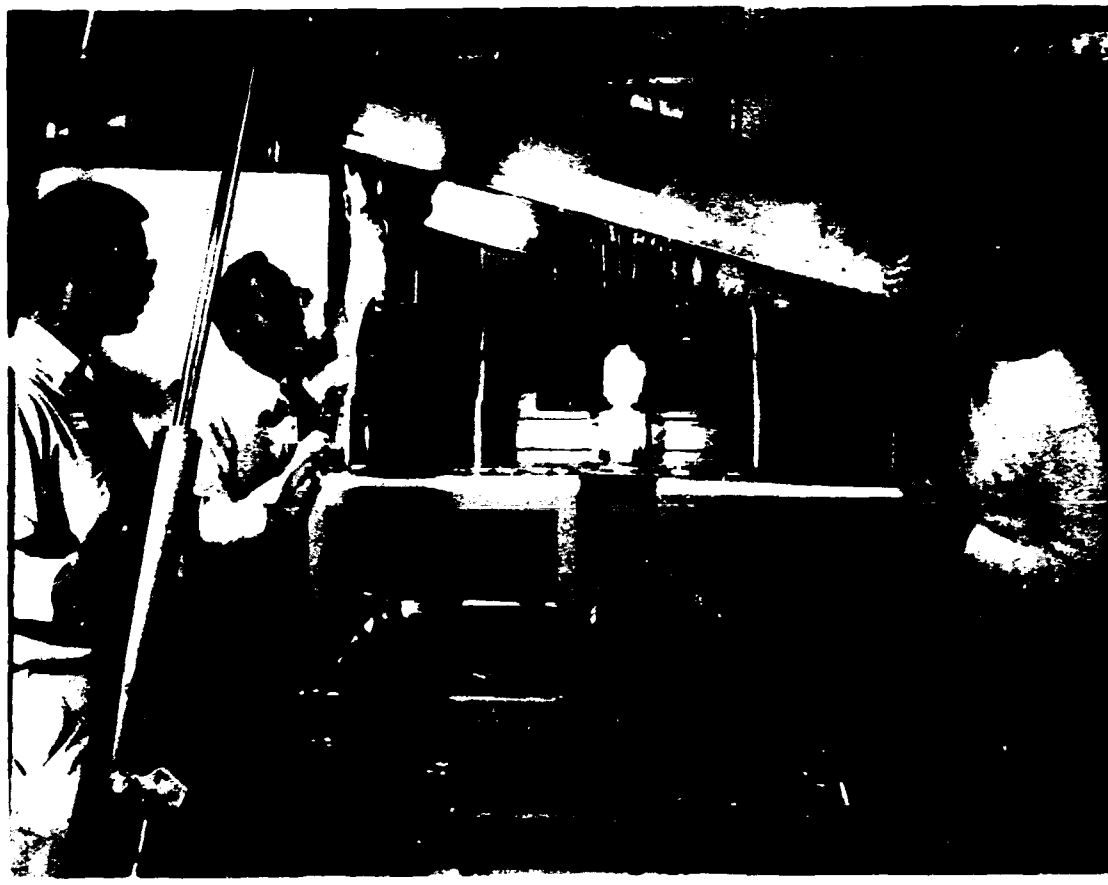

Fig. 5.2-5 Photograph of the rf cavity with the top half of the outer conductor raised above the structure. The ferrite core configuration has 8 rings on each end of the cavity. Water lines are attached to each of the ferrite cooling rings and extended to the water manifolds on the lower part of the cavity stand. Some of the several vacuum capacitors which comprise the 8000 pF of accelerating gap capacitance are also visible.

single-ended, 400-W, rf power amplifier through a ferrite-core transformer which provides a balanced output at appropriate impedance level. The complete cavity will need a 20-kW amplifier with a balanced output.

5.3 Prototype Dipole Magnet

The critical path for HISTRAP construction involves the design, engineering, prototyping, measuring, modifying, production, installation, and alignment of a laminated pulsed magnet system consisting of dipole, quadrupole, sextupole, and corrector elements. The dipoles are the most important magnetic elements and present some special problems. These dipoles are short with a large sagitta, producing a complicated 3D geometry and integrated field profiles which depend heavily on end effects. In addition, the dipoles have a large gap to contain vacuum bake-out insulation, have a "C" design to allow for merged laser beam studies, require a maximum field of 1.6 T, and need good field quality at both high and low excitation. Because of these uncertainties, a prototype dipole has been designed, fabricated, and is being measured.

5.3.1 Dipole Design

A sketch of the dipole was shown in Fig. 4.5-1. The yoke is 123-cm long, has a 12.8-cm sagitta, and has parallel ends giving 22.5° beam entrance and exit angles. A 7-cm gap and 12-cm horizontal good-field width are required. The 110-cm-high x 101-cm-wide lamination cross-section is standard and the shims and Rogowski roll-off were essentially scaled from the Fermi National Accelerator Laboratory (FNAL) designed and measured Loma Linda medical synchrotron dipole [Lo87]. The initial Rogowski end cuts also follow standard FNAL practice. Figure 5.3-1

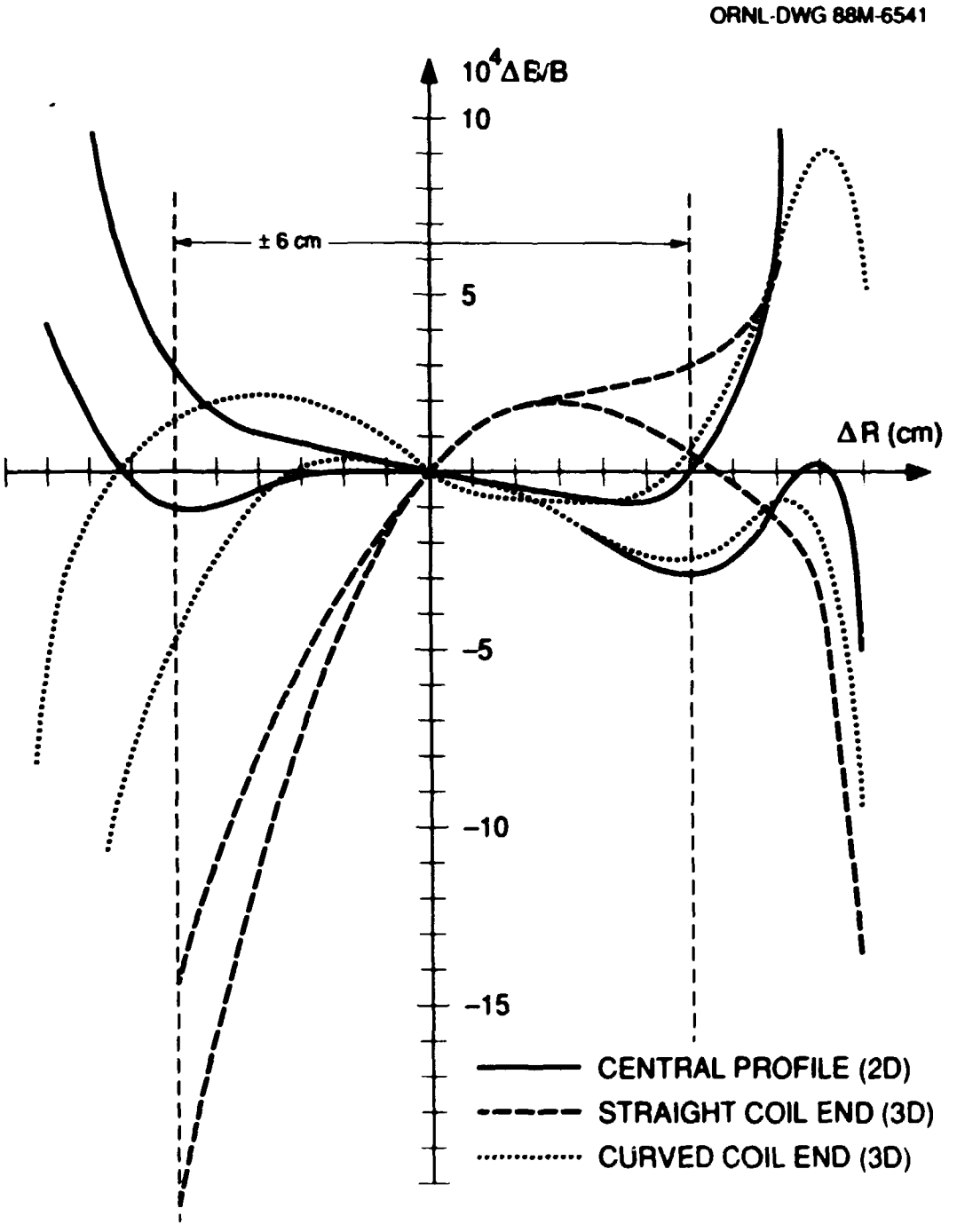

Fig. 5.3-1 Tosca calculations of field profiles for the HISTRAP prototype dipole magnet. Results for both the low, 0.8 T, lower curves, and high 1.6 T, upper curves are shown. The 2D profiles show the calculated field in the center of the dipole, whereas the 3D profiles show the calculated field, with end effects, integrated along an ion trajectory through the complete magnet. Results for both straight and curved coil ends are shown.

shows relative deviations from a pure dipole field as a function of horizontal distance from the central trajectory as calculated by the 3D magnet code TOSCA [Ve88] for excitation at 0.8 T and 1.6 T. The upper curve of each type in Fig. 5.3-1 is the low-field result at 0.8 T of excitation and the corresponding lower curve of each type is the high-field result at 1.6 T of excitation. The solid curves are the field profiles in the center of the dipole and are identical to results from the 2D magnet code Poisson [Ha66]. The permeability drop at high field causes the two curves to separate by about 4×10^{-4} at ±6 cm, the horizontal good-field requirement. Equal inside and outside shims give a small quadrupole component to the field profile.

The dashed and dotted curves show calculated 3D TOSCA results, including end effects. These profiles are average field deviations obtained from integrating along the ion trajectories through the dipole. The dashed curves show the integrated profiles with straight end coils parallel to the yoke end. The end effects are large and produce appreciable quadrupole and sextupole components. These components were set to zero by curving and angling the coil ends, as shown in Fig. 4.5-1. In particular, the angle of the end coil with respect to the yoke adjusts the integrated quadrupole component, and the curvature of the end coil adjusts the integrated sextupole component. These parameters were optimized to give the calculated field profiles shown as the dotted lines in Fig. 5.3-1. With this technique, most of the calculated integrated field deviations from the dipole ends were, in principle, corrected locally by the end coil shape.

5.3.2 Dipole Fabrication

From this physics design, a prototype dipole magnet was constructed by FNAL. In particular, FNAL was responsible for the detailed engineering and tooling design, yoke and coil fabrication, and the final magnet assembly. The yoke design and assembly was similar to that used for the Indiana University Cooler Ring dipoles [S187]. In particular, the yoke was fabricated from laminations which were punched from 16-gauge SAE 1004-1006 cold-rolled sheet steel purchased from Inland Steel. The steel had a phosphate coating to provide electrical insulation between laminations and had a measured permeability of 182 at an excitation level of 100 Oersteds.

In order to eliminate dimensional problems induced by the stress in the steel, the laminations were punched with a two-stage die. The first punch produced laminations from the blanks which were about a half-inch larger than desired. These laminations were then allowed to relax over night before the final dimensions were punched. Sample laminations were dimensionally checked with a Cordax coordinate measuring machine. The pole tips were flat and parallel within 0.001 in. as required in the specifications.

After being washed to improve adhesion and coated with a thin layer of epoxy, the laminations were stacked in an assembly fixture. This fixture was used to stack both the dipole and also the end assemblies, which consisted of removable 3.0-in.-thick end packs bolted to 1.0-in.-thick back packs. Four end packs were fabricated; two end packs were machined with the design Rogowski contours, and two are spares, should new end cuts be required. The laminations were stacked

between these fabricated end assemblies with the gap facing down. The laminations were centered about a vertical spacer projecting into the gap and were stacked on two rails which determined the curvature of the magnet yoke. The yoke was then compressed to the proper length with a 25-ton press and fixed in length with long thru bolts in the stacking fixture. Steel plates, 0.75 in. thick, were welded to the top and bottom of the dipole and four curved plates were welded into the side indentations. Finally, the epoxy between laminations was cured at 300°C for five hours. Laminations were glued together with the exception that the end packs were bolted to the back packs.

The four coil pancakes were wound and cured using only one fixture. The 0.625-in. x 1.750-in. copper conductor was first wrapped with one layer of half-lapped B-stage 7-mil mica tape, and then second wrapped with one layer butted B-stage 7-mil glass tape. Each entire pancake was first wrapped with one layer butted 30-mil scotch ply, and then second wrapped with one layer half-lapped B-stage 7-mil polyester/glass tape. The coils were cured on the winding fixture at a temperature of 300°C for five hours. The electrical leads, water leads, and jumpers connect to the coils at the outside center of the dipole. The coils can be tilted at an angle to the pole face as an adjustment to cancel a measured quadrupole field in the dipole. Figure 5.3-2 is a photograph of the assembled magnet.

5.3.3 Field Mapping System

A system was designed and constructed to map the magnetic field of the prototype dipole and other magnetic elements including the EBC solenoids and toroids. The field sensing device is a temperature-

ORNL Photo 10259-88

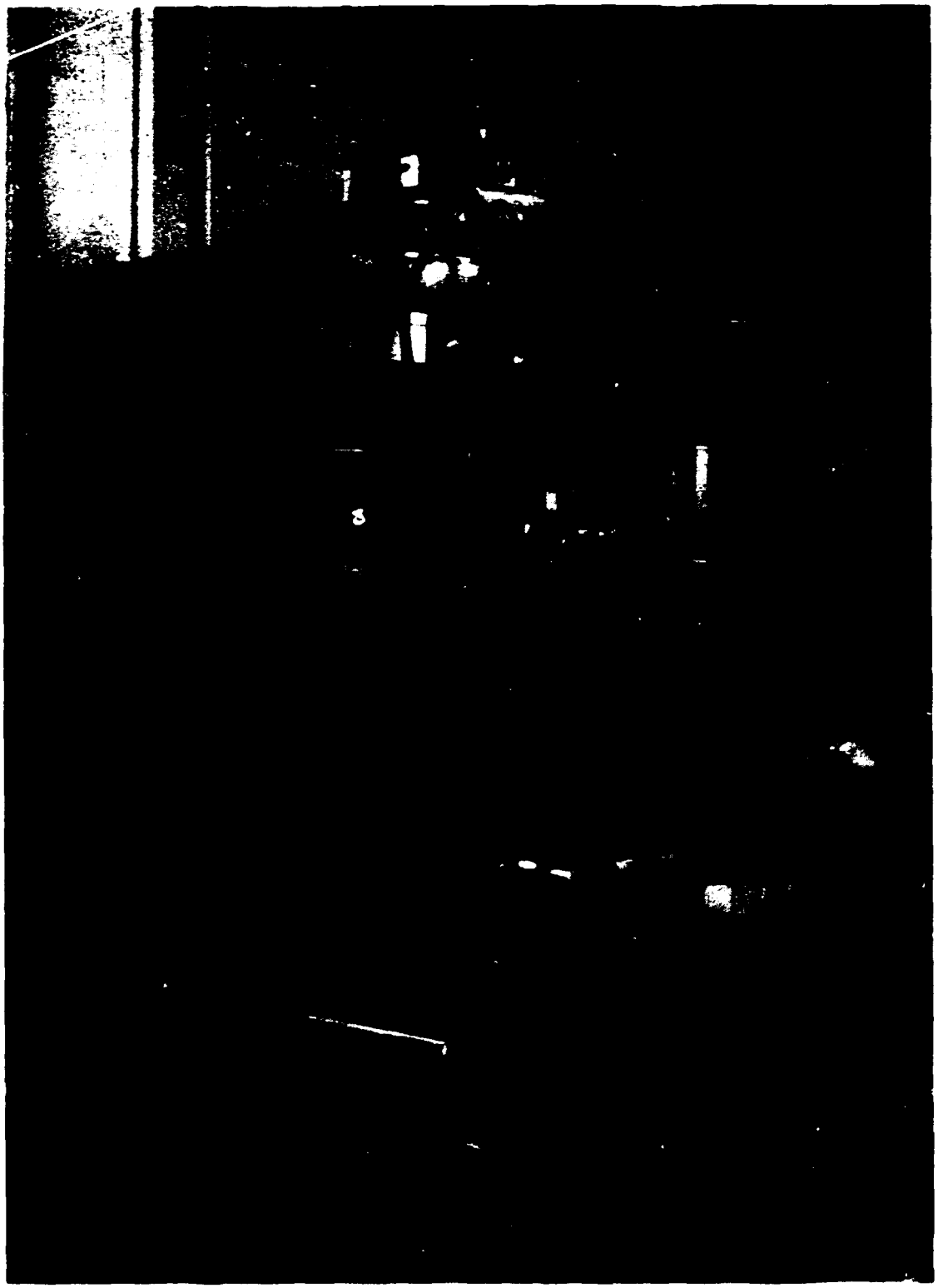

Fig. 5.3-2 Photograph of the HISTRAP prototype dipole.

compensated Hall-effect probe. Positioning of the probe within the field area is accomplished by a personal computer (PC) based, x-y positioning system. The mapping structure shown in Fig. 5.3-3 is built on a 4 x 10 ft, nonmagnetic, stainless-steel laser table. Two case-hardened and ground-bearing shafts are mounted along the 10-foot dimension at a separation distance of 43.75 in. on center. Twin ball-bearing bushings are mounted on each rail and are spanned by an aluminum bridge assembly, to yield one degree of motion. Similarly, two shafts and associated bearings are mounted along the bridge, spanned by an aluminum plate, to yield the second degree of motion. Two slide and vise assemblies are mounted vertically on the top bridge to hold a horizontal boom to position the Hall probe in the dipole gap.

A cantilevered, nonmagnetic boom was constructed to hold the Hall probe using lightweight honeycomb paper wrapped with resin-impregnated, graphite tape. Boom dimensions are 1.5 in. thick, 4 in. wide, and approximately 10 ft long. Baking at approximately 180°F hardened and bonded the tape. A G-10 (epoxy/fiberglass) clamp was inserted into a notched end of the boom to hold the probe. Motion in each of the two horizontal degrees of freedom is accomplished by electronic control. Ball screws driven by stepping motors are attached to the bridges by preloaded ball bearing housings. Travel in the horizontal plane is limited to 85 by 35 inches and the maximum manual vertical adjustment is 6 inches.

The control and data acquisition system is shown in Fig. 5.3-4. A stepper motor controller board is mounted in the PC. The board controls the initial and maximum stepping rates, acceleration rate, stepping

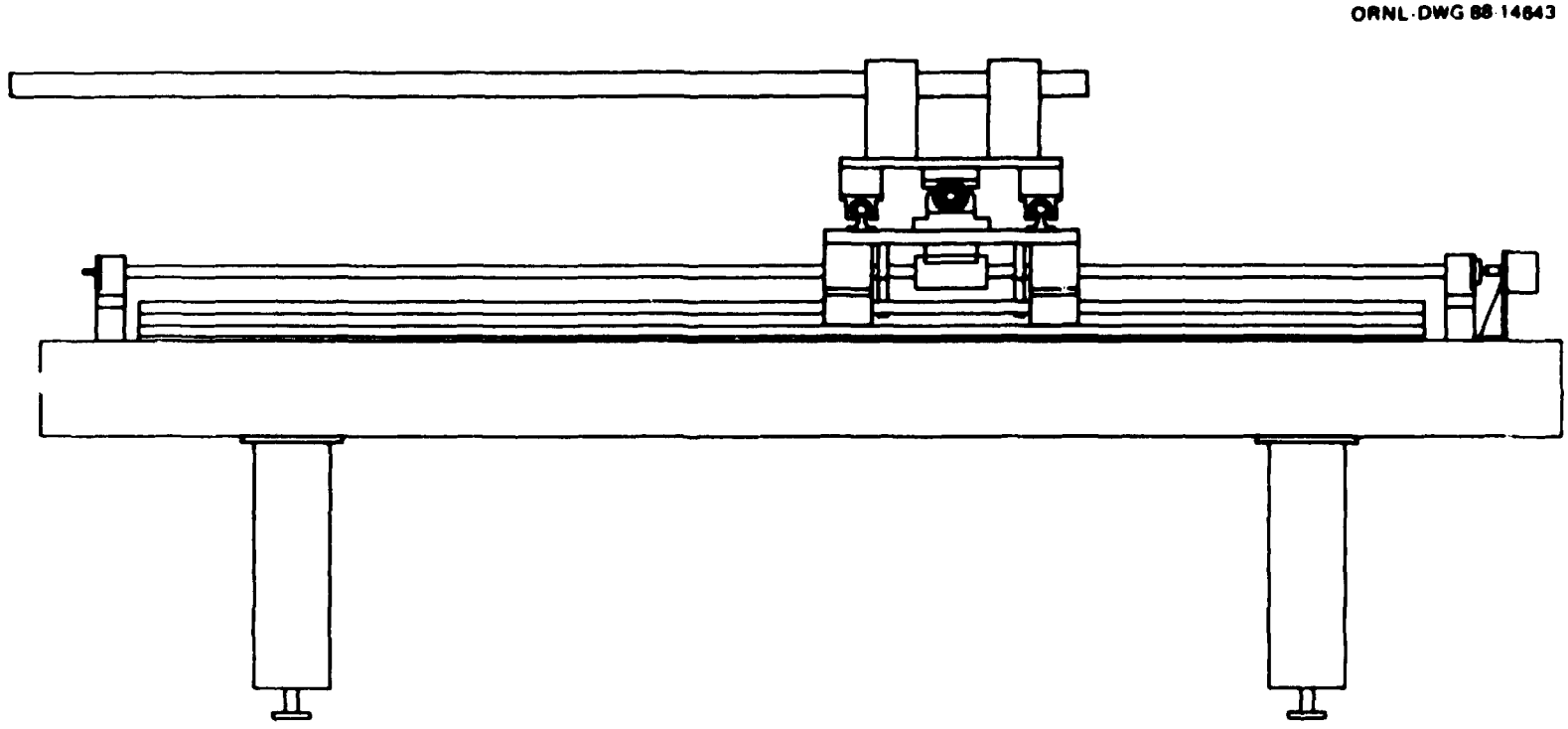

Fig. 5.3-3 Computer controlled magnetic field mapping structure. Fields in a horizontal area of about 4 feet by 8 feet can be measured.

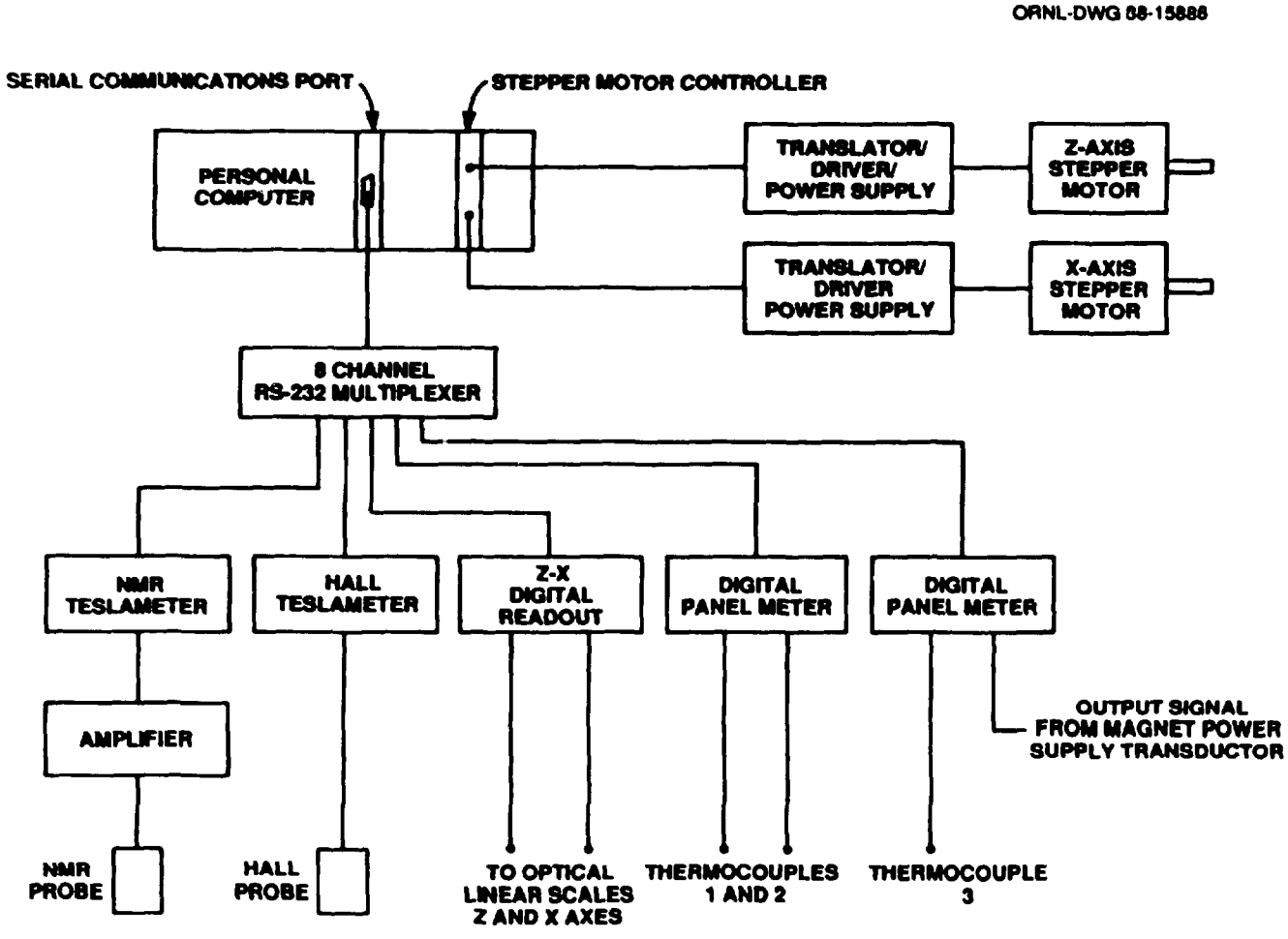

Fig. 5.3-4 PC based control and data acquisition system for the magnetic field-mapping structure.

direction, and number of steps for a maximum of two motors. Step-to-pulse translator/driver/power supply units provide a necessary external interface between the PC board and motors. Each step corresponds to a 1.8° rotation of the motor shaft. Motors are coupled to the lead screws using timing belts to damp out vibrations.

Optical linear scales of 0.01-mm resolution are mounted along each of the horizontal axes to provide position feedback. Signals from the scales are input to a digital readout box which converts them to ASCII strings for display and transmission to the PC. The Hall probe contains a thermal sensor and is connected to a Teslameter which compensates for fluctuations in temperature. A removable NMR probe is mounted in the center of the dipole for calibration of the Hall probe. At regular intervals during the mapping process, the Hall probe is positioned over the NMR and comparisons made. Three external thermocouples are used to provide temperature measurements on and near the dipole. Each of the above devices provides output through an RS-232 serial communication interface.

During the mapping process, horizontal motion is controlled by a compiled BASIC program, written in-house, through programming stepping motor controller integrated circuits on the PC board for specified motion patterns. The software also inputs information from the RS-232C devices, displays it, records relative extrema, and writes the information to a floppy disk for later data reduction.

5.3.4 Field Measurements

Preliminary mapping of the prototype dipole has been completed at low excitation levels. The field was mapped along 21 orbits, 10 orbits

on either side of the design orbit. The orbits were separated by 1 cm. Mapping points along an orbit were separated by a path length of 5 mm and a total path length of 209 cm was measured. Positioning accuracy along a single axis is guaranteed to within 0.04 mm for each of the 8799 mapping points.

Measurements have been completed at 50, 100, 180, 300, 400, and 500 A of excitation, spanning a magnetic field range from 430 to 3540 G. The results of these measurements are shown in Fig. 5.3-5, which plots field profiles in the central region of the dipole and field profiles integrated along the ion path length for the six excitation levels. These preliminary measurements at 300, 400, and 500 A of excitation, show a small quadrupole component in both the central profiles and integrated profiles. This quadrupole component was not predicted by either TOSCA or POISSON and also appears in the IUCF [S187] and Heidelberg [Kr88] dipoles. The origin of this difference is not understood. In any event, this quadrupole component can be compensated, if needed, by adjusting the main quadrupole strengths, fabricating pole face windings, or making small geometrical changes. The measured sextupole and octupole components of the field are small, and consistent with the magnet code predictions. With increasing excitation, the quadrupole component decreases and changes sign. This decrease is consistent with a remnant field measurement of 30 G with a ±2-G quadrupole component at ±6 cm. The field quality at about 900 G of excitation, required for storage of decelerated ions, would be excellent. Field maps will be made for higher excitation levels when the required power supply is delivered.

ORNL-DWG 89-16495

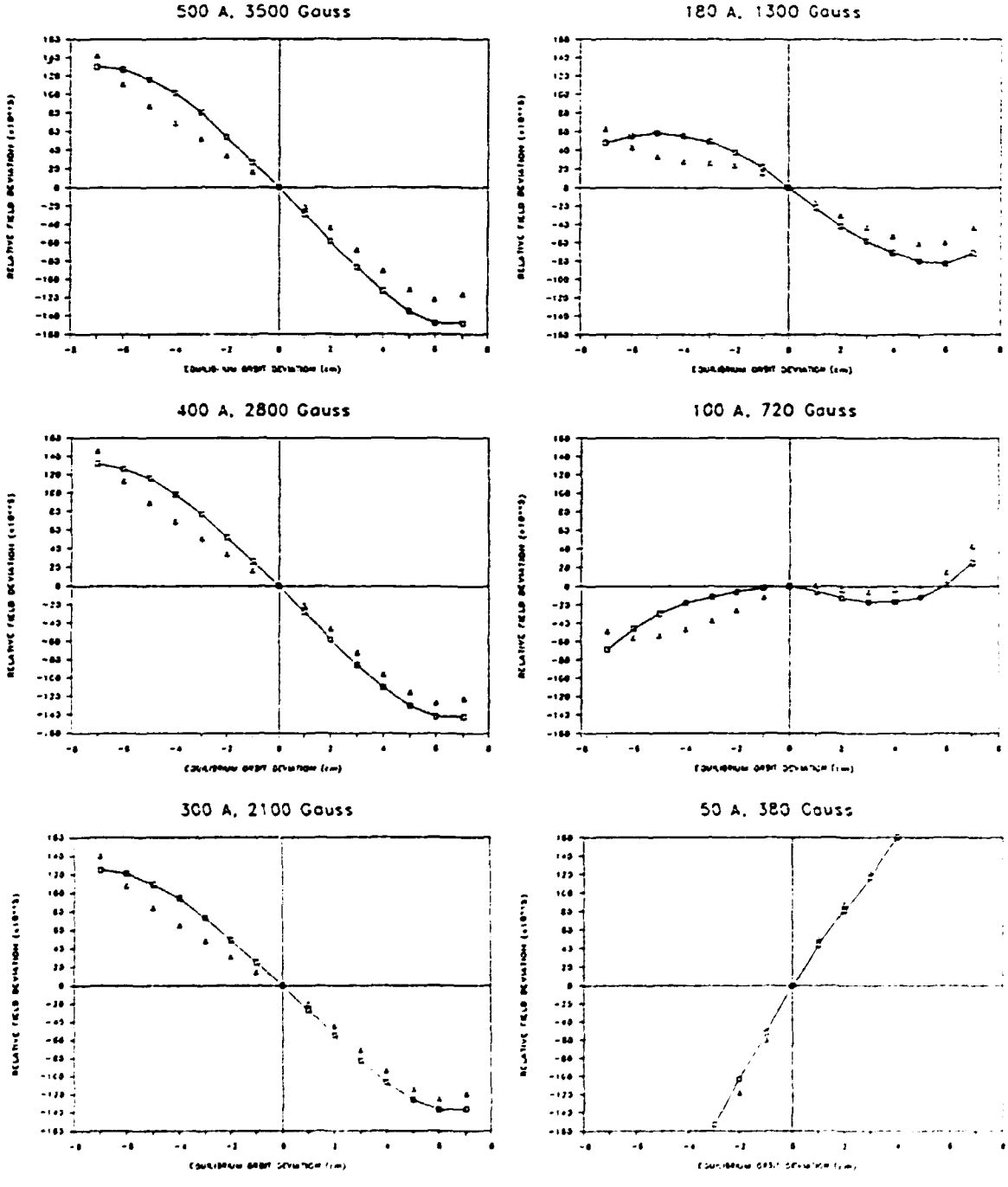

Fig. 5.3.5 Measured central (2D) and integrated (3D) magnetic field profiles of the HISTRAP prototype dipole at low excitation levels. The integrated results are the circles connected by straight lines, whereas the central results are the triangles.

5.4 Prototype Control System

The conceptual design for the HISTRAP control system was shown in Fig. 4.5-19. A MicroVAX II/GPX workstation will provide all operator interaction with HISTRAP and will maintain the complete HISTRAP data base. A major advantage of the MicroVAX is that it provides a software environment which is acceptable to accelerator physicists who must access the HISTRAP data base and provides an operating system for which several accelerator physics codes exist. However, many hardware and software features of the MicroVAX are not ideally suited for real-time control systems. Consequently, all real-time functions will be relegated to approximately eight VMEbus processors. The MicroVAX and the VMEbus processors will communicate over a private local area network.

The hardware for a prototype control system, a subset of the HISTRAP control system, has been purchased. This subset consists of the MicroVAX connected directly to one VMEbus crate. All control hardware will be in the VMEbus crate. Initially, all control functions will be provided by the MicroVAX since real-time response is not critical. However, the hardware interface between the VMEbus crate and the MicroVAX will allow operation of a VMEbus processor in conjunction with the MicroVAX. Therefore, this system will also be used to investigate software development problems associated with a distributed processor control system. The prototype control system was used initially to control the vacuum test stand.

5.5 Electron Beam Cooling Experiment

One Physics Division staff member spent six months on assignment at CERN in Geneva, Switzerland, working with the Low-Energy Antiproton Ring (LEAR) electron beam cooling group, a collaboration between CERN and the Kernforschungszentrum Karlsruhe. The electron beam cooling device had been developed and built, based on experience and hardware from the CERN Initial Cooling Experiment. During this time, the cooler was not installed in LEAR; the operation of the cooler was still being optimized and much hands-on experience was gathered. Eighteen months later, following the installation of the cooler in LEAR, our staff member returned to participate in experiments to cool proton beams.

The first cooling experiments in LEAR were performed using proton beams having energies of 49 and 21 MeV with momenta of 310 and 200 MeV/c, respectively. The number of stored protons ranged from 10^7 to 3×10^9. The diagnostics used to determine the effects of electron cooling were primarily the neutral hydrogen detector signal and the Schottky signal. A schematic diagram of LEAR and the electron cooling device is shown in Fig. 5.5-1.

Radiative recombination (RR) of protons with the electrons of the cooling beam produces fast H atoms. The H atoms are unaffected by the dipole magnet following the cooling section and, as shown in Fig. 5.5-1, continue in a straight line into an extension of the vacuum system. They then exit the vacuum system through a thin Al window and strike a multiwire proportional counter (MWPC) combined with scintillation detectors which allow one to determine their rate of arrival (RR rate) and

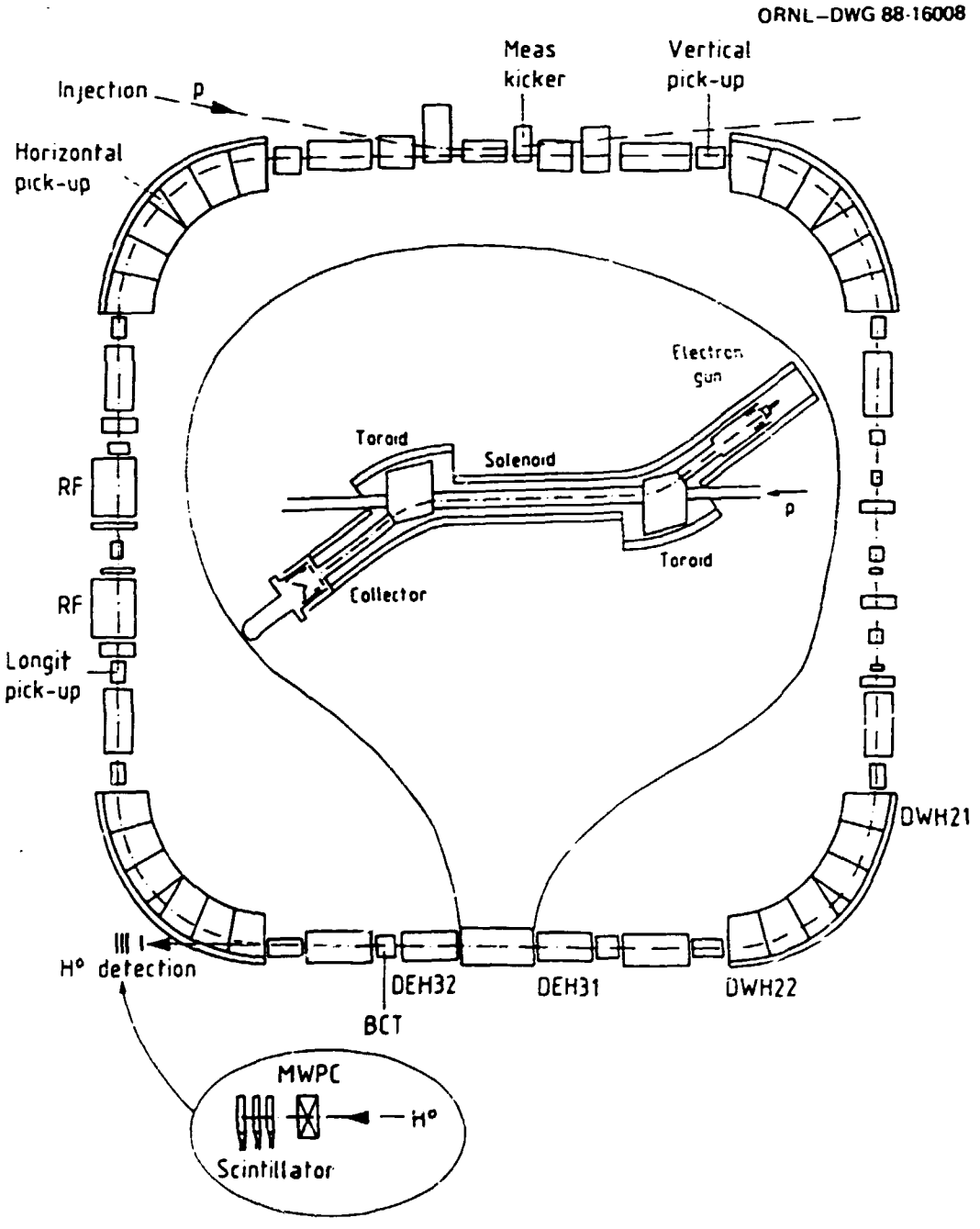

Fig. 5.5-1 Schematic diagram of LEAR; the inset shows the electron cooler in more detail.

their spatial distribution in the transverse beam direction. The RR rate is related to the transverse energy spread or effective transverse "temperature" of the electron beam. The colder the electron beam, the lower will be the emittance ε and momentum spread $\Delta p/p$ of the cooled proton beam. The size of the beam as determined by the MWPC was related to the emittance of the proton beam through the distance from the cooler and the horizontal and vertical beta functions. The values determined from the H atom measurements were: a transverse electron temperature of 0.25 eV, a horizontal and vertical emittance of 2.7 and 7.5π mm-mrad, respectively (initially $\varepsilon = 30\pi$ mm-mrad). The Schottky signals were analyzed with fast spectrum analyzers as used in the standard operation of LEAR and the width Δf of the frequency spectrum is related to the width of the momentum distribution by

$$\Delta f/f = n\, \Delta p/p \ . \qquad (5.5\text{-}1)$$

The broad Schottky trace prior to electron cooling is shown in Figure 5.5-2 and the superimposed narrow trace was taken a few seconds after the start of cooling. Figure 5.5-3 shows a series of such spectra recorded every second after proton injection which illustrates the reduction in $\Delta p/p$ from 6×10^{-3} to a value below the spectral resolution of 3×10^{-4} within 5 seconds. The lowest momenta spread measured was 2×10^{-5}. Observation of the sidebands of the Schottky signal induced in the transverse pickups allowed the extraction of transverse cooling times. The height of the satellite peaks of the transverse Schottky signal, relative to the height of the peak of the longitudinal Schottky signal, is proportional to the square root of the beam emittance. By measuring the decrease of this ratio as a function of time, as shown in

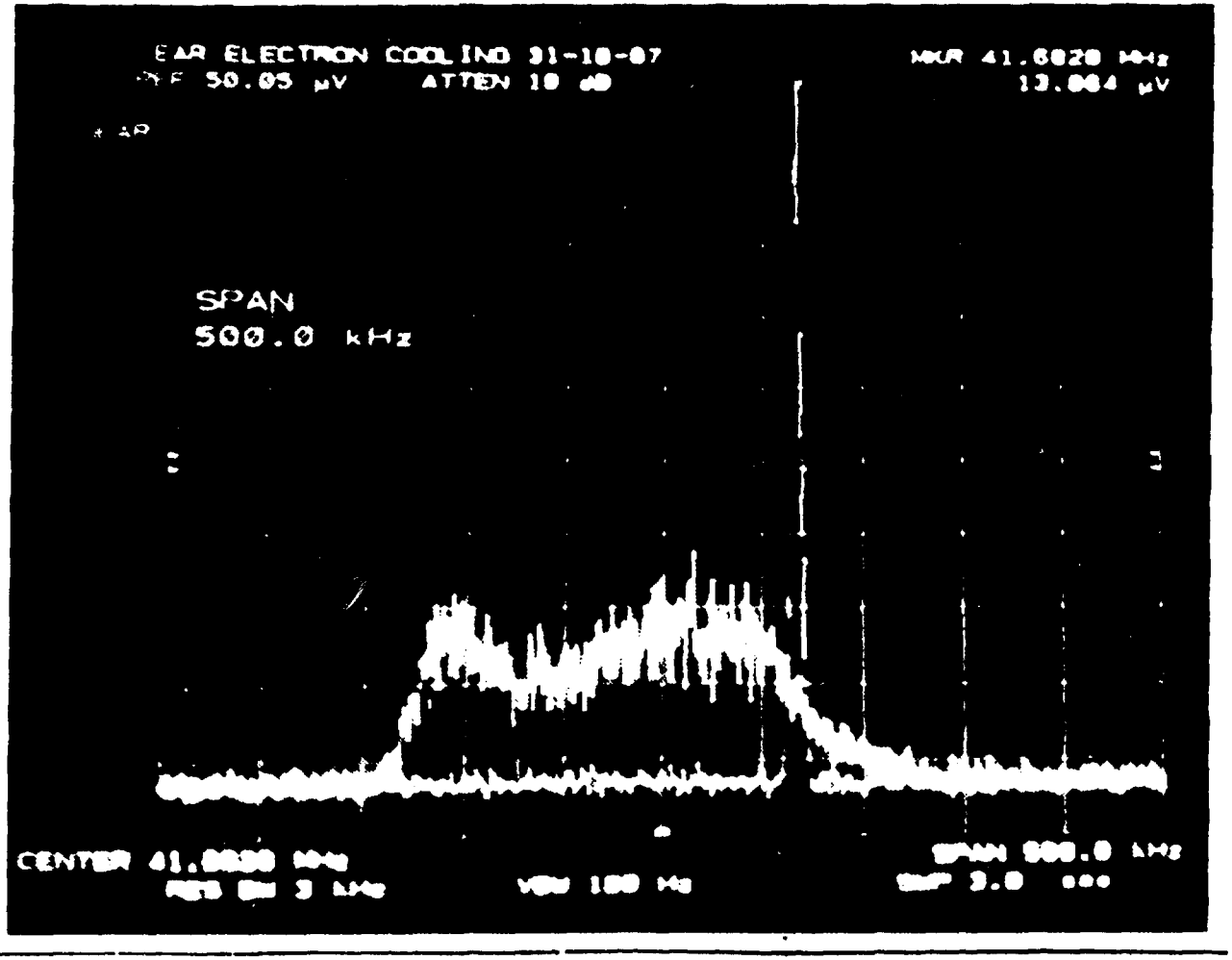

longitudinal Schottky scan

Fig. 5.5-2 Frequency spectrum of LEAR proton beam just after injection without cooling. Second trace, the sharp peak, shows the frequency spectrum after a few seconds of cooling.

ORNL-DWG 88-16006

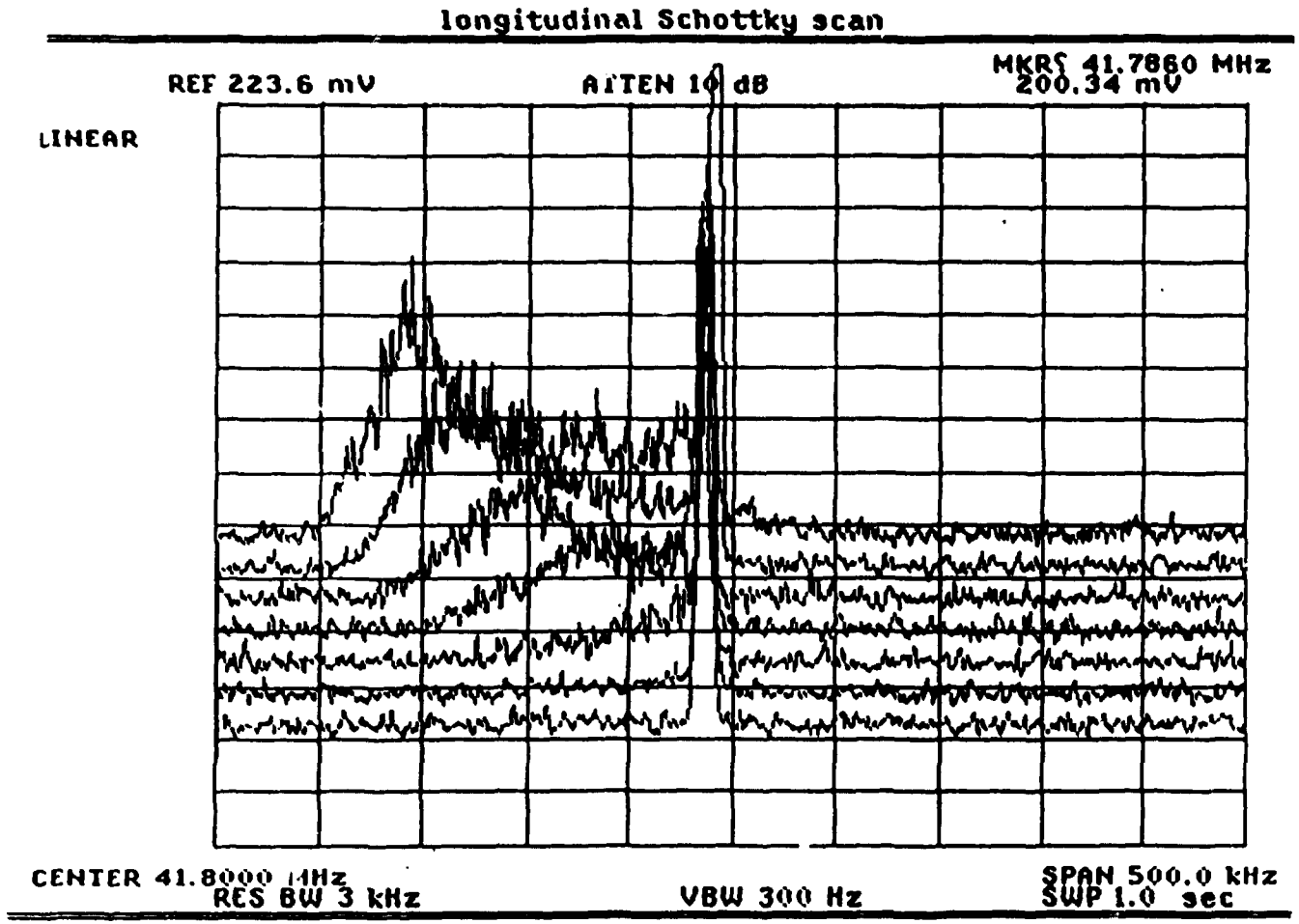

Fig. 5.5-3 LEAR proton frequency spectra measured every second after injection with electron beam cooling.

Fig. 5.5-4, the transverse cooling time was determined to be about 1.5 s.

Cooling experiments were also carried out with bunched proton beams. The proton beam was injected and rf bunched and then the cooling was initiated. The decrease in Δp, caused by the cooling, reduced the bunch length and increased the signal amplitude observed on a position pickup. The change in signal amplitude with time, Fig. 5.5-5, was used to deduce the longitudinal cooling time of 3 s for a bunched beam. The H atom arrival times are bunched when the proton beam is bunched. A time-to-digital converter (TDC) was started with the arrival of an H atom pulse and stopped with a reference phase signal from the rf bunching circuit. The TDC output was fed into a multichannel analyzer to yield the time distribution of the H atom arrivals and, using the known velocity of the protons, the spatial extent of the bunched proton beam. The time spectrum shown in Fig. 5.5-6 has a clean Gaussian distribution and little background, indicating that all protons are captured in the stationary rf bucket. The time distribution implies a bunch length of 2.5 m. During bunched-beam operation, the average RR rate and the beam profile were also determined from which one can deduce that the beam size is the same as for a coasting beam, but that the transverse electron temperature, equal to 0.32 eV, is slightly higher than for a coasting beam.

These experiments show that electron cooling can increase the phase-space density of particle beams stored in LEAR by many orders of magnitude within a few seconds. The short cooling times and small equilibrium emittances measured are in accordance with design estimates

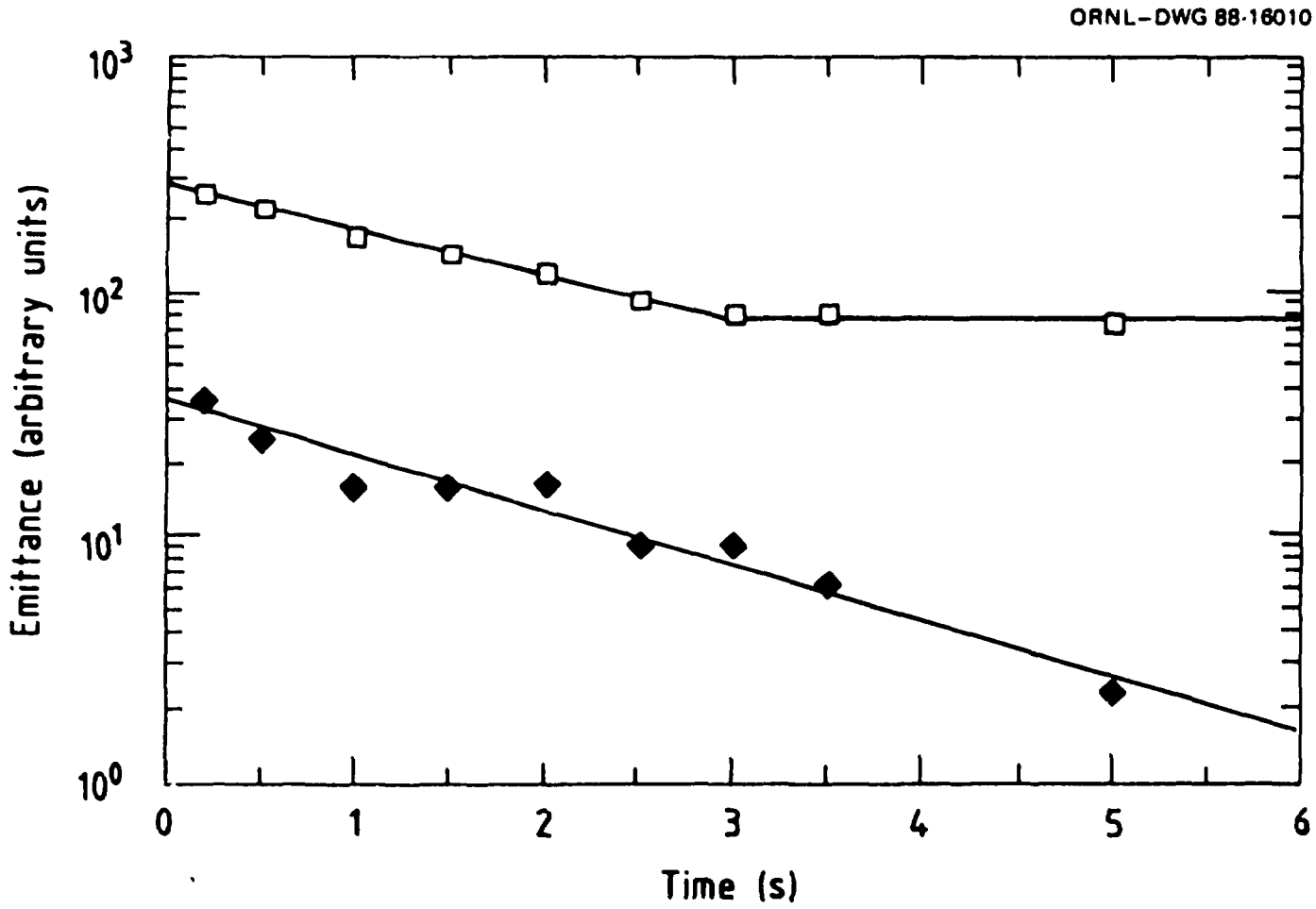

Fig. 5.5-4 Evolution of horizontal (empty square symbol) and vertical (solid diamond symbol) beam emittances as a function of time after cooling was activated.

ORNL-DWG 88-16009

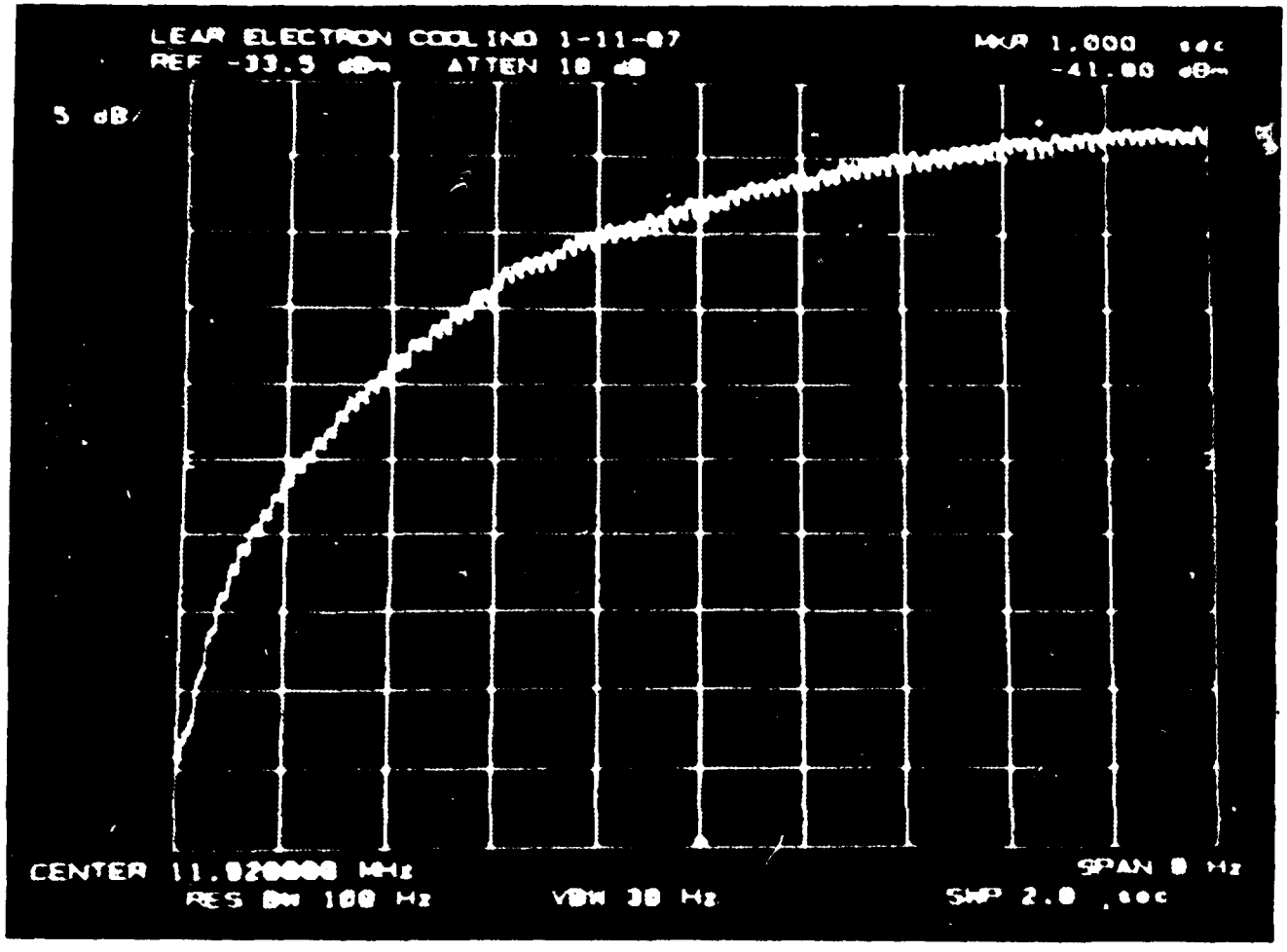

Fig. 5.5-5 The time evolution of the 10th harmonic of the bunch signal observed on one of the LEAR position pick-ups (sum signal) after cooling is activated. (Ordinate = log scale of 5 dB/div.)

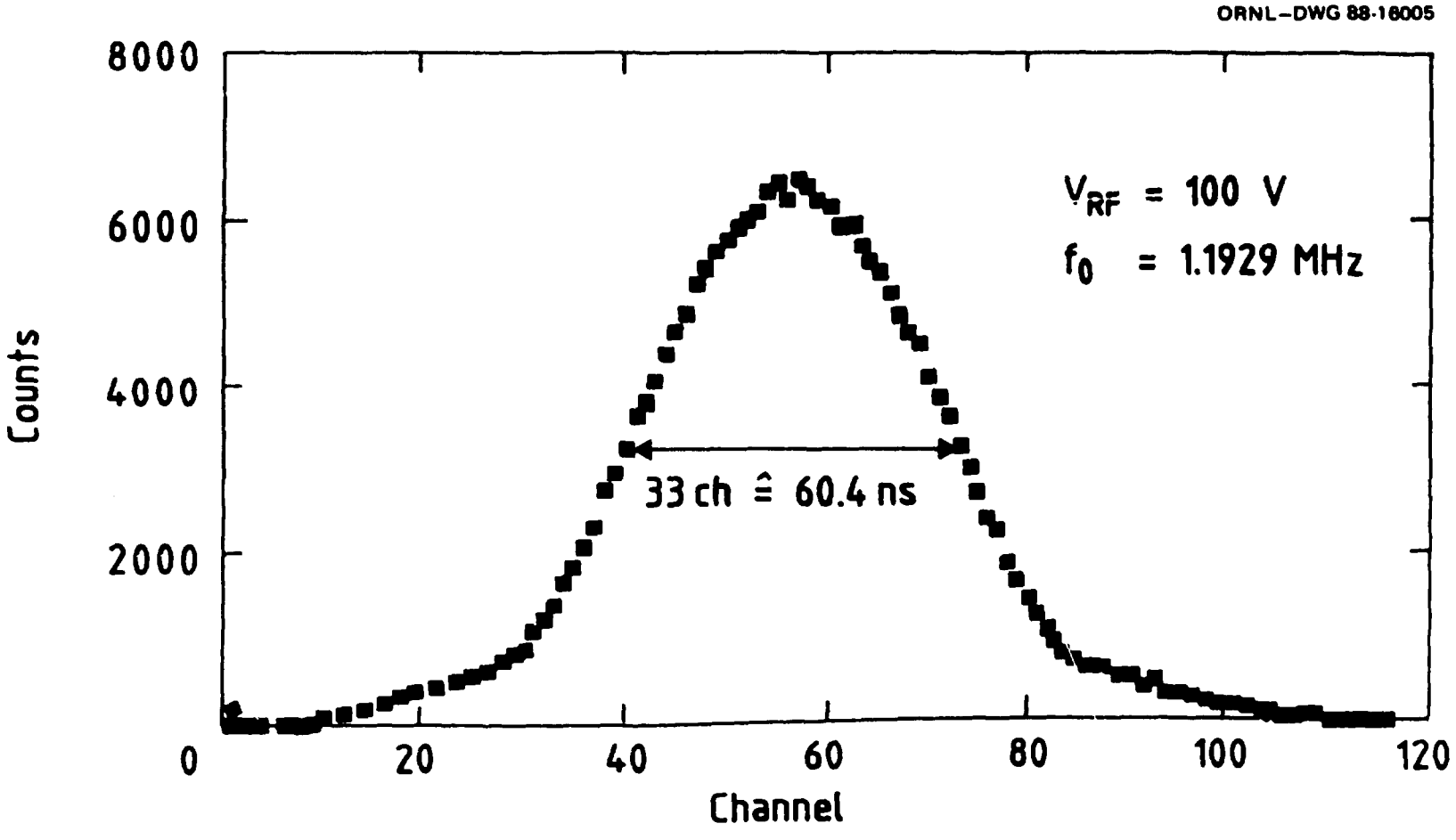

Fig. 5.5-6 *Time distribution of the H atom arrival times with respect to the RF phase for a bunched proton beam.*

and goals set for electron cooling, and confirm the high quality of the electron beam. This experience will impact directly on the final design and operation of the electron cooler for HISTRAP.

6.0 CONVENTIONAL FACILITIES

The principal factor influencing the present building concept was the requirement to utilize the Holifield Facility 25-MV tandem electrostatic accelerator as one of the injectors for HISTRAP. The final configuration thus reflects the desire to capitalize on the presence of the best injector available anywhere in the world, and to make optimum use of available resources associated with the facility.

6.1 Building Structure

The new building construction planned for this project will include two additions to the Holifield Facility complex; a south-side addition to house the HISTRAP ring, in the space remaining adjacent to the tower housing the 25-MV tandem; and a second floor addition to the existing atomic physics annex to house power supplies and electrical distribution equipment. Some reconfiguration will be done within the existing atomic physics annex to convert it to the synchrotron injector room, by providing for the injection line from the tandem and installing the ECR/RFQ alternate injection system. In addition, the tandem control room within the existing facility will be expanded to accommodate the HISTRAP control system.

In more detail, the building additions and modifications to the existing facility consist of the following.

6.1.1 Synchrotron Room

The new ring room, with an area of approximately 4000 sq ft, will be located as shown in Fig. 6.1-1. The construction site will be excavated to rock, which is approximately 7 ft below the future floor elevation of 807 ft 6 in. The excavation will be backfilled with compacted crushed rock to an elevation of approximately 806 ft to prepare a working surface for construction. Site preparation will also include relocating an existing 16-in. cast iron water line. The existing building ground grid system will be extended around the new building addition. New walls will be reinforced 12-in. concrete blocks. The roof will be designed for a live load of 300 psf. The roof will be furnished with a 10 ft x 10 ft equipment hatch and a 12 ft x 16 ft reinforced concrete pad which will serve as a temporary loading/unloading pad for the existing overhead monorail at the top of the tandem tower. A grating walkway will be placed across the roof of this addition to connect the existing second floor computer room emergency exit to a new exterior steel stairway.

6.1.2 Utility Room

A second floor addition to the atomic physics annex, covering approximately 3000 sq ft in area, will house power supplies for the ring magnets and rf system, and contain suitable substations to accommodate the required pulsed and dc loads. The existing built-up roof and insulation on the existing structure will be replaced with a reinforced concrete slab. New concrete block walls will be constructed over the perimeter of the first floor structure to form the second floor

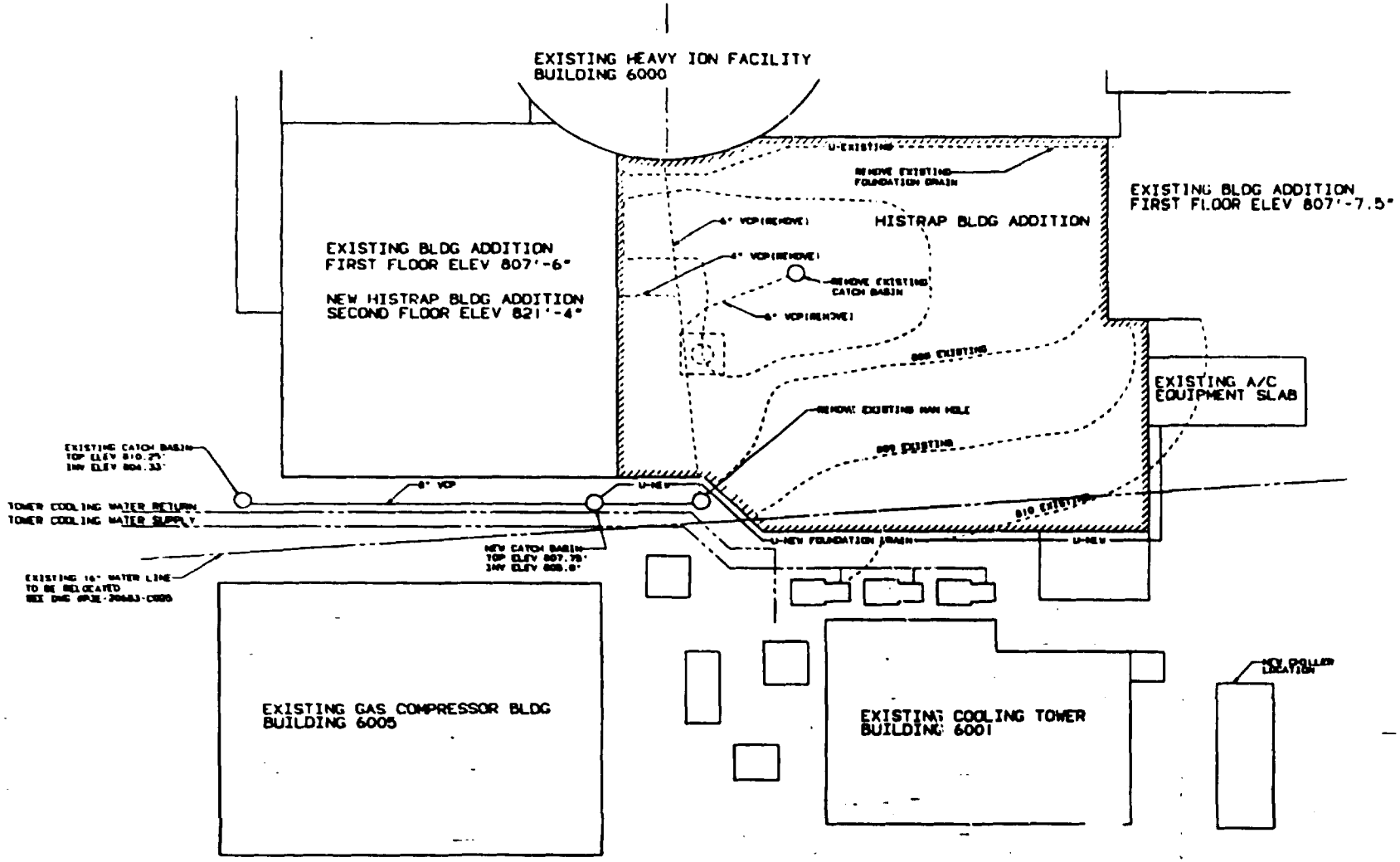

Fig. 6.1-1. HISTRAP building addition site plan.

addition. The new room will have a roof consisting of bar joists, metal decking, rigid insulation, and a built-up roof.

6.1.3 Control Room

The present area housing the control computers and console for the HHIRF tandem accelerator will be enlarged by removing existing lath and plaster walls and expanding into the two offices located immediately to the west of this area. A new raised computer floor will be installed in this expanded space and will match to the existing control room floor.

6.2 Building Services

The accelerator ring and the electrical equipment rooms will be heated and air-conditioned by separate roof-mounted air handling units containing a chilled water coil, hot water coil, 95% efficiency filters, and supply and return fans. The units will also utilize an economizer section capable of introducing 0-100% outside air into the space. Supply air will be distributed through externally insulated galvanized ductwork.

In the synchrotron injector room, the existing two five-ton fan coil units will be modified by the installation of high efficiency (95%) filter housings. The existing fan motors and drive sheaves will be replaced to compensate for the increased pressure drop of the high efficiency filters. Existing ductwork will be modified to accommodate the longer filter sections.

The control room will be air-conditioned by a down-flow computer room air conditioning system containing chilled water coils, electric reheat coils, humidifier, and 60% efficiency filters.

A new packaged air-cooled water chiller (100-ton unit) will be installed to meet the cooling demands of the new building additions. This unit will contain ethylene glycol for freeze protection, and will be installed in parallel with the existing 275-ton water chiller. A new concrete pad (approx. 10 ft x 20 ft) will be provided for the new chiller.

New 3-in. demineralized water headers will be installed from the main existing supply and return headers located on the third floor of the Holifield Facility. Three new 2-in. branch circuits will serve the injection room, the synchrotron room, and the second floor equipment room. Process water is available from a 1-in. header in the synchrotron injector room. This header will be extended through the east wall into the new addition. Hot water for the HVAC units will be obtained from the hot water/steam converter located on the third floor.

Fire protection will be provided by a new 6-in. line tapped into the existing 12-in. water main buried west of the facility. A wet sprinkler system will be connected. About 5,000 sq. ft. will be protected, requiring approximately 50 heads. The existing halon fire protection system in the tandem accelerator control room will be extended to the raised floor area of the new HISTRAP control room.

Electrical service, for the equipment to be located in the new addition, will be provided by two new unit substations to be located in the new second floor addition. Pulsed power loads (the synchrotron magnets and rf power supplies) will be served by a 2000-KVA substation. A 1000-KVA substation will serve the remaining power loads.

6.3 Radiation Safety System

The potential radiation level in the new HISTRAP synchrotron ring will cover a wide range, depending on the type of projectile, the energy, and the intensity. The principal hazardous radiation component is prompt, fast neutrons which are emitted when the energy of a heavy-ion beam striking a target exceeds the Coulomb barrier energy of the target material. This energy is typically 4-6 MeV/nucleon. In one extreme, the new facility will often be used to deliver beams with radiation levels that would allow personnel to work nearby throughout an eight-hour shift without receiving any significant fraction of the permissible dose. An example of such a beam is gold at 4 MeV/nucleon, or 788 MeV total energy. At the other extreme, the high-energy carbon beams can produce radiation levels of several tens of rem/hr at a distance of 1 meter.

Because of the potential for radiation fields on the order of 100 rem/hr, the installation is classified as a "high level irradiation facility," as defined in Sect. 2.13 of the ORNL Health Physics Procedures Manual. The radiation protection system will be designed to comply with the rules and procedures set forth in that document. At the same time, to make effective use of the facility, the proposed system will permit entry into radiation zones when the radiation fields are significantly lower. The design is such that personnel cannot receive more than a permissible dose and, in fact, through administrative control will generally be limited to no more than a small fraction of the permissible dose.

The system is based on the radiation protection system used successfully on the ORNL EN-Tandem for more than two decades and the Holifield Facility for seven years. It is a system of tested and proven reliability and safety, and has been adopted in recent years at other major accelerator facilities.

There are two radiation zones that will be part of the new addition to the existing controlled-entry system. The status of each zone can be either "secured" or "unsecured." The secured mode is used only when the area, by searching, is known to be free of personnel. An area is secured after the search by closing all barriers (doors) to that area and pushing a "secure" button. When an area is secured, a rotating magenta beacon is illuminated and a warning horn sounds. A secured area becomes "unsecure" when a barrier to that zone is opened. This action will cause an audiovisual alarm at the control console of the accelerator and will activate the controlled entry protection system. Each zone contains neutron-gamma ray monitors. Currents proportional to their radiation levels are sent to a "selector" circuit when the zone is unsecured. The largest of the currents is integrated, and if this total exceeds a predetermined limit (less than the allowable radiation dose), the beam is removed from the area by positive means. If the radiation level in any unsecured area exceeds a higher predetermined level (in the HHIRF system this is 1.25 mrem/hr), the beam is removed immediately. In either case, the radiation control officer or other designated persons will review the situation and take appropriate actions.

In order that no single failure can disable the system, critical circuitry is designed to fail in an "alarm" (safe) condition, and all

monitors and all protective circuitry are duplicated to provide redundant channels of protection.

In addition, the system has provisions for selecting operation under completely secured conditions when this mode is deemed appropriate for administrative reasons.

7.0 OAK RIDGE AS A SITE

There are a number of advantages that make Oak Ridge National Laboratory uniquely suited for the site of HISTRAP. These can be characterized by the existence at ORNL of (1) a large effort in experimental and theoretical atomic physics; (2) a strong tradition of university participation; (3) the presence of the 25-MV tandem accelerator of the Holifield Facility; (4) sophisticated support systems already developed in conjunction with Holifield; (5) strong support for HISTRAP from Laboratory management; and (6) the presence of the Joint Institute for Heavy Ion Research. Together, these provide a strong assurance that HISTRAP will be built and operated as a world-class atomic physics user facility. In the following, we address briefly each of these points.

(1) The Physics Division at ORNL supports a large program in atomic physics, almost all of which is devoted to the physics of multiply-charged ions. One group in this program specializes in accelerator based atomic physics, using a dedicated EN tandem Van de Graaff as well as a significant effort on the Holifield tandem. Another group is concerned with basic atomic physics in support of the controlled fusion program and specializes in low-energy, multiply-charged-ion collisions using an electron cyclotron resonance (ECR) ion source. A theoretical group develops new methods for the interpretation of multicharged ion collision phenomena. Members of these groups have contributed much to knowledge in this field and have developed an international reputation for excellence. These existing groups will provide the backbone for a

strong research program on HISTRAP. Publications of these groups, related directly to R&D in support of HISTRAP, are listed in Appendix A.

(2) The Physics Division has a long history of collaborative research with university groups, and of providing use of on-site special facilities to university researchers. A significant amount of atomic physics research, particularly at the EN tandem facility, is performed by guest university faculty and students. These research efforts have a natural evolution to the HISTRAP facility.

(3) The broad selection of ion species and high charge states available from the Holifield 25-MV tandem make it the most powerful injector in the world for a HISTRAP-type device. No other available device can provide the level of performance that will be available here. This injector, in conjunction with the alternate ECR/RFQ injector, also make possible the studies of ion-ion collisions in the HISTRAP ring.

(4) The data acquisition/reduction system developed for the Holifield Facility is generally regarded as the most powerful system available at any nuclear physics facility. This system, and the associated computer personnel, would be available to support the HISTRAP research program. in addition, other specialized areas of technical support developed in conjunction with Holifield research will be available as a resource to the research efforts on HISTRAP.

(5) The strong interest of ORNL management in the HISTRAP project is evidenced by the support provided over the past three years for R&D on critical areas of the HISTRAP design. The principal items developed

under this program were (a) the high-vacuum test stand, (b) the prototype ring dipole magnet, (c) the prototype rf cavity, and (d) the prototype control system. This work will make possible a rapid start on the HISTRAP construction project. Results from these studies are discussed in detail in Chapter 5.

(6) The Joint Institute for Heavy Ion Physics is a joint venture of Oak Ridge National Laboratory, Vanderbilt University, and the State of Tennessee through the University of Tennessee. The purpose of the Institute is to promote research at the local accelerator facilities by providing support to outside users and by maintaining an active visiting scientist program. Housed in two buildings totaling about 10,000 sq ft, the Institute provides short-term office and living accommodations for users during experimental runs. This is particularly attractive for groups with students, since even beginning students can actively participate on the experimental runs at quite minimal cost to the research contract. Visiting scientists are supported for periods ranging from a few days to a year. Last year, the Institute supported 54 guests for an average appointment term of four months. The atomic physics program has already benefited from the Institute program and, with the construction of HISTRAP would anticipate increased support.

8.0 COSTS AND SCHEDULE

8.1 Construction Cost

The cost estimate listed in Tables 8.1-1 and 8.1-2 covers the procurement, installation and testing of a synchrotron ring and injection systems in building additions to the HHIRF, Building 6000, at ORNL. Associated services such as electrical power, cooling water, fire protection, radiation protection, and instrument air have been provided. The building additions consist of a ground floor shielded room, approximately 72 ft x 58 ft, for the synchrotron ring and a second floor addition, approximately 46 ft x 60 ft, to house power supplies and substations. These tables summarize a very detailed cost estimate made by the Physics Division of ORNL and MMES Engineering.

The major cost drivers of the HISTRAP project are the synchrotron ring magnets, magnet power supplies, and an RFQ accelerator. These items are custom fabricated. The estimate is based on detailed bills of material (BM) prepared by all engineering disciplines and by ORNL's Physics Division. The BMs were converted into estimates using cost estimating standard data bases such as Richardson, Means, and an internal data base. These data have been adjusted to reflect the Oak Ridge Operations area and recent experience with FPPC, FPSC, and Energy Systems contracts and forces. Vendor data and prices were used. For most equipment items, potential vendors were contacted and budget quotations were obtained. The pricing of many items reflects experience from previous purchase orders. A number of adjustments have been made to

these prices. Miscellaneous mark-ups ranging from 0% to 10% were used, depending on the type of activity and an evaluation of the completeness of the BMs. These mark-ups are to cover items not called out specifically on the BMs. Indirects for fixed-price contractors are those approved by the Department of Energy, 31% for material and 24% for labor. The indirect for Energy Systems procurement, also approved by the Department of Energy, is 9.5% for procurement. The indirect for Energy Systems labor is included in the labor rate.

The engineering cost estimate is based on work-hour estimates prepared by the participating disciplines. The work-hours are based on the number of documents to be generated and an estimate of management manpower required to execute this project. The estimate work-hours required was developed based on actual experience required to perform similar type projects. The project contingency was determined by an analysis at the third level work breakdown structure. A 20% contingency was used as the base and modified upward or downward based upon the completeness of design and the degree of difficulty.

Table 8.1-1 divides the accelerator facility cost into the major systems in FY 1989 dollars. The first column of Table 8.1-2 lists the major components of the total construction cost in FY 1989 dollars. The second column of Table 8.1-2 gives these costs escalated to 1992, the midpoint of the proposed 1990 to 1994 construction schedule. The total escalated cost of HISTRAP with engineering and contingency as a 1990 project is $16.0M. This estimate does not include cost for existing hardware.

Table 8.1-1. Accelerator cost (FY 1989)
($ x 1000)

Injection beam line - Tandem	$ 665
Injection beam line - ECR-RFQ	1,323
Magnet system	2,169
Rf system	382
Electron cooling system	489
Vacuum	1,342
Beam instrumentation	287
Control	777
Beam line services	189
Total	$7,623

Table 8.1-2. Heavy Ion Storage Ring for Atomic Physics (HISTRAP)
Cost Estimate
($ x 1000)

	FY 1989	Escalated*
Engineering	$ 1,570	$ 1,697
Construction	10,082	11,583
Building Addition	1,502	1,674
Synchrotron Ring	7,623	8,854
Construction Management	957	1,055
Subtotal	11,652	13,280
Contingency	2,396	2,720
Total	$14,048	$16,000

*Midpoint of FY 1990-1994 construction schedule

8.2 Construction Schedule

With funds from the ORNL Director, a prototype dipole has been designed, engineered, fabricated, and measured. This dipole will be acceptable for HISTRAP use. The engineering drawings and tooling for this dipole exist, allowing an immediate procurement of the single most important component of the ring. In addition, the rf cavity for HISTRAP has been fabricated and tested; a vacuum test stand that reaches a pressure of 4×10^{-12} Torr has been built; and a prototype control system has been assembled. This work will allow a rapid and sure procurement of the remaining components required for these systems.

The critical path for the HISTRAP project is established by the time to complete the building for occupancy and the time required to design, engineer, procure, inspect, install, and align the ring magnet system, followed by the installation and connection of the other systems and final subsystem and system tests. The building will be completed and the 8 dipoles, 12 quadrupoles, and 16 sextupoles will be delivered by month 27 of the project. Inspection, installation, and alignment of the magnet system will take until month 33. An additional six months will be required for installation, connection, and alignment of other ring components such as the injection septum, rf cavity, electron cooler, vacuum chambers, and beam line components. Installation of cable trays, magnet power wiring, cooling water supply, vacuum pump systems, and instrumentation and control systems will take the next six months. The final six months will be spent in subsystem and system testing and adjustments as required. The total construction schedule

will be 51 months. After 48 months, some beam should be circulating in HISTRAP.

8.3 Operating Cost

Present programmatic operating costs of the ORNL BES Atomic Physics Programs are about $1500K per year. This includes all professional personnel costs. These costs are not expected to change when the experimental program is transferred from the EN tandem accelerator to the HISTRAP facility. In addition, the fusion energy program supports an atomic physics effort in the Physics Division with an operating cost of about $1500K per year. Some of this work would be performed with the HISTRAP facility. The scientists supported by these existing budgets will insure that HISTRAP will be a world class atomic physics facility.

It is anticipated that HISTRAP will be operated about 4000 hours per year. The power consumption is expected to average about 500 kW, or $120K/year for power at $45/MWh, the present ORNL rate from TVA. It is expected that an operations staff of three operators and one half-time technician, costing $267K at FY 1989 rates, will be needed. Craft support equivalent to one person will be needed and materials and services costs of $50K are assumed. It is also expected that a professional staff consisting of one each mechanical engineer and instrumentation and controls engineer costing $268K will be needed.

This estimate yields an expected operating cost of $795K per year, consisting of $353K for personnel and $260K for materials, services, crafts, and utilities. The present expenditures for the accelerator atomic physics program include $350K for operating the EN tandem Van de

Graaff accelerator. The operation of HISTRAP would thus represent an incremental operating increase of $445K per year. A capital equipment budget, for both accelerator and experimental needs, of $200K per year is projected.

REFERENCES

A188a G. D. Alton and J. W. McConnell, Nucl. Instrum. Methods Phys. Res. A268, 445 (1988).

A188b G. D. Alton, Y. Mori, A. Takagi, A. Ueno, and S. Fukumoto, Letters to the Editor, Nucl. Instrum. Methods Phys. Res. A270, 194 (1988).

A187a G. D. Alton, Proceedings, Eleventh Symposium on Ion Sources and Ion-Assisted Technology, Tokyo, Japan (1987) p. 157.

A187b G. D. Alton, J. W. McConnell, S. Tajima, and G. J. Nelson, Nucl. Instrum. Methods Phys. Res. B24/25, 826 (1987).

A186a G. D. Alton, Nucl. Instrum. Methods Phys. Res. A244, 133 (1986).

A186b G. D. Alton, R. M. Beckers, and J. W. Johnson, Nucl. Instrum. Methods Phys. Res. A244, 146 (1986).

A186c G. D. Alton and C. M. Jones, Nucl. Instrum. Methods Phys. Res. A244, 170 (1986).

A185 G. D. Alton and G. D. Mills, IEEE Trans. Nucl. Sci. NS-32, No. 5, 1822 (1985).

A185 G. D. Alton and C. M. Jones, Fourth International Conference on Electrostatic Accelerator Technology, Nucl. Instrum. Methods Phys. Res. A244, 170 (1986).

A182 Jose Alonso and Harvey Gould, Phys. Rev. A 20, 1134 (1982).

A179 G. D. Alton, IEEE Trans. Nucl. Sci. NS-26, No. 3, 3708 (1979).

An88 L. H. Anderson, H. Knudsen, P. Hvelplund, and S. Datz, unpublished.

REFERENCES (contd)

Be88 J. R. Beene, F. E. Bertrand, D. J. Horen, R. L. Auble, B. L. Burks, J. Gomez del Campo, M. L. Halbert, R. O. Sayer, W. Mittig, Y. Schutz, J. Barrette, N. Alamanos, F. Auger, B. Fernandez, A. Gillibert, B. Haas, and J. P. Vivien, "Heavy-Ion Coulomb Excitation and Photon Decay of the Giant Dipole Resonance in ^{208}Pb," submitted to Physical Review C.

Be88 F. E. Bertrand, J. R. Beene, and D. J. Horen, "Excitation and Photon Decay of Giant Multipole Resonances — The Role and Future of Medium-Energy Heavy Ions," invited paper presented at the Third International Conference on Nucleus-Nucleus Collisions, Saint Malo, France, June 6-11, 1988, to be published in proceedings.

Be84 D. S. Belić, G. H. Dunn, T. J. Morgan, D. W. Mueller, and C. Timmer, Phys. Rev. Lett. 50, 339 (1983); see also A. Müller, D. S. Belić, B. D. DePaula, N. Durić, G. H. Dunn, D. W. Mueller, and C. Timmer, Phys. Rev. A 36, 599 (1987).

Be81 J. S. Bell and M. Bell, Particle Accelerators 11, 233 (1981).

Bo85 F. Bourg, J. Debernardi, R. Geller, B. Jacquet, R. Pauthenet, M. Pontonnier, and P. Sortais, Proceedings, Sixth International Workshop on ECR Sources, Berkeley, CA, January 17-18, 1985, p. 1.

Bo70 C. Bovet, R. Gouiran, I. Gumowski, and K. H. Ralch, "A Selection of Formulae and Data Useful for the Design of AG Synchrotrons," CERN/MPS-SI/Int. DL/70/4, April 23, 1970.

Bu76 G. I. Budker et al., Particle Accelerators 7, 197 (1976).

REFERENCES (contd)

Ca67 R. S. Calder and G. Lewis, Br. J. Appl. Phys. 18, 1459 (1967).

Ca70 Thomas A. Carlson, C. W. Nestor, Jr., Neil Wasserman, and J. D. McDowell, Atomic Data 2, 63-99 (1970).

Ca88 C. Carlsund in IC88.

Ca88 "Ion Storage Rings for Atomic Physics Research," National Academy of Sciences Press (1988).

Di88 P. F. Dittner, S. Datz, R. Hippler, H. F. Krause, P. D. Miller, P. L. Pepmiller, C. M. Fou, Y. Hahn and I. Nasser, Phys. Rev. A 38, 2762 (1988).

Di87a P. F. Dittner, S. Datz, P. D. Miller, P. L. Pepmiller, and C. M. Fou, Phys. Rev. 35, 3668 (1987).

Di87b P. F. Dittner, S. Datz, P. D. Miller, P. L. Pepmiller, C. Bottcher, C. M. Fou, D. C. Griffin, and M. S. Pindzola, Phys. Rev. A 36, 33 (1987).

Di86 P. F. Dittner, S. Datz, P. D. Miller, P. L. Pepmiller, and C. M. Fou, Phys. Rev. A 33, 124 (1986).

Di83 P. F. Dittner, S. Datz, P. D. Miller, C. D. Moak, P. H. Stelson, C. Bottcher, W. B. Dress, G. D. Alton, N. Nesković, and C. M. Fou, Phys. Rev. Lett. 51, 31 (1983).

Do89 D. T. Dowling, R. S. Lord, S. W. Mosko, D. K. Olsen, and B. A. Tatum, "Design, Construction, and Field Mapping of the HISTRAP Prototype Dipole," submitted to the Particle Accelerator Conference, Chicago, March 1989.

REFERENCES (contd)

Ec84 Proceedings, Workshop on Electron Cooling and Related Applications (ECOOL-84), E. Poth, ed., Karlsruhe, W. Germany, KfK 3846.

Ge88 R. Geller, F. Bourg, P. Briand, J. Debernardi, M. Delaunay, B. Jacquot, P. Ludwig, R. Pauthenet, M. Pontonnier, and P. Sortais, NSCL Report #MSUCP-47, J. Parker, ed., December, pp. 1-32 (1987).

Go85 R. A. Gough, J. Staples, R. Caylor, D. Howard, R. MacGill, and J. Tanabe, IEEE Trans. Nucl. Sci. NS-32, 3205 (1985).

Gr88 D. C. Gregory, M. S. Huq, F. W. Meyer, M. Sataka, D. Swenson, and S. Chantrenne, to be published in Physical Review A.

Gu78 G. Guiguard, "A General Treatment of Resonances in Accelerators," CERN 78-11/C1 (1978).

Ha85 C. Habfast et al., CERN-EP/85-49, (1985).

Ha88 D. Habs in "Crystallization of Particle Beams" in Frontiers of Particle Beams, Springer-Verlag 1988, in press.

Ha80 K. Halbach, Nucl. Instrum. Methods Phys. Res. 169, 1 (1980).

He73 W. B. Herrmannsfeldt, SLAC Report 166 (1973).

Ic88 Proceedings, Workshop on Ion Cooling Experiments (ICE-88), Abisco, Sweden, May 4-6, 1988.

Is85 C. Iselin, "The MAD Program," CERN-LEP/TH-85/15 (1985).

Jo88 J. W. Johnson, W. H. Atkins, D. T. Dowling, J. W. McConnell, W. T. Milner, and D. K. Olsen, American Vacuum Society 35th National Symposium and Topical Conference, Atlanta, October (1988).

REFERENCES (contd)

Ka70 I. M. Kapchinskii and V. A. Teplyakov, Pub. Tech. Eksp. 2, 19 (1970).

Ki87 H. J. Kim and R. K. Janev, Phys. Rev. Lett 58, 1837 (1987).

Kr88 D. Kramer, B. Holzer, E. Jaeschke, W. Ott, and B. Repnow, "The Magnet System of TSR," European Particle Accelerator Conference, Rome, Italy, June 1988.

La88 M. Larsson in IC88.

Le87 I. Y. Lee, J. A. Martin, J. B. McGrory, W. T. Milner, D. K. Olsen, and G. R. Young, Proceedings, 1987 IEEE Particle Accelerator Conference, Washington, D.C., p. 310 (1987).

Lo88 R. S. Lord and D. K. Olsen, "Three Dimensional Design of the HISTRAP Prototype Dipole Magnet," Baltimore, APS Meeting, April (1988).

Ly85 C. M. Lyneis and D. J Clark, IEEE Trans. Nucl. Sci. NS-32, 1745 (1985).

Me88 F. W. Meyer, NSCL Report #MSUCP-47, ed. by J. Parker, December, 1987, pp. 520-546.

Me87 F. W. Meyer and J. Hale, Proceedings, 1987 IEEE Particle Accelerator Conference, March 16-19, 1987, Washington, D.C., pp. 319-321.

Me85 F. W. Meyer, Nucl. Instrum. Methods Phys. Res. B9, 532 (1985).

Mi83 R. Middleton, Nucl. Instrum. Methods Phys. Res. 214, 139 (1983).

Mi83 J. B. A. Mitchell, C. T. Ng, J. L. Forand, D. P. Levac, R. E. Mitchell, A. Sen, D. B. Miko, and J. W. McGowan, Phys. Rev. Lett. 50, 335 (1983).

REFERENCES (contd)

Mo88 Y. Mori, G. D. Alton, A. Takagi, A. Ueno, and S. Fukumoto, to be published in Nucl. Instrum. Methods in Physics Research.

Mo87 Y. Mori, A. Takagi, K. Ikegami, and S. Fukumoto, Proceedings, Fouth International Conference on Production and Neutralization of Negative Ions and Beams, edited by James G. Alessi (AIP Conf. Proceedings No. 158, New York, 1987), p. 378.

Mo89 S. W. Mosko, D. T. Dowling, and D. K. Olsen, "Prototype RF Cavity for the HISTRAP Accelerator," submitted to the Particle Accelerator Conference, Chicago, March 1989.

Mp84 Proceedings, Workshop on Physics with Heavy Ion Storage Rings, Max Planck Institute für Kernphysik, Heidelberg, W. Germany, 1984.

Mu88 A. Müller, K. Tinschert, G. Hofmann, E. Salzborn. and G. H. Dunn, Phys. Rev. Lett. 61, 70 (1988).

Ol87 D. K. Olsen, G. D. Alton, S. Datz, P. F. Dittner, D. T. Dowling, D. L. Haynes, E. D. Hudson, J. W. Johnson, I. Y. Lee, R. S. Lord, C. A. Ludemann, J. A. Martin, J. B. McGrory, F. W. Meyer, P. D. Miller, W. T. Milner, S. W. Mosko, P. L. Pepmiller, and G. R. Young, "The HISTRAP Proposal: Heavy Ion Storage Ring for Atomic Physics," Proceedings, 1987 IEEE Particle Accelerator Conference, Washington, D.C., p. 310 (1987).

REFERENCES (contd)

Ol86 D. K. Olsen, G. D. Alton, S. Datz, P. F. Dittner, D. T. Dowling, D. L. Haynes, E. D. Hudson, J. W. Johnson, I. Y. Lee, R. S. Lord, C. A. Ludemann, J. A. Martin, J. B. McGrory, F. W. Meyer, P. D. Miller, W. T. Milner, S. W. Mosko, P. L. Pepmiller, and G. R. Young, "The HISTRAP Proposal: Heavy Ion Storage Ring for Atomic Physics," Proceedings, Eleventh Conference on Cyclotrons and Their Applications, Tokyo, Japan, p. 134 (1986).

Or86 Proceedings, Workshop on Atomic Physics with Stored Cooled Heavy Ion Beams, Oak Ridge, Tennessee, S. Datz, ed., ORNL-CONF-860144 (1986).

Po87 A. Poncet, CERN (private communication).

Po84 A. Poncet, in "Mini-Symposium on UHV-Systems in Connection with Particle Accelerators," Stockholm, Sweden, Oct. 9-11, 1984, eds. T. Lindblad, L. Bagge, and L. Westerberg.

Po84 H. Poth, ECOOL-Workshop, Karlsruhe, 1984.

Pt88 "Physics Today," September 1988, pp. 17-20.

Ra87 A. Rahman and J. P. Schiffer, Phys. Rev. Lett. 57, 1133 (1986).

Ru77 C. Rubbia, CERN-EP/77-2, (1977).

Sc84 Alfred S. Schlachter, Tenth International Conference on Cyclotrons and Their Applications, MSU, April 29 - May 3, 1984. ed. F. Marti, IEEE Catalog No. 84CH1996-3, pp. 563-70.

Sk87 R. Skeltan, BNL (private communication).

REFERENCES (contd)

S187 T. Sloan, O. Dermois, and M. Yurko, "Fabrication and Magnetic Field Measurements of the IUCF Cooler Ring Dipole Magnets," IEEE No. 87CH2387-9, 1443 (1987).

St85 J. Staples, R. Dwinell, R. Gough, J. Halliwell, D. Howard, J. Lax, S. Lundgren, R. Richter, G. Stover, and J. Tanabe, IEEE Trans. Nucl. Sci. NS-32, 3208 (1985).

St81 R. M. Stokes, T. P. Wangler, and K. R. Crandall, IEEE Trans. Nucl. Sci. NS-28, 1999 (1981).

Th83 P. Thieberger, M. McKeown, and H. E. Wegner, IEEE Trans. Nucl. Sci. NS-30, No. 4, 2746 (1983).

Th83 P. Thieberger, M. McKeown, and H. E. Wegner, IEEE Trans. Nucl. Sci. NS-30, No. 40, 2749 (1983).

Ty76 P. Tykesson, H. H. Andersen, and J. Heinemeier, IEEE Trans. Nucl. Sci. NS-23, No. 2, 1104 (1976).

Wi84 J. F. Williams, Phys. Rev. A 29, 2936 (1984).

Yo84 R. L. York and R. R. Stevens, Proceedings, Third International Conference on the Production and Neutralization of Negative Ions and Beams, edited by Krysto Prelec (AIP Conf. Proceedings No. 111, New York, 1984) p. 410.

APPENDIX A

BIBLIOGRAPHY OF HISTRAP RELATED PAPERS AND PRESENTATIONS BY ORNL STAFF MEMBERS

1 9 8 4

S. Datz, P. F. Dittner, P. D. Miller, and P. L. Pepmiller, "Dielectronic Recombination in a Single Pass Experiment," Proceedings, Workshop on Electron Cooling and Related Applications (ECOOL-84), ed. E. Poth, Karlsruhe, W. Germany, KfK 3846, pp. 401-414.

1 9 8 6

Conceptual documents for budget year 1988; Heavy Ion Storage Ring for Atomic Physics; X-OE-324,-325,-327; Martin Marietta Energy Systems, Inc. Engineering, March 1986.

Detailed Cost and Schedule Document for Budget Year 1988, Heavy Ion Storage Ring for Atomic Physics; Martin Marietta Energy Systems, Inc. Engineering, February 1986.

G. D. Alton and C. M. Jones, "Pulsed Mode Evaluation of an Axial Geometry Cesium Sputter Negative Ion Source," Nucl. Instrum. Methods Phys. Res. A244, 170 (1986).

S. Datz, "Heavy Ion Storage Rings: A Survey," Proceedings, Workshop on Atomic Physics with Stored Cooled Heavy Ion Beams, S. Datz editor, USDOE Conf. 860144, April 1986.

D. K. Olsen, G. D. Alton, S. Datz, P. F. Dittner, D. T. Dowling, D. L. Haynes, E. D. Hudson, J. W. Johnson, I. Y. Lee, R. S. Lord, C. A. Ludemann, J. A. Martin, J. B. McGrory, F. W. Meyer, P. D. Miller, W. T. Milner, S. W. Mosko, P. L. Pepmiller, and G. R. Young, "The HISTRAP Proposal: Heavy Ion Storage Ring for Atomic Physics," Proceedings, Eleventh Conference on Cyclotrons and Their Applications, Tokyo, Japan, p. 134 (1986).

R. Schuch, "Electron-Ion Collisions with Heavy Ion Cooler Ring," (Invited) Proceedings, U.S-Mexico Atomic Physics Symposium on Two Electron Phenomena, Mexico City, January 8-11, 1986.

R. Schuch, "Recombination at a Heavy Ion Cooling Section Investigated by Photon Spectroscopy and Laser Interaction," Proceedings, Workshop on Atomic Physics with Stored Cooled Heavy Ion Beams, S. Datz editor, USDOE Conf. 860144, April 1986.

R. Schuch, "Atomic Physics with Heavy Ion Storage Rings," (Invited) Proceedings, Colloque National de Collision Atomique, Metz, France, June 16-20, 1986.

1 9 8 6 (contd)

G. R. Young, "HISTRAP: The Oak Ridge Proposal," Proceedings, Workshop on Atomic Physics with Stored Cooled Heavy Ion Beams, S. Datz editor, USDOE Conf. 860144, April 1986.

G. R. Young, "Storage Ring for Heavy Ion Atomic and Nuclear Physics," Proceedings, Second Conference on Interaction Between Particle and Nuclear Physics, (Invited) Lake Louise, Canada, May 1986.

1 9 8 7

S. Datz, "Atomic Physics Experiments with Cooled Heavy Ion Beams," (Invited) Nucl. Instrum. Methods Phys. Res. B24, 3 (1987).

I. Y. Lee, J. A. Martin, J. B. McGrory, W. T. Milner, D. K. Olsen, and G. R. Young, "Lattice Design of HISTRAP: Heavy Ion Storage Ring for Atomic Physics," Proceedings, 1987 IEEE Particle Accelerator Conference, Washington, D.C. (1987), p. 310.

D. K. Olsen, G. D. Alton, S. Datz, P. F. Dittner, D. T. Dowling, D. L. Haynes, E. D. Hudson, J. W. Johnson, I. Y. Lee, R. S. Lord, C. A. Ludemann, J. A. Martin, J. B. McGrory, F. W. Meyer, P. D. Miller, W. T. Milner, S. W. Mosko, P. L. Pepmiller, and G. R. Young, "The HISTRAP Proposal: Heavy Ion Storage Ring for Atomic Physics," (Invited) Nucl. Instrum. Methods Phys. Res. B24/25, 26 (1987).

R. Schuch, "Storage Rings for the Investigation of Ion-Atom Collisions," (Invited) Proceedings, Third Workshop on High Energy Ion-Atom Collisions, Debrecen, Hungary, August 3-5, 1987.

R. Schuch, "Heavy Ion Storage Rings," (Invited) Proceedings, Workshop on Opportunities for Atomic Physics with Highly Charged Ions, Argonne National Laboratory, January 12-13, 1987.

G. D. Alton, Y. Mori, A. Takagi, A. Veno, and S. Fukumoto, "A Versatile High Intensity Plasma Sputter Heavy Negative Ion Source," Letters to the Editor, Nucl. Instrum. Methods Phys. Res. A270, 194 (1988).

G. D. Alton, Y. Mori, A. Tekagi, A. Veno, and S. Fukumoto, "A High Brightness Plasma Sputter Negative Ion Source," (Invited) The Tenth Conference on Applications of Accelerators in Research and Industry, Denton, Texas (1988).

C. Carlsund, N. Elander, R. Mowat, D. C. Griffin, and M. Pindzola, "On Recombination Losses in Electron Cooling of Highly Charged Ions," Physica Scripta T22, 243 (1988).

1 9 8 8 (contd)

S. Datz, "HISTRAP Status Report," Proceedings, Workshop on Ion Cooler Rings (ICE-88), (invited) Abisco, Sweden, May 4-6, 1988.

S. Datz, "Dielectronic Recombination," Proceedings, Workshop on Ion Cooler Rings (ICE-88), (invited) Abisco, Sweden, May 4-6, 1988.

S. Datz, L. H. Andersen, J. P. Briand, and D. Liesen, (invited) "Experimental Atomic Physics in Heavy Ion Storage Rings," Physica Scripta T22, 224 (1988).

S. Datz, D. Olsen and G. Young, "HISTRAP - The Oak Ridge Heavy Ion Storage Ring for Atomic Physics," (oral presentation) Proceedings, Workshop and Symposium on the Physics of Low-Energy Stored and Trapped Particles, Stockholm, Sweden, June 14-18, 1987.

P. F. Dittner, "Dielectronic Recombination Measurements of Multicharged Ions," Physica Scripta T22, 65 (1988).

J. W. Johnson, W. H. Atkins, D. T. Dowling, J. W. McConnell, W. T. Milner, and D. K. Olsen, "HISTRAP Vacuum Test Stand for Pressures of 10^{-12} Torr," American Vacuum Society 35th National Symposium and Topical Conference, Atlanta, October 1988.

R. S. Lord and D. K. Olsen, "Three Dimensional Design of the HISTRAP Prototype Dipole Magnet," BAPS 33, 1027 (1988).

H. Poth, W. Schwab, B. Seligman, M. Wörtge, A. Wolf, S. Baird, M. Chanel, H. Haseroth, C. E. Hill, R. Ley, and P. F. Dittner, "First Results of Electron Cooling Experiments at LEAR," Zeitschrift für Physik A (in press).

R. Schuch, H. Poth and A. Wolf, "X-Ray Measurements at the Stand-Alone Electron Cooler for LEAR," Proceedings, European Particle Accelerator Conference, Rome, Italy, June 7-11, 1988.

A. Wolf, H. Poth, W. Schwab, B. Seligman, M. Wörtge, P. Dittner, S. Baird, J. Bosser, M. Chanel, H. Haseroth, C. E. Hill, R. Ley, D. Manglunki, D. Möhl, G. Molinari, G. Tranquille, and J.-L. Vallet, "Results from Electron Cooling Experiments at LEAR," Proceedings, European Particle Accelerator Conference, Rome, Italy, June 7-11, 1988.

1 9 8 9

S. Datz, (invited) "Atomic Physics in Heavy Ion Storage Rings," Physics Today.

D. T. Dowling, R. S. Lord, S. W. Mosko, D. K. Olsen, and B. A. Tatum, "Design, Construction, and Field Mapping of the HISTRAP Prototype Dipole," submitted to the 1989 IEEE Particle Accelerator Conference, Chicago, March 1989.

S. W. Mosko, D. T. Dowling, and D. K. Olsen, "Prototype RF Cavity for the HISTRAP Accelerator," submitted to the 1989 IEEE Particle Accelerator Conference, Chicago, March 1989.

APPENDIX B

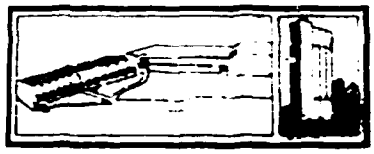

Workshop on

ATOMIC PHYSICS WITH STORED COOLED HEAVY ION BEAMS

Oak Ridge, Tennessee

January 13-15, 1986

December 6, 1985

WORKSHOP PROGRAM

ATOMIC PHYSICS WITH STORED COOLED HEAVY ION BEAMS

January 13-15, 1986
Oak Ridge, Tennessee

Monday Morning, Jan. 13 (chairman) J L Duggan, North Texas State University

8:30	Introduction & Welcome	A Zucker, ORNL
9:00	Heavy Ion Storage Rings: A Survey	S Datz, ORNL
9:30	Aarhus Project	P Hvelplund, Aarhus Univ.
10:00	COFFEE BREAK	
10:30	Heidelberg Project (TSR)	R Schuch, University of Heidelberg
11:00	Brookhaven Proposal	K W Jones, Brookhaven National Lab
11:30	Oak Ridge Proposal (HISTRAP)	G R Young, ORNL
12:00	LUNCH	

Monday Afternoon, Jan. 13 (chairman) C Bottcher, ORNL

1:30	Electron Cooling of Stored Beams	R E Pollock, Indiana College
2:00	Laser Cooling of Stored Beams	A Migdall, NBS, Washington
2:20	COFFEE BREAK	

ION-ATOM COLLISIONS

2:30	Charge Transfer in High Energy Ion-Atom Collisions: Experiment	A S Schlachter, Lawrence Berkeley
3:00	Charge Transfer in High Energy Ion-Atom Collisions: Theory	J Macek, University of Nebraska
3:30	Low Energy Collision Physics Using Recoil Ion Beams	C L Cocke, Kansas State University
4:00	Collision Experiments with Decelerated and Cross'd Beams in Heavy Ion Cooler Rings	R Schuch, University of Heidelberg
[illegible]	Forward Ejected Auger Electron Spectroscopy	N Stolterfoht, Hahn Meitner Institute, Berlin (ORNL)

[illegible]
Oak Ridge National Laboratory
[illegible]

[illegible]
Joint Institute for Heavy Ion Research
Holifield Heavy Ion Research Facility
Oak Ridge, Tennessee
[illegible]

Sponsored by:
Physics Division of
Oak Ridge National Laboratory
Joint Institute for Heavy Ion Research

Tuesday Morning, Jan. 14 (chairman) R Schmieder, Sandia National Laboratory

ELECTRON-MULTICHARGED ION INTERACTIONS

9:00	Excitation and Ionization in Electron Multicharged Ion Collisions: Experiment	G H Dunn, Joint Institute for Laboratory Astrophysic
9:30	Excitation and Ionization in electron Multicharged Ion Collisions: Theory	R J W Henry, Louisiana State Univ
10:00	Dielectronic Recombination of Multicharged Ions	P D Miller, ORNL
10:30	COFFEE BREAK	
11:00	Theory of Recombination with Multicharged Ions	D C Griffin, Rollins College
11:30	Recombination at a Heavy Ion Cooling Section Investigated by Photon Spectroscopy and Laser Interaction	R Schuch, Heidelberg Univ.
12:00	LUNCH	

Tuesday afternoon, Jan. 14 (chairman) K MacAdam, University of Kentucky

1:30	On the Possibility of Forming "Crystalized" Ion Beams	J P Schiffer, Argonne National Lab.
2:00	Precision Spectroscopy of One and Two Electron Ions	R D Deslattes, National Bureau Standards
2:30	Laser-Ion Spectroscopy	H G Berry, Argonne National Lab.
3:00	Spectroscopy of Molecular Ions	T Oka, University of Chicago
3:30	Interaction of Synchrotron Radiation with Stored Beams	B M Johnson, Brookhaven Nat. Lab.
4:00	COFFEE BREAK	
4:30	Atomic Data for Highly Charged Ions: Applications to X-Ray Lasers and Plasma Spectroscopy	S M Younger, Lawrence Livermore Lab.

Wednesday morning, Jan. 15

9:00 - 12:00 noon
Panel Discussions on New Research Opportunities With Stored Cooled Ion Beams

ACKNOWLEDGMENTS

This proposal was prepared by the Physics Division of Oak Ridge National Laboratory. We would like to acknowledge the contributions of Janette McBridge, Lynda Saddiq, Shirley Ball, Christine Wallace, Kay Thacker, and Audrey Livingston for their help in preparing this document.

Information for this proposal was prepared by the following members of the Physics Division:

G. D. Alton	Ion Source
W. H. Atkins	Computer Controls
J. B. Ball	Physics Division Director
F. E. Bertrand	Physics
J. A. Biggerstaff	Computer Controls
S. Datz	Physics
P. F. Dittner	Physics, Electron Cooling System
D. T. Dowling	Magnets, RF, Vacuum
D. C. Gregory	Physics
D. L. Haynes	Building Services, Injection Line
E. D. Hudson	Magnets
J. W. Johnson	Vacuum, Survey
C. M. Jones	HHIRF Accelerator Section Head
R. C. Juras	Computer Controls
I. Y. Lee	Design Group
R. S. Lord	Magnets (Consultant)
J. E. Mann	Building Services
J. A. Martin	Design Group
J. B. McGrory	Design Group
F. W. Meyer	ECR Source, RFQ Linac
J. W. McConnell	Computer Controls
P. D. Miller	Physics
W. T. Milner	Design Group
S. W. Mosko	RF, Power Supplies
D. K. Olsen	Design Group
D. J. Pegg	Physics
P. L. Pepmiller	Physics, Beam Instrumentation
R. A. Phaneuf	Physics
M. L. Plotkin	RF System (Consultant)
B. A. Tatum	Magnets
C. R. Vane	Beam Instrumentation
G. R. Young	Design Group

With assistance from the following members of the Martin Marietta Energy Systems Engineering Division:

R. M. Beckers	Principal Engineer and Mechanical Design
J. T. Cleveland	Electrical Engineering
D. A. Keith	Estimating
J. D. Lawrence	Site Engineering
D. E. Lind	Structural Engineering
J. M. Morrison	Environmental Control
J. A. Murray	Engineering Project Manager
J. N. Turpin	Engineering Mechanics
C. D. Williams	Engineering Quality Assurance